UNIVERSITÀ
DI SIENA
1240

DEPARTMENT OF INFORMATION ENGINEERING AND MATEHEMATICS

Ph.D. Course in
INFORMATION ENGINEERING AND SCIENCE
XXXV Cycle

Autonomous Sensing Nodes for IoT Applications

Supervisor:
Prof. Ada Fort

Candidate:
Irene Cappelli

Coordinator
Prof. Mauro Barni

Contents

List of Figures

List of Tables

Introduction

One of the greatest challenges of modern days is the realization of intelligent devices offering an accurate remote monitoring service and whose life-time duration is the highest possible, in order to minimize the human intervention on the field. If this requirement can be partially disregarded in case of sensor nodes powered by electrical sockets, it becomes mandatory for those applications deployed in large quantities or in critical scenarios, where the connection to the electricity grid is not accessible or affordable and thus the careful management of the available energy represents the only solution. Nowadays, the use of disposable batteries is the main adopted answer to face the lack of energy availability, but in the long term it is no more a sustainable solution since the battery replacement represents a high cost in terms of human and economic resources and, in general the nodes might be deployed in places that are hard to be reached.

The number of wireless sensing systems and smart devices employed either in the Internet of Things (IoT) or in the Wireless Sensor Network (WSN) frameworks is rapidly expanding. The impact of this phenomenon is highlighted by the numbers shown in Figure 1: compared to a number of mobile connections equal to almost 8 billion, there are already over 12 billion connected IoT devices in 2021 [1], a huge number destined to grow in a massive way in coming years. This aspect makes the use of disposable batteries unthinkable and by now anachronistic and pushed towards the definition of new paradigms.

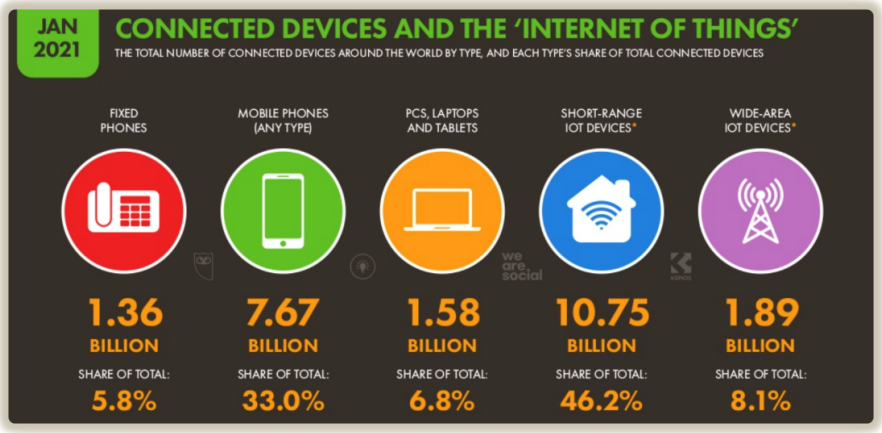

Figure 1. Number of connected devices around the world until January 2021 [1].

These challenges are growing hand in hand with a novel sensitivity, both in public opinion and in the scientific community, towards issues related to environment protection and energy saving, that also led in recent years to a remarkable increase in the use of renewable energy [2] as promising and environmentally friendly alternative to fossil fuels, especially in those areas without connection to the energy grid. The IoT and in general the WSNs can potentially benefit most from this trend, foreseeing the usage of clean energy as main power source to guarantee the system energy autonomy for a certain amount of time or in sight of expanding at least its average lifetime. Thus, energy scavenging technologies show great promise in powering the IoT explosion, solving the bottleneck of battery replacement for remote deployments.

However, the careful management of the available energy must not only go through the study of new techniques for energy provisioning but must also pay attention to the design phase of the device, both at the hardware level and for the programming techniques. Moreover, when developing IoT-based distributed systems, a challenging aspect related to power consumption concerns the integration of sensing and data transmission features on board since these tasks are often conflicting with the low-power requirement. For this reason, strong efforts have been made in the last years to develop novel telecommunication technologies with the aim of satisfying two crucial requirements: low power consumption and long-range data transmission. This led to the emergence of a new set of telecommunication technologies indicated in general as Low Power Wide Area Networks (LPWANs), among which Long Range Wide Area Network (LoRaWAN) is a de-facto standard. Regarding sensing, a compromise must always be sought between the required accuracy and the energy limits, which translates into a thoughtful choice of sensing mechanisms and electronic devices, and an adequate electronic design that minimizes consumption. In addition, since the foreseen applications are framed in a perspective of distributed sensor networks, further constraints to be considered in the design phase might be the cost – both for the components and for the harvester –, the availability of the components – if possible off-the-shelves devices that can be retrieved on large scale – and the dimensions of the entire device – which results especially in small-sized area harvesters.

The present doctoral thesis fits into the energy harvesting framework, presenting the development of low-power nodes compliant with the energy autonomy requirement, and sharing common technologies and architectures, but based on different energy sources and sensing mechanisms.

The adopted approach is aimed at evaluating multiple aspects of the system in its entirety (i.e., the energy harvesting mechanism, the choice of the harvester, the study of the sensing process, the selection of the electronic devices for processing, acquisition and measurement, the electronic design, the microcontroller unit (MCU) programming techniques), accounting for very challenging constraints as the low amounts of harvested power (i.e., [μW, mW] range), the careful management of the available energy, the coexistence of sensing and radio transmitting features with ultra-low power requirements. Commercial sensors are mainly used to meet the cost-effectiveness and the large-scale reproducibility requirements, however also customized sensors for a specific application (soil moisture measurement), together with appropriate characterization and reading circuits, are also presented.

Two different strategies have been pursued which led to the development of two types of sensor nodes, which hereinafter are referred to as 'sensor tags' and 'self-sufficient sensor nodes'. The first term refers to completely passive sensor nodes without an on-board battery as storage element and which operate only in the presence of the energy source, provisioning energy from it; systems of this type are not suitable for continuous monitoring applications but can still find application in all those contexts where the quantities of interest are needed on demand. In this thesis, an RFID (Radio Frequency Identification) sensor tag powered by the impinging electromagnetic field is presented. The second term identifies sensor nodes equipped with a battery rechargeable through energy scavenging and working as a secondary reserve in case of absence of the primary energy source; this approach is necessary in all those situations in which the monitoring of the parameters of interest must be continuous. These nodes are also equipped with a radio transmission module to make the data remotely accessible to the operator.

Chapters 1 and 2 are dedicated respectively to a brief introduction on the physical principles linked to RFID sensor tags and to an overview of the designed prototype specifically thought for soil moisture monitoring, paying great attention to the preparation, the modeling, and the characterization of the employed prototype sensors. Chapters 3-7 deal with self-sufficient sensor nodes, embedding LoRaWAN transmission and provisioning energy from different energy sources, both from the point of view of the preliminary study and of the practical implementation. In particular, Chapter 3 illustrates some basic principles linked to the considered energy harvesting mechanisms and harvesters and the architecture of a typical power management unit (PMU) for the energy provisioning. In the following Chapters some developed systems are reported: the focus is primarily posed on the selected harvester and the

realized sensor node, then the energy autonomy of the system is investigated in view of deploying install-and-forget pervasive monitoring sensor networks. In more detail, Chapters 4-7 explore the applicability boundaries of harvesting respectively from thermoelectricity, diffused solar light, indoor white light, and artificial colored light for quasi-real-time multi-purpose monitoring LoRaWAN nodes. While in Chapters 4 and 5 a preliminary study is presented, also providing an overview of the LoRa technology, Chapter 6 and 7 investigate specific applications which are respectively indoor localization via visible light and monitoring of environmental quantities in indoor greenhouses. Finally, in Appendix A, the theoretical study of the transmission performance of the LoRaWAN radio technology in case of critical operative scenarios (i.e., transmission from underwater and from a thick layer of ice) is reported and validated with in-field tests.

Chapter 1
HF Sensor Tags: principle and technology

Since its emergence, RFID technology has been employed for items identification and tracking [3, 4, 5, 6] with applications primarily limited to industrial and commercial fields. Between the set of RFID techniques, NFC (Near Field Communication) has recently found a vast use in contact-less payment systems, thanks to the availability of NFC-enabled smartphones in place of specific RFID readers. In the latest years, the development of low-power components and the rising awareness on green electronics technology have encouraged the emergence of the so-called sensor tags. They are RFID transponders that overcome the traditional usage for basic item identification, providing additional sensing capabilities, thanks to the integration of electronic components like MCUs and sensors. The versatility, the reduced dimensions, the energy efficiency, the general-purpose nature, the virtually unlimited lifetime are some of the advantages that make sensor tags ideal solutions in several contexts, from the monitoring of environment and civil structures to the safeguard of human health, also finding application in a wide range of different industrial sectors.

1.1. Sensor Tag classification

Sensor tags share with traditional RFID systems the same classifications based on powering method (i.e., active, passive, semi-passive) and operating frequency ranges (i.e., LF – low frequency, HF – high frequency, UHF – ultrahigh frequency, microwaves). Moreover, two operating principles can be distinguished: systems equipped with sensors on board, both commercial or customized, which are usually managed by an onboard MCU, and sensor-less systems where the sensing is obtained as alterations in the tag response due to variations of the tag antenna material or shape, induced by changes in the physical quantities to be measured. Although this second method requires the presence of a more limited hardware on board of the tag, the complexity increases at the receiver side, where appropriate customized hardware and software must post-process the received signal to recover the sensing information. On the contrary, the presence of a MCU on board of the tag allows to send already

processed data which are therefore readable with any commercial reader working at the appropriate frequency.

Moreover, passive and semi-passive tags – which respectively do not have any power supply on board or mount a battery used as energy storage to power up the circuitry – allow to design completely autonomous sensing devices where the required energy is extracted by the incoming electromagnetic field generated by the reading instrument. The retransmission is attained by backscattering the reader incoming field without autonomous generation of the carrier frequency on board. Accordingly, when the tag is outside the interrogation zone of the reader, power supply and downlink communication are absent.

1.2. RFID physical principles

An RFID system is broadly composed of two elements [7, 8]:

- Reader. It is the querying system which interrogates the remote tag; it has a RF Tx/Rx module on board, a control unit, a transmitting antenna and a serial interface to the host device which performs data management;
- Tag. It is the remote element equipped with a receiving antenna, coupled to the one of the interrogator. It can mount a storage element and a microchip in charge of converting the incoming radio-frequency energy in a rectified voltage used to supply the on-board circuitry, retransmitting the information to the reader through modulation and storing the tag information in a programmable memory. Electronic circuitry may also be present for the autonomous generation of the carrier frequency for retransmission.

In case of HF RFID applications, simple loop antennas can be used both for tag and reader and the working principle exploited is inductive coupling: when tag and reader antennas are close to each other, an alternate current in the reader coil gives rise to an alternate magnetic field according to Ampère's Law which concatenates with the tag antenna, inducing a voltage on it for Faraday-Neumann-Lenz's Law; this voltage difference produces a current flow in the tag loop and accordingly a magnetic flux which, interacting with the reader magnetic field, causes changes in its current.

The coupling flux will depend on the medium, the geometry of both coils and their relative positions: in fact, the maximum power transfer is obtained when the two antennas are

in line-of-sight and parallel to each other (i.e., the directions of maximum intensity of the radiation diagrams of the two coils are aligned).

Each coil equivalent circuit is the series of the self-inductance L, and of a resistance R accounting for the ohmic losses of the wire; the presence of a parasitic capacitance responsible of the antenna self-resonance can be neglected. The self-inductances of the primary and secondary coils $L_{1,2}$ represent the property of the circuits to oppose to the variations of the current, that determine time-varying magnetic fluxes, and are defined as $L_{1,2} = \frac{\Phi(i_{1,2})}{i_{1,2}} = -v_{1,2}\left(\frac{di_{1,2}}{dt}\right)^{-1}$ where $\Phi(i_{1,2})$ is the magnetic field flux through the coil n ($n = 1,2$) generated by the current in the same coil, i_n.

The coupling of the two coils is described by the mutual inductance defined as $M = M_{12} = N_1 \frac{\Phi_{1,2}(i_2)}{i_2} = M_{21} = N_2 \frac{\Phi_{2,1}(i_1)}{i_1}$, with N_1 and N_2 number of the turns of first and second coil and $\Phi_{n,m}(i_n)$ the flux through the coil n generated by the current i_m ($n = 1,2$; $m = 1,2$). Another formulation is $M = k\sqrt{(L_1 L_2)}$ where k is the coupling coefficient: when k = 0 also M = 0 hence there is full decoupling, while when k = 1 there is total coupling.

When connecting the second coil to a resistive load R_L, that in the presented application can represent the input impedance of the tag chip, the equivalent circuit of Figure 2 is obtained and the voltage across the load, used to provide its supply, can be derived as $v_2 = M\frac{di_1}{dt} - i_2 R_2 - L_2 \frac{di_2}{dt}$, which in the Fourier domain gives $V_2 = \frac{j\omega M I_1}{1+\frac{R_2+j\omega L_2}{R_L}}$.

The efficiency can be increased by adding a parallel capacitor C_2 as in Figure 3 forming with L_2 a resonant circuit at frequency $f_r = \frac{1}{2\pi\sqrt{C_2 L_2}}$ and modifying V_2 as $V_2 = \frac{j\omega M I_1}{1+(R_2+j\omega L_2)\left(j\omega C_2+\frac{1}{R_L}\right)}$. Hence the capacitor C_2 can be chosen in such a way to obtain a resonant frequency f_r equals to the working frequency of the interrogator.

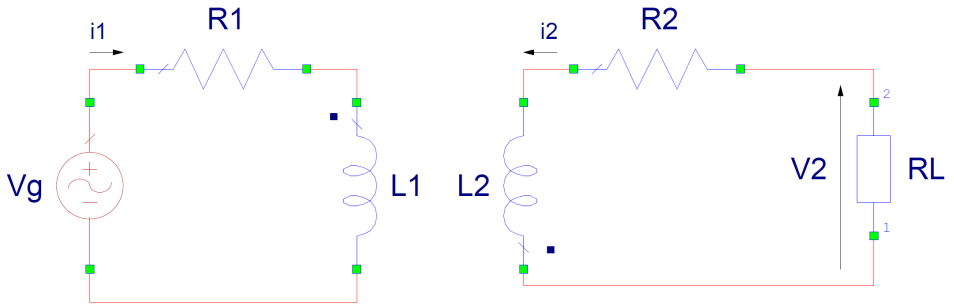

Figure 2. Equivalent circuit of two coupled coils, the receiver one is closed on a resistive load R_L.

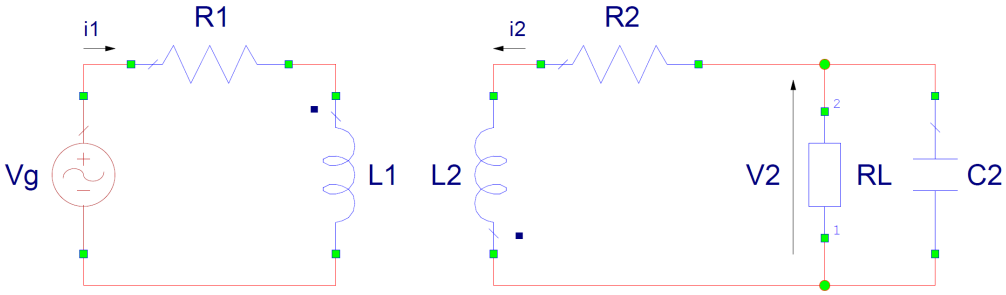

Figure 3. Equivalent circuit of two coupled coils, the receiver one is closed on a load R_L and a capacitor C_2.

The effect of C_2 is visible in Figure 4a, where the trend of $|V_2|$ in frequency is reported both for the non-resonant and the resonant circuits assuming equal coils for tag and reader and k = 0.5, I_1 = 0.01 A, L_1= L_2= 5 μH, R_1= R_2= 9 Ω, C_2= 27 pF, R_L = 5 kΩ: when adding the parallel capacitor C_2 the amplitude of the voltage at the load in correspondence of the reader working frequency f_r increases.

The Q factor can be used to compare the stored and the dissipated energy of a resonant circuit. A general expression is $Q = 2\pi f_r \frac{\text{energy stored}}{\text{power loss}}$ but can be also defined in terms of f_r and –3 dB bandwidth Δf as $Q = \frac{f_r}{\Delta f}$. A higher Q means lower losses and greater frequency selectivity to the detriment of the system bandwidth, indeed if Q is too high the bandwidth can become too narrow, and a degraded communication may happen unless a very accurate tuning of f_r to the reader operating frequency is always granted. Applied to the circuit in Figure 3, the Q factor at the resonance is $Q \simeq \omega_r \frac{\frac{1}{2}L_2|I_2|^2}{R_2|I_2|^2+\frac{|V_2|^2}{R_L}} = \frac{1}{2}\frac{1}{\frac{R_2}{\omega_r L_2}+\frac{\omega_r L_2}{R_L}} = \frac{1}{2}\frac{1}{\frac{R_2}{\omega_r L_2}+\frac{1}{R_L \omega_r C_2}}$; its trend as a function of L_2 and computed for $f_r = \frac{\omega_r}{2\pi}$ =13.56 MHz, R_2= 9 Ω and R_L = 5 kΩ is reported in Figure 4b.

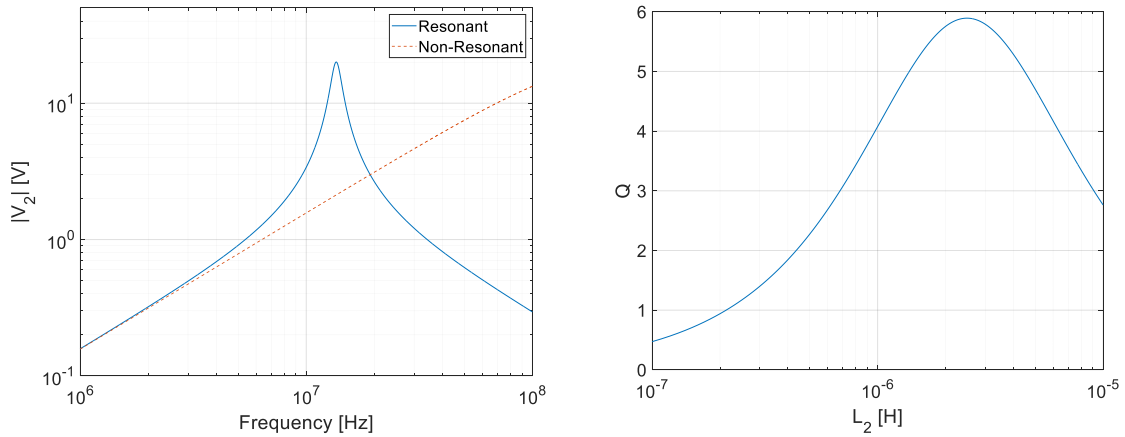

(**a**) (**b**)

Figure 4. **a**) Trend of $|V_2|$ in frequency in case of non-resonant (red plot) and resonant (blue plot) circuits, computed assuming equal coils for tag and reader and k = 0.5, I_1 = 0.01 A, L_1= L_2= 5 μH, R_1= R_2= 9 Ω, C_2= 27 pF, R_L = 5 kΩ. **b**) Trend of the Q factor as a function of L_2 in case of resonant circuit and computed for $f_r = \frac{\omega_r}{2\pi}$ =13.56 MHz, R_2= 9 Ω and R_L = 5 kΩ.

1.3. Data transmission, protocols and standards

The uplink data transfer from reader to tag follows these steps: coding of the data stream that must be delivered to the tag, modulation of the carrier according to the coded baseband signal, transmission by means of magnetic field (inductive coupling).

The baseband coding choice depends on different factors such as the characteristics of the transmission channel, the tolerated transmission error, the power consumption, the anti-collision and the non-interference constraints. Some examples of coding procedures are: Non-Return to Zero, Unipolar Return to Zero, Manchester, Miller, Differential and Pulse Position. Pulse Position is one of the codings that best meets the requirements of maximizing the transmitted signal energy and synchronizing with the reader since it has an almost constant high value (guaranteeing continuous power supply during the transfer) and it is based on pulse duration (producing a time-controlled coded sequence which allows to simplify the synchronization circuitry on board of the passive tag) [7, 8]. For example, using 1 out of 256 Pulse Positions each byte is represented by the position of one pause on 1 of 256 successive time periods.

The coded signal is then converted from baseband to radio-frequency band using a digital modulation procedure which establishes an association between the 'high' and 'low' states of the coded signal and two amplitude, frequency or phase values depending on whether ASK (Amplitude Shift Keying), PSK (Phase Shift Keying) or FSK (Frequency Shift Keying) is chosen. In the uplink communication the modulation technique employed must be as elementary as possible to limit the complexity of the demodulation circuit. The ASK modulation [7, 8] allows to work even with basic low-power receivers since the demodulation procedure is quite simple and can be performed even with low-complexity envelope detectors. Indeed, this modulation produces in time a modulated signal as product of the coded signal and the carrier, therefore in frequency domain their convolution results in the spectrum of the digital coded signal translated at the frequency of the sinusoidal carrier.

A different procedure is followed during the downlink communication from tag to reader, since in case of passive and semi-passive tags no RF carrier can be generated at the transponder: generally, the most used method is the load modulation, which is based on the principle of varying the impedance of the tag resonant circuit switching it to a different load according to the data stream to be transmitted. With this procedure the signal transmitted by the tag is none other than the carrier transmitted by the reader and backscattered, once suitably modulated in amplitude, phase or frequency in accordance with the original data stream.

A process frequently used in conjunction with load modulation is the subcarrier modulation to ease the decoding procedure at the reader side by separating the spectral components of the modulated signal coming from the tag with respect to the carrier signal coming from the reader. The data stream to transmit is employed to modulate a lower frequency subcarrier, used in turn to switch the external load, thus obtaining a carrier signal modulated by the modulated subcarrier; in this way the reader can easily recover the transmitted information by simply filtering one of the sidebands of the received signal.

In the transmission from tag to reader, the lack of available energy at the tag can be a criticality that hinders the correct detection and the easy carrier suppression at the receiver side. Manchester coding [7, 8] is often used for downlink transmission, in conjunction with load modulation using a subcarrier. The great advantage of this coding scheme lies in the fact that each bit occupies a time slot interval with fixed dimension and presents one transition (the '0' is encoded as a positive transition, absence of modulation in the first half bit and presence in the second one, a '1' is encoded as a negative transition, presence of modulation

in the first half bit and absence in the second one), thus minimizing the loss of clock synchronization at the reader.

RFID technologies require interoperability between devices provided by manifold developers, for this reason the standardization of the protocols, describing how the communication must take place, is mandatory. The main ISO (International Organization for Standardization) standards realized for specific uses of RFID technologies are distinct between animals identification, contact-less smart cards and payment systems, and item management [9]. The ISO 15693 is the standard used for vicinity cards working at 13.56 MHz ±7 kHz with reading range < 1.5 m. It is divided into 3 parts: physical characteristics, air interface and initialization, anti-collision and transmission protocol.

Among the sets of communication protocols, even the NFC must be mentioned, that is part of the short-range technologies working at operating distances lower than 10 cm. It works at 13.56 MHz on ISO 18000-3 air interface and is based on RFID standards ISO 15693 and 18092; it is also compatible with ISO 14443 used for contact-less smart cards. The NFC can be employed to read information stored on passive tags and to establish a complete peer-to-peer communication between enabled devices, with the advantage that even an NFC-enabled smartphone can be comfortably used as tag interrogator without resorting to dedicated hardware.

Chapter 2
HF Sensor Tags: the developed system

In this Chapter, the prototype of a battery-less HF sensor tag (Standard ISO 15693) for soil moisture measurements is presented. The sensors integrated in the tag are custom devices based on an oxidized silicon substrate functionalized with a nanostructured titanium dioxide (n-TiO_2) solution and characterized for moisture measurements [10, 11]. The proposed solution is totally passive thanks to the usage of an NFC/RFID chip in charge of converting the incoming electromagnetic field into a rectified voltage used as onboard power supply. The proposed application is within the Smart Agriculture scenario [12, 13], where sensor tags have already been used for monitoring of soil moisture by means of unmanned aerial vehicles mounting RFID readers on board [14]. However, the compatibility with the ISO 15693 Standard enhances the sensor tag usability, making it interrogable by long range HF readers or by NFC-enabled devices like common smartphones, thus opening up to possible scenarios in domestic applications for monitoring soil moisture in plant pots or vegetable gardens.

2.1. Soil moisture measurement techniques

One of the first sensing methods traditionally presented in the literature for soil moisture measurement is the capacitive one. The capacitive sensing approach is performed by directly placing two metallic elements in the soil, which behaves as the lossy dielectric of a capacitor formed between the two electrodes, acting in turn as capacitor plates. The operating principle is based on the fact that dry and wet soils have different relative dielectric constants ε_r depending on the presence or the absence of moisture (ε_r=3.8 in case of dry soil with quartz particles and ε_r=78 for deionized water [15]). This kind of sensors gives a coarse approximation of the moisture level unless the soil conductivity, dependent on soil composition and salinity, is not accounted; moreover, a pre-calibration procedure for each type of soil is needed.

To obtain a ‘true’ capacitive sensing of the soil water content, thus measuring the sole dielectric characteristics of soil and avoiding the response to the soil conductivity, the metal

electrodes should be properly insulated, and the operating frequency must be very high. Planar capacitance structures are often used [15, 16], usually exploiting an interdigitated capacitor layout modified with a porous ceramic layer placed on top of the insulated coating and acting as coupling medium. The sensed quantity is the fringe capacitance which varies according to the soil permittivity changes, mostly due to the water content. Generally, these sensors have a small sensitivity and need complex front-end electronics working at high operating frequency since small capacitive variations must be detected. If no insulation procedure is realized, soil impedance sensors are obtained, exploiting oxidation-resistant conductive elements directly buried in the ground.

The sensing mechanism is performed by impedance measurements under AC excitation across the electrodes since DC excitation is not recommended because of possible slow polarization effects and induced chemical modification of the electrode surfaces. The water kept in the soil is electrically modelled as a two-electrodes electrochemical cell composed of a series of two parallel R-C groups accounting for the conduction in material and for the metal/soil interfaces. The capacitances can be modelled as phase constant elements to describe the double layer capacitive behavior. Both conductivity and relative permittivity of soil are strongly affected by the water content since when passing from dry to wet conditions the impedance moves from an almost capacitive behavior to an almost resistive one. Due to this fact, this family of sensors finds large application even in commercial products (e.g., ECH2O EC-20 probe).

To obtain a sensing system completely independent from the soil composition, a possible solution is to measure the relative humidity (RH) of the air enclosed in a porous chamber buried in the ground. The RH is defined as the ratio between the pressure due to water vapor contained in an air mass and the maximum pressure in the same air mass at the same temperature of the water vapor at saturation, in formula $\mathrm{RH} = 100\frac{\mathrm{P_{H_2O}}}{\mathrm{P_{H_2O_{sat}}}}$. The RH% expresses the amount of water vapor as a percentage of the maximum concentration determining the condensation phenomenon. In this situation, until water is present in the soil surrounding the chamber, the RH value is around 100%, whereas when the soil in the neighborhood of the chamber becomes completely dry, the relative humidity decreases until it reaches low RH values. This method, which does not require any calibration related to the soil type, is actually a ‘threshold’ method able to signalize a very low soil water content (approximately lower than 10% w/w) and thus trigger the watering as soon as the soil becomes

completely dry, under the assumption that in the deeper layers the soil moisture is still sufficient for the plant life.

In these thesis work, three sensor tags based on the same architecture but exploiting the different soil moisture measurement strategies discussed above were developed, characterized, and compared: a sensor tag uses the soil impedance measurement, one exploits the fringe capacitance variation measurement, and finally a sensor tag embeds a RH sensor which indirectly senses soil moisture as variations of the air humidity inside a buried measurement chamber. The three developed tags differ in terms of measurement strategy and of low-power conditioning circuit, to design which in-depth characterizations of the sensing elements and of their measurement performance were carried out.

2.2. System architecture

The general architecture of the designed sensor tags is depicted in Figure 5 and five parts can be distinguished:

- the loop antenna;
- the NFC/RFID dynamic chip with the power management part;
- the microcontroller;
- the sensor conditioning circuit;
- the sensor.

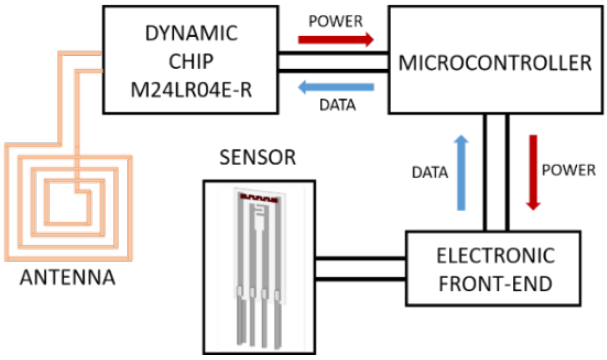

Figure 5. Architecture of the proposed sensor tag.

While the functioning of the NFC/RFID dynamic chip and the antenna design will be presented in this Section, the description of the sensors and their characterization will be topics of Sections 2.3 and 2.4 respectively while the conditioning circuits will be described in Subsection 2.5.1. As mentioned before, the conditioning circuit architectures and the measurement strategies were defined after preliminary characterizations of the sensors, which had been performed with ad-hoc developed measurement chains and electronic circuits. Therefore, the front-ends of the prototyped sensor tags were tailored on the specific substrate accounting for the low-power constraint and the results derived from the previous modeling.

Concerning the microcontroller, the STM32L073RZ belonging to the low-power family of ST Microelectronics was used. Its operating range [1.65 V, 3.6 V] and the extremely low current consumptions make it a valid solution for the low-power requirements of the sensor tag. The MCU dealt with the initialization and the programming of the dynamic chip, the supply of the sensor reading circuit, the generation of the signals needed to read the sensor, the sampling of the sensor outputs and its processing, and the transcription via I^2C protocol of the processed data in the EEPROM of the chip, where they can be accessed by the reader for reading the soil moisture level.

2.2.1. Dynamic chip

The integrated circuit (IC) used was the dynamic chip M24LR04ER from STMicroelectronics. It works according to standards ISO/IEC 15693 and ISO/IEC 18000-3 at 13.56 MHz ± 7 kHz. In uplink communication uses an ASK modulation with index 10% or 100% with 1 out of 4 or 1 out of 256 pulse position coding (9.44 μs-long pause), giving respectively a data rate of 26.64 kbit/s and 1.65 kbit/s. In downlink, the data are encoded through Manchester coding and transmitted by means of load modulation with subcarriers, whose frequencies are obtained as binary division of the carrier operating frequency, in particular ASK modulation (subcarrier at 423.75 kHz) or FSK modulation (switching between two subcarriers at 423.75 kHz and 484.25 kHz) are used.

The IC can be powered-up by an external power supply V_{CC} or from the incoming electromagnetic wave when an antenna is present. The chip is equipped with a 4 kB programmable EEPROM, where the data of interest can be saved before being read with the interrogating reader. The chip also features energy harvesting capabilities providing – as long as the power available at the tag antenna exceeds the minimum power required to activate the chip – a rectified and non-regulated voltage useful to switch on the external circuitry and four

possible configurable sink currents options, depending on the maximum current absorption of the load. In the considered application, the configuration providing the maximum current (i.e., 6 mA at the minimum rectified voltage of 1.7 V) was selected. The energy harvesting option is disabled by default hence must be preliminary activated before the first use.

The IC features a I^2C (Inter Integrated Circuit) serial interface, consisting of a bidirectional serial data line (SDA) and a serial clock line (SCL), regulated by a master/slave relationship [17]; in the presented application the chip operates as a slave and the MCU as a master. The two bus lines are open drain/open collector, so they are connected to the positive supply voltage through two pull-up resistors forcing the buses to the high voltage level when the chip is not interrogated. Standard Mode is used with transfer rates up to 100 kbit, the I^2C logical levels are $V_{IL} = 0.3\ V_{CC}$ for the low-level input voltage and $V_{IH} = 0.7\ V_{CC}$ for the high-level input voltage. The values of the pull-up resistors R_p and the bus capacitance C_p, due to capacitance of wires, connections, and pins, affect the operation of the bus itself and the correspondent time constant, in fact their increase limits the maximum usable rate and the signal readability. The R_p value was chosen on the basis of a compromise between rate, power consumption and readability of the signal: in the presented application, assuming a realistic value of 25 pF for C_p, the exact value chosen is R_p = 12 kΩ, nevertheless, given the power criticality, a higher value for R_p could be eventually selected to reduce current and power consumption, at the detriment of the signal decodability.

A typical I^2C data transfer procedure is depicted in Figure 6: the master first sends the start bit, then forwards the slave address (7 bits) followed by the Read/Write bit, and waits/sends an acknowledgment (ACK); data bytes are transferred with the most significant bits (MSB) first from master to slave in case of writing operation or from slave to master in case of reading operations and each byte stream is terminated by the transmission of an ACK; finally the master sends the stop bit.

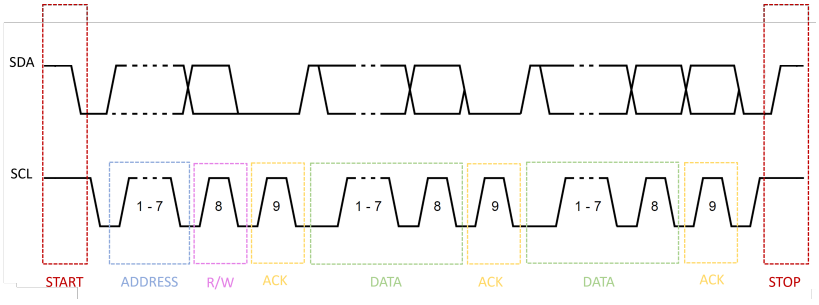

Figure 6. Data transfer scheme of I^2C protocol.

During preliminary tests, the chip communication was debugged with a Tektronix MSO64 oscilloscope embedding protocol analyzer functions to verify the proper functioning of the I^2C protocol: the rise time of the signal was evaluated to ascertain that the chosen R_p allowed the signal to reach the high level in a proper time to be correctly read by the receiving device; moreover, examining the SCL line, the protocol rate was assessed (i.e., ~54 kbit/s).

In summary, the dynamic chip carried out the functions of input and output communication acting as an interface between reader and sensor tag, storage of the tag data in a programmable memory and conversion of the incoming radio-frequency energy in an output voltage useful to supply the electronics on board of the tag itself.

2.2.2. Antenna design and prototyping

The loop antenna was designed using CST Studio Suite and realized by acid bath on a FR4 substrate covered with a 35-μm copper layer. It had dimensions 52 mm × 52 mm, 6 loops with width 0.4 mm and equally spaced by 0.4 mm, specifically chosen to obtain a coil inductance $L_{coil} \simeq 5$ μH, capable to resonate in accordance with the input capacitance of the chip (i.e., Z_{chip} = 27.5 pF) at the working frequency f_r =13.56 MHz.

The actual resistance and reactance of the antenna were then verified with a network analyzer Keysight E5071C: the reflection coefficient S_{11} was acquired from 12.56 MHz to 14.56 MHz (steps of 5 kHz) and assuming an impedance at the port $Z_0 = 50$ Ω the values $L_{coil} = 5.163$ μH and $R_{coil} = 9.864$ Ω were found at f_r. To verify the correct resonance of the system at f_r, a further measurement was performed evaluating the parallel impedance of the antenna and a capacitance with the same value as the input capacitance of the chip ($Z = Z_{chip} \| Z_{coil}$) and the results were compared with simulations in CST Studio. The measured and simulated impedances in terms of real and imaginary components are shown in Figure 7 and confirm the parallel resonant behavior of the circuit.

A mismatch between the resonant frequency of the simulated system (i.e., 14.14 MHz) and the one of the actual system (i.e., 13.56 MHz) can be noted. As expected, the measured impedance presents a lower Q factor and a lower resonance frequency with respect to the simulated one, due to the additional parasitic capacitances and the parasitic losses existing in the actual prototype.

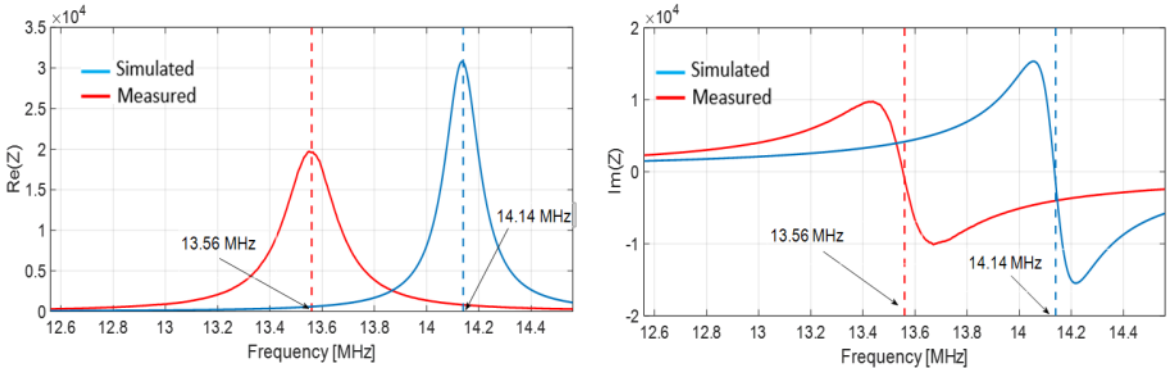

(**a**) (**b**)

Figure 7. (**a**) Real part and (**b**) imaginary part of the impedance $Z = Z_{chip} || Z_{coil}$ measured (red plot) and simulated using CST Studio (blue plot).

The antenna prototype was then connected to the M24LR04E-R chip (without onboard load) and the energy harvesting functionality of the system was tested with three different commercial readers by measuring the rectified voltage with an Agilent 34410A multimeter (configured with 10 PLC and 6 ½ digit resolution):

- Huawei smartphone equipped with NFC technology and NFC-V reader application;
- Reader ID CPR-PR50 by Softwork with integrated antenna, powered by computer and interfaced with ID ISOStart program;
- Reader FEIG ID ISC.LR2000 with external antenna, powered by computer and interfaced with ID ISOStart program.

In all the three cases, a maximum rectified voltage of ~3 V was found, strongly dependent on mutual position between reader and tag antennas and on the eventual current absorption of the load; for this reason, only low-power devices with reduced current absorption and low working voltage levels can be selected. The smartphone with the app interface allowed for an easier and more practical access to the chip's EEPROM but at the same time the gainable currents were lower than in computer-powered readers, therefore this solution was usable only with very low-power sensors. On the other hand, even if the other two readers allowed to harvest a higher power, they presented more coupling problems, in particular the greatest difficulties were encountered with the third reader because of the very different dimensions of the two used coils causing decoupling even in case of small spatial shifts. Accordingly, in final tests only the NFC-enabled smartphone was used.

2.3. Sensors preparation and modeling

The presented system was integrated with non-commercial sensors, appropriately obtained exploiting as substrates thin-film mm-size circuits. In particular, the prototype sensors were obtained through proper modification or functionalization of the substrates with a solution of nanostructured TiO_2. In detail, the used substrates were custom realized through photolithography, physical vapor deposition by sputtering (100 nm of Pt over an adhesion layer of 20 nm of Ti) and lift-off on an oxidized silicon substrate (standard doped silicon wafer (6'' width) with 2000 nm-thick oxidized layer of SiO_2). The structure of the circuit with the seven terminals indicated and its equivalent lumped parameter network are shown in Figure 8.

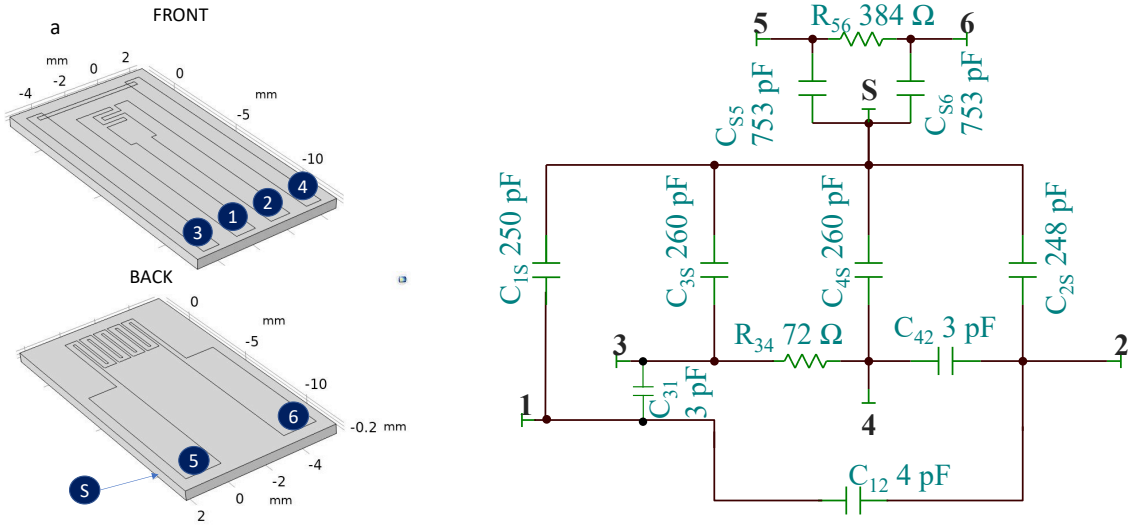

(**a**) (**b**)

Figure 8. (**a**) Thin-film circuit layout. Front view: the inner tracks associated to terminals 1 and 2 provide the electrical contact to the interdigital electrodes whereas terminals 3 and 4 are connected to a Pt resistor; back view: terminals 5 and 6 are connected to a second Pt resistor. (**b**) Electrical equivalent circuit: the resistances and capacitances values are extracted by FEM assuming the pristine circuit in dry air.

The circuit included two interdigitated electrodes (connected to terminals 1 and 2 and used as electrical contacts for the functionalization layer, i.e., the deposited sensing film) and two platinum resistors on each side of the substrate and usable for temperature measurements (terminals 3-4 and 5-6). The Pt lines were characterized by a sheet resistance $R_{\square} = 2.1\ \Omega/\square$

thus giving a resistance of 72 Ω for the front resistor and 384 Ω for the back resistor. The floating terminal S identifies the silicon substrate, assumed as perfectly conductive.

In the equivalent network, the most relevant circuit elements are shown, where the subscripts i and j indicate the terminals to which the element is connected; even the most significant parasitic effects are accounted with parasitic resistances, due to leakage currents, and parasitic capacitances, caused by coupling with ground and external bodies. The resistances and capacitances values reported in the figure were extracted by finite element method (FEM) analysis using COMSOL Multiphysics simulation software and refer to the pristine circuit surrounded by dry air.

2.3.1. RH sensor

The RH sensor was obtained by functionalization of the pristine substrate over the interdigitated electrodes with a subtle coating of n-TiO_2, which is proven to be a very hydrophilic material because of its ability of adsorbing large quantities of water molecules in gas phase and promoting water dissociation. The sensing material used for the deposition was a crystalline anatase nanoparticles suspension in water with a concentration of $32 \cdot 10^{-3}$mol/l, viscosity 2.0 cPs and nanoparticles diameters in the [25 nm, 55 nm] range (ITALVERNICI-FELCE150). An amount of 0.5 μg of TiO_2 causes the adsorption of about 20 ng of water molecules at 20% RH and 25 °C [18]. The film formation was realized by drop-casting the solution using a micropipette and drying it in free air at room temperature.

The usage of metal oxide (MOX) nanoparticles and nanostructures for humidity/gas detection is well-known in the literature: the high surface/volume ratio of these materials favors the adsorption of gaseous species on their surface and the modifications of the electrical behavior. However, the grainy nature of the sensing film, differently from compact films, determines the formation of interstitial intergranular pores with nanometric dimensions between the nanoparticles, which must be accounted in case of air humidity detection since gas concentrations near vapor saturation are experienced. In this case, the size and geometry of the nanopores greatly affect the response of the sensing layer, because of possible water condensation in the pores and capillary growth [18, 19, 20].

The equivalent electric model of the functionalized substrate changes with respect to Figure 8b because of the addition across terminals 1-2 of the impedance contribution of the deposed TiO_2 film, which is electrically represented by the series of three parallel R-C groups accounting for the conduction in the sensing film (i.e., $R_F \| C_F$) and for the phenomena

occurring at the electrode/film interfaces (i.e., $R_{E1}\|C_{E1}$ and $R_{E2}\|C_{E2}$), both affecting the impedance variations with RH (see Figure 9a). To perform the RH sensing the terminals 1, 3 and 5 were shorted while terminals 4 and 6 were not driven, thus with some approximations the electrical model can be simplified obtaining the circuit shown in Figure 9b.

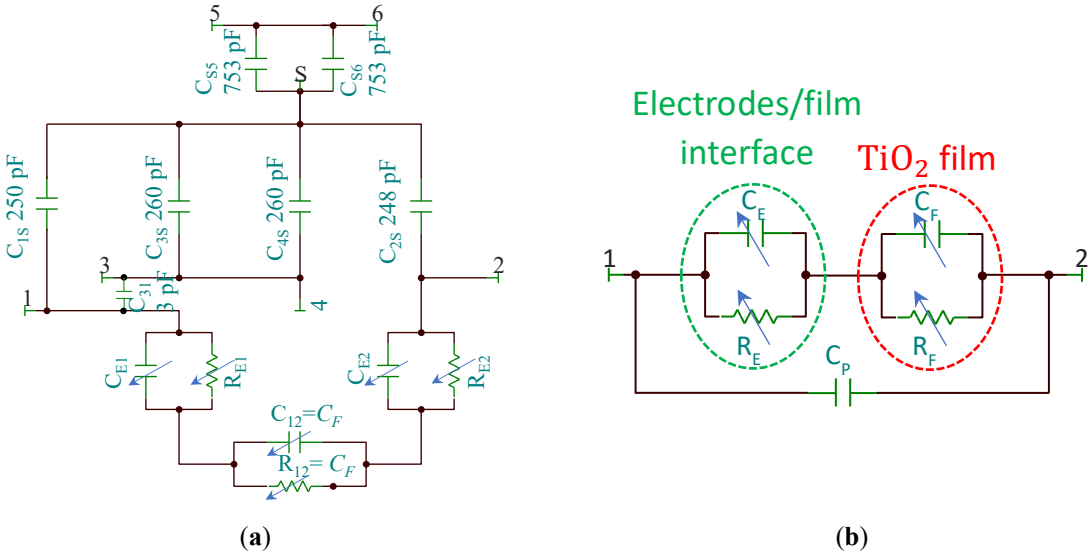

(**a**) (**b**)

Figure 9. (**a**) Equivalent electric model of the RH sensor prototype; (**b**) simplified equivalent circuit.

This model remains valid for all the RH concentrations however, for RH>40-50% different absorption mechanisms occur, becoming dominant for RH>75%; thus while for low RH a simplified model with one R-C group is sufficient to fit the impedance behavior of the sensing film, for higher RH two R-C groups must be used where the capacitances should be modeled with non-ideal phase constant elements approximating the charge double layers imperfect capacitive behavior related to ionic conduction.

Indeed, at room temperature the water vapor is adsorbed with a multilayer mechanism: in the first layer, chemisorbed dissociated water forming hydroxyl ions is expected and a charge transfer between adsorbates and sensing film, affecting its conductivity, takes place; then, subsequent layers of molecular physiosorbed water are formed by means of hydrogen bonds, in these layers electrical conduction is possible due to proton hopping. At higher RH values the water uptake remarkably increases because of the ongoing condensation of water in the nanopores, therefore a water film is created above the sensing film constituting a further path for current conduction through protonic conduction mechanism [21, 22]. At this stage, the structure and the adhesion property of the TiO_2 film with the substrate could change [23]

and the model reported could not be capable to correctly describe the very large sensor response [21], which, in some cases, can become hysteretic, non-linear and non-reproducible, and sometimes the structure of the sensing layer can be irreversibly transformed because of changes in the nanopores arrangement.

Summarizing, the RH sensor obtained by deposition of TiO_2 nanoparticles, can be modeled by an impedance which depends on the RH level, characterized by small variations of the resistive components caused by changes in the film conductivity due to electron exchange between adsorbate and sensing film at very low humidity, by large variations due to the establishing of proton hopping in the multi-layered structure at intermediate humidity levels, and by very large variations due to conduction in water condensed in the nanopores at very high humidity levels. On the other hand, the variation of the capacitive components is related to changes in the film electric permittivity or in the charge stored at the double layer interface capacitances.

2.3.2. Fringe capacitance sensor

The pure capacitive sensor was obtained by covering the thin-film circuit with an insulating varnish to avoid the direct influence of soil conductivity (solder mask, ε_r=2.5); even in this case terminals 1, 3 and 5 were short circuited and terminals 4 and 6 were not driven. The resulting equivalent circuit is shown in Figure 10: C_{11} and C_{12} are the capacitances due to the insulation layer, while R_G and C_G represent respectively the conduction mechanism and the fringe capacitance in soil, which are strongly influenced by the presence of liquid water. The thinner is the insulating layer, the larger are the C_{11} and C_{12} values and the higher is the sensor sensitivity. Note that even if, ideally, the capacitive sensor should sense only the variations of the soil dielectric constants, the sensor admittance encompasses a conductance, related to soil conductivity, that even in the presence of moderate water is very large and largely influence the measurement unless operating at very high frequency.

Therefore, the usage of this sensor requires a pre-calibration procedure, depending on the different soil type employed during the field test. The total capacitance across terminals 1-2 is estimated with FEM electrostatic analysis in different measurement conditions considering for dry soil a permittivity value ε_r=5.3 (water content 10% v/v) and for wet soil ε_r=34.5 (water content 50% v/v) [24]; the results predicted with FEM analysis are reported in Table I, which shows the capacitance across electrodes 1 and 2 in the considered operating conditions, also taking into account the presence of insulating layers with different thickness.

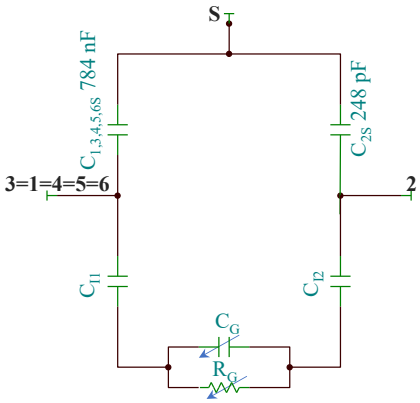

Figure 10. Equivalent electric model of the fringe capacitance sensor prototype.

Table I. Predicted values of the sensor capacitance across terminals 1-2 with different media and thickness of the insulating layer obtained by FEM analysis.

Medium	Capacitance Electrodes 1-2 [pF] (insulating layer 1 μm)	Capacitance Electrodes 1-2 [pF] (insulating layer 10 μm)	Capacitance Electrodes 1-2 [pF] (insulating layer 50 μm)	Capacitance Electrodes 1-2 [pF] (insulating layer 100 μm)
Air	183.5	184.5	185.0	185.0
Dry soil	220.3	204.4	205.2	204.0
Wet soil	228.6	210.1	209.1	207.6
Water	257.1	229.8	221.5	219.8

2.3.3. Soil impedance sensor

The soil impedance sensor was obtained by directly burying the pristine thin-film circuit in the ground: the conductivity of the soil was measured directly from terminals 1-2 in contact with the soil. Electrodes 1, 3 and 5 were shorted and electrodes 4 and 6 were not driven. The equivalent system is the same of Figure 8b, but in this case C_F and R_F describe the electric behaviour of the soil (C_{soil} and R_{soil}) while C_E and R_E account for the electrode/soil interface. Conduction in wet soil is expected to be ionic, therefore double layer capacitance can play an important role. For this type of measurement, re-calibration is required each time the sensor is used in a different location or with a different soil sample.

2.4. Sensors characterization and calibration

In this Section, the measurement set-up employed for the characterization and the calibration of the sensors presented in Section 2.3 is described, together with the results of the characterization.

2.4.1. Measurement set-up

Concerning the RH sensor, a measurement chain was developed to test it in different RH concentrations. The architecture of the automated measurement set-up is shown in Figure 11: the desired RH concentration levels were set using a mass flow-meters bench (BronkHorst F-201C), remotely controlled by a PC, and were obtained by combining in different percentages two flows of dry and wet (100% RH) synthetic air; the wet flow was obtained by means of a bubbler, through which the dry air flow was saturated. The measurement chamber where the constant 100 ml/min air flow at known RH% was conveyed was a sealed IP68 plastic box with internal dimensions 5 cm × 3 cm × 3 cm and two apertures ensuring the correct flow inlet and outlet; the chamber housed the sensor prototype under test and a commercial humidity sensor HIH-4000 by Honeywell (3.5% RH of accuracy) used to compare the sensors response at variable humidity. An ad hoc developed Lab-VIEW Virtual Instrument (VI) allowed to control the flow meter system and the data acquisition process in real time. When dealing with the fringe capacitance and the soil impedance sensors, no flow meter bench was used since the substrates were directly tested in soils with different levels of water concentration (w/w), prepared by adding different amounts of water to a dry soil sample.

The designed conditioning circuit, whose simplified schematic is reported in the inset of Figure 11, was a dual supply charge/current amplifier based on a large bandwidth operational amplifier (OP-AMP) (LM6172 from Texas Instruments) and followed by an amplification stage in such a way that the amplitude of the output response, V_{out}, varied according to the sensor impedance Z_S. The excitation voltage V_{in} was a zero-offset sinusoidal signal with amplitude $|V_{in}| = 1$ V, generated at different operating frequencies, depending on the specific substrate under test, using an AG33220A Agilent waveform generator. The dual supply at ± 5 V was provided by a GW INSTEK GPC-3030D DC power supply.

A National Instruments acquisition board NI PCI-6070 (12 bits of resolution, 1.25 MS/s maximum sampling rate) was used for the acquisition of the voltage signals (V_{in} and V_{out}). The AC signals were acquired at fast rate during long windows to mitigate the noise effect, then the root mean square (RMS) was computed and averaged over several windows to have 1 sample per second, which can be considered a good sampling frequency for quite slow

processes as those due to RH absorption. The measurement uncertainty was defined by the instrument performance since the type A uncertainty was found to be negligible (i.e., <100 μV) with respect to the type B uncertainty introduced by the instrument (i.e., $\frac{\text{max\_error}}{\sqrt{3}} \simeq 5.5$ mV with max_error ≃10 mV). However, the uncertainty related to the quantization and the measurement of the parameter was always evaluated as less significant than all the other possible uncertainty contributions (e.g., the reference humidity measurement).

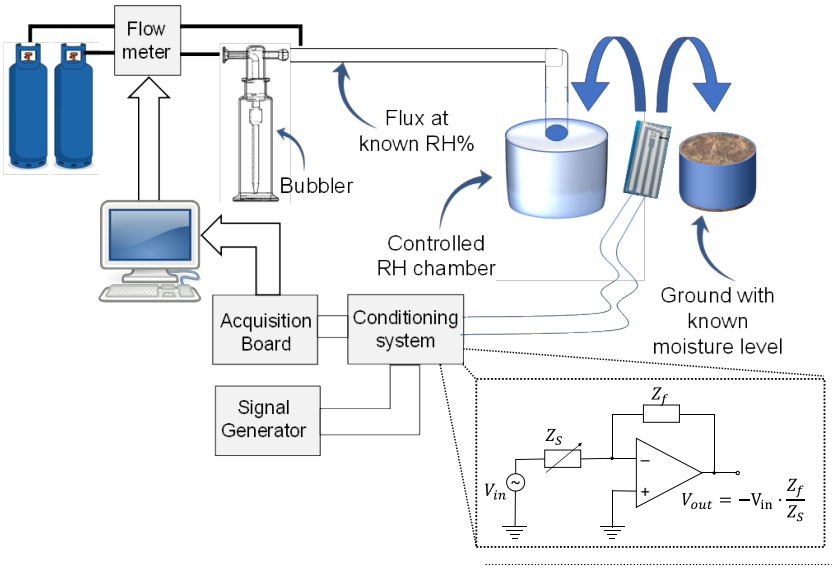

Figure 11. Architecture of the automated measurement chain used for the characterization of the sensors; in the inset the simplified schematic of the electronic front-end used for the characterization of the substrates.

The sensor impedance was evaluated from the measurement of the amplitude of V_{out} and V_{in} and of their phase difference as $Z_s = -\frac{Z_f}{V_{out}} V_{in}$, being Z_f the known feedback impedance. The characterization results reported in the following Subsections were obtained by generating sinusoidal waveforms V_{in} with frequency f_{in} spanning in the [50 Hz, 80 kHz] range, and are displayed in terms either of the output voltage amplitude $|V_{out}(s)|$ or of the impedance magnitude $|Z_S(f)|$ at the selected frequency.

2.4.2. RH sensor

The preliminary measurements were performed functionalizing the substrate with increasing depositions of n-TiO_2 at steps of 2 µl (i.e., 2 µl, 4 µl and 6 µl).

The functionalized sensors were tested during 25 min-long measurement campaigns performed at room temperature by keeping constant to 100 ml/min the flow in the measurement chamber and by properly varying the RH percentage with steps of approximately 25% during a complete cycle theoretically set as RH = 0%-100%-0% (i.e., 4 min of dry air flux followed by 2 min of humid flow for each desired RH concentration, except the intermediate phase, theoretically set to RH=100%, and the final phase whose durations were of 4 min). The system was excited with the voltage signal V_{in} at three different operating frequencies f_{in}, i.e. 0.1 kHz, 20 kHz, and 80 kHz, using the front-end electronics presented in Subsection 2.4.1 ($Z_f = R_f \parallel C_f$ with $R_f = 100$ kΩ and $C_f = 100$ pF).

The responses as a function of time are shown in Figure 12: plot (a) reports the theoretical RH profile and the humidity profile measured by the commercial sensor HIH-4000, while Figures (b)-(d) show the measured RMS of the system output voltage V_{out} when the system is excited at $f_{in} = 0.1$ kHz (Figure 12b), 20 kHz (Figure 12c), and 80 kHz (Figure 12d). The concentration level of the RH theoretically set by the system and the one actually measured by the commercial sensor, used as reference, did not correspond and the sensor did not reach RH=100% and RH=0% probably because of leakages in the measurement chamber. Furthermore, the commercial sensor seems to have a time constant larger than the one declared in the datasheet (i.e., 5 s), whereas the prototype sensor responds faster than the commercial one.

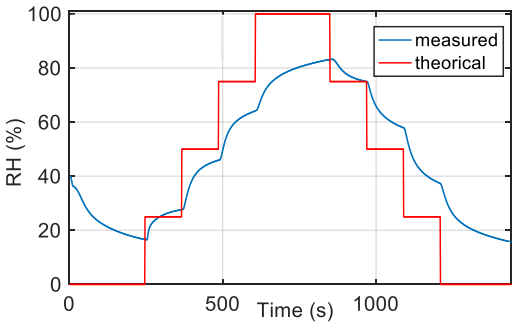

(a)

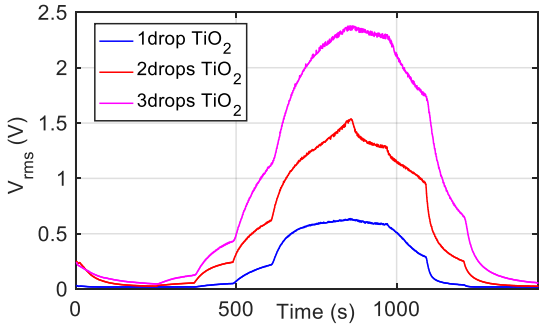

(b)

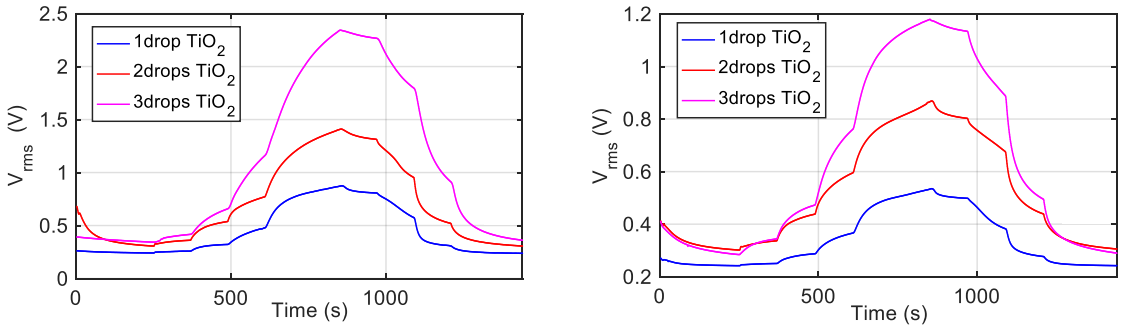

Figure 12. (**a**): RH% in the measurement chamber measured by the commercial humidity sensor (in blue) with the theoretical RH levels (in red). RMS of the system output V_{out} for the prototype functionalized with one (blue line), two (red line) and three (magenta line) TiO_2 depositions with V_{in} at f_{in} = 0.1 kHz (**b**), 20 kHz (**c**) and 80 kHz (**d**).

These first results show that the humidity sensitivity of the prototype sensors increases with the deposited TiO_2 mass, as expected. Furthermore, the sensitivity of the prototype sensor in terms of $|Z_f(f)|$ considerably increases with the RH level in the whole tested frequency range. Therefore, even a small amount of sensing material grants a large response to RH for large RH levels, whereas the deposition of at least 10 µg of TiO_2 ensures satisfactory sensitivity at low RH values [18]. Because of the observed very high sensitivity in the high RH range, probably due to the water condensation and to the protonic conduction mechanism presented in Subsection 2.3.1, the tested sensor is particularly suitable for the considered application (i.e., the RH sensor in the buried chamber operates close to 100% RH in wet soils).

To further the study, the impedance spectra in a wide frequency range were measured and interpreted exploiting the model proposed in Figure 9. To this end, a substrate with 4 depositions was realized (i.e., 8 µl of n-TiO_2 corresponding approximately to the deposition of 20 µg of TiO_2) and the sensor impedance magnitude spectrum was measured at RH=0%, 25% and 50% with a frequency sweep of f_{in} from 50 Hz to 80 kHz (steps of 50 Hz) and electronic front-end with $Z_f = R_f = 100\ k\Omega$; then on the collected results a nonlinear least square fitting is performed on the basis of the proposed equivalent electric model. In Figure 13 the measured impedance and the results of the fitting process are shown, whereas the estimated parameters, R_E, C_E, R_F and C_F are reported in Table II.

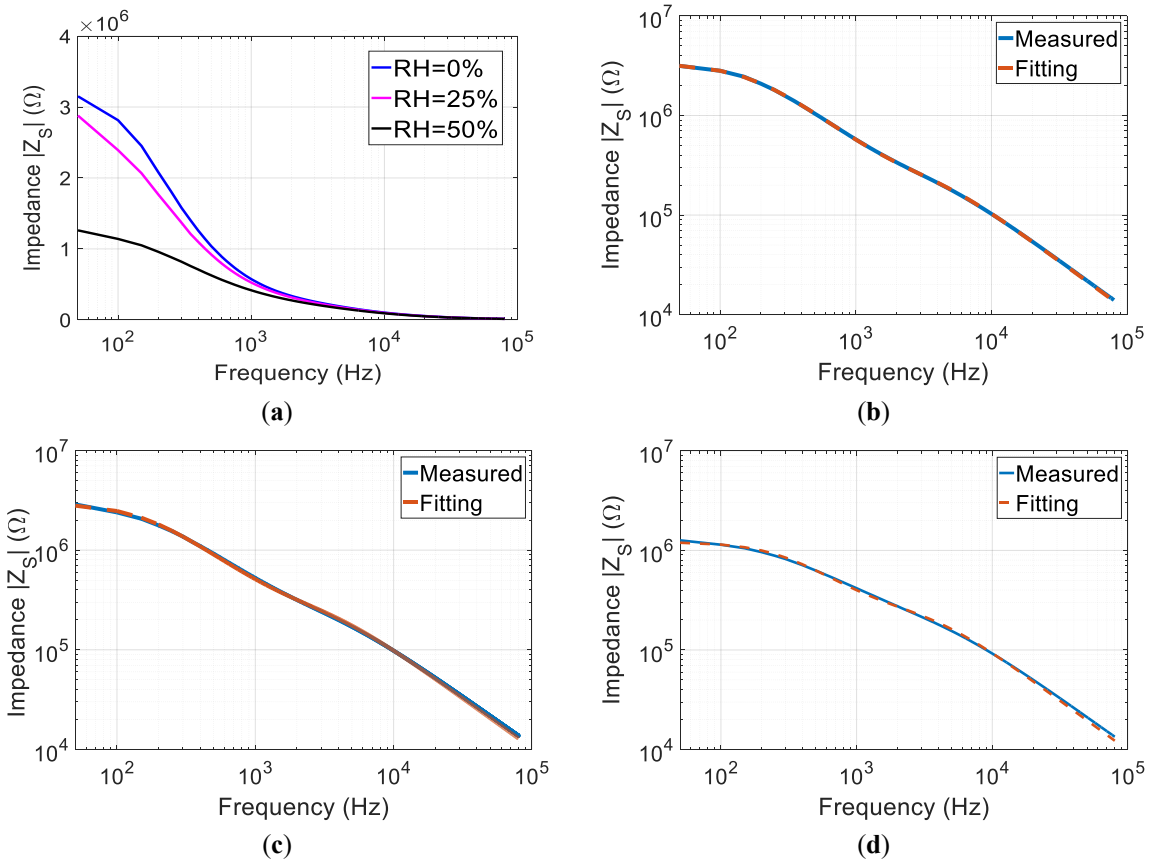

Figure 13. (**a**) Impedance magnitude of the RH sensor evaluated in the frequency range [50 Hz, 80 kHz] (steps of 50 Hz) at constant humidity levels RH=0% (blue line), 25% (magenta line) and 50% (black line). Results of the fitting procedure (red dashed line) on the measured impedance magnitude (blue line) at (**b**) RH=0%, (**c**) 25% and (**d**) 50%.

Table II. Optimal fitting parameters for the RH sensor.

RH	R_E [Ω]	C_E [F]	R_F [Ω]	C_F [F]
0%	3.32e+05	42e-12	2.97e+06	214.88e-12
25%	3.35e+05	52.8e-12	2.6e+06	280.3e-12
50%	2.9e+05	58.17e-12	0.92e+06	500.42e-12

The resistive and capacitive contributions of the electrodes are in the order of $\sim 10^5$ Ω and $\sim 10^{-12}$ F and do not show a great variation with humidity changes, whereas the greatest impedance variations are those due to the TiO_2 coating: C_F increases with the RH% growth while R_F decreases with comparable relative variations. Concerning fitting, the matching

between the actual impedance (blue plot) and the trend of the analytical model (red dashed plot) can be appreciated. With higher RH levels, the same electric model should be fitted but non-ideal capacitance with phase linear element should be used to model the film capacitance.

Finally, the sensor was characterized in terms of its admittance magnitude $|Y_s| = 1/|Z_s|$ at f_{in} = 100 Hz, performing a 60 min-long humidity cycle varied theoretically in the range RH=0%-100% with steps of 25% each 15 min-long. The working frequency of 100 Hz was selected looking for a compromise between the substrate sensing performance and the simplicity of the measurement technique to be implemented in the conditioning electronics presented in Section 2.5.1, since in the final sensor tag prototype the excitation signal will be generated by the onboard MCU. The measured admittance magnitude, correlated to the humidity measurements at steady state performed by the commercial sensor, is shown in Figure 14 as blue plot, while the red dashed line is the 3rd order polynomial least square fit of RH vs. $\log(|Y_s|)$.

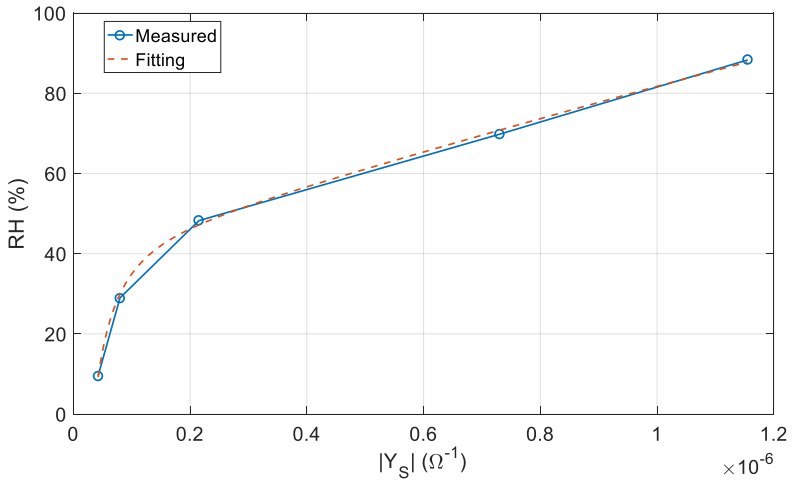

Figure 14. Characterization of the RH sensor obtained correlating its admittance magnitude ($|Y_s| = 1/|Z_s|$) and the actual RH levels measured at steady state by the commercial sensor HIH-4000 (blue plot); 3rd order polynomial least square fit of RH vs. $\log(|Y_s|)$ (red dashed plot).

Therefore, after calibration the measured humidity can be expressed as

$$RH_{meas} = a_3 \log^3(|Y_s|) + a_2 \log^2(|Y_s|) + a_1 \log(|Y_s|) + a_0 + e_{model}(RH) \quad (1)$$

where $e_{model}(RH)$ represents the fitting error whose maximum value, e_M=1%RH, was estimated by the maximum error among the fitting residual, and a worst-case uniform distribution can be assumed. As a consequence, the uncertainty on the measured RH can be expressed as

$$u(RH_{meas}) = \sqrt{\left(\frac{\partial RH}{\partial |Y_s|}\right)^2 u^2(|Y_s|) + \sum_{i=0}^{3}\left(\frac{\partial RH}{\partial a_i}\right)^2 u^2(a_i) + \frac{e_M^2}{3}} \quad (2)$$

where $u^2(|Y_s|)$ is the admittance measurement uncertainty, which can be evaluated from the voltage measurement uncertainty and the front-end circuit parameters uncertainty. Indeed, this uncertainty was estimated using some reference impedances to be lower than 2%. Concerning the uncertainties of the calibration coefficients, these will depend on the procedure used for fitting, therefore each coefficient is a function of the calibration point measurement couples, (log $(|Y_s|_i)$, RH_{R_i}). Thus, its uncertainty can be written as

$$u(a_j) = \sqrt{\sum_{i=0}^{N}\left(\frac{\partial a_j}{\partial |Y_s|_i}\right)^2 u^2(|Y_s|_i) + \sum_{i=0}^{N}\left(\frac{\partial a_j}{\partial RH_{R_i}}\right)^2 u^2(RH_{R_i})}\,. \quad (3)$$

From calculations it emerged that the main contribution was due to high uncertainty provided by the reference RH sensor, with a maximum error of about 3.5%RH, so (3) becomes

$$u(a_j) \approx \sqrt{\sum_{i=0}^{N}\left(\frac{\partial a_j}{\partial RH_{R_i}}\right)^2 u^2(RH_{R_i})}.$$

The measurement uncertainty related to the calibration curve reported above was then evaluated by a Monte Carlo analysis, accounting for random errors superimposed to the reference humidity values measured by the reference sensor and to the measurements of the admittance magnitude. Both random variables were gaussian distributed with standard deviation respectively of 3.5%RH/3 and relative standard deviation equal to 2%. Accounting also for the model error, the combined uncertainty for the RH measured according to (2) resulted in less than 2%.

2.4.3. Fringe capacitance sensor and soil impedance sensor

The fringe capacitance sensor and the soil impedance sensor were characterized and calibrated by measuring their impedance in different soil moisture conditions: three soil samples were prepared, starting from 20 g of dry topsoil and adding 5 g, 10 g and 15 g of water, corresponding respectively to 25% w/w, 50% w/w and 75% w/w of water content.

For the fringe capacitance sensor, the impedance measurements at the three soil moisture levels, in air and in water at the working frequency of 1 kHz were used to compute the capacitance values across terminals 1-2 shown in Table III and which result quite similar to those predicted in Table I for a 100 μm insulating layer, net of the specific soil characteristics. However, the thickness of the insulating coating makes the sensor little

sensitive to water content variations, consequently, to detect such small capacity changes, more complex front-ends working at higher frequency f_{in} with respect to those used with the RH sensor must be adopted.

Table III. Estimated values of the capacitance across terminals 1-2 for the fringe capacitance sensor in three different soil moisture conditions (i.e., 25% w/w, 50% w/w and 75% w/w), in air and in water.

Medium	Capacitance Electrodes 1-2 [pF]
Air	188
25%	200
50%	203
75%	205
Water	212.3

The impedance magnitude spectra of the soil impedance sensor at the three moisture levels and with a frequency sweep of f_{in} from 50 Hz to 80 kHz (steps of 50 Hz) are shown in Figure 15, together with the non-linear fitting according to the model of Figure 10, while the estimated parameters are summarized in Table IV. The obtained results are indicative of the sensor behavior, but they actually depend on the particular soil specimen used and on the positioning of the sensor in the soil sample. Indeed, multiple factors linked to the positioning of the sensors, as the coupling between the soil particles and the sensing substrate or the non-uniformity of the soil moisture in the considered medium, could potentially influence the presented result in quite different and unpredictable ways. However, it can be seen that a very large difference between the impedance values in dry soil (water content lower than 25%) and wet soil (water content larger than 50%) are found; therefore, a simple and rough calibration procedure can be performed just taking two measurements in dry and wet conditions. Moreover, as the water content increases, the fitting is less accurate, and this can be caused by the non-ideal behavior of the electrodes capacitances which are into direct contact with water.

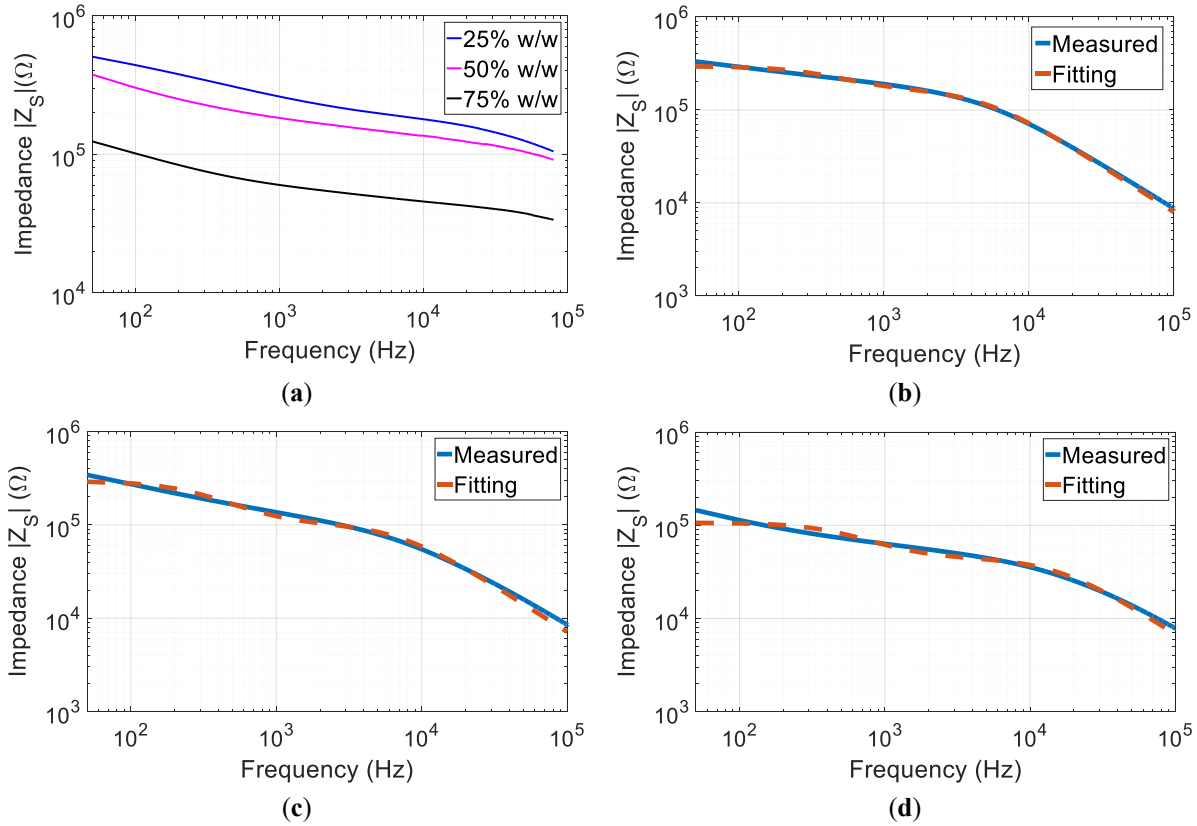

Figure 15. (**a**) Impedance magnitude of the soil impedance sensor evaluated in the frequency range [50 Hz, 80 kHz] (steps of 50 Hz) using soil samples at constant water content: 25% w/w (blue line), 50% w/w (magenta line) and 75% w/w (black line). Results of the fitting procedure (red dashed line) on the measured impedance magnitude (blue line) at w/w=25% (**b**), 50% (**c**) and 75% (**d**).

Table IV. Optimal fitting parameters for the soil impedance sensor in three different soil moisture conditions (i.e., 25% w/w, 50% w/w and 75% w/w).

WC	R_E [Ω]	C_E [F]	R_{Soil} [Ω]	C_{Soil} [F]
25%	1.25e+05	3.25e-9	1.71e+05	39.29e-12
50%	1.89e+05	2.88e-9	1.05e+05	63.65e-12
75%	0.62e+05	4.97e-9	0.45e+05	72.93e-12

As for the RH sensor, the best sensitivity was found in the low frequency range, thus the characterization in terms of the admittance magnitude $|Y_s| = 1/|Z_s|$ is performed at working frequency $f_{in} = 100$ Hz and the correspondent results are reported in Figure 16.

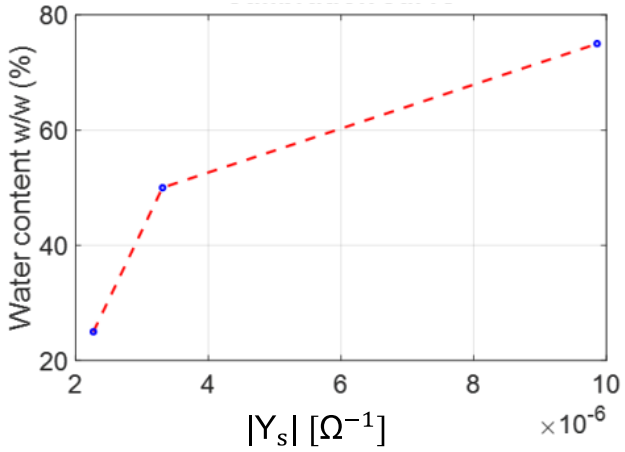

Figure 16. Characterization of the soil impedance sensor derived from the admittance magnitude ($|Y_s| = 1/|Z_s|$) at 100 Hz as a function of the water content in soil (25% w/w, 50% w/w and 75% w/w).

2.5. Tests and results

According to the results derived from the characterization phase and keeping into account the low-power and low-complexity constraints imposed by the measurement technique to be implemented in the sensor node, two front-end circuits for the sensors readings were developed. Field tests on a standard topsoil sample were performed using a proper test-bench and finally the functioning of the integrated system powered by an NFC-enabled smartphone was proven.

2.5.1. Front-end circuits

On the basis of the characterization results, two tailored low-cost conditioning circuits were designed, whose schematics are shown in Figure 17.

Both applied an AC voltage V_{in} to the sensors to avoid polarization phenomena at the electrode/medium interfaces (i.e., square wave generated by pulse width modulation (PWM) of the MCU with 50% duty cycle, amplitude $|V_{in}| = 2$ V and offset voltage $|V_{off}| = \frac{|V_{in}|}{2}$) and were based on a micropower zero-drift rail-to-rail OP-AMP (TSZ122IYDT by STMicroelectronics), working at the 2 V single-supply provided by the MCU.

To recover the sensor impedance magnitude, an AC/DC conversion was accomplished by synchronously sampling the V_{out} with the MCU analog-to-digital converter (ADC): the

output square wave was sampled with a fixed delay with respect to the square wave edges to avoid transients, and the average value of four subsequent samples was taken.

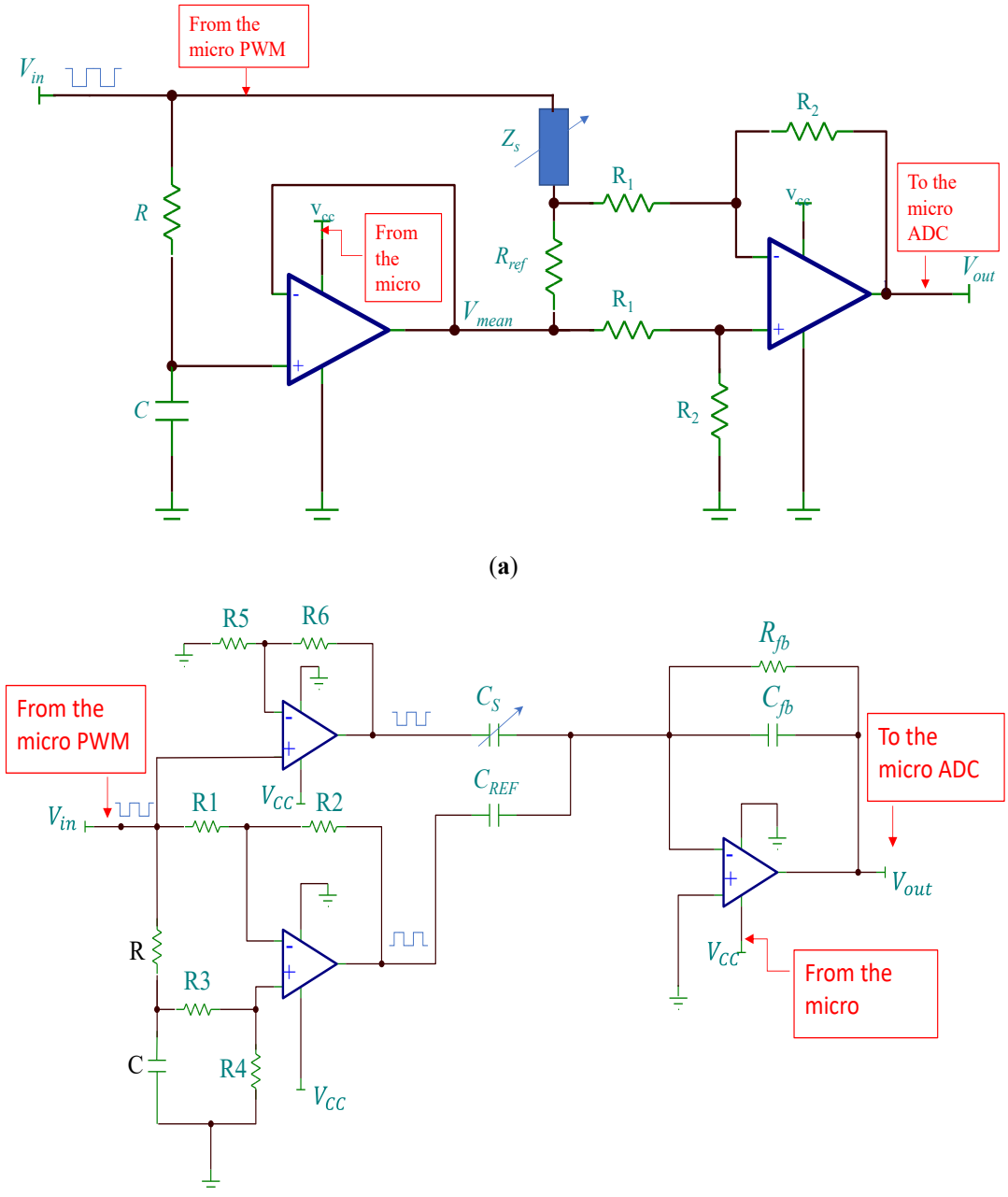

Figure 17. Reading circuit electronics for the RH and the soil impedance sensors (**a**) and for the fringe capacitance sensor (**b**).

The circuit of Figure 17a was used for impedance readings of the RH and the soil impedance sensors. The choice of driving the sensor with a low-frequency signal at 100 Hz, generated with the PWM output of the MCU, was dictated by the results of the characterization and by the need of simple and robust electronic circuits on board of the tag.

The sensor forms a voltage divider with the reference resistance R_{ref}, whose value is selected depending on the sensor type to impose at the sensor terminal a voltage approximately equal to the average value of V_{in}, V_{mean}, which is extracted by a low pass R-C filter (R-C in the figure). This condition is satisfied for R_{ref} much lower than Z_S so that its voltage drop will be sufficiently low, and the entire circuit will practically perform a measurement of the sensor current. In this way, the V_{mean} is subtracted to V_{in} thus accomplishing the goal of non-polarization of the sensor. The R-C behaviour of the sensor causes the voltage divider to behave as a high pass filter with cut-off frequency and asymptotic gain dependent on the RH level. The last stage is a differential amplifier, which allows for amplifying only the high portion of the voltage divider output waveform, compatibly with the desired sensitivity.

In particular, with reference to the symbols defined in Figure 17a, being $R_1 = R_3$ and $R_2 = R_4$, R_{ref} much smaller than Z_S and R_2 greater than R_1 (where this last condition determines a voltage approximately equal to V_{mean} at the non-inverting input of the OP-AMP), the output voltage V_{out} can be described by the following Equation:

$$V_{out} = \begin{cases} \frac{R_2}{R_1}(V_{in} - V_{mean})\,\frac{R_{ref}}{R_{ref}+Z_S} & \text{if } V_{in} = V_H \\ 0\ V & \text{if } V_{in} = 0\ V \end{cases} \quad (4)$$

The response of the reading circuit ($R_1 = 560$ kΩ, $R_2 = 10$ MΩ, V_{in} square wave generated by an Agilent AG33220A waveform generator with 50% duty cycle, amplitude $|V_{in}| = 2$ V and offset voltage $|V_{off}| = \frac{|V_{in}|}{2}$) equipped with the RH sensor at two different RH levels, acquired with a Tektronix MSO64 oscilloscope, is shown in Figure 18a: the black dots correspond to the timing of the synchronous signal sampling. It can be seen that the sensor, in conjunction with the electronic front-end, behaves as a high pass filter with cut-off frequency and asymptotic gain dependent on the RH level.

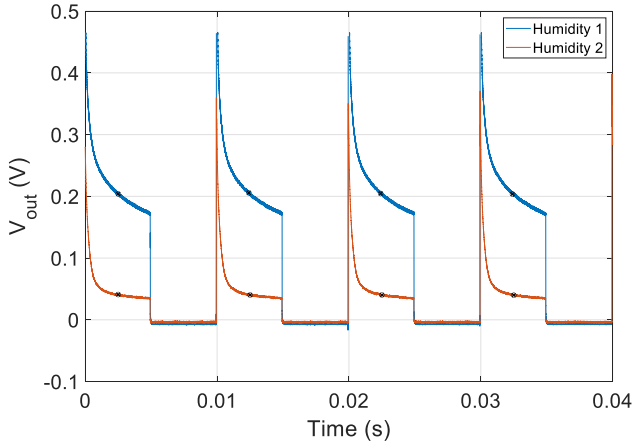

Figure 18. Output response of the reading circuit of Figure 17a equipped with the RH sensor at two different RH levels; the black dots identify the sampling instants.

For the fringe capacitance sensor, the more complex front-end of Figure 17b was used, operating at f_{in} = 1 kHz and specifically designed for sensing small capacitance variations. The first stage is needed to create two square waves out of phase by 180° while the last stage is a differential charge amplifier, with gain set by C_{fb} (R_{fb} has a large value and is needed to avoid large DC errors). The sensor capacitance C_S is compared with a reference capacitance C_{REF}, equal to C_{S_Max} hence, in analogy with the previous circuit, only the high part of the waveform is outputted. In summary, the voltage output for this circuit can be described by the following equation (the effect of R_{fb} is neglected):

$$V_{out} = \begin{cases} \dfrac{V_{in}(C_{REF} - C_s)}{C_{fb}} & \text{if } V_{in} = V_H \\ 0\ V & \text{if } V_{in} = 0\ V \end{cases} \quad (5)$$

2.5.2. Measurement set-up

Three similar tests were performed during natural soil drying with the conditioning electronics of Subsection 2.5.1, where the circuit components were selected to ensure a [0% w/w, 50% w/w] measurement range for the water content. The RH sensor was housed in a sintered porous metal steel chamber specifically designed for soil moisture sensors and properly manufactured to avoid water infiltration, sealed up with a plastic insulating rubber material and positioned under the soil level; a HIH-4000 humidity sensor and a LM35

temperature sensor (0.5 °C of accuracy) were housed in the same measurement chamber to have a humidity reference and to account for temperature variations. The soil impedance sensor and the fringe capacitance sensor were instead directly buried in the soil, whereas the commercial humidity and temperature sensors were kept in the measurement chamber located under the soil and close to the prototype sensors.

To have a continuous and uniform monitoring of the sensors response, the outputs of the three substrates were monitored via an ad-hoc LabVIEW VI during prolonged tests. In particular, in the front-end circuits of Figure 17 the MCU was substituted with a NI PCI-6070 acquisition board (12 bits of resolution, 1.25 MS/s maximum sampling rate) for the synchronous sampling of the sensors output and with an Agilent AG33220A waveform generator for the generation of the AC input square signal (i.e., 50% duty cycle, amplitude $|V_{in}| = 2$ V and offset voltage $|V_{off}| = \frac{|V_{in}|}{2}$) at $f_{in} = 100$ Hz for the RH and the soil impedance sensors and f_{in}=1 kHz for the fringe capacitance sensor. The same considerations about the measurement uncertainty reported in Subsection 2.4.1 are valid, however in this case no RMS was computed: the sensors response was derived as an average value over 100 samples taken at fixed delay with respect to the square wave edges during the high half period of the signal, and 1 sample per s was collected.

The average consumption of the sensor tag equipped with the RH sensor was finally estimated from a set of measurements carried out using the Agilent 34410A multimeter and continously keeping the NFC-enabled smartphone presented in Subsection 2.2.2 at 2 cm from the tag antenna.

2.5.3. Field tests

The tests were performed with the measurement set-up described in Section 2.5.1 and by filling a cylindric plastic container with a soil sample realized from 100 g of the standard topsoil used during the characterization with 50% w/w of water content. The results are shown in Figure 19: the prototype sensors responses are in red color while the output trends of the HIH-4000 and the LM35 sensors are reported respectively in blue and yellow colors.

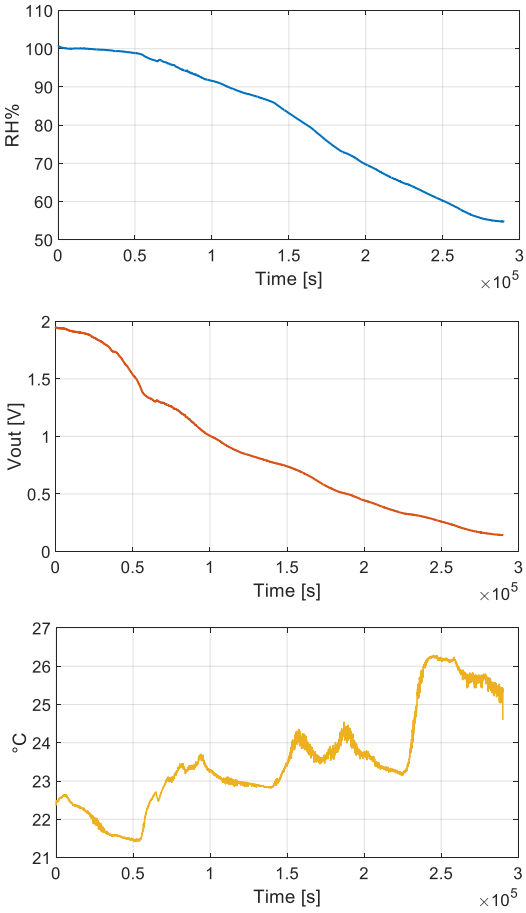
RH%
Time [s]
×10^5
Vout [V]
Time [s]
×10^5
°C
Time [s]
×10^5

(a)

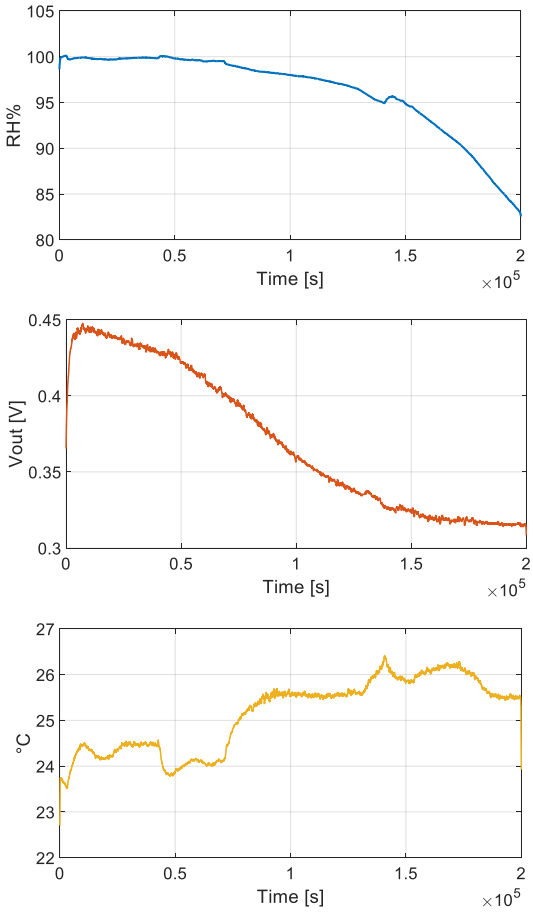
RH%
Time [s]
×10^5
Vout [V]
Time [s]
×10^5
°C
Time [s]
×10^5

(b)

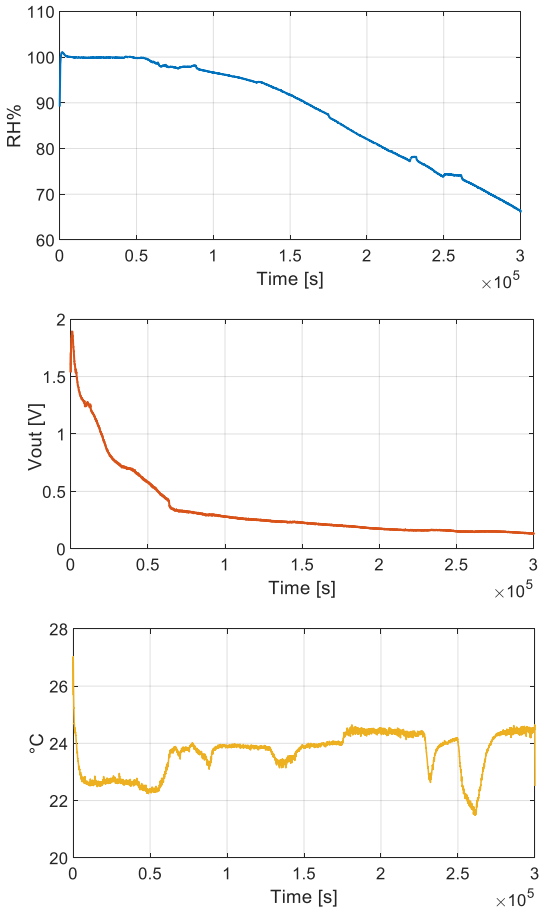

(**c**)

Figure 19. Behaviors of the commercial humidity sensor HIH-4000 (upper subfigure, blue plot), the prototype sensor (central subfigure, red plot) and the commercial temperature sensor LM35 (lower subfigure, yellow plot) during natural wet topsoil drying in free air at room temperature for (**a**) the RH sensor, (**b**) the fringe capacitance sensor and (**c**) the soil impedance sensor.

For the RH sensor, the measurements confirm that the humidity of the air inside the chamber tends to saturate even in the presence of a very small water content, therefore the threshold that identifies the need to wet the ground was experimentally set to around 95%. In fact, when the RH drops below 90% the water content is below 10% whereas when the RH falls below 100% the water content is below 25%, therefore the soil is quite dry and there is need to wet it. The greatest advantage of using the RH sensor is the fact that it can be employed with different types of soils without needing pre-calibration because the moisture level is inferred indirectly from the air humidity inside the chamber. Conversely, it detects the

decrease of water in the ground with great delay and when the water content in soil is already extremely low.

By comparing the results of the soil impedance sensor and the fringe capacitance sensor with respect to the HIH-400 it is confirmed that both sensors provide more information with respect to the humidity measurement. In particular, when the RH values become lower than 100%, both sensors indicate a water content lower than 25% w/w, whereas the RH value 90% corresponds to a water content lower than 10% w/w. Exploiting the measurements of these two sensors, watering can be scheduled also at intermediate water contents.

The soil impedance sensor provides a large sensitivity in the range [50% w/w, 25% w/w] of water content. On the other hand, the fringe capacitance sensor and the tailored front-end provide an almost linear behavior in this range. However, both these substrates require an ad hoc calibration every time their position or the type of used soil changes. Moreover, the fringe capacitance sensor is more critical from the point of view of the measurement procedure, since the water content level is sensed only by the small variations of the fringe capacitance in the ground, and of the front-end driving complexity. Therefore, among the three different sensing solutions, the one based on the functionalization of the substrate represents an innovative solution and proved to be the most sensitive at high RH levels.

The input-output curve of the system mounting the RH sensor derived from the previous field test during soil drying is shown in Figure 18, with respect to the RH = 50%-100% levels (steps of 5%), measured by the HIH-4000 sensor.

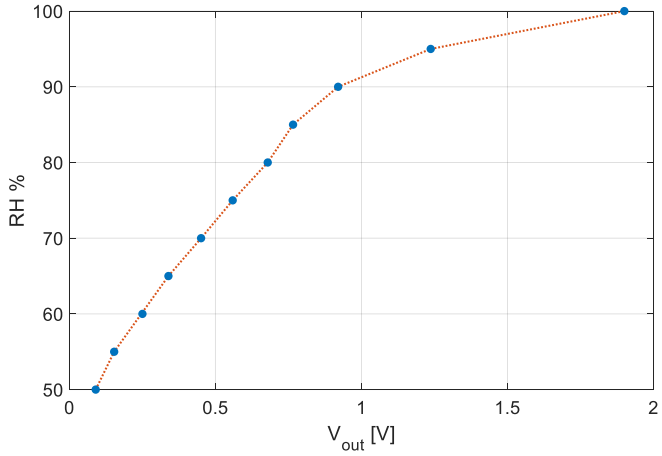

Figure 20. Input-output curve of the RH sensor obtained correlating the actual RH levels measured by the commercial sensor HIH-4000 (i.e., RH = 50%-100% at steps of 5%) and the V_{out} of the reading circuit during the natural soil drying test.

2.5.4. Final sensor tag

Once the behaviour of the substrates was analysed in prolonged measurement campaign, the overall sensor tag was developed, integrating all the components as per the architecture proposed in Section 2.2.

In Figure 21a, the final sensor tag prototype equipped with the RH sensor is shown and the different parts composing the overall architecture are highlighted: in pink the RFID dynamic chip, in orange the microcontroller, in blue the power management part used to regulate and stabilize the rectified voltage recovered from the incoming electromagnetic field, in green the conditioning circuit of the sensor. In Figure 21b the sensor tag electronic is housed in an ABS box by Gewiss with dimensions 120 mm × 80 mm × 50 mm and class protection IP56 in order to avoid damages caused by the possible interaction with the external environment, the HF antenna is fixed on the internal part of the box lid and pointing upwards. Finally, in Figure 21c the sensor tag deployed in a plant pot during field tests is shown.

Since it is an NFC system, the coupling between tag and reader antennas occurs only at very short distances, in our case the maximum reading distance of the tag is about 2 cm, however greater operating distances can be achieved using long range HF readers instead of exploiting the NFC technology.

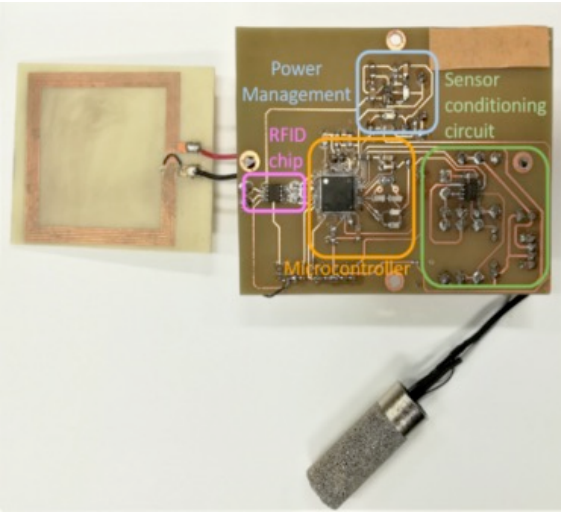

(**a**)

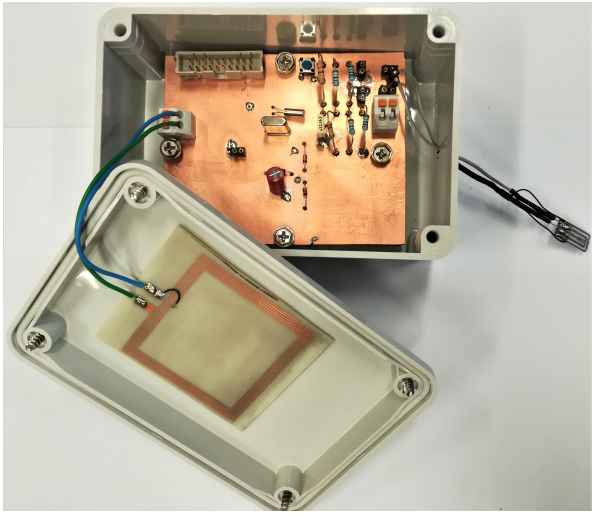

(**b**)

(**c**)

Figure 21. (**a**) Sensor tag prototype PCB with the HF antenna on the left and the RH sensor insert in its sintered metal chamber on the right; the different parts composing the overall architecture are shown: in pink the RFID dynamic chip, in orange the microcontroller, in blue the power management part, in green the conditioning circuit of the sensor. (**b**) Sensor tag electronic housed in an ABS IP56 plastic box; the antenna is fixed on the internal part of the box lid. (**c**) The sensor tag deployed in a plant pot during field tests.

No thorough self-sustainability analysis was performed since this device did not embed a storage element and it turned on only when the reader field was present. The average absorption of the overall system (i.e., the sensor, the front-end, the MCU and the RFID chip) when powered by the NFC-enabled smartphone, estimated as reported in Subsection 2.5.1, was ≃0.8 mA with rectified power supply equal to 2 V, which perfectly complies the energy harvesting requirement (absorbed power of few mW). Indeed the conceived solution managed to realize a completely energy autonomous sensor tag without need to resort to additional storge elements as capacitors or batteries. However, the fact that the device turned on in the presence of the EM field was considered as a preliminary information that the node dimensioning was correct, but it was also ascertained that the device was measuring correctly. To this end, some tests were performed with the same set-up but connecting some well-known impedances in place of the sensor and checking if the measurement results fall within the expected uncertainty range.

Chapter 3

Self-sufficient nodes: principle and technologies

Energy harvesting refers to the process of capturing the ambient energy, present for free in the surrounding environment and generally unexploited, and its conversion into usable electricity. The energy harvesting systems, in their simplest form, consist of three main components: a harvester which is the part of the system that converts the environmental energy into electrical energy; a PMU that extracts the maximum possible amount of energy from the harvester making it ready for use or for storage; the load, which includes those electronic devices that consume the collected energy (e.g., MCUs, circuits, actuators, sensors, radio modules etc.). The applications presented in the following Chapters 4-7, although designed for different operating scenarios and thought for scavenging from disparate energy sources, share this common architecture. In particular, the load generally consists of an MCU, a LoRaWAN transceiver and eventually some commercial sensors. The PMU is employed, among the others, to charge a rechargeable battery, used as energy storage element for the node in the periods of absence of the energy source; therefore, in the rest of the thesis the PMU will be referred to as battery management system (BMS).

The energy source that has seen the largest exploitation in energy self-sufficient WSNs is for sure the direct sun light [25, 26]. However, the development of more effective harvesting techniques, combined with the advent of electronic devices and transmission technologies increasingly oriented towards the low-power, high-efficiency and low-complexity perspectives, makes promising the development of self-sustaining sensor nodes even based on low-intensity and intermittent power sources, which are generally less conventional harvesting sources. Several energy sources were proposed in the scientific literature: these include, among the others, wind [27], see wave motion [28], thermoelectricity [29, 30], electromagnetism [31], vibrations [32, 33], radiofrequency [34], hydroelectricity [35], microbial fuel cells [36], diffused sunlight [37, 38] and artificial light [39, 40, 41, 42, 43], both with white and colored spectrum.

In this Chapter, some basic principles linked to the energy harvesting mechanisms exploiting thermoelectricity and photovoltaic effect are resumed, focusing also on the different types of harvesters and their current-voltage (I-V) and power-voltage (P-V) characteristics. Moreover, the architecture of a general BMS is illustrated, describing in detail the different subsystem composing it.

3.1. Thermoelectric harvesting

The basic principles linked to thermoelectricity and thermoelectric generators (TEGs) are resumed in this Section. First, a brief survey of the main thermoelectric effects is performed, then the mathematical expressions linking electric generation and heat exchange in TEG are given together with its corresponding electric model.

3.1.1. Thermoelectricity

The thermoelectricity studies the physical phenomena which link the conversion of heat (induced by thermal conduction or by radiation) into electricity, finding a relationship between heat flow in a material and generated electric current. In particular, the thermoelectric materials are those materials presenting significant thermoelectric characteristics and that can be exploited, among the others, for energy harvesting tasks. The thermoelectric effect, to be exploited, requires the formation of junctions between two different conductors realizing a closed circuit; it involves five distinct effects: Seebeck effect, Peltier effect, Thomson effect, Joule effect and heat conduction [44, 45].

The Seebeck and Peltier effects are opposite manifestations of the same phenomenon occurring in homogeneous materials. According to the Seebeck effect, the establishment of a temperature gradient between two junctions determines an electric current flow from hot junction to cold junction and consequently a thermoelectric voltage difference proportional to the applied temperature gradient according to the so-called Seebeck coefficient $S = dV/dT$ [μV/K], which depends on the materials and on the junction temperature. From now on this coefficient will be considered constant, i.e., independent form temperature, therefore its definition can be simplified to $S = \Delta V/\Delta T$. The sign of the Seebeck coefficient strictly depends on the type of majority carriers of the conductor: a material with p-type majority charge carriers has a positive Seebeck coefficient, negative in case of n-type majority charge

carriers. Conversely, the Peltier effect explains the induction of a temperature gradient because of the passage of an electric current through the conductors, in particular the generated or absorbed thermal power at the junctions is linearly proportional to the current circulating in the circuit (either externally introduced or induced by Seebeck effect) through the so-called Peltier coefficient $\pi = \dot{Q}/I$ [V] where $\dot{Q}$ is the power [W]. Modifying the sign of the thermal gradient, the direction of circulation of the diffusion current will change, analogously by reversing the direction of the current flowing in the circuit, the direction of the thermal exchange is reversed.

It is possible to define the dimensionless figure of merit of thermoelectric materials as $zT = \frac{S^2\sigma}{\kappa}T$, where σ [S/m] is the electric conductivity and κ [W/m·K] is the thermal conductivity ($K = \kappa\gamma$ [W/K] is the thermal conductance, being γ [m] a geometrical factor linked to the body). In good thermoelectric materials zT must be high, meaning that the material should have a high Seebeck coefficient, a low thermal conductivity to maintain the temperature difference across the junction and a low electrical resistance to allow the current flow minimizing the losses due to the Joule effect. Indeed, Joule heating is derived as $\dot{Q} = RI^2$ while Fourier thermal conduction is computed as $\dot{q} = -\kappa\nabla T$ where $\dot{q}$ is the heat flux density [W/m^2] and ∇T is the temperature gradient [K/m]. The Thomson effect puts together Seebeck and Peltier effects by establishing that in a homogeneous conductor carrying a current and subjected to a temperature gradient the generation or the absorption of the heat depends on whether the direction of the electric current and the thermal flow are coincident or opposite. The thermal power absorbed or generated per unit of length is proportional to the product of the current flowing in the circuit and the temperature difference according to the so-called Thomson coefficient $\zeta = \dot{Q}/(I \cdot \Delta T)$ [μV/K]. From the Thomson relationships derived by Kelvin it can be assessed that $\pi = ST$ and $\zeta = TdS/dT$.

A thermocouple is a passive sensor generating a voltage in response to a temperature gradient and is composed of two different conductors (e.g., in case of semiconductor devices a p-type and a n-type semiconductor) joined together to form a closed loop through junctions. If the two junctions of a thermocouple are kept at different temperatures (T_H and T_C respectively for the cold and the hot junction) a current is induced with electrons (and holes) accumulating at the cold junction for the n-type (and p-type) material, thus establishing a voltage difference balancing the diffusion mechanism and due to the reversible Seebeck effect; moreover, the temperature difference at the two junctions is always accompanied by

irreversible heat conduction with the environment. Furthermore, the passage of electric current is combined with reversible Peltier heating/cooling at the junctions of the dissimilar materials and irreversible Joule heating. Finally, the combination of temperature difference and current flow is always accompanied by reversible Thomson heating/cooling along the conductors.

3.1.2. Thermoelectric generators

The thermoelectric effect can be exploited to generate electricity, measure temperature, or change the temperature of objects by heating or cooling it. When a temperature gradient is applied at the ends of two conductors and a voltage difference is generated, we talk about TEGs: they are composed of a thermoelectric (TE) module, a heat source, and a cold source (generally containing heat exchangers as heat sinks). A TE module is composed of n semiconductor thermocouples electrically connected in series by means of conductive contacts and thermally connected in parallel by two plates of insulating material, generally some ceramic material owning extremely high thermal conductivity and low electrical conductivity (see Figure 22).

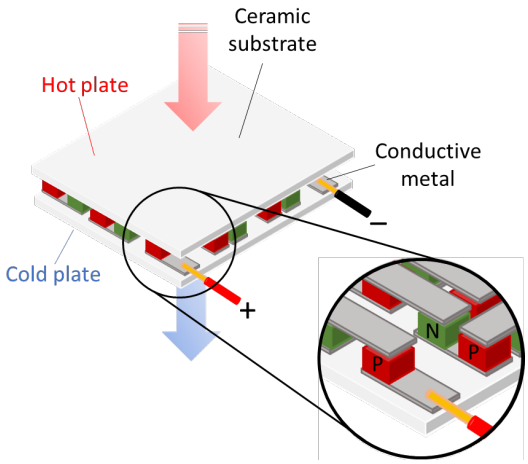

Figure 22. Graphical representation of a TEG module.

If an external load R_L is connected in series with the TEG terminals a current i starts flowing in the load and the corresponding simplified electric model is the circuit shown in Figure 23, where the TEG behaves as a temperature-controlled voltage generator with internal resistance nR_{in} (n is the number of thermocouples connected in series and R_{in} is the resistance associated to each thermocouple; the contribution of the contact resistance due to the

connections between the thermocouples, the hot side and the cold side junctions is assumed negligible).

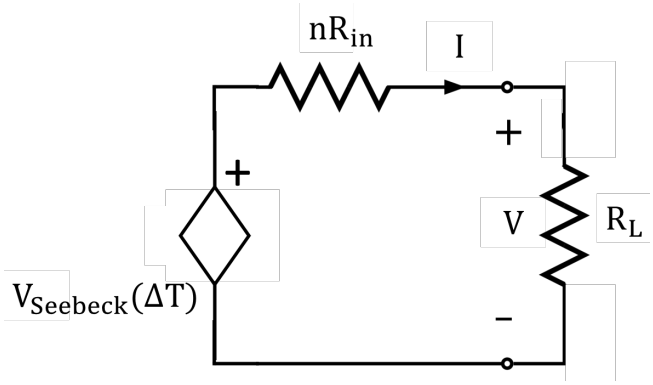

Figure 23. Equivalent electrical model of TEG module.

Neglecting the Thomson effect, the heat exchange rates at the hot and cold sources, depending on Peltier effect, Joule effect and thermal conduction, are respectively [46] $\dot{Q}_H = n\left[S_{pn}T_H i - \frac{R_{in}i^2}{2} + K\Delta T\right]$ and $\dot{Q}_C = n\left[S_{pn}T_C i + \frac{R_{in}i^2}{2} + K\Delta T\right]$, while the power generated by the TEG is $P = \dot{Q}_H - \dot{Q}_C = n\left[S_{pn}(T_H - T_C)i - R_{in}i^2\right] = n\left[S_{pn}\Delta T i - R_{in}i^2\right]$ which equals the power absorbed by the load. Consequently, the generated current is derived as $i = \frac{\Delta V}{nR_{in}+R_L} = \frac{nS_{pn}\Delta T}{nR_{in}+R_L}$ where ΔV is the voltage difference due to Seebeck effect (corresponding to the TEG open circuit voltage, V_{OC}) and $S_{pn} = S_p - S_n$ is the relative Seeback coefficient. The I-V characteristic is linear, and the V/I ratio is equal to the sum between the load resistance and the internal resistance of the module. The electric output power absorbed by the load is $P_L = \left(\frac{nS_{pn}\Delta T}{nR_{in}+R_L}\right)^2 R_L$ and the P-V characteristic has a parabolic behavior achieving the maximum value when $nR_{in} = R_L$, corresponding to $P_{L\_max} = \frac{(nS_{pn}\Delta T)^2}{4R_L}$. In this operating point, known as the Maximum Power Point (MPP), $V_{max} = \frac{nS_{pn}\Delta T}{2} = 0.5V_{OC}$. Hence, the maximum gainable power depends on the square of the temperature difference, as a consequence the greater the temperature gradient the greater is the electrical power extracted from the module. The TEG electrical efficiency can be computed as $\mu_{TEG} = \frac{P_L}{\dot{Q}_H}$.

Bismuth telluride (Bi_2Te_3) is by far the most used thermoelectric material for commercially available TEGs: it has figure of merit zT close to unity but a limited operating

temperature range lower than 200 °C [47], which makes it unsuitable for high temperature applications. The design simplicity and the high scalability of TEGs makes them easily applicable to heat sources of considerably different dimensions and temperature gradients, which translates into an ample presence in the literature of contributions presenting their use in different application scenarios. Moreover, the realization of flexible TEGs and heat sinks allows the application to any curved surface, enhancing the harvested power.

3.2. Light harvesting

The basic physical quantities and principles linked to light measurement [48] and solar cells operations [49, 50] are treated in this Section. First, a brief survey of the light-related quantities and of the fundamental properties of the materials used for solar cells fabrication is reported then, a description of the basic operating characteristics of the solar cells is performed, also deriving the mathematical formulation of the main parameters characterizing the I-V equation of an ideal solar cell. Finally, some considerations are made on the different solar cell types employed in the applications presented in this thesis.

3.2.1. Radiometry and Photometry

In the following, a brief overview of the light-related quantities used in the next Chapters is provided.

The radiant flux is defined as $\Phi_R = \frac{\partial Q_R}{\partial t}$ [W], namely it is the emitted, transmitted, reflected, or received radiant energy Q_R per unit of time. The irradiance is defined as the received radiant flux per unit area and is computed as $E_R = \frac{\partial \Phi_R}{\partial A}$ [W/m^2] where A is the area; the corresponding spectral quantity is the spectral irradiance, namely the irradiance of a surface per unit wavelength, defined as $E_{R,\lambda}(\lambda) = \frac{\partial E_R}{\partial \lambda}$ [W/m^3] where λ is the wavelength. The spectral irradiance $E_{R,\lambda}(\lambda)$ can be recovered also as $E_{R,\lambda}(\lambda) = \frac{\partial(\Phi_{ph} Q_{ph}(\lambda))}{\partial \lambda}$ where $Q_{ph}(\lambda) = \frac{hc}{\lambda}$ is the energy of a single photon at wavelength λ with h =6.62607015×10^{-34} J·s Planck constant and c =2.998×10^8 m/s speed of light, and Φ_{ph} is the flux of photons defined as the number of photons per unit time and area. From $Q_{ph}(\lambda)$ formulation it can be seen that the shorter is the wavelength, the greater is the energy carried by the photon hence, to have the

same spectral irradiance, the needed flux should be lower if composed of short-wavelength photons.

The radiant exposure is the radiant energy Q_R received by a surface per unit area and integrated over the time of irradiation, it is defined as $H_R = \int_0^{t_D} E_R(t)dt$ [J/m^2] where t_D is the duration of the irradiation. In the case of sunlight, it is often reported in terms of daily solar irradiation, indicated in [kWh/m^2].

In the following Chapters, the spectral irradiance $E_{R,\lambda}$ is usually reported in [W/m^{2}nm] and is addressed as 'irradiance', the irradiance E_R is called 'intensity' since it is generally computed as integral of the corresponding spectral quantity.

It is possible to associate to each radiometric quantity a corresponding photometric quantity. The luminous flux is the analogous in photometry of the radiant flux but limited to the human eye sensitivity band. It is calculated as $\Phi_P = 683.002\ \text{lm/W} \cdot \int_{380\ \text{nm}}^{780\ \text{nm}} V(\lambda)\Phi_{R,\lambda}(\lambda)d\lambda$ [lm] by integrating in the visible spectral range the spectral radiant flux $\Phi_{R,\lambda}(\lambda)$ multiplied for the luminous efficiency function $V(\lambda)$ and for the maximum possible value of luminous efficacy in [lm/W] for a monochromatic radiation at 555 nm. Similarly, the homologous of the irradiance is the illuminance defined as the incident luminous flux per unit area and is computed as $E_P = \frac{\partial \Phi_P}{\partial A}$ [lx = lm/m^2].

3.2.2. Photovoltaic effect

The photovoltaic effect indicates the physical phenomenon occurring when an electron in the valence band of a material passes to the conduction band, thus releasing a positive carrier, because of the absorption of a sufficiently energetic incident photon. Indeed, photons with energy below the band gap of the material are not absorbed and the material is practically transparent to that radiation, while photons with energy above the band gap induce the carrier generation but part of the energy is lost as heat rather than converted into usable electrical energy (more details about this topic are given in Subsection 3.2.4). This phenomenon of charge generation is at the basis of electricity production in photovoltaic cells and relies mostly on the use of semiconductor materials, among them Silicon is the most employed in the realization of commercial modules since its absorption characteristics well-match the solar spectrum.

When a luminous flux invests the crystalline lattice of a semiconductor, part of the energy of the absorbed photons is delivered to the material and frees additional charge carriers that must be separated to avoid recombination. This mechanism is achieved by forming a junction between an n-type semiconductor and a p-type semiconductor and exploits the charge space region to separate them. In fact, when the junction is exposed to light, electron-hole pairs are created due to energetic photons absorption and the built-in potential separates the charge carriers which collects at the edges of the material yielding a photo-dependent forward voltage that opposes to that already existing at the junction, thereby reducing the net electric field, and favoring the carriers' diffusion. In open circuit condition, no net current is present since drift and diffusion currents compensate; when connecting the junction to an external conductor forming a closed circuit, a current flowing from n-region to p-region is established.

To summarize, the current generation in p-n junction solar cell requires two processes to occur: the absorption of the incident photons, and thus the creation of electron-hole pairs, and the spatial separation of the generated carriers. The first process depends on the absorption capability of the material (more details are given in Subsection 3.2.4), the second process is achieved by establishing a p-n junction in the material which avoid carrier recombination thanks to action of the electric field formed at the junction.

3.2.3. Solar cell characteristic

In the case of a semiconductor p-n junction solar cells, at first approximation, the corresponding electrical model in non-illumination conditions is that of a diode, therefore the I-V characteristic curve can be described through the Shockley equation as

$$I = I_0 \left(e^{\frac{V}{nV_T}} - 1 \right) \tag{6}$$

where I_0 is the reverse saturation current, n is the ideality factor (between 1 and 2) and $V_T = \frac{k_B T}{q}$ (~26 mV at room temperature) is the thermal voltage with $k_B = 1.380649 \times 10^{-23}$ J/K Boltzmann constant, T temperature in Kelvin and $q = 1.602 \times 10^{-19}$ C the electron charge. I_0 is the reverse saturation current, due to the diffusion of the minority carriers (i.e., electrons and holes respectively for the p-region and the n-region). Its intensity is dependent on temperature and almost unaffected by the magnitude of the applied reverse voltage. When the cell is illuminated, an opposite term related to the contribution of the photo-generated current is

present, with the effect of translating the I-V curve. Assuming positive the direction of the photogenerated current, Equation (6) becomes

$$I = I_{ph} - I_0\left(e^{\frac{V}{nV_T}} - 1\right). \tag{7}$$

In practice, resistive contributions due to the losses inside the material, to the resistance of the metal contacts and to the manufacturing defects are present and can be modeled respectively with a series resistance R_s and a shunt resistance R_{sh} which, as I_{ph} and I_0, are strongly dependent on the physical size of the solar cell. Therefore, Equation (7) can be rewritten to account for these non-idealities as

$$I = I_{ph} - I_0\left(e^{\frac{V+IR_s}{nV_T}} - 1\right) - \frac{V + IR_s}{R_{sh}} \tag{8}$$

while the power P delivered by the cell is derived as $P = VI$.

The equivalent electric circuit for a homo-junction solar cell becomes the one depicted in Figure 24a, where the diode models the p-n junction behavior of the cell ($I_D = I_0\left(e^{\frac{V+IR_s}{nV_T}} - 1\right), V_D = V + IR_s$) and the current generator models the photo-generated current I_{ph}. In Figure 24b the typical I-V and P-V characteristics of an ideal solar cell as in Equation (7) are reported while in Figure 24c and Figure 24d respectively the effects of R_s and R_{sh} on the I-V characteristic are highlighted.

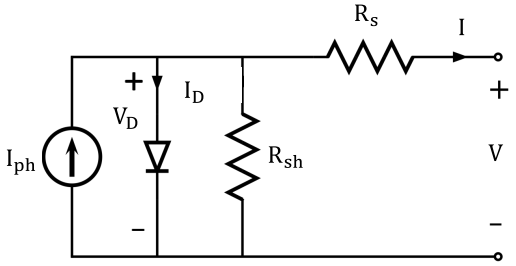

(a)

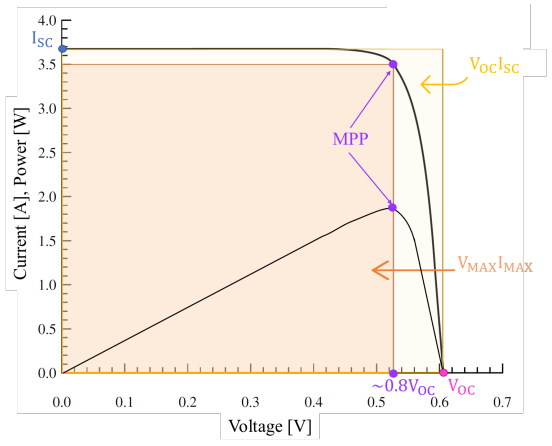

(b)

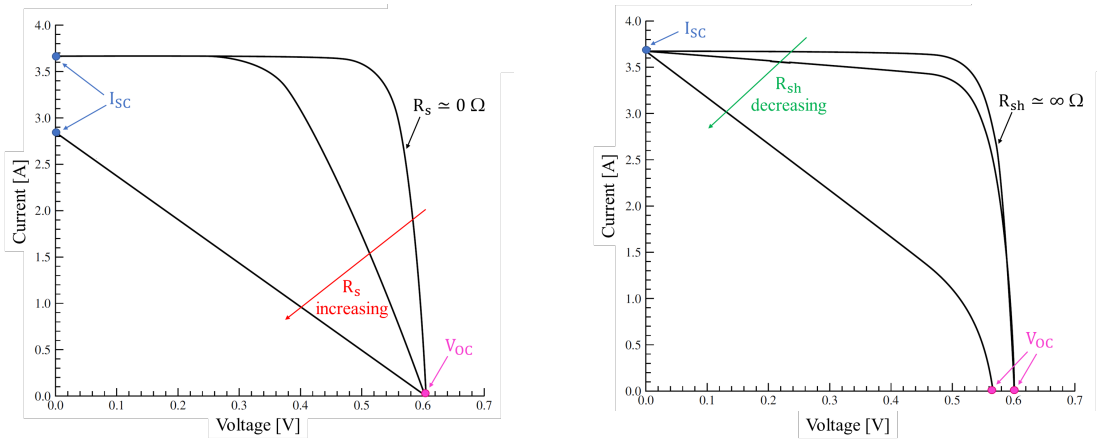

(c) **(d)**

Figure 24. (**a**) Single diode equivalent circuit of a homo-junction solar cell; (**b**) typical I-V and P-V characteristic of an ideal solar cell; effect of R_s (**c**) and R_{sh} (**d**) on the I-V curve.

The short circuit current density, I_{SC}, is defined as the current produced by the cell when no voltage potential at the terminals of the cell is present. If the losses due to R_s and R_{sh} are neglected, it coincides with the photo-generated current, so it is at first approximation proportional to the incident light. The V_{OC} is the voltage produced when the cell is not connected to a circuit. Graphically, as can be seen from Figure 24b, the I_{SC} can be found as the intersection of the I-V characteristic with the y-axis, while V_{OC} corresponds to the intercept of the I-V characteristic with the x-axis.

Neglecting the losses and knowing I_{SC}, the V_{OC} can be found from Equation (7) by setting $I = 0$ and considering that the photo-generated current coincides approximately with the short circuit current, thus obtaining

$$V_{OC} = nV_T \ln\left(1 + \frac{I_{SC}}{I_0}\right) \sim nV_T \ln\left(\frac{J_{SC}}{J_0}\right) \quad (9)$$

where J_{SC} and J_0 are respectively the short circuit and the reverse saturation current density in [A/m^2] defined as the ratio of I_{SC} and I_0 for the active area of the solar cell.

The presence of non-infinite R_{sh} and non-zero R_s significantly decreases the produced voltages and currents and modifies the solar cell characteristic causing a flattening of the curve since the resistive behavior dominates. In particular, as can be seen from Figure 24c, high values of the series resistance reduce I_{SC} and affect the slope of the I-V in correspondence of V_{OC}; analogously, as shown in Figure 24d, low values of the shunt resistance reduce the voltage obtained from the solar cell and affect the slope of the I-V in correspondence of I_{SC}

and this effect is critical especially at low light intensity. Even temperature variations influence the I-V curve, impacting mostly on V_{OC} and to a lesser extent on I_{SC}.

The maximum power ideally gainable from a cell is $P_{MAX_{ideal}} = V_{OC}I_{SC}$ since V_{OC} and I_{SC} corresponds to the maximum voltage and current produced by the cell; practically, in short circuit and in open circuit conditions the power produced by the cell is null therefore the real maximum achievable power is lower than the theoretical one and is defined as $P_{MAX_{real}} = V_{MP}I_{MP}$, where the point ($V_{MP}$, I_{MP}) is the MPP that approximately corresponds to the (I,V) point in correspondence of $V \simeq 0.8V_{OC}$. The ideal and real maximum gainable powers are reported in Figure 24b as subtended rectangular areas respectively with yellow and orange color. The cell resistance in correspondence of the MPP is the characteristic resistance of the solar cell, computed as $R_{CH} = V_{MP}/I_{MP}$; to make the cell operate at MPP, thus theoretically transferring the maximum power to the load, the load resistance should equal the characteristic one. The fill factor FF is derived as $FF = \frac{P_{MAX_{real}}}{P_{MAX_{ideal}}} = \frac{V_{MP}I_{MP}}{V_{OC}I_{SC}}$ and is a parameter measuring the ideality of the cell since it gives an indication of how much the real I-V characteristic differs from the ideal one; typical values are around 80%. The resistive contributions R_s and R_{sh} degrades the FF since they cause a flattening of the I-V curve.

The efficiency η of a solar cell is computed as the ratio of the power produced by the cell and the incident light power P_{inc} which corresponds to the previously defined radiant flux Φ_R; supposing that the cell is working at MPP, the efficiency can be formulated as $\mu_{PV} = \frac{P_{MAX_{real}}}{P_{inc}} = \frac{FF\,V_{OC}I_{SC}}{P_{inc}}$. The efficiency is the most commonly used parameter to compare the performance of solar cells therefore, in order to have comparable results, it is conventionally computed under controlled conditions, called Standard Test Conditions (STC), that include environmental temperature of the cell (25 °C), irradiance of 1 sun (1000 W/m^2) and Air Mass (AM) 1.5 (the concept of AM is analyzed in Section 5.1). For a constant temperature, the efficiency of the solar cell degrades with the decreasing of the irradiance level.

The quantum efficiency (QE) of a solar cell quantifies its ability to generate electron-hole pairs, and therefore a current, in the presence of incident light. It is generally expressed as a function of the wavelength of the incident photons, but it does not account for the photon energy. If the QE is integrated over the whole electromagnetic spectrum, it gives information of the amount of produced current when the cell is exposed to light. It depends not only on light absorption but also on the charges collection capability of the material, indeed if the

electron-hole pairs generated from photons absorption are not collected at the junction because of charge recombination, a drop in the QE is experienced.

The external quantum efficiency (EQE) is defined as the ratio of the number of photo-generated electrons N_e collected by the solar cell and the number of incident photons per unit wavelength $N_{ph,inc}$ (corresponding to the photon flux Φ_{ph}), so it includes the effect of losses due to transmission and reflection and is defined as: $EQE(\lambda) = \frac{N_e(\lambda)}{N_{ph,inc}(\lambda)}$. The internal quantum efficiency (IQE) is the ratio of N_e and the number of the incident photons $N_{ph,a}$ actually absorbed by the cell, thus excluding the reflected and transmitted photons: $IQE(\lambda) = \frac{N_e(\lambda)}{N_{ph,a}(\lambda)} = \frac{N_{ph,inc}(\lambda)}{N_{ph,a}(\lambda)} EQE(\lambda)$.

QE is closely related to the spectral responsivity, which provides the same information in terms of the current output from the device per unit of incident power in [A/W]. It is defined at each wavelength as $\mathcal{R}(\lambda) = \frac{EQE\, q\lambda}{hc}$, hence the spectral response decreases at small photon wavelengths. A relationship between short circuit current density, EQE and incident light can be found considering that at first approximation the short circuit current J_{SC} coincides with the photogenerated current density J_{ph}, which in turn can be derived as $J_{ph} = q \int N_e(\lambda)\, d\lambda$. Indeed, J_{ph} can be computed by multiplying the spectral responsivity with the incident spectral irradiance $E_{R,\lambda}$ thus obtaining:

$$J_{sc} = \int_0^{\infty} \mathcal{R}(\lambda) E_{R,\lambda}(\lambda) d\lambda = \frac{q}{hc} \int E_{R,\lambda}(\lambda) EQE(\lambda) \lambda\, d\lambda \qquad (10)$$

from which, assuming constant EQE, $\mathcal{R} \approx \frac{J_{sc}}{E_R} = \frac{I_{sc}}{\Phi_R}$ and $EQE = \frac{hc\, J_{sc}}{q\lambda\, E_R}$.

3.2.4. Semiconductor-based solar cells

Semiconductor types

The relation between the minimum photon energy and the bandgap energy of the material needed to trigger the photovoltaic effect depends on the considered semiconductor. Semiconductors can be distinguished between direct and indirect band gap depending on the relative position between the minimal-energy state of the conduction band and the maximal-energy state in the valence band in the band structure of the material, which defines the relationship between electron energy and crystal momentum, that is the momentum of

electrons in a crystalline lattice with periodicity spacing ℓ. This is equal to $p_{cry} = \hbar k$, where $\hbar = h/2\pi$ is the reduced Planck constant and k is the wave vector corresponding to the solutions of the wave equation for a crystal potential periodic in the lattice spacing ℓ. If restricting the solution to the Brillouin zone, the range of the crystal momentum in the simplified 1-D space is $p_{cry} = h/\ell$. It differs from the photon momentum, whose magnitude $p_{ph} = h/\lambda$ is generally negligible if compared to p_{cry}.

If the minimum of the conduction band and the maximum of the valence band are aligned, namely they occur at the same crystal momentum, the semiconductor is referred as direct (e.g., amorphous silicon, a-Si), as indirect otherwise (e.g., crystalline silicon, c-Si). Both electron energy and momentum must be conserved during the photon absorption, as a consequence in direct semiconductors the photon can be directly absorbed if its energy overcomes the bandgap energy of the material and the transition in the band structure is approximately vertical; conversely, in the indirect case a higher energy is required to compensate the misalignment in the crystal momentum. In this case, the transition is still possible at lower energy if a two-step process is performed involving an additional particle to provide both the required energy and momentum: the process consists of a photon absorption and a phonon absorption, where the phonon describes the quantized thermal vibration of a rigid crystal lattice and is characterized by low energy and high momentum. However, since this process involves multiple particle interactions, the probability of its occurrence is lower and therefore a photon with energy close to the band gap can penetrate more deeply into the indirect semiconductor before being absorbed. Consequently, absorption in indirect semiconductors is more unlikely than in direct semiconductors.

This outcome emerges also from the absorption coefficient of the material, which gives information on the depth at which a radiation at a specific wavelength penetrates inside a material before being absorbed, thus contributing to the current generation. The inverse of the absorption coefficient corresponds to the penetration depth which is an important parameter influencing the thickness of the semiconductor. Hence, both the absorption coefficient and the penetration depth depend on the material and on the wavelength of the radiation; their trends are reported in Figure 25 for c-Si [51] and a-Si [52] as example of indirect and direct semiconductors (more details about c-Si and a-Si are given in the following).

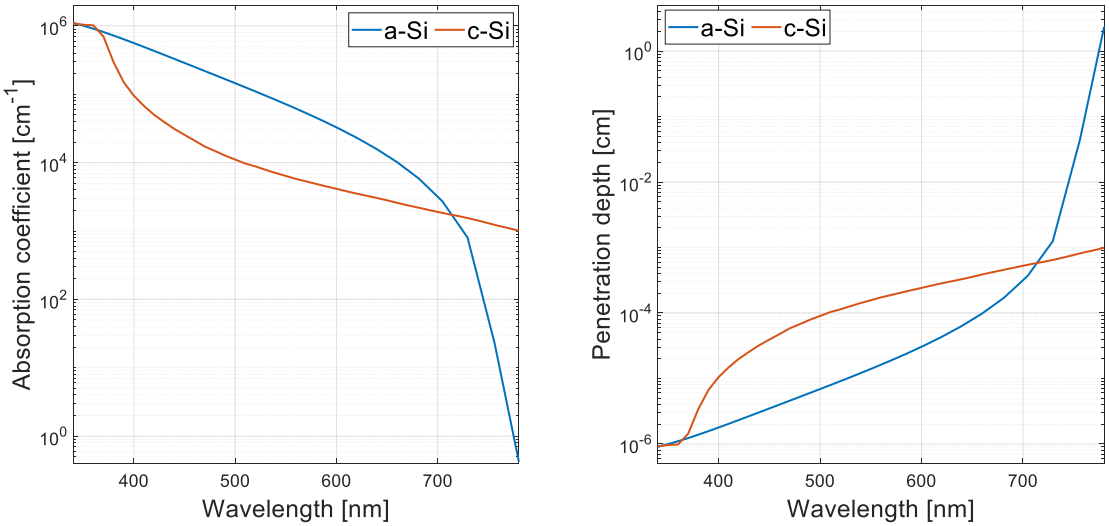

(**a**) (**b**)

Figure 25. (**a**) Absorption coefficient and (**b**) penetration depth for c-Si [51] (red plot) and a-Si [52] (blue plot) at 300 K as function of the wavelength in the range approximately covering the one of visible radiation.

Higher energy radiation, corresponding to a shorter wavelength, has lower penetration depths since a larger number of electrons can interact with the photon and the probability of absorption increases. Conversely, lower energy radiation has greater penetration depths since the photons are not readily absorbed. As a consequence, in a polychromatic radiation the blue component is absorbed at shorter depth from the surface, while the red components are absorbed at higher depths. Moreover, it can be noticed that in the visible spectrum range the penetration depth of c-Si is larger than that of a-Si and analogously the c-Si has a lower absorption coefficient than a-Si, coherently with the different nature of the two semiconductors according to which the absorption in the indirect semiconductors is less likely. As a result, thinner layers in direct semiconductors can absorb the same amount of light as a thicker indirect semiconductor. This outcome also influences solar cells manufacturing, indeed typically c-Si substrates have thickness of hundreds of μm while a-Si substrates have thickness of tens of μm.

However, the current generation is subjected not only to the absorption coefficient but also to the separation probability, which depends on several factors linked to the characteristics of the material, as recombination velocity, thickness, carrier lifetime and diffusion length. The diffusion length is the distance traveled by the carrier from points of generation and recombination; it strongly depends on the type of recombination processes happening in the semiconductor, which in turn are severely influenced even by the fabrication

processes of the material, the presence of defects and impurities, the level of doping. Indeed, the recombination rate is different from the bulk and the surface of the material since the dangling bonds existing on the surface, due to the interruption of the crystal lattice, cause a higher local recombination rate. Therefore, the separation probability can be defined as the probability that the absorption-generated carriers are collected because of the distance that they must travel to reach the junction with respect to the diffusion length. It has a non-uniform trend in the material: for carriers generated in the depletion region the probability is high while it drops at more than one diffusion length away from the junction. Since both the generation rate and the separation probability vary with the position in the material, analogously even the light-generated current is a function of the device depth. Furthermore, the spatial non-uniformity of the collection probability, combined with the spectral variability of the absorption coefficient, also determines a spectral dependence in the light-generated current.

According to their structure, three main types of semiconductors can be distinguished: monocrystalline, polycrystalline, and amorphous. In monocrystalline semiconductors each atom occupies a specific location in the lattice following a regular periodic structure which is continuous in the entire solid, hence they present no grain boundaries, they have few defects, and high electronic quality. Polycrystalline semiconductors are composed of separate crystals grains (or crystallites) with inclined crystal planes, at the grain boundaries the atoms do not match originating in defects (e.g., recombination sites) which degrade the electronic performance of the material and hinder the current flow. Finally, in amorphous semiconductors the chemical bonding of atoms is nearly unchanged from that of crystals, however, a small variation in the angles between the bonds degrades the regular lattice structure. Consequently, a good material with high chemical purity and structural perfection is required to increase the carrier mobility and to avoid recombination.

Silicon solar cells

Up to now, the dominant semiconductor material used in photovoltaics is c-Si, particularly mono-Si. According to NREL (National Renewable Energy Laboratory) chart [53], mono-Si solar cells achieve higher efficiency than poly-Si and a-Si: the results achieved to date in research led to a maximum efficiency (in STC) of ~27 % for the mono-Si, ~24 % for the poly-Si and ~14% for the a-Si. However, mono-Si cells are also the most expensive solutions due to the manufacturing processes required to produce very chemical-pure and structurally perfect silicon, free from those crystal defects present in poly-Si and a-Si and

which lower the electrical and thermal conductivity of the material. The ultra-pure silicon, also called semiconductor grade silicon, that is the starting material for producing the c-Si used in photovoltaics, is obtained from the metallurgical grade silicon with very expensive purification techniques, as the Siemens method. In case of mono-Si production, the Czochralski (Cz) method is the most used production technique: the structural quality of the semiconductor grade silicon is improved by melting it and solidifying it very slowly around a rotating crystalline seed; in this way, cylindrical single crystalline ingots are obtained that are subsequently sliced to get mono-Si wafers. Conversely, poly-Si is produced from faster and cheaper techniques as the directional solidification where large grains with different crystallographic orientations are formed by slowly cooling the melted ultra-pure silicon with specific temperature profiles. In this case, the loss of efficiency is compensated for the lower fabrication cost. Concerning a-Si, it is usually obtained by deposition using techniques as sputtering and chemical vapor deposition, while plasma deposition with glow discharge in SiH_4 leads to the production of hydrogenated amorphous silicon (a-Si:H), which owns improved optoelectronic properties explainable by the presence of hydrogen atoms bonded into the amorphous silicon structure.

In c-Si, which includes both mono-Si and poly-Si, the atoms are arranged in a diamond lattice with tetrahedral bonding: each atom has four covalent bonds with the four nearest atoms and the angle between any two bonds is ~109°. The a-Si basically retains the same crystal structure of c-Si, that is each atom is surrounded by on average four atoms, but no crystal lattice is present. In a-Si:H, silicon–hydrogen bonds are formed: a percentage of the silicon atoms makes dangling covalent bonds with only three silicon neighbors while the fourth valence electron is bonded to a hydrogen atom.

The a-Si is one of the most consolidated materials in the manufacturing of the so-called thin-film solar cells, namely cells obtained by deposing one or more thin layers of photovoltaic material on an insulating substrate. Thin-film cells have faced the market only recently and a large part of the current research in the emerging third generation cells concerns the development of thin-film devices comprising innovative technologies, based on different materials as organic and dye-sensitized solar cells (DSSCs) (the latter are treated in Subsection 3.2.5). In thin-film cells, the film thickness is in the order of tens of μm, in contrast with c-Si cells which are based on wafers with thickness in the order of hundreds of μm. This allows to create structures with stacked layers with absorption capacity in different portions of the spectrum to increase the efficiency of the device. However, substrates so thin are not self-

standing structure, hence a thicker support is needed (e.g., glass, plastic), made conductive by a layer of transparent conducting film (TCF). Thinner wafers not only allow to save material but also to decrease the bulk recombination within the solar cell at the expense of a higher surface recombination.

Concerning a-Si thin-film solar cells, the presence of defects and dangling bonds hinders the carrier mobility and favors recombination, thus reducing the diffusion length and the carrier lifetime. To establish a sizable electric field promoting the drift current, also for this type of cells p-i-n junctions are realized by interposing a thicker layer of intrinsic silicon between two thinner layers of p-type-doped (put on the top of the stack where light intensity is higher) and n-type-doped silicon. This structure takes advantage of the fact that the depletion region formed in the intrinsic material occupies the greatest thickness of the total solar cell, hence the carrier separation is improved by the significant electric field established in the depletion region, promoting the transport of charge carriers from the p-region to the n-region and compensating the low lifetime of the material.

The higher absorption coefficient of the a-Si justifies the better performance of this material with respect to the more efficient mono-Si in those working conditions characterized by low intensity radiation, diffuse radiation, and light sources with spectral power distribution in the typical range of artificial indoor lighting. In addition, the higher bandgap of a-Si (1.6 eV-1.8 eV [49]) with respect to c-Si (1.1 eV [49]) – visible in the abrupt edge in the absorption coefficient of Figure 25 which occurs at lower wavelength with respect to c-Si – demonstrates that the a-Si has a narrower response band restricted to the visible range and worse absorption capability with respect to c-Si in correspondence of red and far-red components of the spectrum. This different response band is further confirmed by the EQE shown in Figure 26 for mono-Si [54], poly-Si [55] and a-Si [56]. Therefore, for applications that exploit direct sunlight or lights with a high content of red and far-red components, c-Si-based cells can be preferred, especially poly-Si; conversely, in case of indoor deployment with artificial white light, a-Si thin-film cells are preferable. Hence, for each application it is essential to accurately select the cell type that matches the spectral irradiance of the available light source.

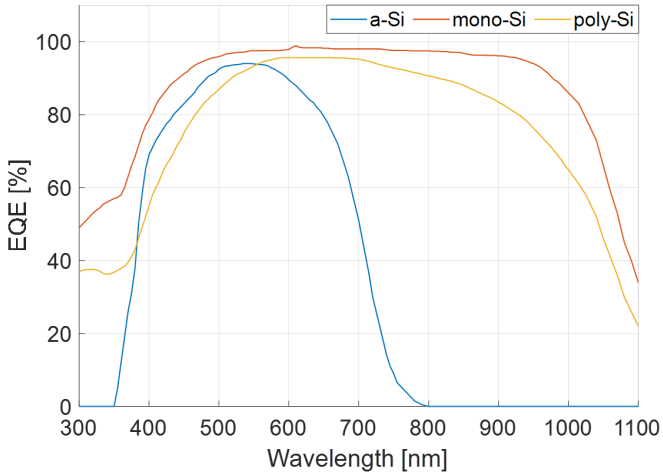

Figure 26. EQE as a function of wavelength for mono-Si [54] (in red), poly-Si [55] (in yellow) and a-Si [56] (in blue).

3.2.5. Grätzel cells

DSSCs, also known as Grätzel cells, are thin-film solar cells differentiating from traditional homo-junction solar cells since they exploit photoelectrochemical mechanisms for carrier formation, the main current contribution is the one due to diffusion. The achieved efficiency is generally lower than that of other thin-film cells (~10% [53]) but they can be realized with low-cost materials and simple manufacturing techniques, as screen printing.

They are composed of a thin-film of oxide semiconductor (generally TiO_2) deposed on a transparent substrate coated with a TCF, a light-sensitive dye adsorbed on the oxide surface, an electrolyte containing I^- (iodide)/ I_3^- (tri-iodide) redox ions, and a counter electrode. In a standard DSSC three interfaces can be identified: TCF/oxide, oxide/dye/electrolyte, electrolyte/counter electrode. The sensitization process involves the absorption of the incident photons on the oxide surface thanks to the presence of the photosensitizer (i.e., the dye) and then the injection of the electrons into the conduction band of the semiconductor itself, provided that the energetic level of the excited electrons is lower than the energy level of the conduction band of the oxide. Hence, the light-harvesting capability of the device depends on the amount of dye adsorbed by the semiconductor and on the absorption range of the dye. Consequently, significant improvements in the performance of DSSCs can be reached either by studying dyes with wider absorption span and by increasing the surface/volume ratio of the adsorbent semiconductor acting as photoelectrode. This last challenge is achieved by employing nanostructured oxides, which expose to the photosensitizer a larger contact

surface. The overall process of current generation is depicted in Figure 27 and can be summarized as follow:

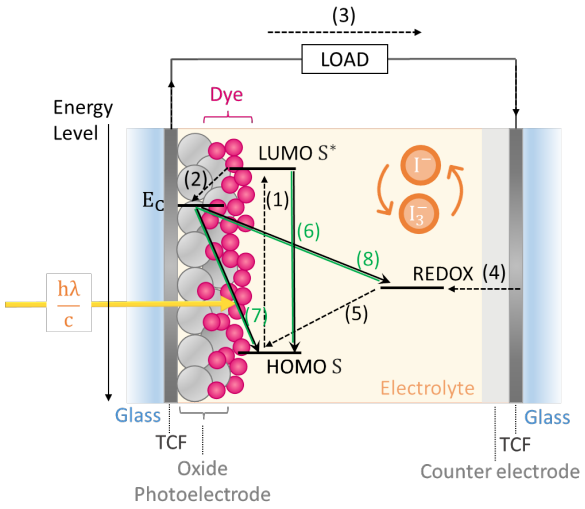

Figure 27. Basic structure and operating mechanism of current generation in DSSC, with black-green arrows the recombination processes.

- The photosensitizer adsorbed on the oxide surface absorb the incident photons passing from the ground state S (i.e., the highest occupied molecular orbital (HOMO)) to the excited state S^* (i.e., the lowest unoccupied molecular orbital (LUMO)): $S + \frac{h\lambda}{c} \rightarrow S^*$ (process (1));
- The photogenerated electrons are passed to the oxide causing the oxidation of the dye (S^+ state) and the formation of cations as long as the S^* level is sufficiently more positive than the conduction band E_C of the oxide: $S^* \rightarrow S^+ + e^- (TiO_2)$ (process (2));
- The injected electrons in the conduction band of the oxide diffuse toward the TCF contact and reach back the counter electrode through the external circuit (process (3));
- The I_3^- diffuses towards the counter electrode where is reduced to I^- ions thanks to the electrons collected from the external circuit and re-introduced into the electrolyte from the counter electrode: $I_3^- + 2e^-(counter - electrode) \rightarrow 3I^-$ (process (4));
- The oxidized photosensitizer is regenerated by accepting electrons from the I^- redox mediator of the electrolyte and the I^- is oxidized to I_3^- while the ground

state S is regenerated, as long as the S level is sufficiently more positive than the redox potential of the I^-/I_3^- reaction: $S^+ + \frac{3}{2}I^- \rightarrow S + \frac{1}{2}I_3^-$ (process (5)).

Therefore, the photosensitizer acts like an electron donor, the oxide as an electron acceptor, the organic dye is the electrochemical pump, the counter electrode collects the electrons from the external circuit re-introducing them into the electrolyte to perform I_3^- reduction into I^-, hence it should have good electrocatalytic activity.

The performance of the DSSC depends on four energy levels: the excited state and the ground state of the dye, the Fermi level of the oxide, and the redox potential of the mediator in the electrolyte. The difference between S^* and S determines the photocurrent, in analogy with the energy band gap in semiconductors. The voltage developed at the terminal of the DSSC depends on the energy interval between the Fermi level of the oxide and the redox potential of the mediator. In case of TiO_2 oxide and I^-/I_3^- mediator, the maximum established voltage is around ~0.9 V, in contrast with the built-in voltage in silicon p-n junction which is equal to ~0.7 V.

The behavior of the DSSC EQE is related to the photosensitizer and typically the used dyes have poor absorption in the red part of the spectrum. The EQE of the DSSC in [57], based on a layer of dye sensitized TiO_2, is plotted in Figure 28 with the EQE of a-Si [56] for comparison: the two materials have similar response curve and a narrower response band with respect to c-Si, this makes DSSCs good candidates for working with artificial white light and low-intensity sources as in case of diffused solar radiation.

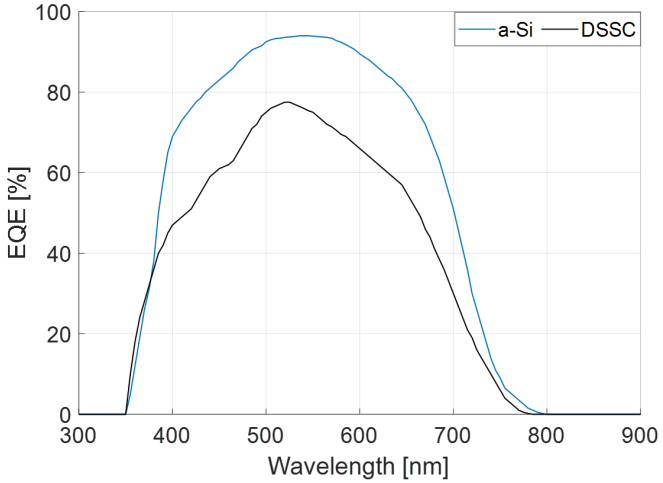

Figure 28. EQE of DSSC [57] (in black) and of a-Si [56] (in blue) as a function of wavelength.

In the DSSCs, three possible recombination processes can occur: direct recombination of the excited dye (process (6)), back-electron transfer reaction from the conduction band of the oxide to the oxidized sensitizer ($S^+ + e^-$ (TiO_2) → S, process (7)), recombination of the injected electrons with the oxidized redox acceptors in the electrolyte occurring at the interface oxide/electrolyte or in the regions of the TCF not covered by the semiconductor and directly exposed to the electrolyte ($I_3^- + 2e^-(TiO_2) \rightarrow 3I^-$, process (8)). To avoid recombination and accomplish effective charge separation, the electron injection process should be faster than the decay time of the dye from S^* to S, then the reaction of regeneration of the oxidized dye by accepting electrons from I^- ions should be faster than the time required by the injected electrons to recombine with the oxidized sensitizer, and finally the re-reduction of I_3^- into I^-, and consequently the transport of the electron through the oxide, should be faster than the recombination rate of the injected electrons with the oxidized acceptors in the electrolyte. The transfer rate of the electron from dye to oxide strongly depends on how the photosensitizer material is adsorbed on the semiconductor surface and on the energy gap between LUMO state in the dye and conduction band of the semiconductor. It was demonstrated for N3 Ruthenium dye that the excited state lifetime of the dye is typically in the [20 ns, 60 ns] range while the charge recombination between injected electrons on the oxide and cations of the dye occurs in a time interval ranging from μs to ms [58], thus above the time required for electron injection in the oxide, which settles around fs [59]. Concurrently, to have effective charge separation and current generation, the fast regeneration of the oxidized dye from the I^- ions must occur and it was found that for N3 Ruthenium the transfer rate of the electrons from the I^- ions is of hundreds of ns [60]. Regarding the recombination of electrons with acceptors in the electrolyte, it can compete with the transport time of the electrons through the oxide since both the phenomena occur in similar time scale of ms [54].

The electric model of DSSCs for DC operations is the same of Figure 24 used for a homo-junction solar cell and Equations (8)-(10) remain valid, where the photogenerated current is the current injected in the oxide (I_{inj}) and the reverse saturation current occurring at the oxide/electrolyte interface depends on the recombination of the I_3^- ions with the semiconductor. However, for non-steady conditions a different equivalent circuit should be used to describe the dynamic impedance of DSSC related to the kinetics of the diffusion transport of the electrons in the oxide film, the charge transfer at the counter electrode, the diffusion of I^-/I_3^- in the electrolyte and the recombination process at the oxide/electrolyte

interface, which, as discussed above, are mechanisms characterized by quite different time constants. Moreover, the dynamic impedance behavior varies with the cell potential and in the most general case the dynamic model typically used is the circuit of Figure 29, where the following three main contributions can be identified [61, 58]:

- High frequency: charge transfer at the counter electrode/electrolyte porous interface, electrically modelled as a Voigt element, constituted by the parallel between a charge transfer resistance R_{CE} and a Helmholtz or double layer capacitance C_{CE} (usually a constant phase element is used to represent the non-ideal frequency dependent capacitance due to a non-uniform distribution of the current in the material);
- Middle frequency: electron transport in the oxide and electron-electrolyte recombination (8), electrically modelled as a finite-length transmission line impedance Z_{TL} and two Voigt element accounting for substrate contact resistance R_{TO} and capacitance C_{TO} at the TCF/oxide interface (generally the TCF/oxide resistance is negligible), and for substrate charge transfer resistance due to recombination R_{ctTE} and substrate double layer capacitance C_{TE} at the TCF/electrolyte interface (generally TCF/electrolyte recombination is negligible with respect to oxide/electrolyte recombination);
- Low frequency: finite-length Nerst diffusion of I_3^- ions into the electrolyte, electrically modelled as a Warburg short element Z_D.

Moreover, the resistance $R_{S_{TCF}}$ accounts for the series resistive loss of the cell due to the contact resistances and the resistance of the TCF substrate. The impedance Z_{TL} is derived from the transmission line model and is used in place of concentrated element impedance. Indeed, an electrochemical system composed by an electrode immersed into an electrolytic solution containing ionic species in usually modelled with the Randle's circuit, which is composed of a Voigt element with a Warburg short element in series to the charge transfer resistance, in turn in series with a resistance modeling the electrolytic solution. However, in case of porous electrode, its behavior is not constant along the pore length and each oxide particle act as a resistance coupled to the electrolyte through an oxide/electrolyte interface hence the overall impedance is represented as the sum of infinitesimally short segments of transmission line constituted of an electron transport resistance in the oxide r_t in series with a

Voigt element composed of a double layer capacitance c_μ in parallel with a charge transfer resistance due to recombination r_{ct}.

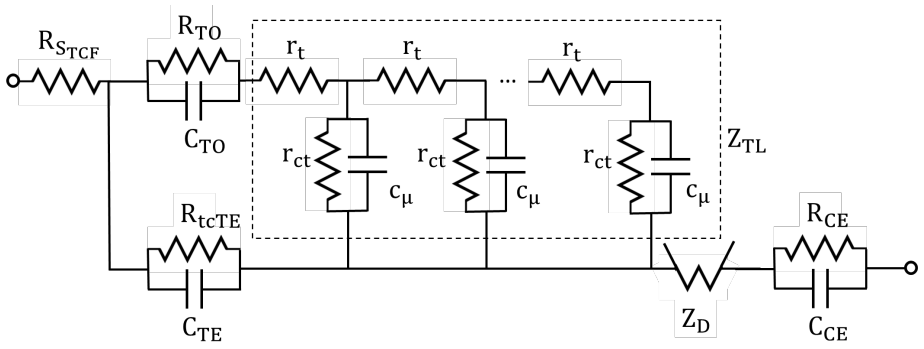

Figure 29. Equivalent electric circuit for DSSC [61].

From the parameters of the model, generally extracted through electrochemical impedance spectroscopy and fitting, several electron transport parameters can be inferred as effective electron lifetime, electron diffusion length, rate for recombination, effective electron chemical diffusion constant. The capacitances due to the charged layers at the oxide/dye and oxide/electrolyte interfaces are larger than those due to the junctions in the Si-based solar cell (in the order of mF/cm² [62, 63]) since the use of nanoparticles oxide increases the contact surface between semiconductor, dye and electrolyte, which becomes greater than the geometric area of the electrode; this results in longer charging times. Moreover, the electric diffusion constant for DSSCs is $<5\times10^{-4}$ cm^2/s [64] in contrast with that of Si-type solar cell ($\sim$1 cm^2/s), hence the electron diffusion in the oxide may be much slower than that in crystalline silicon. For all these reasons the DSSC settling time increases and a considerably long transient in the cell response is observed, for example when the cell moves from two different working points or when open circuit voltage decay is observed, unlike what happens in Si solar cells that show faster responses and photocurrent generation. The charge transfer mechanism in DSSCs, characterized by a large time constant, requires greater attention when using such cells in operative contexts characterized by alternating lights or when the MPP tracking (MPPT) is based on shortly switching the cell from the load to a very high resistance to provide the measurement of V_{OC}; indeed, there is the risk of not making the cell work in steady state conditions or of setting working points different from those prevented due to the incorrect achievement of the steady-state V_{OC}.

3.3. Battery management system

A BMS is a fundamental device in autonomous sensor nodes relying on energy harvesting from unstable sources, acting as a connecting element between the harvester and the load. It is composed of different subsystems in charge of carrying out distinct tasks, all necessary for the functioning of the system. The basic architecture of a BMS, analogous to that employed in the sensor nodes described in the next Chapters, is the one reported in Figure 30, together with the load, the harvester and a storage element to guarantee the functioning of the node even in periods of absence of the energy source.

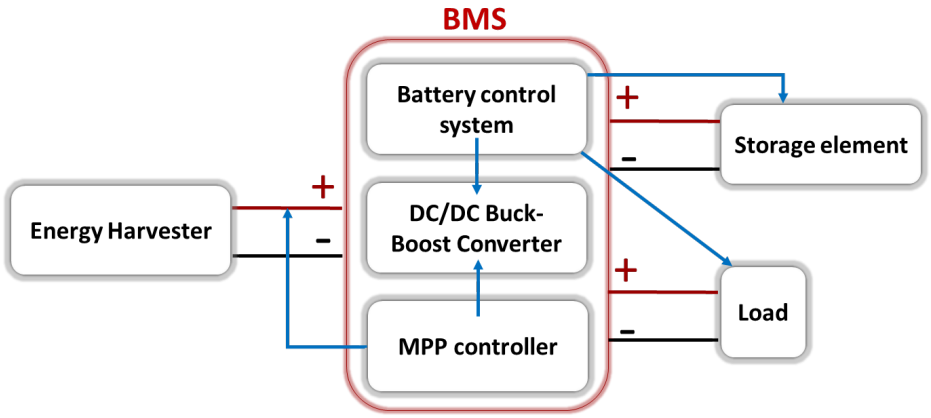

Figure 30. Block diagram of the battery management system; in blue the control signals.

The following elements can be distinguished, which will be thoroughly analyzed afterwards:

- The MPP controller in charge of implementing the tracking algorithm to extract the maximum power from the harvester;
- A DC-DC converter which effectively sets the working point determined by the MPP controller, it deals also with the battery charge and the generation of a regulated voltage used to supply the load;
- A battery control system to ensure the operation of the storage element in the optimal working conditions defined by the specification.

As seen in the previous Sections, for both solar cells and TEGs an MPP can be identified in correspondence of the working condition where the maximum power is extracted from the harvester. A MPPT algorithm can be defined to continuously correct, in the shortest possible

time, the operating point of the harvester adapting its power output to achieve maximum efficiency of conversion in every working condition, namely when the load or the energy source intensity (e.g., level of illuminance or temperature gradient) are modified. Various MPPT algorithms can be implemented to track the MPP, acting with a recursive approach on the control logic of the DC/DC converter. Some MPPT strategies are reported in the following [65]:

- Perturb and Observe (P&O): at the time t_i the voltage V_i and the current I_i outputted by the harvester are measured and the corresponding power P_i is computed; then the voltage or the current at the harvester is perturbed and a new power at time t_{i+1} is computed; finally P_i and P_{i+1} are compared and if the power is increased the voltage is perturbed again in the same direction, otherwise it is perturbed in the opposite direction. The perturbation process is iterated until the MPP, or a point close to the MPP, is reached. This methodology loses efficiency in case of sudden changes in the source intensity;
- Incremental conductance method: the incremental current and voltage changes are measured and the derivative of the power output with respect to its voltage is evaluated, i.e., $dP/dV \simeq I + V(\Delta I/\Delta V)$, whose slope is positive to the left of the MPP, negative to the right and equal to zero in correspondence of the MPP. The MPP can be found by comparing the instantaneous conductance (I/V) with the incremental one ($\Delta I/\Delta V$) and the direction of displacement of the MPP is evaluated depending on the changes in the measured voltage or current. This strategy can theoretically converge to the true MPP, although the smallest is the perturbation, the longest will be the time needed to reach the MPP;
- Constant voltage method: this technique regulates the output voltage of the harvester to a pre-determined constant value independently on the changes in the environmental conditions. This method is characterized by a great realization simplicity to the detriment of the accuracy since the MPP is never exactly reached;
- Open voltage method: the output voltage is regulated to be a pre-determined ratio of the measured V_{OC} (e.g., $\sim 0.5V_{OC}$ for TEGs and $\sim 0.8V_{OC}$ for solar cells), assuming that this ratio is constant as the intensity of the energy source varies. The harvester is detached from the converter during the time required to measure

the V_{OC}, this must be performed periodically to update the operating voltage according to the changes in the external operating conditions, hence this disconnection causes a periodic interruption in the harvesting process. Even this strategy can attain the true MPP just in limited cases and if the operating conditions are changed the true MPP is just approached.

However, even if the MPPT is the tool used to track the MPP by changing the voltage across the harvester, it does not perform the actual setting of the voltage, which is attained through a DC/DC converter by modifying the impedance seen by the harvester acting with a switching strategy [49]. Generally, the converter takes as input the non-regulated voltage generated by the harvester which is affected by the variations of the energy source and transforms this variable voltage into a stable one at a different level compatible with the requirement of the load or of the storage device. Switching DC/DC converters use one or more switches to transform the DC voltage from one level to another. In the case of PWM technique, the average value of the output is regulated acting on the closing and opening times of the switch by keeping constant the switching frequency and modifying the duration of the switch closing and consequently the duty cycle. The main topologies of DC/DC converters are buck (step-down), boost (step-up) and buck-boost. The buck converter generates an average output voltage lower than the input voltage while the boost converter generates an average output voltage greater than the input voltage. The buck-boost converter can be used to either step up or step down the input voltage. In PWM-based converters the ratio between input and output voltages is set by the duty cycle value.

The energy storage is another important aspect accounted in the implementation of BMS to compensate the discontinuous electricity generation from the energy sources or to supply the system even in its absence (e.g., dark hours in case of sunlight). Depending on the specific application and design constraints, such as operating temperature, power source availability, energy density, capacity and operating voltage, a different storage element is needed [66]. For daily storage demand, the most favorite storage technology is the battery, since traditional capacitors and novel supercapacitors are less suitable for long-lived applications because of the small energy density of the former and the severe self-discharge of the latter. In particular, supercapacitors are valid candidates in applications requiring short-lived storage and fast power delivery since they can exchange charge much rapidly and they tolerate more charge/discharge cycles than the batteries. Specifically, rechargeable batteries are good solutions to store excess electrical energy, which can be re-used during the period of absence

of the energy source. Typical examples for rechargeable batteries are lithium-ion (Li-Ion) and lithium-polymer (Li-Po) batteries, which have high energy density and good charge/discharge characteristics.

In conjunction with the storage elements, charge controller devices should be used to ascertain that the battery operates within the safe limits specified for the chosen technology. Indeed, to preserve the battery lifetime, it is fundamental to charge and discharge batteries at the right voltage and current levels and to avoid overcharging and undercharging of the device which can cause the degradation of the battery performance until the irreversible damage. The charge controller prevents overcharging by decoupling the harvester from the battery until a pre-set voltage threshold is reached, at which the harvester is connected to the battery again. Analogously, the load is disconnected to avoid excess drainage until the storage element reaches again a good charge level.

The devices chosen for the applications presented in the next Chapters 4-7 are the BQ25570 manufactured by Texas Instrument and the SPV1050 manufactured by ST Microelectronics since they are off-the-shelves IC owning all the characteristics required by the proposed applications, indeed the implementation of a customized battery charging system went beyond the scope of this thesis. They are specifically designed for micro harvesting from high impedance DC sources providing sporadic and time-varying energy. They accept respectively minimum input power in the mW and in the hundreds of mW ranges for normal charging operations, which are compatible with applications involving the use of TEGs with small temperature gradients and of small-sized solar cells under unconventional lighting conditions such as artificial lights or diffused sunlight. They embed a boost charger to charge an energy reserve and a buck converter providing a regulated voltage supply to power up a low-power sensor node without directly draining the battery. Moreover, in the same package, they provide a user programmable MPPT logic, based on the open voltage method and the adaptation of a variable load with switching modality, that periodically (every 16 s) samples the open circuit voltage at the input of the IC for optimizing the power transfer from the source. Finally, a battery control logic implements user-settable battery voltage thresholds to manage the detaching of the load from the power rail in case of excessive battery depletion and the stopping of the battery charging in case of risk of overcharging.

Chapter 4

Self-sufficient LoRaWAN node via TEGs-based harvesting

The waste heat, generated by a variety of both natural and human-made phenomena, is available free of charge in several application scenarios; this has led to a growing interest in the possibility of powering sensor nodes exploiting the thermoelectricity mechanism by means of TEGs as harvesters. One of the most common uses of TEGs is with direct solar irradiation both as sole harvesting devices [67] or in hybrid solutions in conjunction with solar cells [68]. Hybrid harvesting systems which embed flexible and stretchable TEGs are also adopted to power Wireless Body Area Networks (WBANs) to harvest body heat [69]. Other innovative solutions include the use of TEGs for harvesting energy directly from the surrounding environment for example by exploiting the so-called "ground-air thermoelectric generators" [70, 71] (i.e., the temperature gradients induced between the air temperature and the ground temperature, that remains stable for most of the day even at small depths), the temperature gradient between the tree trunk and the ambient air [72] and the heat coming from volcanic fumaroles [73]. Furthermore, thermoelectricity is the most suitable harvesting mechanism in the Industrial IoT context, where elevated temperature gradients can be easily reached on numerous surfaces such as pipes or factory machineries to recover heat wasted as part of different processes [29, 74].

The application proposed in this Chapter is aimed at demonstrating the advantages of a thermoelectric energy harvesting system embedded in a general purpose LoRaWAN node, which exploits at most two commercial TEGs as harvesters and a Li-Po battery as storage element. No specific sensor is embedded on board since the focus is on the data transmission aspect and on exploring the applicability boundaries of this harvesting mechanism when designing quasi-real-time remote monitoring systems requiring a continuous low bit-rate flux. Indeed, the feasibility of quasi real-time transmissions even in the case of very low gradients (i.e., 5° C) is a remarkable result which legitimizes the use of this technology with numerous natural and artificial phenomena, opening to new uses both in outdoor and indoor scenarios.

Moreover, in this Chapter an overview of the LoRa technology integrated in all the self-sufficient nodes described in the rest of the thesis is given, while in Appendix A some preliminary studies of its transmission performance in case of critical operative scenarios (i.e., underwater to above water and under ice to above ice transmission) are provided.

4.1. LoRa technology

In recent years, a wide range of wireless transmission technologies specifically conceived to operate efficiently and reliably in critical conditions (e.g., in case of noisy environments, with reduced power availability or in presence of severe attenuation) have emerged. These technologies are especially thought for the Machine-to-Machine (M2M) communication scenario, with limited data rates and very low receiver sensitivities. Several of these technologies operate within the so-called Sub-GHz frequency bands, which includes the frequencies below 1 GHz [75], and among them the LoRa [76] technology is probably the one that has received the largest attention and is now considered as a de-facto standard within the LPWAN domain. Its rapid growth is mainly due to the very long achievable transmission ranges and the possibility to deploy dense distributed monitoring infrastructures still guaranteeing reduced power consumption. Above this proprietary physical communication layer of the protocol stack, also an ad-hoc Media Access Control (MAC) layer protocol has been developed, named LoRaWAN [77].

Furthermore, the adoption of the LoRa technology offers different advantages in terms of power consumption and employment which facilitate the achievement of the system autonomy even in the case of relatively high transmission rates, close to the limit on the duty cycle posed by the law regulations. While similar results may be achieved also with other LPWAN technologies, the flexibility related to the customization of the LoRaWAN network infrastructure, if compared with other proprietary technologies, greatly simplifies the deployment of large-scale distributed monitoring systems. These aspects, combined with all the advantages presented above, concur to create a highly versatile architecture whose main peculiarities are durable energetic autonomy and low maintenance needs.

LoRa is a long-range wireless technology (range over 10 km in rural areas, 3-5 km in urban areas), characterized by low transmission power and low energy consumption. On the other hand, it does not allow the transfer of a large amount of data and has a reduced

transmission rate (about 50 kbps) because of the compliance with regulations on the duty cycle. It is a spread spectrum frequency modulation technique derived from Chirp Spread Spectrum (CSS) modulation [78, 79]. A chirp, which basically corresponds to a symbol, is a sinusoidal carrier signal whose spectrogram is a ramp varying over time in the range between two fixed minimum and maximum frequencies (up-chirp when increases, down-chirp when it decreases); a transition between up-chirp and down-chirp corresponds to the start of a new signal. The chirp is transmitted in short bursts, i.e., the chips, and the corresponding information is coded as frequency initial shifts: symbols are transmitted by selecting the initial frequency of cyclic shifted up-chips from a set of 2^{SF} possible choices, being SF the Spreading Factor, with the frequency of the chirp signal increasing until the fixed maximum frequency is reached and then wrapped to the fixed minimum frequency. As a result, the signal is transmitted using a fixed channel bandwidth considerably wider than that necessary with other modulations.

The network is characterized by a star topology composed of four fundamental elements:

- End nodes: they consist of a radio module with an antenna and a microprocessor to collect sensor data; they bidirectionally communicate through gateways to the server;
- Gateway: consisting of a radio module with an antenna and a microprocessor; it works as a transparent bridge allowing the bidirectional transport of data between the end devices and the server;
- Network server: connects to multiple gateways through a secure TCP/IP connection, wired or wireless; it filters the duplicate packets and performs security checks;
- Application server: collects and analyzes the data coming from the nodes and determines the response actions.

When an end-node performs a transmission, it broadcasts the packet to all the gateways closest to it, subsequently these data pass from the gateway to the network server where the latter analyzes them, eliminates duplicates and determines the gateway that has the best reception. To optimize energy consumption, LoRaWAN differentiates between three classes of end-devices on the basis of the opening time of the downlink window, while the uplink is managed in the same way:

- Class A (Bi-directional end-device): it is the default modality supporting the bidirectional asynchronous communication with the gateway, it is more efficient from the point of view of the power management since the nodes try to remain inactive for a longer time possible. An end-device can start an uplink every time it has data to send, after that it waits for a certain time interval for an answer from the server, which can take place only in two pre-established downlink windows open at different time instants;
- Class B (Bi-directional end-device with scheduled receive 5 slots): this modality extends the functionality of class A by implementing additional downlink windows in planned times;
- Class C (Bi-directional end-device with maximal receive slots): the functionality of class A is extended by implementing a downlink window continuously open. This allows communication with low latency, since the end-node listens constantly over time, but it greatly increases energy consumption.

The LoRa modulation works on free ISM bands that are assigned according to the development region; in Europe, it works at 868 MHz and on 8 possible uplink channels. The performance of the technology can be evaluated in terms of SNR (signal-to-noise ratio), RSSIs (received signal strength indicators) and packet loss (PL). The basic radio settings that can be manually set by the user to analyze this technology are:

- Bandwidth (BW): indicates the difference between the upper and the lower frequencies occupied by the chirp, namely is the bandwidth of the spectrum of the transmitted signal; it can be modified to increase the transmission speed at the expense of the obtainable sensitivity since more noise is added;
- Spreading Factor (SF): it gives information about the amount of desired diffusion of the spectrum. It indicates the number of raw bits that can be encoded within a symbol (one symbol has SF bits) and the number of chips per symbol (there are 2^{SF} chips in one symbol, equal to the number of possible coded values, and each symbol indicates the encoding of a chirp). Moreover, this parameter gives an indication of the trade-off between receiver sensitivity, and consequently PL percentage, and power consumption. A high SF implies better receiver demodulation capability even for lower RSSIs, thus a better signal coverage, at the expense of a more relevant power consumption; for this reason,

the SF variation should affect the PL percentage and not considerably the RSSI of the received packets;

- Coding Rate (CR): indicates the amount of non-redundant data in the data-stream. Indeed, LoRa uses a Forward Error Correction (FEC) mechanism for detection and subsequent correction of errors to improve the performance in case of interference. According to its modification, the robustness of the transmission is increased since each symbol is wider in time and packets with lower reception power can be better demodulated by the receiver, but a resource overhead is introduced thus increasing the transmission duration and consequently the power consumption. It is expected that the RSSI will not be affected by the CR while PL should slightly decrease in the case of smallest CR.

In LoRa, the BW corresponds to the chip rate R_C [chips/s], the SF relates chips and symbols as 2^{SF}chips=1 symbol, so the symbol rate R_S [symbols/s] is related to R_C as $R_S = \frac{BW}{2^{SF}} = \frac{R_C}{2^{SF}}$; the raw bit rate [bits/s] is $R_b = SF\frac{BW}{2^{SF}} = SF \cdot R_S$ while the actual rate of user data bits carrying information is reduced by a factor linked to the CR and is equal to $R_{b_{user}} = R_b \cdot \frac{4}{4+C_R}$, as a consequence $R_C = \frac{R_b}{SF} \cdot 2^{SF}$. Increasing the BW, the R_b increases while the symbol duration $T_S = \frac{1}{R_S}$ decreases; conversely, increasing the SF, R_b decreases and T_S increases, in particular, if SF increases by one, T_S doubles while R_b is approximately halved. The correlation between SF and T_S is given in Figure 31.

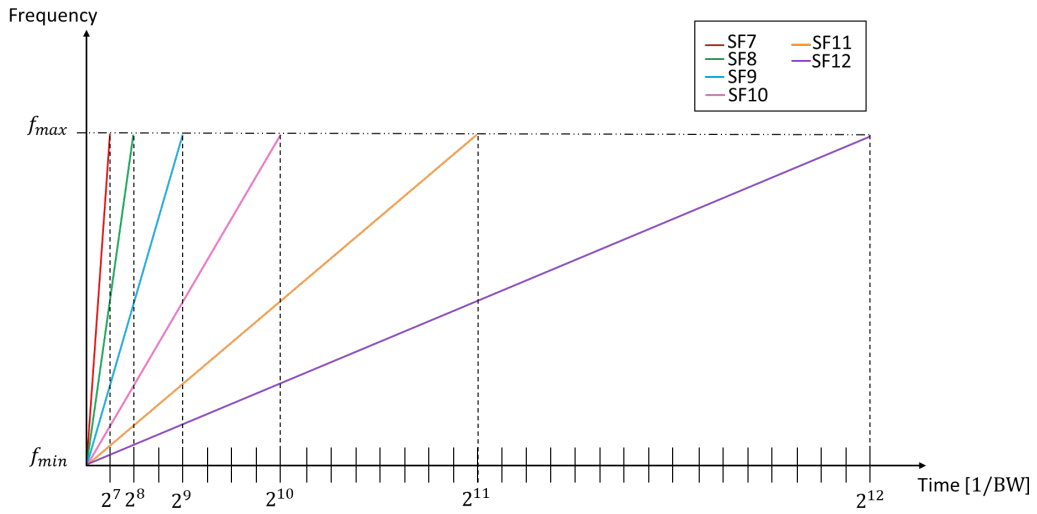

Figure 31. Correlation between SF and T_S for a given fixed BW.

As already mentioned, LoRa characterizes the Physical Level which is composed of the radio part and the modulating part, so it can be implemented on different types of networks and protocols. Among these, the LoRaWAN protocol is developed to define the upper layers of the network with the idea of optimizing the LoRa modulation. It is standardized by LoRa Alliance and includes the MAC level and the Application Level as well as specifications on the communication rates and frequencies, the types of network architecture, security controls, Adaptive Data Rate, and many other features. Moreover, LoRaWAN uses a 128-bit Advanced Encryption Standards with two independent layers of protection to guarantee the safety of the wireless transmitted data. The first is defined by the Network Session Key and is used by both the end-node and the network server to ensure the integrity of data sent; the second is defined by the Application Session Key and is used by the end-node and by the application server to guarantee the communication in uplink and downlink. This results in an extremely high level of security since the package can be decoded only with the knowledge of both keys. Concerning the LoRaWAN packet, depending on the implicit header or explicit header option, its structure is divided into preamble, header and payload. When changing the number of information bytes sent, we act on the so-called FRMPayload (frame payload) which forms the overall PHYPayload together with at least 12 additional configuration bytes. When the FRMPayload is present, the overhead bytes added by the LoRaWAN protocol are 13 and are composed as follows: MHDR (MAC Header, 1 byte), DevAdr (device address, 4 bytes), FCtrl (frame control, 1 byte), FCnt (frame counter, 1 byte), FOpts (frame options, 1 byte), FPort (frame port, 1 byte) and MIC (message integrity code, 4 bytes). For this reason, the shortest transmittable PHYPayload has a length of 14 bytes (i.e., just 1 byte of FRMPayload). Depending on the set SF, there is a maximum number of bytes which can be transmitted over the radio link: 222 bytes in case SF=8 and 7, that is the maximum data rate allowable by the LoRa technology, down to 51 bytes in case SF=12, 11 and 10. The length variation of the payload has an effect mainly on the total air transmission time (i.e., Time on Air (ToA) or packet duration (T_{packet})), since a different number of information bytes are sent, and consequently on the power consumption of the system, whilst no effect should be present on SNRs and RSSIs. For a LoRaWAN packet the transmission duration is calculated as preamble duration plus payload duration ($T_{packet} = T_{preamble} + T_{payload}$). The preamble duration is calculated as $T_{preamble} = (n_{preable} + 4.25) * T_S$ and for EU868 $n_{preable} = 8$. The payload

duration is computed as $T_{payload} = T_S * \left(8 + \max\left(\left\lceil \frac{8PHYL - 4SF + 28 + 16CRC - 20H}{4(SF - 2DE)} \right\rceil * (CR + 4), 0 \right) \right)$ where PHYL is the length of the PHYPayload, the CRC parameter is used to enable ($CRC = 1$) or disable ($CRC = 0$) the cyclic redundancy check (for LoRaWAN $CRC = 1$ by default), the H parameter disables ($H = 1$) or enables ($H = 0$) the header according to implicit or explicit mode (for LoRaWAN $H = 0$ by default), the DE parameter is used to activate ($DE = 1$) or deactivate ($DE = 0$) the low data rate optimization (for LoRaWAN $DE = 1$ by default when $SF = 11,12$). By increasing the SF, the ToA and the radio coverage increase to the detriment of higher power consumption, therefore it is better to use higher SFs when the signals are weak due to high interference or large distance of the node from the gateway. In case of LoRaWAN implementation, the SF can range from 7 to 12, the BW can be 250 kHz just for SF=7 and 125 kHz for all the others SF, the CR can assume values between 4/8 (the smallest CR, 4 data bits are encoded with 8 transmission bits,) and 4/5 (largest CR). Moreover, according to the European regulations, the maximum transmission power in uplink is limited to 25 mW (14 dBm) and, depending on the channel, an 0.1% or 1.0% duty cycle per day is mandatory.

One of the greatest advantages of LoRa, together with the corresponding LoRaWAN protocol, is the satisfactory decoding capacity even in presence of critical noise and attenuation in the radio channel. In this context and with the aim of exploring the possibility of applying this protocol to networks of self-sufficient nodes operating in critical environment, a part of the activity of my PhD research was devoted to the investigation of the transmission performance of this technology in terms of maximum achievable transmission range, both theoretically and experimentally, in scenarios characterized by severe attenuation. The details of this analysis are reported in Appendix A, where a simple study of the behavior of lossy transmission media, used to model the transmission performance, is presented together with the experimental results obtained in two specific critical scenarios and concerning the collection of data from underwater [80, 81] and from a thick layer of ice [82].

In the applications presented in the following Chapters 4-7, the radio module used is the RFM95x by HopeRF electronics equipped with different types of directional antennas and mounting the SX1276 chip. Concerning the server-side structure, it is composed of a network server in charge of managing the incoming packets from multiple sources and of an

application server for data storage, the data are then available from a customized web interface. The used infrastructure includes a set of three gateways of two different typologies: some are custom-made devices while others are LG308 Dragino commercial devices. The transmitted packets can be received by one or more gateways and the adopted policy for the duplicated packets removal is based on the minor detected RSS.

4.2. System architecture

A general purpose LoRaWAN node was realized, in which two main parts can be distinguished: the energy harvesting and the wireless subsystems.

The energy harvesting subsystem consists of three main components: the harvester, a Li-Po rechargeable battery (3.7 V, 750 mAh) and the BMS. Commercial Bi_2Te_3 TEGs were used (model SP1848 27145 SA) with size 40 mm × 40 mm × 3.4 mm, maximum temperature of 150 °C, electric conductivity in the range [850 $\Omega^{-1}cm^{-1}$, 1250 $\Omega^{-1}cm^{-1}$], thermal conductivity around 15×10^{-3} W/(cm°C), figure of merit zT lower than unity and heat-to-power conversion efficiency lower than 3%. The energy management of the entire node was attained using the BQ25570 mounted on the BQ25570EVM-206 evaluation board and with MPPT set to around 50% or 80% of the open circuit voltage of the harvester, depending on the test performed. By changing the hardware configuration of the board, the output voltage of the buck converter was set to 1.8 V, that is the minimum supply voltage for the MCU and the radio transceiver. More details about the BMS IC functioning are provided at the end of Section 3.3.

The wireless section of the prototype was implemented with the RFM95x low-power LoRa transceiver, equipped with a 2 dBi gain λ/8 whip antenna and an ATtiny84 microcontroller by Atmel. A simple LoRaWAN network was established between a LoRaWAN Class A end device and a LoRaWAN gateway, sending the received packets to network and application servers and making the data available from a customized web interface.

The sensor node was configured with operating frequency 868 MHz, CR 4/8, BW 125 kHz, transmitted power 14 dBm, and SF 12, which was chosen to set up a worst-case condition in terms of longest airtime duration and thus largest power consumption. The transmitted packets contained a generic alphanumeric string with fixed length of 23 bytes (13 bytes of overhead + 10 bytes of payload), assumed as an average dimension of a LoRaWAN packet

carrying sensor data. Depending on the performed test, a sleep policy foreseeing the periodic packets transmission at fixed time intervals was adopted. The ToA for the settings adopted was 1974.3 ms, thus entailing a transmission every 195.5 s ≃ 3 min to comply with the law regulations defining a maximum 1% duty cycle; however, during some tests, the duty-cycle regulations were violated to emulate a worst-case scenario.

4.3. Tests and results

A preliminary test campaign was performed to electrically characterize the used TEGs under different temperature gradients, then several tests were set up to evaluate the charging/discharging process of the on-board battery by changing two crucial parameters: the temperature gradients applied to the harvester and the frequency of the radio transmissions performed by the transceiver. The results of these test campaigns and the measurement set-up employed are presented in the following Subsections.

4.3.1. Measurement set-up

A proper test bench was set up to attain different temperature gradients ΔT at the two faces of the TEG and was used either to perform the characterization of the TEG and the self-sufficiency tests of the entire system.

In particular, the hot side of the TEG was placed in contact by means of thermal paste with a high temperature source consisting of a metal plate heated from the heat wasted by an Arcol HS25 aluminium-housed power resistor (maximum power dissipation of 25 W), screwed to the plate and connected to a Mastech HY3005D-3 DC linear voltage supply. Conversely, an aluminium heat sink was fixed on the cold face of the TEG by means of thermal paste to ensure a better heat transfer. The temperature in the contact points between the TEG faces and the heated metal plate or the heatsink were acquired by means of type K standard thermocouples (accuracy of ±2.2 °C) connected to a digital multimeter. The measurements were performed after having waited for the heatsink to reach a stable temperature value, to spot out the steady state temperature gradient ΔT reached after the transient phase.

In case of the TEG characterization tests, a simple circuit was realized, exploiting the method of variable resistor: it was a series connection of the harvester, a 1 Ω-R_{shunt} resistor

for current sensing and a variable resistor with maximum value of 50 Ω. The variable resistor was varied in steps in order to change the load and sense the different (I,V) couples from short to open circuit condition. An NI PCI-6070 acquisition board (12 bits of resolution, 1.25 MS/s maximum sampling rate) monitored via LabVIEW was used to acquire the voltage output of the TEG module, V_t, and the current flowing through R_{shunt}, I_{shunt}.

During the second test campaign, the overall system presented in Section 4.2 was used and the voltage of the on-board rechargeable battery was monitored using an Agilent 34410A multimeter (configured with 10 PLC and 6 ½ digit resolution) controlled via LabVIEW with sampling period of 1 s. The initial battery voltage level was set to approximately 3.9 V, in the range where the typical charge vs voltage characteristic for a Li-Po battery is not flat, in this way the voltage variation was a sufficient indication of the charge status of the battery.

The type A uncertainty (i.e., <80 μV) and the type B uncertainty derived from the instrument specifications (i.e., $\frac{max\_error}{\sqrt{3}} \simeq 100$ μV with $max\_error \simeq 180$ μV) were comparable giving an overall measurement uncertainty $u \simeq 130$ μV. This analysis is valid when the battery variations are slow, and the monitored voltage can be assumed substantially constant, while during the radio transmission peaks the uncertainty drastically grows and can't be quantify since the impulsive peaks are recorded by the instrument as an average value. However, for the performed tests, we were interested in appreciating a growing trend in the battery voltage level, having just an indication that a transmission took place.

This measurement set-up for the battery voltage monitoring was then replicated during the self-sufficiency tests presented in the following Chapter 5-7 (i.e., Subsections 4.3.1, 5.3.1, 6.4.1 and 7.4.1) and the uncertainty considerations remain also valid.

4.3.2. TEG characterization

The TEG characterization was performed at three temperature gradients (i.e., ΔT = 18 °C, 26 °C and 30°C), using the measurement set-up and the methods described in Subsection 4.3.1. The collected results are visible as scatter plots in Figure 32a, where the TEG current and voltage correspond to the acquired I_{shunt} and V_t, while the dashed lines are obtained as polynomial fitting of the measured data. In Figure 32b the P-V characteristic is reported, where the power generated by the TEG is derived as $P_{TEG} = V_t \cdot I_{shunt}$. From the interpolation of the curves, it emerges that the harvestable power for one single TEG covering an area of 16 cm^2, under temperature gradient lower than 30 °C, is in the order of tens of mW.

Moreover, the obtained results confirm the TEGs physics: as expected, the power delivered by the TEG is maximum when the extracted voltage is 50% of its V_{OC}, and this MPP linearly grows as the temperature gradient increases (see the inset of Figure 32a).

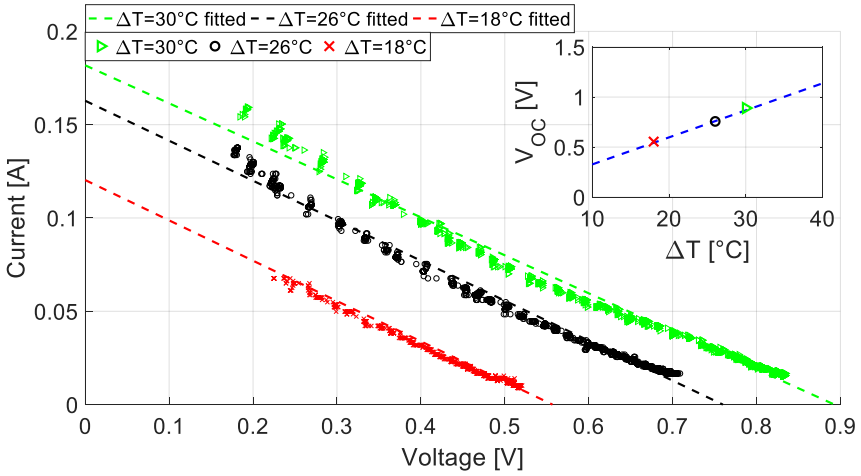

(**a**)

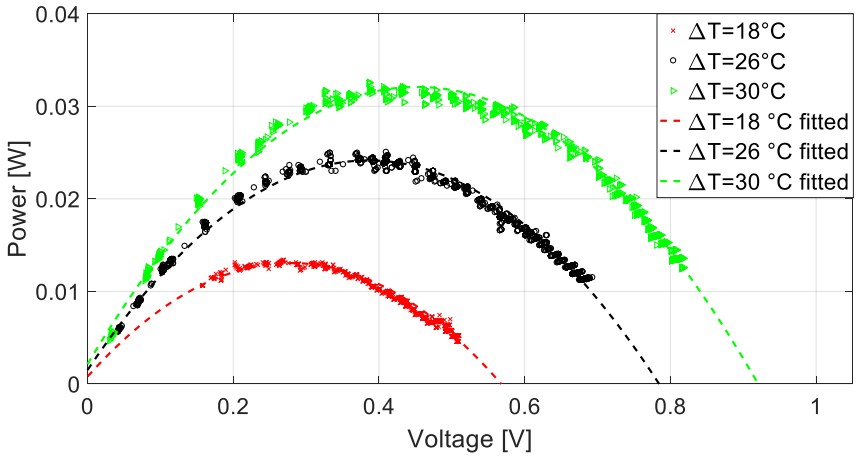

(**b**)

Figure 32. I-V (**a**) and P-V (**b**) characteristics measured (scatter plots) and fitted (dashed lines) at three temperature gradients: ΔT=18 °C (red), ΔT =26 °C (black) and ΔT =30 °C (green); in the inset of (**a**), the V_{OC} at the three temperature gradients.

4.3.3. Node self-sufficiency tests

The second laboratory tests campaign concerned the examination of the overall system by establishing a temperature gradient at the ends of the TEGs (one single TEG or two TEGs in series depending on the performed tests) with the method described in Section 4.3.1. Every

test was performed for about 24 h to have an exhaustive view of the node behavior during one day, with the heat source always present. The MCU was programmed according to several sleep policies for managing different radio transmissions frequencies. Depending on the number of TEGs connected to the BMS, different MPPT settings were used to not violate the minimum ratings requirements of the evaluation board. The purpose was to thoroughly investigate the relation among the temperature gradients and the maximum achievable transmission rates and to prove the energy independence of the system even in the case of extremely low temperature gradients.

The first three tests were implemented with the MPPT set to 50%, $\Delta T = 30$ °C and by changing the rate of the radio transmissions. The battery voltage trend is shown in Figure 33, respectively for transmissions every hour (a), every 10 minutes (b) and every minute (c). The downward periodic voltage peaks visible in the graph are due to the radio transmissions, but they do not significantly affect the charging process. Indeed, the three graphs show that the slopes of the battery voltage trend remain positive even decreasing the sleeping period of the wireless node and increasing the frequency of the radio packets, reaching quasi-real time transmissions.

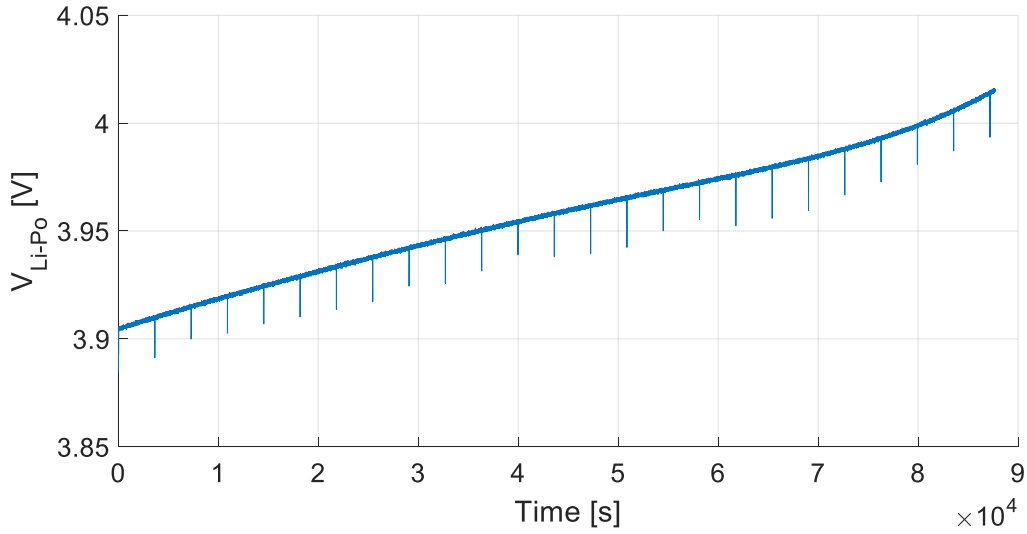

(a)

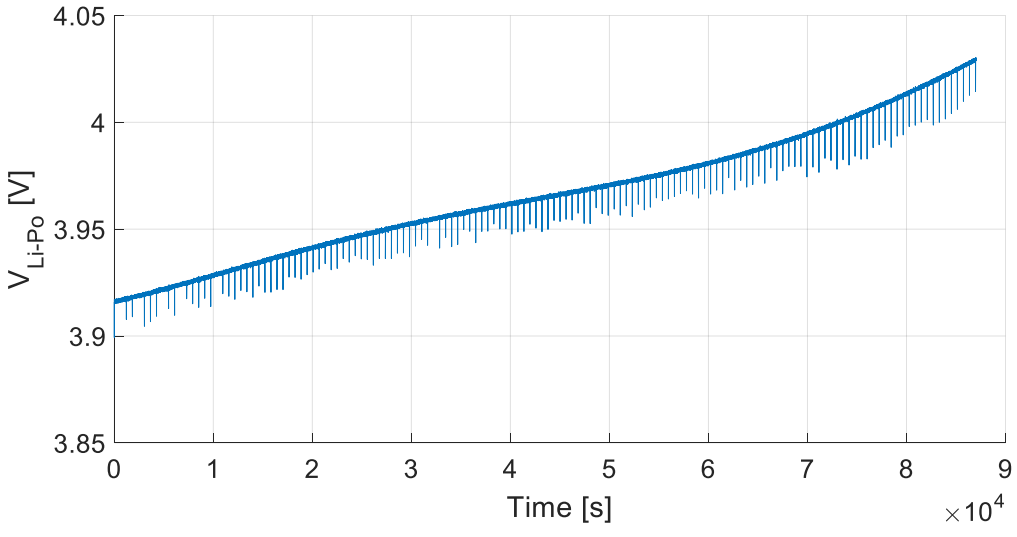

(**b**)

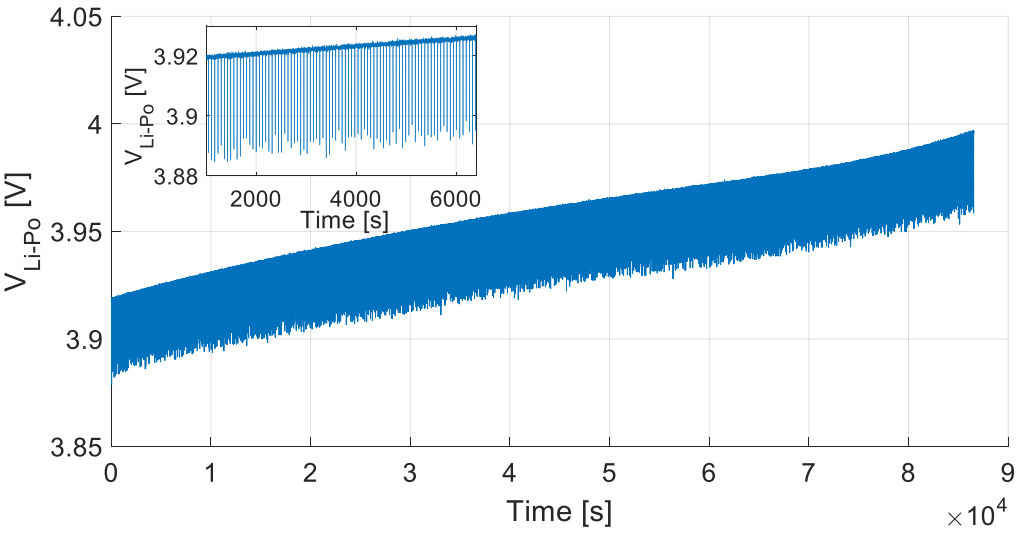

(**c**)

Figure 33. Li-Po voltage trend with radio transmissions every hour (**a**), every 10 minutes (**b**) and every minute (**c**) at ΔT = 30 °C. The inset of (**c**) shows a magnified 90 min-section of the plot.

As a consequence, a second test was performed decreasing the temperature gradient to 15 °C while the sleep period of the MCU was left unaltered with transmissions every minute. The voltage trend is reported in Figure 34: even in this case a positive trend of the voltage battery is maintained. Due to this positive outcome, tests with 10 min and 1 h transmission frequencies were not performed for this temperature gradient.

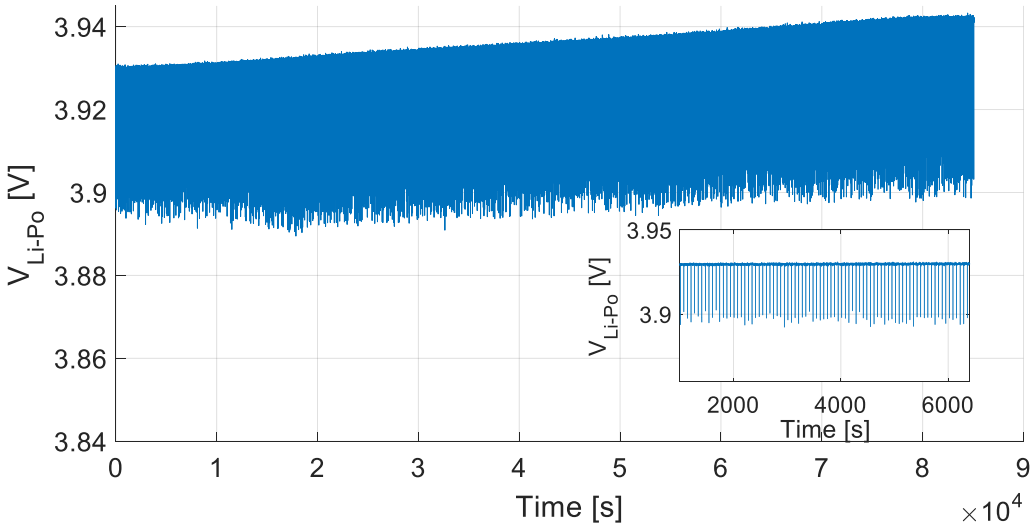

Figure 34. Li-Po voltage trend with radio transmissions every minute and ΔT = 15 °C. The inset shows a magnified 90 min-section of the plot.

By further decreasing the temperature gradient, the TEG produces smaller voltages which can be critical for the BMS since a minimum $V_{OC} = 130$ mV is required. With the presented set-up a single TEG was not able to develop such a voltage with low temperature gradients, causing the BMS to remain in its 'cold start' stage. To overcome this problem, two TEGs of the same model were connected in series, and the MPPT was changed to 80% of the full-scale value. This last modification, even if causing a ~40% decrease in the power supplied by the TEGs, is necessary to ensure the minimum voltage required by the used BMS.

Further analyses were performed involving the new set-up to observe the system behavior in case of low-temperature gradients. Figure 35 shows the results of the test performed with radio transmissions every 30 min and ΔT = 5 °C, which is the minimum tested temperature gradient since with the employed heating/cooling system the temperature across the harvester became uniform by further lowering the temperature difference. Moreover, by going below ΔT = 5 °C, the voltage generated by the TEGs would be insufficient to supply the BMS, thus requiring more TEGs in series to overcome the cold start phase of the IC. Depending on the considered application, some strategies can be adopted to increase the temperature difference, for example by favoring the cooling of the cold side of the devices.

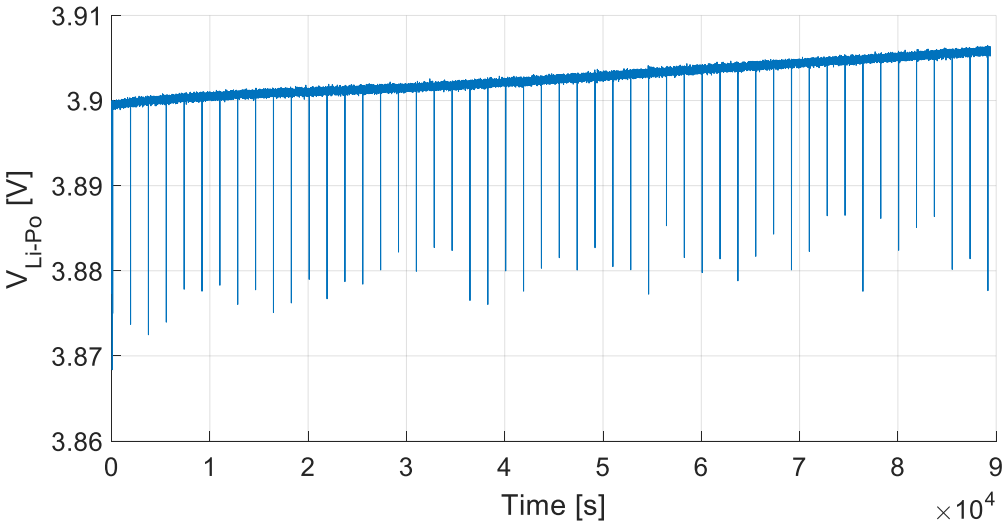

Figure 35. Li-Po voltage trend with radio transmissions every 30 minutes with ΔT = 5 °C.

Two remarkable outcomes emerged from the tests: the energy autonomy of the system is demonstrated even for high frequencies of radio transmissions and under very low temperature gradients, thus leading to two significant results. On one side, in case of temperature gradients sufficiently high but more critical to be reached outside industrial contexts, the system can be configured for quasi-real-time applications and in general for all those deployments requiring a continuous low bit-rate flux of data coming from various sensors; on the other side, the reaching of the node self-sufficiency in case of very low gradients with a still satisfactory radio transmissions rate, opens the way for a plethora of monitoring scenarios, from rural areas to industrial facilities, where both natural and artificial phenomena are sufficient for reaching the required ΔT (e.g., by directly exposing the TEGs to sunlight).

Chapter 5

Self-sufficient LoRaWAN node via harvesting from diffused low-intensity solar radiation

The use of photovoltaic cells in energy self-sufficient wireless sensor nodes is quite common for deployments in sites with direct sunlight exposition, nevertheless solar harvesting is much more challenging in case of applications exposed to low-intensity diffused solar radiation. The validation of an energy-autonomous sensor node in this scenario opens the way to several monitoring applications deployable in outdoor shady environments (i.e., in the proximity of tall buildings, among the trees in a forest) or under unfavorable weather conditions (i.e., cloudy and winter days); typical situations include for example the monitoring of fires in forests or structural health monitoring of bridges. Good candidates for light energy harvesting when very low light intensities are experienced are DSSCs, which are among the most promising new generation photovoltaics devices. Contributions discussing the use of this harvesting technique within the IoT domain, proving its efficiency in the mentioned operating conditions [83, 84], or presenting DSSC-powered wireless sensing devices [85, 86, 87, 88] already exist in literature, nonetheless generally few details on the used DSSCs and no characterization in this challenging operating conditions are presented and even the harvesting part is not deeply analyzed.

The application proposed in this Chapter explores the feasibility of using DSSC modules for powering LPWAN-based devices under low-irradiation intensity for long-range remote data acquisition purposes, paving the way for pervasively settled IoT devices in conditions of diffused sunlight. Two commercial DSSC modules, a flexible thin-film module and a glass thin-film module both with area smaller than an A4 sheet of paper, are preliminary characterized to investigate their efficiency when exposed to non-direct solar light, then they are used as power sources for two wireless sensor nodes embedding LoRa capability. Laboratory tests are performed under diffused sun light with unfavorable lighting and weather conditions, thus reconstructing a worst-case scenario.

5.1. Preliminary analysis of the lighting conditions

In this Section a detailed study on the theoretical concepts related to solar radiation is reported, focusing in particular on the diffused component of the radiation since it is the one mainly exploited in the proposed application. The purpose of this investigation is to guide the choice of the test set-up used in the following tests, to accurately replicate in the laboratory the working conditions foreseen in real applications.

When considering external photovoltaic applications, it is necessary to carefully evaluate the availability of solar radiation (i.e., insolation) and the variability of its spectral distribution, which are strongly influenced by the sun elevation (which in turns depends on the time of the day, the latitude and the season of the year), the atmospheric effects (including absorption, scattering, and reflection and those local variations influencing the clarity of the sky as the presence of water vapor, clouds, and pollution) and the shadow conditions (linked to the presence of nearby obstacles). In this respect, a detailed analysis of the lighting conditions expected for the sensor node operations is reported hereafter.

The sun elevation is defined as the angle between the sun rays and the horizon at the considered latitude and its value through the day can be computed as $\alpha=\sin^{-1}\left(\sin\delta\sin\varphi + \cos\delta\cos\varphi\cos(\mathrm{HRA})\right)$, where δ is the sun declination, φ is the latitude and HRA is the hour angle; the previous formula simplifies for the north hemisphere at noon as $\alpha=90°-\varphi+\delta$. The sun declination δ, which is the angle between the sun rays and the equatorial line, varies according to the season of an amount of $\delta = \pm 23.45°$ (positive for summer months and negative for winter months in the north hemisphere), that is the amount of tilt of the earth orbit with respect to its axis of rotation. It can be evaluated as $\delta = -23.45°\cos(\frac{360°}{365}(D+10))$ where D are the days passed since January 1st and the factor 360/365 converts the day number to a position in the sun orbit, assumed circular. The HRA converts the local solar time (LST), in hours, into the degrees traveled by the sun in the sky; it can be computed as $\mathrm{HRA} = 15°/\mathrm{h}(\mathrm{LST} - 12\ \mathrm{h})$, considering that the earth rotates 15° per hour (HRA negative before noon and positive after noon).

The zenith angle θ is the complementary angle of the elevation α, thus it is the angle between the sun rays and the vertical to the horizon at the considered latitude. It is used in the computation of the so-called air mass (i.e., AM), which is a measure of how much atmosphere is crossed by the sun rays to reach the earth surface. Since the atmosphere absorbs and scatters

the solar radiation, the AM is also a measure of the power light reduction, indeed a larger AM corresponds to less insolation and lower sun elevation in the sky. When earth curvature is considered, AM can be computed as $AM = \frac{1}{\cos(\theta)+0.50572(96.07995°-\theta)^{-1.6364}}$. Generally, the AM is given as ratio with respect to the shortest possible path length, namely when the smallest amount of atmosphere is crossed (i.e., when the sun is at the zenith, $\theta = 0°$): this situation is referred to as AM1 and any AM greater than this gives an information of how much more of the atmosphere the sun rays have to pass through (e.g., AM2 indicates that a double path in the atmosphere must be crossed compared to the AM1 case).

The sun elevation α as a function of the azimuth angle ζ at the latitude of our test-site (Siena, Italy) is shown in Figure 36a, where the azimuth angle corresponds to the angle on the horizontal plane between North direction and sun position: the curves corresponding to summer and winter solstices enclose the band of possible values achievable during the year (the curve corresponding to the days involved in the measurement campaign described in the following is in yellow color). In Figure 36b, the AM values calculated from the zenith angle θ at the considered latitude as a function of the time of the day are reported for winter and summer solstices and are typically in the [2.5, 6] range.

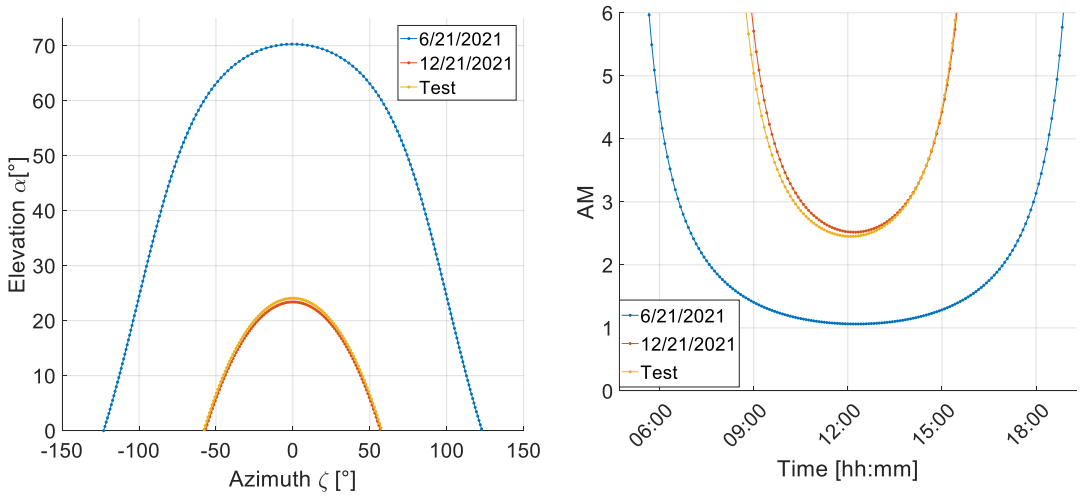

(**a**) (**b**)

Figure 36. (**a**) Sun elevation α as a function of the azimuth angle ζ, calculated for the test-site (Siena, Italy) in the case of June/December solstices (blue and red plots) and for the measurement campaign described in this work (yellow plot); (**b**) corresponding AM values calculated from zenith θ angle as a function of the time of the day.

As solar radiation passes through the atmospheres of sun and earth, gasses (e.g., O_3, CO_2, water vapor), dust and aerosols absorb the incident photons depending on the wavelength radiation; while the gasses absorption primarily causes changes in the spectral content of the radiation with the formation of minima, the absorption and scattering due to particles cause a broadband reduction of the solar radiation intensity and this effect increases with the distance travelled by the rays to reach the earth surface. The global irradiance arriving on the earth surface can be distinguished into direct and diffused components, and the intensity of the latter is considerably smaller than the radiation which directly strikes the earth. A third component that must be accounted for inclined receiver is the reflected irradiance, which accounts for the part of irradiance reflected from the ground onto the receiving device.

The global and diffused irradiances in case of clear sky conditions for different AM values, calculated using the Gueymard SMARTS 295 toolkit [89], are reported in Figure 37a and b. The AM0 stands for the spectrum at the limit of the earth surface so the attenuation in the spectral distribution with respect to the black-body radiation is only caused by the absorption due to the sun atmosphere; when the radiation passes through the earth atmosphere, the minima caused by the gasses absorption increase and the intensity of the irradiance decreases as the path through the atmosphere becomes longer. The global and diffused intensities calculated as integral in the [300 nm,1000 nm] range of the irradiances in Figure 37a and b for AM=1.5, 2, 3, 4, 6 are shown in Figure 37c: the diffused irradiance has intensities about 15% of the global ones, with highest values around 110 W/m^2.

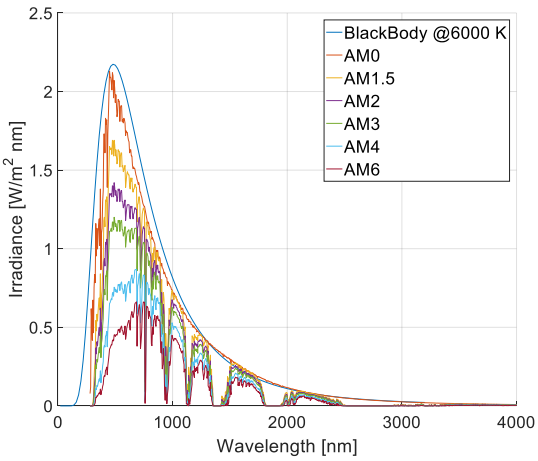

(**a**)

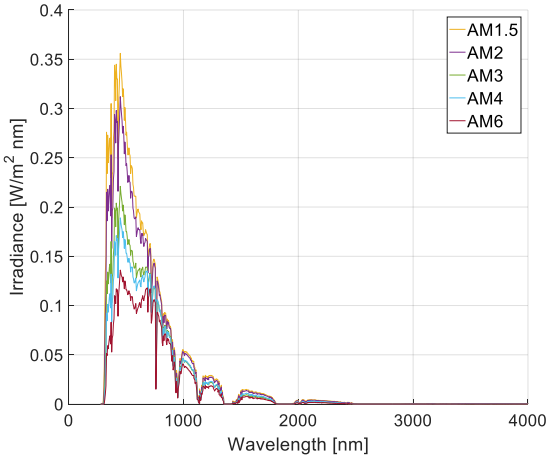

(**b**)

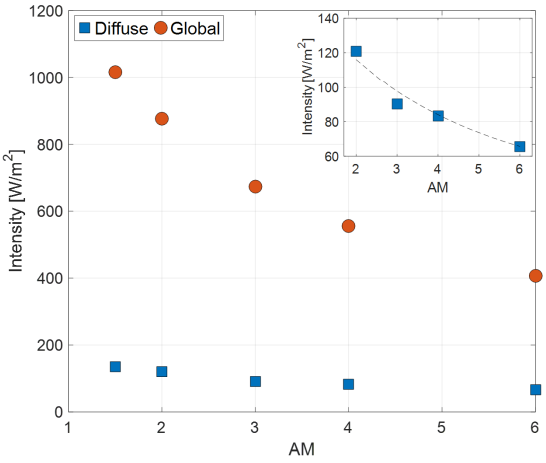

(**c**)

Figure 37. (**a**) Global and (**b**) diffused irradiance spectra in case of clear sky as calculated by the SMARTS simulation toolkit [89] for AM=0,1.5, 2, 3, 4, 6 together with the black-body radiation at 6000 K. (**c**) Intensity calculated as integral in the [300 nm,1000 nm] range of the irradiances given in (**a**) and (**b**) for AM=1.5, 2, 3, 4, 6; in the inset a magnification of the intensity of the diffused irradiance for AM=2, 3, 4, 6.

Nonetheless, in case of cloud covering, shielding and shadowing due to obstacles, the measured intensity can be far lower. As an example, Figure 38a and b show respectively the radiation spectra and the intensity measured in a winter day in proximity of December solstice as a function of illuminance in various diffused irradiation conditions such as cloud covering, shadowing from building and trees, and shielding of a transparent glass window in the absence of artificial light. In particular, the data reported in the following figures were measured using for the intensity of the solar radiation in the visible range a Kipp & Zonen Class C CMP3 pyranometer with nominal sensitivity of 15.66 μV/(W/m^2), spectral range [300 nm, 2800 nm], 64-junction thermopile detector and 4 mm glass dome, and for the illuminance a RS-IM-203 lx/fc lightmeter, based on a silicon photodiode and cosine angular corrector. The spectra in each test condition were measured in the [300 nm, 1030 nm] range by a portable spectrometer Ocean Insight USB4000 UV-VIS equipped with a CC3 UV-S cosine corrector, and are shown in Figure 38a normalized to 1000 lx, together with the DSSC EQE of Figure 28 as black solid line (left axis in the figure) [57].

In Figure 38b, Cloudy sky I and II refer to measurements performed in the same air mass conditions AM 2.5 (middle of the day), but in case of slightly different surrounding environments, originating different diffused intensities; Cloudy sky III refers to measurements performed in a different time of the day (morning), thus characterized by a higher air mass,

AM 4. It can be seen that the intensity data belongs to the [2 W/m^2, 50 W/m^2] range and follow a linear trend with the illuminance, which has value in the [200 lx, 6500 lx] range.

Figure 38c shows the short circuit current density calculated according to Equation (10) and by using the DSSC EQE plotted in Figure 38a (black line), as a function of the diffused solar radiation intensity of the spectra shown in Figure 38a. As expected, the short circuit current density is a linear function of the radiation intensity: the linear best fit has a slope of 0.163 W/A in the overall investigated range. These results specifically concern the flexible DSSC used for the experiments presented in the following, but very similar results can be obtained also for the glass DSSC module, which is characterized by a similar EQE.

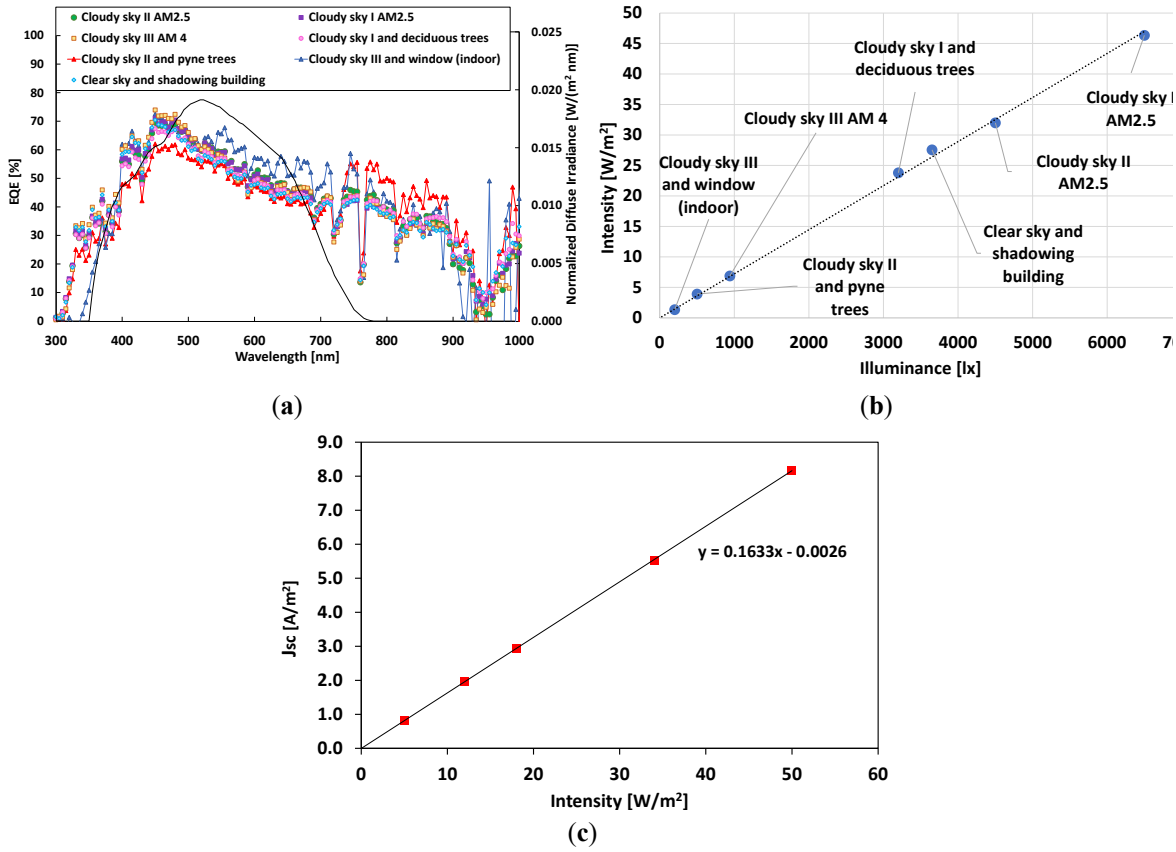

Figure 38. (**a**) Measured diffused spectra normalized to the case of 1000 lx experimented in various outdoor and indoor diffused radiation conditions including cloudy sky, shadowing of trees and building, shielding of transparent glass windows as per legend (right axis); the EQE of the DSSC modules is added for comparison (left axis, solid black line). (**b**) Intensity computed as integral of the spectral irradiances of (**a**) in the [300 nm, 1030 nm] range as a function of the corresponding illuminance in lx: linear best fit is also shown. (**c**) Short circuit current density calculated according to Equation (10) as a function of the diffused solar radiation intensity, using the diffused irradiances and the DSSC EQE reported in (**a**).

Apart from a slightly increasing contribution of the near infrared components for the lowest illuminance conditions and a cut-off at short wavelengths in the case of transparent glass window shielding, the shapes of the normalized diffused spectra are quite similar in the overall investigated range independently on weather, period of the day and shadowing conditions. For this reason, the case of diffused irradiance penetrating from a transparent glass window is selected as best systematic standard condition for the laboratory tests presented in the following. Compared to the normalized spectral irradiances, the DSSC EQE broadband appears to be distributed in the visible range where the diffused spectra have a prominent peak. In particular, the cut at short wavelengths in case of glass window shielding is outside the EQE band, so it does not influence the performance of the photovoltaic module.

5.2. System architecture

This Section deals with a description of the architecture of the designed system, focusing on the employed solar cells and on the general-purpose node, which represents a baseline for other possible sensor nodes. Concerning the energy harvesters, two commercial DSSC modules were used:

- a flexible DSSC G24i module by G24 consisting of a series of 11 1 cm ×19 cm = 19 cm^2 cells and based on a layer of dye sensitized nanostructured TiO_2 deposited on a titanium electrode and placed between PET laminate layers;
- a series of 4 DSSC FDSC-FSC12FGC cells by Fujikura with active area of 7.14 cm^2 each, realized on a glass substrate (nominal peak current of 117 mA and peak voltage at 200 lx of 0.38 V).

The reduced size of the two modules (area smaller than an A4 sheet of paper) makes them extremely versatile and the flexible module adapts even more easily to different types of surfaces.

A general-purpose low-power system was designed to demonstrate the usability of the two solar cells as power sources for monitoring devices in charge of remote data acquisition. The system integrated a low-power 8-bit AVR ATtiny84 microcontroller, a MCP9700-E/TO temperature sensor by Microchip and an RFM95 LoRa module equipped with a 2 dBi gain $\lambda/8$ antenna. Since in several WSN applications the most energy-hungry component of the

node is the transmission module itself, we reputed the addition of application-specific sensors a non-critical factor affecting the actual power consumption.

The node also integrated the nano-power boost charger and buck converter BQ25570, mounted on the CJMCU-2557 board, in charge of managing the charging process of a 3.7 V, 720 mAh Li-Po battery employed as node energy reserve. While for the glass module the MPP was set to 80% of V_{OC}, which corresponds to the ideal MPP for solar cells and optimizes the power transfer from the energy source, for the flexible module it was set to 50% of V_{OC} to comply with the maximum input voltage constraint of the chip, thus decreasing the total power output with respect to its peak value. More details about the BMS IC functioning are provided at the end of Section 3.3.

The MCU was programmed according to a sleep routine which woke it at fixed time intervals (i.e., every hour) to sample the sensor and transmit the processed data via LoRa technology and LoRaWAN protocol. The radio settings were transmitting frequency 868 MHz, output power 14 dBm, CR 4/8, SF 12, bandwidth 125 kHz and they were chosen as a tradeoff between low consumption requirement, radio coverage and signal attenuation, which are critical issues in outdoor application scenario. Indeed, the highest CR=4/8 guarantees the best error correction at the expense of longer ToA and consequently slightly higher power consumption with respect to the lower CRs; also SF 12 has the longest ToA and the highest power consumption, but it provides the highest receiver sensitivity and the lowest packet loss, which are important aspects in deployments in remote and critical scenarios.

As already stated, the most expensive operations from an energy point of view were the radio transmissions, since each one lasts ~1.721 s for 17 payload bytes, namely 4 bytes payload size + 13 bytes overhead size (~41.304 s during the whole day) with estimated peaks of the absorbed current up to 80 mA. Indeed, a raw analysis of the overall consumption of the node was performed exploiting the datasheets of the used components and can be used as starting point to easily predict the absorption of the node when more sensors are integrated.

In sleep mode only the BMS and the microcontroller were actually powered: the latter was operating in power-down mode with current absorption of 0.2 μA at 2.5 V; since the BMS accounts for a typical quiescent current at room temperature in full operation mode of 488 nA, the overall current absorption was estimated being around 0.7 μA, leading to an average power consumption lower than 2 μW. In active mode, until no radio transmission is performed, the absorption is mainly due to the MCU reaching up 800 μA, thus the typical current absorption

of 6 μA of the MCP9700-E/TO results negligible. Conversely, the current absorption of the RFM95 module during the transmission can reach up 80 mA and all the other current absorptions can then be considered marginal, therefore during the active phase an average power consumption of about 200 mW can be considered. The average hourly energy consumption of the node in case of hourly radio transmissions can be estimated as:

$$E=P_{sleep} \cdot T_{sleep} + P_{active} \cdot T_{active}=3598\ s \cdot 0.002\ mW+2\ s \cdot 200\ mW \simeq 407\ mJ=0.113\ mWh \quad (11)$$

and provides an interesting insight on the actual energy requirement of the system which mainly depends on the radio module transmission, that is often one of the main bottlenecks in the design of energy efficient wireless sensor nodes.

5.3. Test and results

Different test campaigns were performed to prior characterize the used DSSCs under diffused irradiation, afterwards their performance as power sources of wireless sensor nodes was evaluated, testing the overall system in working conditions analogous to the real ones, as emerging from the results of the study reported in Section 5.1. A proper test set-up was developed both for the characterization and the self-sufficiency testing.

5.3.1. Measurement set-up

The DSSCs characterization was performed under diffuse outdoor irradiation, keeping the PV modules horizontally to ground, and using a Keithley 2401 source-electrometer controlled via LabVIEW as acquisition system. The radiation intensity was monitored through a Kipp & Zonen Class C CMP3 pyranometer with nominal sensitivity of 15.66 μV/(W/m^2), spectral range [300 nm, 2800 nm], 64-junction thermopile detector and 4 mm glass dome, while the illuminance was measured by a RS-IM-203 lx/fc lightmeter, based on a silicon photodiode and cosine angular corrector.

During the self-sufficiency tests, the DSSC panels were placed in front of a window oriented in the north-east direction at 10 cm from the window glass and in the absence of artificial lighting in the room, in such a way to have similar lighting conditions. The voltages at the rechargeable Li-Po batteries of the two nodes and the voltages at the input of the BMSs

were acquired, using Agilent 34410A multimeters (configured with 10 PLC and 6 ½ digit resolution) controlled via LabVIEW with a sampling period of 1 s. As in the previous test reported in Subsection 4.3.1, the initial battery voltage levels were set to approximately 3.9 V, i.e., in the range where the typical charge vs voltage characteristic for a Li-Po battery is not flat, thus the voltage variation is a sufficient indication of the charge status of the battery. The uncertainty analysis presented in Subsection 4.3.1 remains valid for this test. Simultaneously, the diffused intensity was continuously monitored using the aforementioned pyranometer, serially acquired every 2 s via LabVIEW.

5.3.2. Solar cell characterization

The I-V and P-V characterization of the DSSCs was performed under intensity of 18 W/m^2 and illuminance of 2500 lx: these conditions emulated the diffuse outdoor irradiation typical of a cloudy sky in winter, analogous to that experienced during the self-sufficiency tests presented in the following Subsection. In this respect, Figure 39 shows the I-V and P-V characteristics of a single cell of glass and flexible DSSCs and the corresponding fitting derived according to Equations (8)-(10).

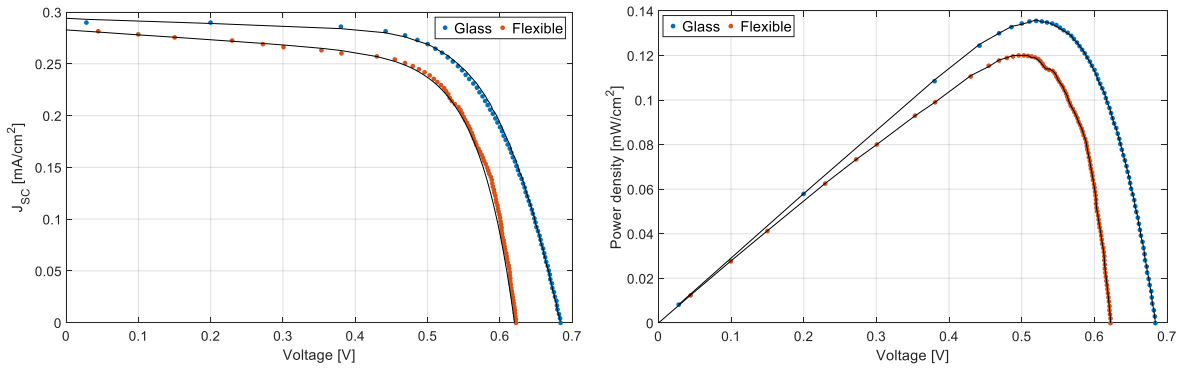

(**a**) (**b**)

Figure 39. (**a**) I-V and (**b**) P-V characteristics of a single cell of the flexible (in red) and the glass (in blue) DSSCs measured under diffused solar radiation (18 W/m^2 and 2500 lx).

The most important static parameters extracted from the fitting procedure of the characterization curves are shown in Table V. It can be observed that the glass DSSC has a slightly better performance in terms of peak power density because of the higher V_{OC} and J_{SC}. Moreover, as reported in Subsection 5.2, the MPP was set to 80% of V_{OC} for the glass module and to 50% of V_{OC} for the flexible one, thus from Figure 39 it can be seen that in these

operating conditions the current expected for the flexible and the glass modules is about 93% and 84% of I_{SC} respectively; however, the efficiency of the flexible cell is reduced from 6.0% to approximately 4.5% while the glass cell works very close to its peak conditions. As a consequence, the total power output of the flexible cell is reduced with respect to the expected peak value of ~30%, but its larger area still guarantees better harvesting capacity with respect to the glass module.

Table V. Main Photovoltaic parameters obtained from DSSCs characterization.

	Glass	**Flex**
Area [cm²]	7.14	19
J_{SC} [mA/ cm²]	0.290	0.285
V_{OC} [V]	0.69	0.62
V_{MAX} [V]	0.53	0.50
J_{MAX} [mA/ cm²]	0.26	0.24
P_{MAX} [mW/ cm²]	0.13	0.12
P_{OP} [mW/ cm²]	P_{MAX}	0.08
FF %	68.00	68.00
R_s [Ω]	20.00	0.00
R_{sh} [Ω]	7000.00	1300.00
N	2.00	2.00
I_O [nA]	2.00	15.00

5.3.3. Node self-sufficiency tests

Two sensor nodes, each equipped with one of the previously characterized PV modules and whose architecture is described in Section 5.2, were tested during a measurement campaign of 6 days (from 29-Dec-21 to 3-Jan-22) performed in the laboratory at the Department of Information Engineering and Mathematics, Siena, Italy using the measurement set-up described in Subsection 5.3.1. As discussed in Section 5.1, the glass window is not significantly altering the diffused spectrum, hence the working condition experimented during the test well replicated the actual conditions in an outdoor shady environment.

The acquired Li-Po battery voltages, $V_{Li-Po_{Flex}}$ and $V_{Li-Po_{Glass}}$, are shown in Figure 40: the increasing segments correspond to the charging of the batteries occurring when the solar light is detected by the pyranometer, while the decreasing parts correspond to the hours in dark, finally the equally spaced vertical lines determining a lowering of the Li-Po voltage level are the absorption peaks caused by the radio transmissions.

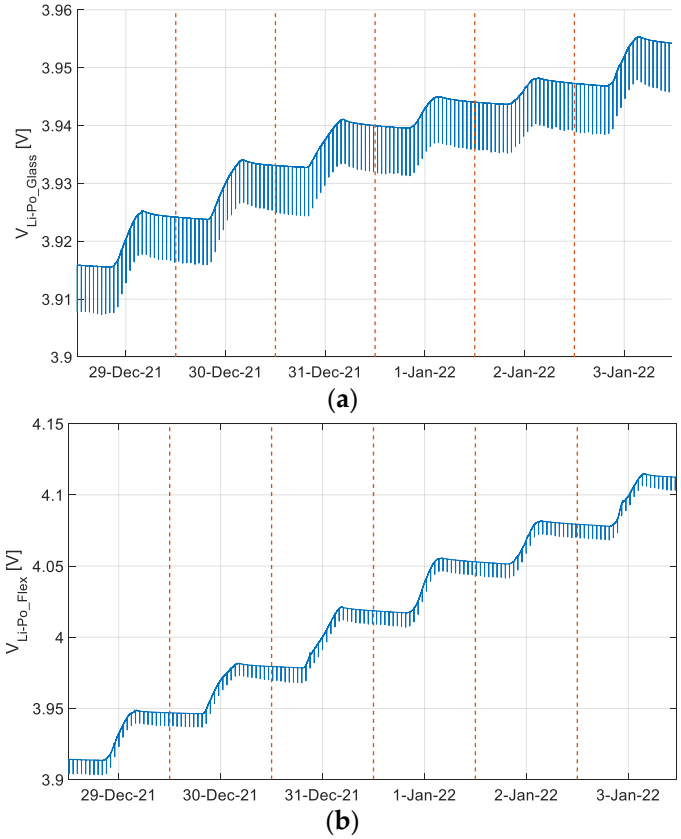

Figure 40. The acquired Li-Po battery voltages in case of Glass (**a**) and Flexible (**b**) DSSCs energy harvesting during the test campaign.

A positive balancing between battery charging and discharging is achieved with both types of cells, in particular the daily net charge obtained as difference of the battery voltage level at the end and at the beginning of each testing day (i.e. $\Delta V_{Li-Po_{Flex}}$ and $\Delta V_{Li-Po_{Glass}}$) is equal to 33 mV, 32 mV, 39 mV, 34 mV, 26 mV and 33 mV (197 mV in tot) for the flexible module and to 8 mV, 9 mV, 7 mV, 4 mV, 3 mV and 7 mV (38 mV in tot) for the glass module, starting with the same value of voltage battery at each node (i.e., 3.9 V). A much higher charge is reached in the case of the flexible DSSC due to the larger active area of the module, in accordance with the results of the characterization.

Figure 41a shows the input voltage of the BMS in the glass DSSC case, $V_{in_{Glass}}$: it is ≃ 0 V during the dark hours and increases with the natural logarithm of the intensity according to Equation (9), the spikes correspond to the 250 ms-typical long disconnections (approximately every 16 s) when the BQ25570 chip performs the MPPT algorithm to obtain a new reference voltage as a fraction of the sampled V_{OC}.

The intensity measured by the pyranometer was compared with the outdoor global solar radiation intensity collected every 300 s by a weather station located in Siena at 1.2 km in a straight line from the laboratory used for the tests and available online [90]. In detail, the diffused intensity measured by the pyranometer and the outdoor solar irradiation given by the local weather broadcast are reported in Figure 41b, respectively in blue and red colors: a correlation between the two quantities can be noticed, however the reduction factor between outdoor and indoor radiation hitting the cells causes them to start harvesting energy with a delay with respect to the appearance of sun light and to stop earlier when there is still sun light outside. Moreover, the measured diffused indoor intensity is coherent with the results of Figure 38b while the outdoor solar intensity is consistent with the experienced weather conditions (i.e., variable sky on 29-Dec-21 and 3-Jan-22, thick fog on 30-Dec-21 and 31-Dec-21, cloudy sky and rain on 1-Jan-22 and 2-Jan-22), characterized by a high component of diffused radiation.

In Figure 41c the radiant exposure of each day (computed as integral of the intensities of Figure 41b) is reported together with the $\Delta V_{Li-Po_{Glass}}$ trend, which follows the radiant exposure behavior quite consistently.

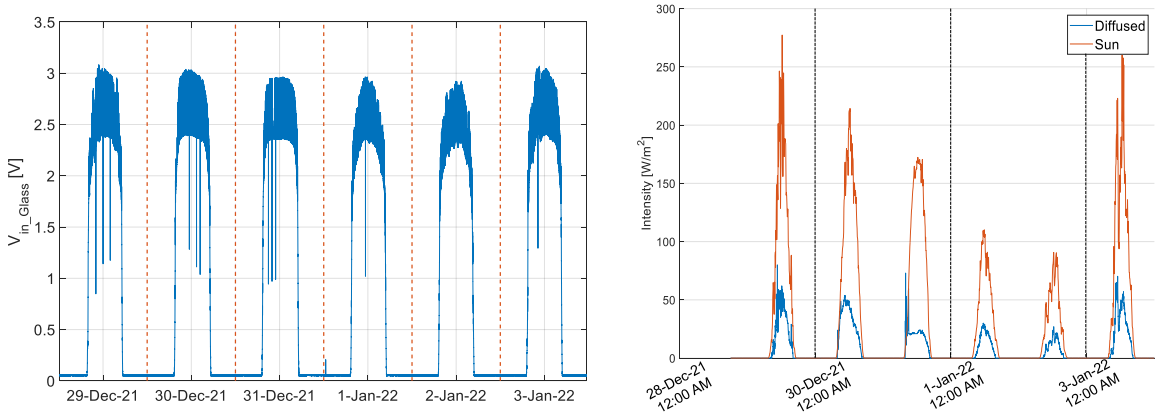

(**a**) (**b**)

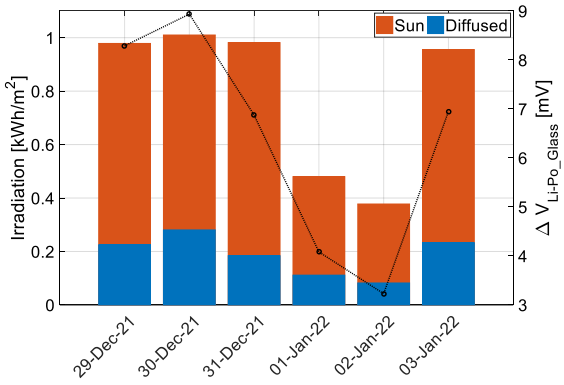

(**c**)

Figure 41. (**a**) The input voltage $V_{in_{Glass}}$; (**b**) the diffused intensity measured by the pyranometer (blue line) together with the outdoor solar irradiation as reported by local weather broadcast (red line); (**c**) the solar irradiation of each day (computed as integral of the intensities of (**b**)) together with the $\Delta V_{Li-Po_{Glass}}$ black trend in mV (right axis).

Finally, Figure 42 shows a comparison between the measured battery voltages and the same quantities predicted exploiting the measured diffused light intensity of Figure 41b. In more details, the measured radiation intensity is converted into the current generated by the photovoltaic panels exploiting the linear conversion factor corresponding to the slope of the curve shown in Figure 38c and by taking into account the area of each PV module. Then, the charge delivered to the battery is obtained by calculating the integral in time of this current net of the consumption of the node reported in (11). Finally, starting from the computed charge, the corresponding voltage trend is derived using as a reference the linear approximation in that voltage range of a typical charge vs voltage characteristic for a Li-Po battery.

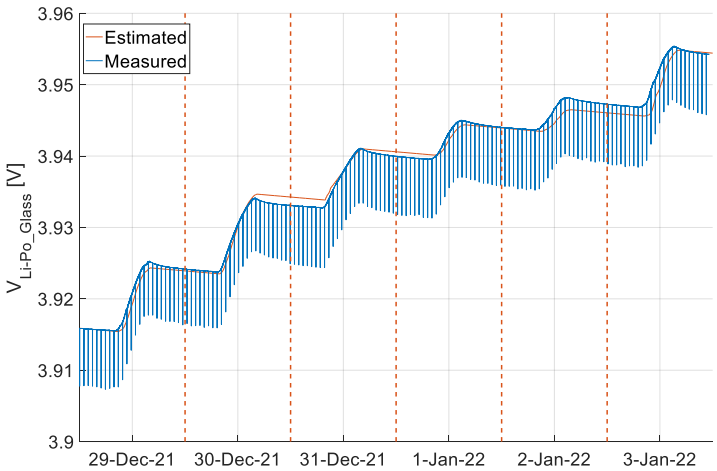

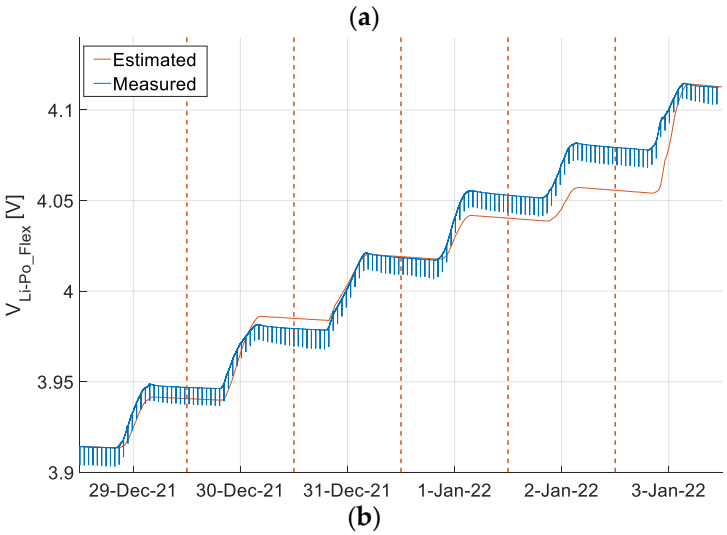

Figure 42. The acquired Li-Po battery voltages (blue plots) and the battery voltages derived by calculating the charge delivered to the systems starting from the diffused radiation intensity of Figure 41b (red plots) for the Glass (**a**) and the Flexible DSSC (**b**).

In general, a good match between measured and predicted Li-Po voltages is observed, assuming that the estimated values must be considered as an approximation of the real behavior of the battery, thus providing a qualitative rather than quantitative trend. In fact, the charge vs voltage relationship of the battery is approximated with a typical Li-Po characteristics that may differ from the real one. Moreover, in the real deployment there are many factors that can influence the battery charging process, such as the temperature variations and the non-perfect alignment between the pyranometer and the cells which can lead to a difference between the measured intensity and the one actually hitting the cells. Furthermore, the measurement uncertainty of the pyranometer, which provides the input for the derivation of the predicted data, increases at low light intensities since a series of offsets existing in class C pyranometers, such as the offset due to the directional response, have a more significant effect when performing measurements at low light intensities, making them less accurate.

Concerning the slightly worse correspondence for the flexible module, it can be due to the fact that the battery undergoes a greater net voltage variation with respect to the glass module case, thus working in a larger range where eventually the linear approximation of the charge vs voltage characteristic is less accurate. However, although some mismatches can be observed, the predicted data satisfactorily approximate the measured ones. This proves that the nodes operate in a proper way in the tested conditions, harvesting the sun energy with a

trend close to the theoretical one. Furthermore, even if the MTTP tracking method implemented by the commercial BQ25570 chip is not optimized for the selected cell technology, the nodes operate correctly also in the conditions of very low diffused solar intensity.

The presented test conditions may be considered as a worst-case scenario, since the test was carried out at the turn of the winter solstice, which is the period of the year when the lighting conditions are the most unfavorable since the sun elevation is minimized, causing low light intensity and reduced hours of lighting. In addition, the weather conditions occurred during the tests, characterized by cloudy sky, rain and fog, further disadvantaged the charge of the node battery. Nonetheless, the measured positive balance of the battery charge allows to affirm with a high degree of confidence that the system would work during the whole year and in all the weather conditions in the considered latitude, thus constituting a valid solution for energy-autonomous monitoring in outdoor scenarios characterized by low irradiation and diffused sun light, as in the proximity of tall buildings, among trees in a forest and during winter days. Since the light source is not constant, it is not possible to establish a priori the maximum achievable radio transmission frequency however, the presented results suggest using an hourly transmission rate, which is a reasonable rate in most sensor network monitoring applications, as a starting point and subsequently adapting it in accordance with the actual light intensity and the power consumption of the node. In fact, the addition of more energy-consuming sensors such as sensors for gas monitoring based on optical techniques could force to reduce the transmission rates in case of prolonged periods of low light intensity.

Chapter 6

2D Indoor positioning and harvesting via white artificial light

Accurate indoor positioning (IP) is one of the most ambitious challenges of our days and its achievement has potential involvements in many sectors where tracking of asset or people is required. Some possible application fields concern healthcare (e.g., monitoring of medical equipment and ambulating patients in hospitals), industry (e.g., asset tracking, robot navigation, automated storage, workers localization in hazardous environments) and Internet of Things (IoT) (e.g., tracking of goods, people, and vehicles in warehouses, public buildings, or civil infrastructures). At the same time, the possibility of exploiting PV modules for energy provisioning from a less canonical energy source, as the white artificial light commonly employed indoor, is gathering growing interest. In view of this, visible light positioning (VLP) can arise as valid opportunity for deploying low-power localizable targets which simultaneously harvest energy from the same light signals used for localization.

The application proposed in this Chapter constitutes an innovative solution for self-sufficient indoor localization. It concerns the realization of an ultra-low power sensor node exploiting the same small-sized amorphous silicon solar cell both as optical receiver for 2D VLP and energy harvester from the lighting signal used for localization. The positioning task is attained by means of optical channel estimation and lateration starting from the FFT (fast Fourier transform)-extracted received light intensities coming from three LED used as reference anchors. The position estimation is performed directly on board of the target to be localized, equipped with a low-power MCU, and made available via LoRa technology, thus avoiding post-processing operations as is the case of RSS-based solutions using radio technologies. Tests were performed in a ~1 m^2 area to evaluate the positioning accuracy of the proposed methodology and to validate the energy self-sufficiency of the node in case of different radio transmissions frequencies [91]. The system in the present form can find application in those scenarios where indoor 2D localization is required and the presence of

obstacles is limited, such as localization of cars in a covered parking area, containers in a warehouse or people moving indoor.

6.1. Indoor positioning

While in the outdoor positioning the global positioning system (GPS) is the dominant navigation technology thanks to its pervasive coverage and its high accurate performance, a technology with similar capabilities has not yet been identified for metropolitan areas and indoor spaces, where the presence of obstacles, walls, interferences, and reflections strongly degrade and distort the signals commonly exploited for localization. Indeed, one of the main difficulties in identifying a unique technology capable of operating with satisfying results in manifold application scenarios is the great heterogenicity of the indoor environments involved: the geometry, the type of obstacles, their arrangement and the required position accuracy greatly vary according to the application proposed, thus the technology and the localization approach should be adequately tailored on the specific deployment.

This has led to the development of indoor positioning systems (IPSs) based on different techniques, extensively treated in the literature with surveys and reviews that compare their advantages and drawbacks [92, 93, 94, 95]. Radio frequency technologies (e.g., RFID, global system for mobile communication (GSM), Wi-Fi, Bluetooth, Zigbee, LoRaWAN), sound-based technologies (e.g., ultrasounds and audible sounds), optical technologies (e.g., infrared and visible light), magnetic field navigation are examples of experimented indoor localization techniques relying on the presence of uniquely identified transmitters (e.g., Wi-Fi access points, light sources, Bluetooth beacons) as anchors to localize the mobile receiving target (i.e., an object with a receiver mounted on board). Other approaches are independent from the presence of reference points since some sensors mounted on board of the target provide absolute localization. This is the case of inertial navigation systems (INSs) [96] – which incorporate inertial measurement units (IMUs), accelerometers or gyroscopes to retrieve the linear acceleration and the rotational rate of the target – and camera-based systems [97], nevertheless frequent recalibration and filtering procedures are required to correct drifting errors and, being these devices more power-consuming, the low consumption requirement is difficult to be met.

The simplest strategy for estimating the coarse position of a target is that of proximity detection, which gives information about proximity to a specific anchor instead of giving a precise position in the reference space. This approximate localization approach finds application in those contexts where a rough knowledge of the position is required (e.g., place recognition). If a higher degree of accuracy is needed, triangulation and fingerprint methodologies can be adopted. The fingerprint method requires an offline training phase for collecting measurements or for simulating data in several test points of the measurement space, establishing a bijective association between training points and known spatial coordinates. Once this mapping is acquired in the form of a database or a look up table, other test points can be inferred from it resorting to machine learning techniques or statistical approaches. The major weaknesses of this method are the time-consuming calibration phase in case of non-simulated training data, whose duration increases with the desired granularity, and the strong dependence on the specific test environment, requiring new time-consuming trainings every time a new operating space is tested. On the contrary, the triangulation approach does not involve training procedures since the geometrical properties of the triangles formed by the target and the fixed anchors are exploited to infer the target location.

Two different methods can be followed in triangulation: angulation – which exploits the estimated angles between the target and multiple reference anchors – and lateration – which uses the estimated distances between the target and multiple reference anchors. The main quantities measured in these localization strategies are Angle of Arrival (AoA) for angulation and Time of Arrival (ToA), Time Difference of Arrival (TDoA) and Received Signal Strength (RSS) for lateration. The first three techniques provide maximum position accuracy to the detriment of greater complexity in the realization of both transmission and receiving devices (e.g., sensor array on board of the target, precise synchronization between target and transmitters or between the transmitters themselves). On the other side, the RSS-based method can rely on simpler and cheaper systems, but it is site-specific and can be affected by errors in the estimation of the path loss model. Indeed, it is sensitive to signal reflections, shaded areas and obstacles between the receiver and the transmitters; moreover, some parameters of the model must be appropriately estimated during a calibration procedure to reduce errors in the subsequent localization phase.

Among the aforementioned IP technologies, VLP, especially in case of RSS-based approaches, not only offers the possibility of creating autonomous nodes through energy scavenging from artificial light but has good positioning accuracy with reduced cost and

complexity both for the transmitting device – the existing lighting infrastructures can be exploited – and the receiving device – a commercial optical receiver with simple conditioning electronics can be used. IPSs based on VLP using LEDs have been widely studied in the literature [92, 94]. A first distinction can be made on the basis of the used receiver, a camera in vision-based applications or an optical sensor as a photodiode or a PV module.

Most of the contributions in literature concerning the usage of solar cells as optical receivers are involved in visible light communication (VLC) [98] or more in general optical wireless communication [99] applications, hence no localization task is performed since the light sources are only used for high frequency data transmission with possible re-uses of the DC component of the optical signal for harvesting features. This approach is widely employed in some critical contexts, such as hospitals, where radio frequency signals could cause dangerous interferences with machinery and instrumentation. Concerning VLP, the photodiode is usually preferred as photodetector, however some contributions to the state of the art exist where indoor positioning by means of a solar cell is performed [96, 100, 101, 102, 103], although its use is justified only for a better performance with respect to the photodiode and not for harvesting reasons, which are often only mentioned as future development without in-depth investigation.

In particular, the contribution presented in this Chapter is the first one presenting an integrated energy self-sufficient LoRaWAN-based device performing on-board 2D indoor positioning using a PV module both for localization and for artificial light energy harvesting. Indeed, some existing solutions in literature differ from the one presented for the greater complexity required by the hardware – customized lighting hardware with MCU, synchronization and code modulation circuits since more elaborated modulations of the light signal are performed [102] – or for the proposed methodology – time-consuming fingerprinting procedure and training of machine learning models [103]. In other contributions, the proposed methodology is similar to the one here presented but there is no implementation of an integrated embedded system, delegating the positioning algorithm and the coordinates extraction to an offline routine running on the PC, thus performing only photo-reception functions on the target [100]. The great advantage of the application proposed in this Chapter relies on the low complexity in the demodulating side – entirely realized resorting to off-the-shelf components thus making the proposed system a valid solution for large scale deployments –, in the receiver side – the RSS-based approach does not require complicated or extremely frequency-precise hardware for the LED drivers – and in the conceived

localization methodology – low-computational localization algorithm and simple calibration procedure based on the collection of only one calibration point. The designed prototype is totally conceived in a low-power perspective with electronic components specifically thought for applications envisaging low consumption. Moreover, resorting to a solar cell-based IPS is inherently a low-power approach with respect to radio frequency positioning methods using power-consuming off-the-shelf receivers (e.g., Sub-GHz band or WiFi). Since the system is designed keeping in mind the low-cost, the low-power and the energy-autonomy requirements, it will not intrinsically reach the sub-cm accuracy of expensive and highly precise devices. Nevertheless, it must be accounted that in a real context of indoor localization the achievement of this level of accuracy is quite unrealistic, since other factors such as the presence of obstacles, shadows and reflections inevitably lead to a degradation of the performance or even to the total impossibility of localization.

6.2. The proposed localization approach

With the proposed approach, the 2D position of the optical receiver is inferred from the RSSs of three LEDs used as fixed anchors, each one univocally identified by a unique driving frequency and whose coordinates in the measurement space are well-known. The RSSs are extracted by FFT of the voltage-converted photocurrent generated by the PV module employed as a photoreceptor and which is proportional to the sum of the incident optical power of the three LEDs. The light sources are ideally coplanar and at fixed distance h from the plane where 2D positioning is performed; the origin of the measurement space is located in the projection of LED_1 on the floor as can be seen in Figure 43, where the geometrical representation of the LEDs arrangement in the measurement space is reported. The localization task is attained in three distinct phases:

- RSSs extraction through FFT algorithm;
- Lambertian optical channel model inversion;
- Lateration method to predict the coordinates of the target, $(x_{\mathrm{R}}, y_{\mathrm{R}}, z_{\mathrm{R}})$.

The fact of having assigned a unique frequency to each LED prevents from interference between the light signals during the reception phase and allows the three sources to simultaneously transmit without needing to elaborate multiplexing strategies for accessing the communication channel. The vector of the FFT-extracted RSSs contains the amplitudes

correspondent to the spectral component of each LED, V_{Ri}; these intensities are thereafter used in the inversion of the Lambertian optical channel equations to recover the distances d_i with i=1,2,3 between the optical receiver and each LED [104, 105].

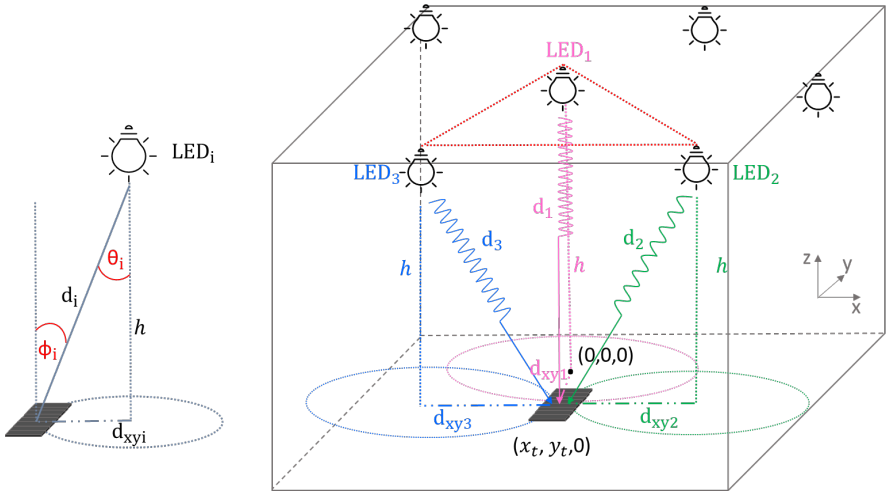

Figure 43. Geometrical representation of the adopted localization approach.

The general equation of the Lambertian channel for LED_i is reported in (12) where P_{Ri} is proportional to the FFT-extracted V_{Ri}, P_{Ti} is the transmitted optical power of LED_i, A is the optical receiver active area, $T(\phi_i)$ and $G(\phi_i)$ are the optical filter and optical concentrator gains in case they are present, m_T and m_R are the Lambertian mode numbers of the LEDs and the photoreceiver derived as $m_R = \frac{\ln(2)}{\ln(\cos \phi_{1/2})} = 1.12$ and $m_T = \frac{\ln(2)}{\ln(\cos \theta_{1/2})} = 0.74$ ($\phi_{1/2}$ and $\theta_{1/2}$ are the half sensitivity receiver and transmitter angles), $\cos \phi_i$ and $\cos \theta_i$ are the cosines of the transmitted angle between light and LED axes and of the receiving angle between light and optical receiver axes as reported in Figure 43.

$$P_{Ri} = P_{Ti} \frac{(m_T + 1)}{2\pi {d_i}^2} AT(\phi_i)G(\phi_i)\cos^{m_T}(\theta_i)\cos^{m_R}(\phi_i) \qquad (12)$$

This model is simplified under the assumptions that h is known and that LEDs and optical receiver planes are maintained parallel, thus $\theta_i = \phi_i = \cos^{-1}\frac{h}{d_i}$ and the inversion of (12) to compute d_i becomes

$$d_i = \sqrt[m_R+m_T+2]{P_{Ti}\frac{(m_T+1)}{2\pi P_{Ri}}AT(\phi_i)G(\phi_i)h^{(m_R+m_T)}} = \sqrt[m_R+m_T+2]{K_i\frac{(m_T+1)}{2\pi V_{Ri}}Ah^{(m_R+m_T)}} \quad (13)$$

where in the second equality a calibration parameter K_i is introduced. Indeed, while some parameters of the model are derived from direct knowledge of the physical characteristics of LEDs and solar cell (i.e., A, m_R, m_T), others contribute to a calibration parameter K_i which takes into account non-modeled factors, such as the linear proportionality between photogenerated voltage and received power. This parameter is estimated through a preliminary measurement performed with the three LEDs on and the photosensor in the centroid of the triangular area subtended by the projections of the LEDs on the floor: considering that the distances d_i of the PV module from each LED are known a priori, by inverting (13) the K_i i=1,2,3 are derived.

Once the distances are retrieved, known the vertical height of the LEDs h, the horizontal distances d_{xy_i} on the receiver plane are extracted and then used in the lateration method to estimate the receiver coordinate (x_R, y_R, z_R) with respect to the fixed reference system. The 2D position is obtained as geometric intersection on the receiver plane of the three circumferences centered in the projection point of the LEDs on the plane and with radius equal to the estimated horizontal distances d_{xy_i} (see Figure 43 for a geometrical representation). This is translated in algebraic form in finding the solution of the system in (14) where (x_i, y_i, z_i) are the known positions of the LEDs in the measurement space (in the presented application $z_1 = z_2 = z_3 = h$ and $z_R = 0$).

$$\begin{cases} (x_R - x_1)^2 + (y_R - y_1)^2 + (z_R - z_1)^2 = d_{xy_1}^2 \\ (x_R - x_2)^2 + (y_R - y_2)^2 + (z_R - z_2)^2 = d_{xy_2}^2 \\ (x_R - x_3)^2 + (y_R - y_3)^2 + (z_R - z_3)^2 = d_{xy_3}^2 \end{cases} \quad (14)$$

With few mathematical manipulations the previous system of three quadratic equations can be written in the following form, becoming a solvable linear system of two equations and (x_R, y_R) unknowns.

$$Cx = B \tag{15}$$

$$\text{with } C = \begin{bmatrix} (x_2 - x_1) & (y_2 - y_1) \\ (x_3 - x_1) & (y_3 - y_1) \end{bmatrix}, x = \begin{bmatrix} x_{\mathrm{R}} \\ y_{\mathrm{R}} \end{bmatrix} \text{ and}$$
$$B = \begin{bmatrix} \left(\mathrm{d}^2_{\mathrm{xy}_1} - \mathrm{d}^2_{\mathrm{xy}_2} + x_2^2 + y_2^2 - x_1^2 - y_1^2\right)/2 \\ \left(\mathrm{d}^2_{\mathrm{xy}_1} - \mathrm{d}^2_{\mathrm{xy}_3} + x_3^2 + y_3^2 - x_1^2 - y_1^2\right)/2 \end{bmatrix} \tag{16}$$

The proposed methodology can be generalized to a realistic wider deployment assuming to divide the localization area into triangular cells each identified by three LEDs chopped at unique frequency giving a total intensity in the cell of about 500 lx, which is the typical illuminance in indoor environments. In situations where more LEDs are deployed, in addition to the three LEDs identifying the cell, even the LEDs of nearby cells could be visible. To handle this situation, the proposed methodology considers only the three highest FFT-peaks among those detected while the other LEDs just contribute modifying the average light intensity inside the cell. Supposing no obstacles in between, these peaks will coincide with the LEDs identifying the cell. The fact of having for each lamp a unique frequency allocation makes the system resilient in the demodulation to background modulated lights at frequency different from those used for positioning or to lights acting as an average illuminance, as is the case of sunlight or DC light sources; the background lights become problematic only if the reached illuminance level causes the saturation of the electronic front-end.

Regarding calibration, one calibration point must be taken in the centroid of each cell hence the complexity of the calibration procedure in the overall space will depend on the number of cells. Resorting to a wider measurement area has no effect on the computational operations performed by the microcontroller, except that increasing the number of cells will increase the size of the look up tables stored in the MCU containing the associations between LEDs and coordinates, and $\mathrm{K_i}$ and cells. However, the methodology is conceived for applications where realistically no more than 10 LEDs will be used, hence in the same space is not possible to have two or more LEDs with the same identifying frequency, that instead can be reused in a different room. Even if the presented methodology is thought for ideal situations where no obstacles and shading are present, the previous considerations can be generalized since even in case of obstacles the three brightest LEDs can be used to perform positioning, however in this case a different calibration procedure can be adopted to reduce the dimensions of the mapping between $\mathrm{K_i}$ and cells (e.g., one $\mathrm{K_i}$ for each LED and computed

under each light source with the other off). Similarly, novel solutions different from the one proposed can be investigated to detect the presence of obstacles, completely or partially shading the light sources, and consequently to discard the result of the localization when not reliable, considering that in most cases these are transient disturbances or fix obstacles that can be accounted in a preliminary calibration phase.

6.3. System overview

In this Section, the lighting system used for the tests and the architecture of the receiver device are presented, motivating also in detail the choice of the LEDs operating frequencies to hinder some side effects such as spectral leakage, interference, and flickering.

6.3.1. The lighting system

The optical sources employed were three 4000 K LEDs, produced by Cree Lighting, with 115° viewing angle, CRI 80, 1563 lm and spectral power distribution in the visible range. They were driven by a properly designed and realized LED driver dealing with the power supply (through a GW INSTEK GPC-3030D DC power supply) and with the control of the driving signals coming from three Agilent 33220A arbitrary waveform generators. The luminous signals issued by the LEDs were chopped at frequencies f_1 = 1100 Hz, f_2 = 825 Hz and f_3 = 975 Hz; a more detailed discussion about the choice of these frequencies is deferred to Subsection 6.3.3.

The three light sources were arranged in a coplanar fashion, perpendicular to the floor of the measurement space at the vertices of an equilateral triangle with side equal to 104 cm. Considering all the three lights on (when in the absence of other external light sources), the average light intensity under each LED, measured using a RS-IM-203 lx/fc photodiode-based lightmeter, was equal to about 500 lx, reaching a minimum value of 410 lx in the centroid of the triangle, compatibly with the lighting specifications for indoor working environments.

6.3.2. System architecture

The architecture of the proposed system, comprising transmitter, receiver and backend side, is depicted in Figure 44; in the inset the pseudocode of the tasks performed by the MCU to attain the 2D positioning estimation is resumed, squared in yellow is the circuit used to

manage the use of the PV module both as harvester and light sensor. A picture of the implemented IPS (without the PV module) is reported in Figure 45.

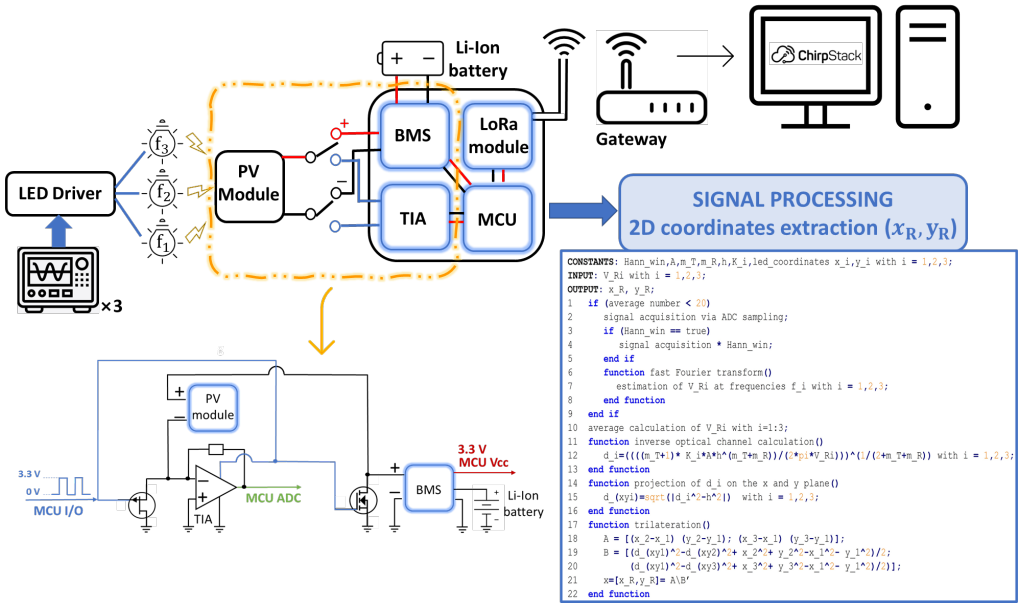

Figure 44. Architecture of the proposed positioning system: the transmitter (i.e., LED driver driven by three waveform generators, three LEDs), the receiver (i.e., the PV module with its conditioning circuit, the BMS, the demodulating system composed of MCU and LoRa transceiver), the backend side (i.e., the LoRa gateway forwarding the transmitted packets to the server). In the inset the pseudocode resuming the sequence of operations performed by the MCU to achieve the localization while squared in yellow is the implemented circuit, relied on a control signal from an I/O port of the MCU, used to manage the use of the PV module both as harvester and light sensor.

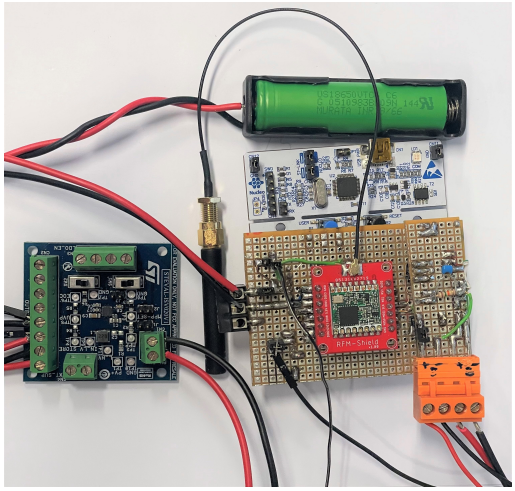

Figure 45. The proposed IPS in charge of demodulating the signal, extracting the 2D position and transmitting it via LoRaWAN protocol; the battery management board is on the left.

The mounted optical receiver was an a-Si:H PV module (AM-1815CA manufactured by Panasonic) since the EQE's response band of amorphous silicon is limited to the visible range with a maximum around 540 nm, well-matching the spectral distribution of the LEDs used in artificial light illumination. The used PV module is made on a glass substrate and is composed of a series of 8 cells with an overall active area A= 23.6 cm^2, it has nominal open circuit voltage V_{OC} = 4.9 V and short circuit current I_{SC} = 47.0 µA at 25°C under 200 lx fluorescent light. The trend of its relative sensitivity with respect to the angular displacement shown in Figure 46, experimentally inferred tilting the module under the light source in steps of 10°, suggests that the angle of half sensitivity is equal to ±67° (graphically identified in the figure by the red-dotted semicircle and segment) and that the proposed methodology can acceptably handle inclinations of the PV module axis with respect to the floor in the order of ±10°. Anyway, PV modules with better relative sensitivity can be selected or a hybrid positioning strategy can be implemented mounting an IMU on board to account for the inclination angles.

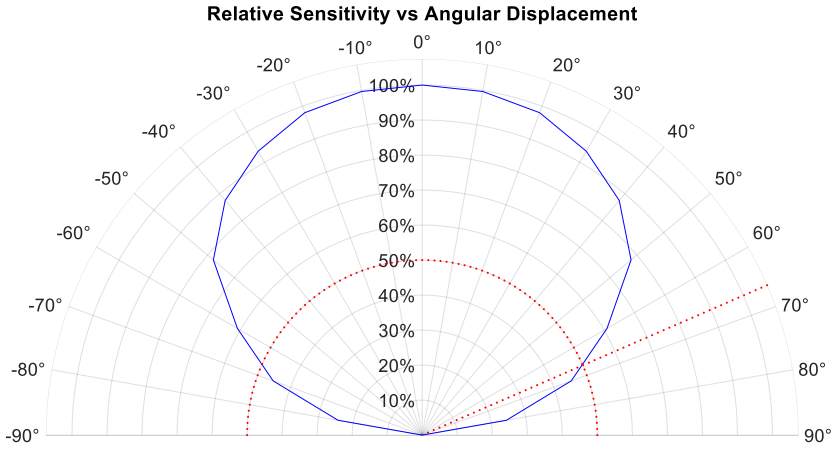

Figure 46. Relative sensitivity [%] versus the angular displacement of the PV module; the semicircle and the segment in red identify the angle of half sensitivity.

During the localization phase, by properly driving the two electronic switches mounted as shown in Figure 44, the cell was disconnected from the BMS and connected in a zero-bias configuration to the low-power OP-AMP TLV237 by Texas Instrument, mounted as transimpedance amplifier (TIA). The TIA presented a very low input impedance, therefore it was able to measure the short circuit current provided by the PV module, and to convert it into a voltage in a first approximation linearly dependent on the level of illumination incident on

the device (the feedback impedance is a parallel connection of a resistance $R_f = 15$ kΩ and a capacitance $C_f = 15$ pF).

The output of the TIA was acquired via the 12 bits-ADC of a STM32L476RGT6 ARM Cortex M4 microcontroller mounted on a NUCLEOL476RG development board from ST Microelectronics. The microcontroller was in charge of digital processing the sampled voltages by performing the discrete Fourier transform (DFT) of the signal by means of FFT algorithm. Once the magnitudes were computed, the trilateration algorithm was performed outputting the estimation of the 2D coordinates. This data was then sent via LoRaWAN protocol to a LP68 Dragino gateway, which redirects the packets to a ChirpStack Server.

The LoRa low-power radio module employed was an RFM95x equipped with a λ/8 antenna. The used radio settings were transmitting frequency 868 MHz, BW 125 kHz, output power 5 dBm, coding rate CR 4/5 and spreading factor SF 7. Both CR 4/5 and SF 7 were chosen since they guarantee the lowest power consumption and the shortest time on air (working currents with peaks up to 45 mA for ~62 ms in transmission) to detriment of worse error correction at the reception and link margin reduction which, however, are not critical aspects in the proposed scenario where kilometric radio coverage is not required.

Low-power components and programming strategies were pursued to realize an energy self-sufficient localization device. Indeed, during the node self-sufficiency test, the MCU was programmed according to a sleep routine which periodically activated the MCU for the time required to retrieve the 2D position of the object and send the data. Since the position was computed on the average of 20 implementations of the FFT algorithm, a run period of approximately 2.5 s can be considered. One digital I/O port was used both to turn on a MOSFET driving the LoRa module and to supply the TIA, in order to switch them off during the sleep periods of the MCU thus avoiding extra power consumption. In this way, the current absorption of the node in standby mode fell below μA.

Finally, the BMS dealt with the energy harvesting through the PV module from the three LEDs. The ultra-low power energy harvester and battery charger employed was the SPV1050 manufactured by ST Microelectronics, mounted on the STEVAL-ISV020V1 board. The internal MPPT functionality was set to $0.8\,V_{OC}$ which theoretically corresponds to the maximum power transfer condition for PV modules. More details about the BMS IC functioning are provided at the end of Section 3.3. In the case study, a rechargeable 3.7 V 3400 mAh Li-Ion battery was employed as power reserve, while the integrated buck converter

provided a regulated voltage supply of 3.3 V used to power the MCU, which in turn drove the system electronics.

Solid-state switches (MOSFET and JFET) relying on a control signal from an I/O port of the MCU were configured as in Figure 44 to manage the same PV module both for energy harvesting and for localization estimation, thus preventing the reading of the light signal from being affected by the MPPT process of the BMS, which fixed a constant voltage at the terminals of the solar cell using a variable load and a switching strategy. As soon as the MCU woke from standby mode, it enabled the same I/O port used to pilot the LoRa module to drive the switches, which temporarily detached the cell from the BMS for few seconds and connected it to the TIA input, therefore during this period no energy was harvested. Once the position coordinates were sent via LoRaWAN and before the MCU re-entered standby mode, the I/O port was disabled, and the PV module was again used for energy provisioning. This strategy assures that in case of deactivation of the load by the BMS (i.e., battery voltage under the undervoltage protection threshold), the PV module remains connected to the BMS input to guarantee battery recharging.

6.3.3. FFT settings

The LED frequencies, the MCU ADC sampling frequency and the number of samples used for the FFT computation, were conveniently chosen to respect several requirements: avoiding light flickering phenomena (signal frequency higher than 160 Hz), satisfying the PV module bandwidth (~3.5 kHz), theoretically preventing spectral leakage in the demodulation phase, and minimizing the interference between the harmonic components of the resulting signal obtained as combination of the three luminous waves. The number of samples required by the FFT algorithm was set to N = 4096 while the ADC sampling frequency was set to f_s = 102400 Hz, giving a frequency resolution Δf = 25 Hz and therefore an integer number of periods of the three incoming signals in the 40 ms-long observation windows.

Even if these precautions guarantee the minimization of the spectral leakage, a small error can still be observed in case of a misalignment between the clock of the microcontroller and the frequencies of the signals driving the LEDs. In this respect, some tests were performed giving as an input of the MCU ADC square signals with known and fixed amplitude and frequencies in the [525 Hz, 50 kHz] range with steps of 1 Hz using the waveform generators used in the test bench; it was found that a misalignment of few mHz is present among the clocks, resulting in errors in the reconstruction of the signal amplitude.

These small frequency errors, due to the quality of the quartz clocks in the test bench, have small effects on the FFT peak amplitude estimation accuracy. Nevertheless, in a low-cost system worse clock accuracy is expected, which can affect the FFT peak measurement accuracy. In fact, in in-field deployments the lighting system will be driven by low-cost relaxation oscillators instead of signal generators. Note that with the chosen setting, a stable misalignment of 12.5 Hz results in a relative peak amplitude error of ~36%. If the clock remains stable, this issue can be compensated by the proposed IP algorithm with the computation of K_i coefficients during the calibration procedure. However, to counteract the other critical situations existing in in-field deployments, a Hann windowing operation was added before FFT, thus reducing the discontinuity between subsequent windows in order to mitigate the spectral leakage even in case of non-correct frequency generation. Interference issues are hindered even by choosing f_1, f_2 and f_3 sufficiently distant in frequency (i.e., minimum 3 side lobes between two consecutive main lobes).

6.4. Tests and results

The system presented in the previous Section was used in several measurement campaigns pursued to evaluate the performance of the localization algorithm – both from the point of view of the positioning accuracy and of the management of some non-idealities in the generation of the signals driving the LEDs (i.e., errors of 1% in the frequency generation of the signal, presence of background light) – and to corroborate the hypothesis of energy autonomy of the node. To perform these tests, a proper test-bench was realized, whose structure replicates the geometrical representation of the measurement space reported in Figure 43.

6.4.1. Measurement set-up

The deployed measurement area is shown in Figure 45. It had dimensions 90 cm × 120 cm × 68 cm, representing a 1:5 scaled version of a real deployment both in the distances and in the illuminance received, which was perfectly comparable to that existing in a real deployment. Hence, considering the 1:5 scale, approximately 5 m between each couple of LEDs can be assumed thus covering a triangular cell of ~22 m^2.

The localization plane, located at 68 cm from the LEDs plane, was subdivided in a grid of 108 10 cm × 10 cm squares identifying 130 distinct equally spaced measurement points (referred to as 'true positions' in the rest of the thesis), which represented the same amount of possible 2D positions in the plane. These grid points and the height h were measured by means of an independent technique using a measurement tape with an uncertainty of 0.1 cm however, considering possible errors due to the manual positioning in the test area, a measurement uncertainty of 0.5 cm can be assumed. No complete shielding of the testing area was performed, since the proposed localization approach should not be affected by other indoor light sources, both continuous and alternate. Concerning reflections, no countermeasures were taken to limit the presence of possible reflections induced for example by the two walls of the testing area (the LEDs were at 40 cm from the closest lateral wall).

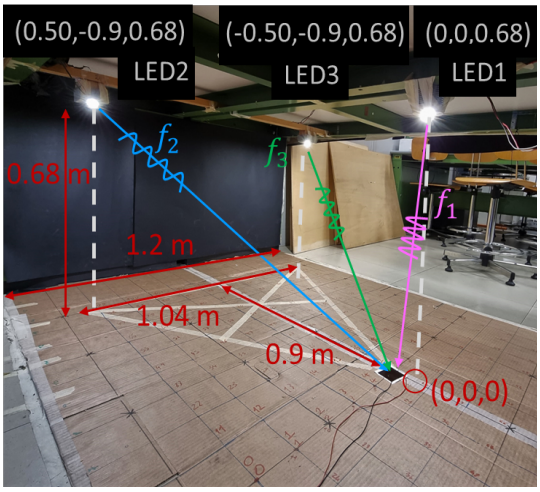

Figure 47. The measurement area with the three LEDs and the localization grid at 10 cm.

The energy autonomy of the node was examined by monitoring the voltage level of the rechargeable Li-Ion battery charged by the energy collected by the PV panel. The voltage was acquired by a Keysight 34470A multimeter (configured with 10 PLC and 7 ½ digit resolution) controlled via LabVIEW with sampling period of 1 s. The type A uncertainty (i.e., <80 μV) and the type B uncertainty derived from the instrument specifications (i.e., $\frac{\text{max\_error}}{\sqrt{3}} \simeq 60$ μV with max_error $\simeq 105$ μV) were comparable giving an overall measurement uncertainty $u \simeq 100$ μV; the other considerations reported in Subsection 4.3.1 about the battery voltage monitoring during the radio transmission remain valid. Even in this case, as for the other self-sufficiency tests presented in this thesis (i.e., Subsections 4.3.1, 5.3.1 and 7.4.1), the initial

battery voltage level was set to approximately 3.9 V, i.e., in the range where the typical charge vs voltage characteristic for the battery is not flat, such that the voltage variation is a sufficient indication of the charge status of the battery.

6.4.2. 2D Indoor positioning tests

During the localization tests the receiver was moved along the grid in steps of 30 cm and 10 cm covering the entire localization area or a subset of it; during its shift, the optical receiver was maintained parallel to the floor without admitting inclination with respect to the LEDs plane. The goodness of the localization algorithm was evaluated by comparing the prediction error, computed as two point-distance between the 'true positions' in the grid and the ones estimated by the proposed methodology, with a threshold on the maximum admissible error.

To evaluate the position accuracy of the proposed system, a preliminary measurement campaign was performed moving the target over the grid at steps of 10 cm covering a portion of 100 cm × 90 cm of the localization area (i.e., the vertices of 90 10 cm ×10 cm squares). The triplets of LEDs RSSs in each measurement point were then used by the on-board microcontroller to recover the 2D position. The measurements were repeated at steps of 30 cm covering a larger surface (i.e., 120 cm × 90 cm) using the Hann window before FFT extraction. The results of the positioning test are reported in Figure 48: Figure 48a gives a qualitative information of how the estimated points are spread in the grid (in red the coordinates estimated without windowing operation, in blue the corresponding 'true positions' of the grid, in green the coordinates estimated using the Hann window, the projections of the LEDs on the floor are identified by the black circles (top of the grid LED_1, bottom right LED_2, bottom left LED_3)). Figure 48b reports as a heatmap the error in cm measured in the non-windowed case as the deviation between the 'true positions' and the ones derived with the positioning algorithm.

Assuming a maximum admissible error equal to 5 cm (since the target was moved in minimum steps of 10 cm), the proposed system well satisfies the requirement: the maximum obtained error is 3.97 cm while the mean error and the standard deviation of the error over the grid are 1.28 cm and 0.92 cm. Since in the test bench f_1, f_2 and f_3 were accurately generated, no substantial difference occurs between windowed and non-windowed estimations. The cumulative distribution function (CDF) F(x) of the positioning error is reported in Figure 49 as a blue line together with the CDF of a Rayleigh distribution computed according to

$F(j|\sigma) = \int_0^j \frac{t}{\sigma^2} e^{-t^2/(2\sigma^2)}\, dt$ considering as scale parameter σ the standard deviation of the positioning error along one axis estimated using the experimental data and as j a vector of 0.1 cm-equally spaced points between 0 cm and the maximum experimental positioning error of 3.97 cm; in the x-axis there is the error in cm.

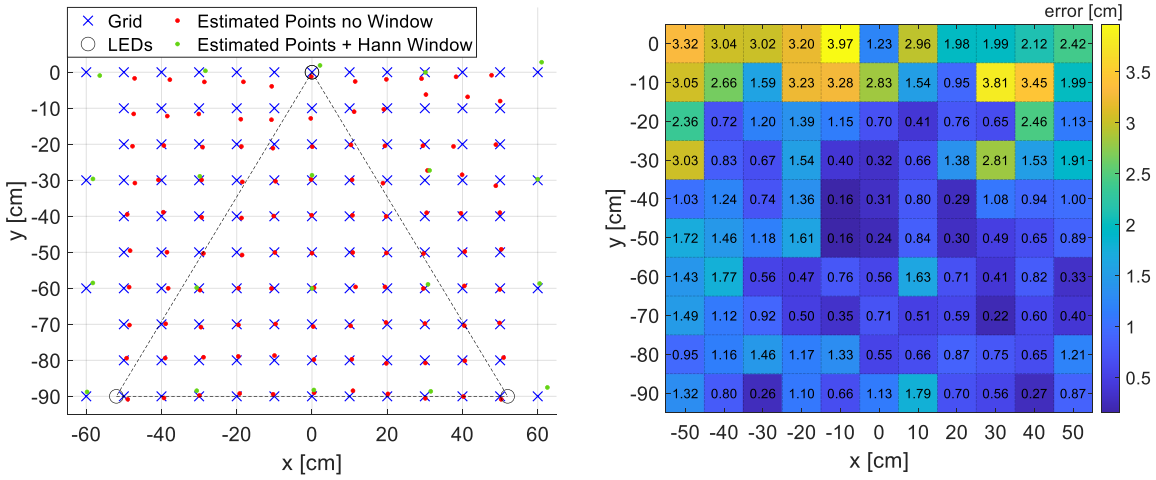

Figure 48. Results of the positioning test. **a)** Qualitative grid representation with the origin of the reference system fixed in correspondence of LED_1: in blue the 'true positions' of the grid points, in red the coordinates estimated at steps of 10 cm without windowing operation, in green the points estimated at steps of 30 cm using the Hann window, in black the circles identifying the LEDs positions (top of the grid LED_1, bottom right LED_2, bottom left LED_3) and the triangular area subtended by the LEDs. **b)** Numeric representation of the error in each point as a heatmap in the non-windowed case, the values in the map report the exact error in cm.

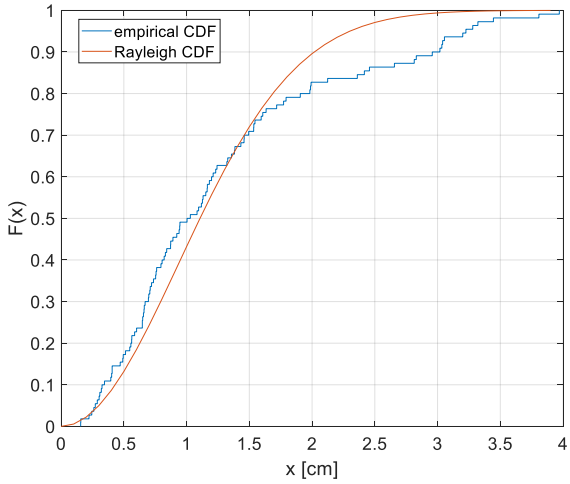

Figure 49. Empirical CDF F(x) of the positioning error (in blue) together with the CDF of a Rayleigh distribution; on the x-axis the positioning error in cm.

Some considerations about the measurement uncertainty propagation in case of a non-scaled measurement area are provided in the following: the terms with apex '*' refer to the non-scaled test environment while the terms without apex refer to the used tested area, a scaling factor $sf = 5$ is considered. The received power P_{Ri}^* in Equation (12) would be equal to P_{Ri} since the higher distance between LEDs and receiver is compensated by a higher P_{Ti}^*, and consequently a higher K_i^*, indeed the illumination in lx at the floor level in scaled and non-scaled environments will be analogous. Excluding the terms which remain constant in the two situations, it can be demonstrated that the measurement uncertainty of x_R^* and y_R^* will behave as $u(x_R^*) = sf \cdot u(x_R)$ (where $u(x_R)$ is the uncertainty of x_R), therefore the error will scale of a factor sf. Hence, the average error of 1.28 cm in the presented set-up will translate in an error of less than 7 cm in a wider deployment which can be reputed a satisfactory result for indoor localization. In general, the accuracy reached by IPSs is very variable, ranging from meters or tens of centimetres in experimental tests (depending on the testing area dimensions) to millimetres in case of simulated tests. A preliminary investigation reveals that the achieved positioning accuracy, appropriately scaling the error in proportion to the dimensions of the measurement area, is comparable with that attained in other scientific works, envisaging also different localization approaches and technologies [106].

The greatest errors are distributed in the highest part of the grid, and they are probably due to external sources of error affecting the estimation of V_{R1} or K_1 as light reflections, non-perfect positioning of the receiver in the grid or slight inclination of the floor under LED_1. This aspect is highlighted in Figure 50 where the discrepancy between the total measured received optical power V_{TOT} (i.e., the sum of the FFT-derived V_{Ri} in each measurement point) and the total reconstructed optical power V_{TOT_rec} (i.e., the sum of the reconstructed V_{Ri_rec} in each measurement point, where every V_{Ri_rec} is derived by inverting the second term in (13) and by substituting to d_i the known distance between solar cell and LED_i, recovered from the height h and the 'true' coordinates (x_k, y_k) of the grid points) is reported. V_{TOT} and V_{TOT_rec} are depicted respectively as a blue and a red 3D surface, the heatmap on the (x,y) plane reports the absolute difference in mV between V_{TOT} and V_{TOT_rec}: it can be seen that the maximum error is in correspondence of LED_1.

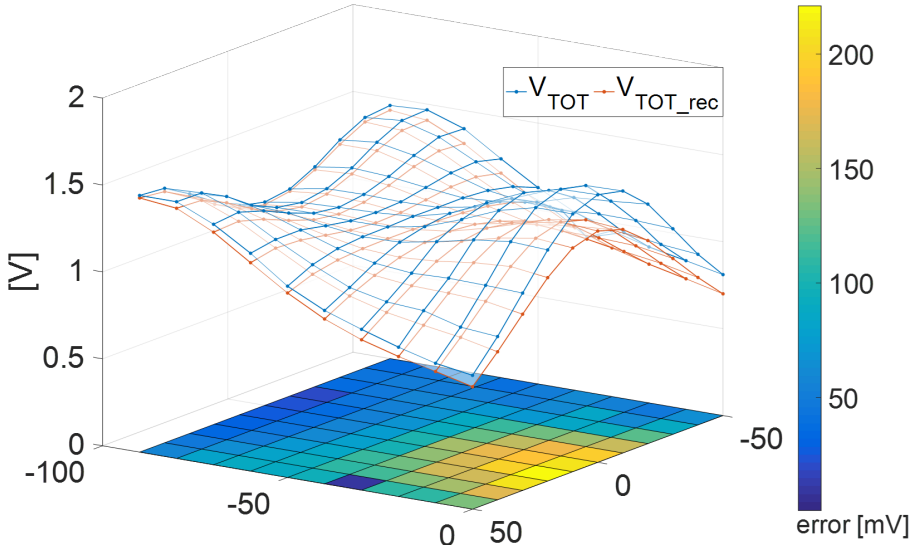

Figure 50. The estimated RSSs distribution of the three LEDs (i.e., the sum of the FFT-derived V_{Ri} in each measurement point, V_{TOT}) (3D blue surface), the reconstructed distribution of the three LEDs (i.e., the sum of the reconstructed V_{Ri_rec} in each measurement point, V_{TOT_rec}) (3D red surface), on the (*x,y*) plane a heatmap reporting the absolute difference in mV between V_{TOT} and $V_{TOT\ rec}$.

This is further highlighted by Figure 51, where in (a), (c) and (e) the 3D distribution of the voltage error in mV for each LED, computed as difference between V_{Ri} and V_{Ri_rec}, is reported; the color mapping gives information about the amplitude of the error: the blue shades identify the points where V_{Ri} is underestimated with respect to V_{Ri_rec}, the yellow shades correspond to the opposite situation. In general, the error tends to increase approaching the LEDs and this is probably due to the adopted method for estimating K_i, which gives best results in the centroid of the grid. However, the larger error under LED_1 can be only partially ascribed to the estimation methodology of K_i since the voltage accuracy remains acceptable under $LED_{2,3}$, consequently the error must be rather introduced by other factors independent from the modelling. In the same figure, the plots of (b), (d) and (f) confirm the previous considerations: the trend of V_{Ri_rec} (in red) and V_{Ri} (in blue) are plotted versus the distance (moving the receiver from the projection point of the LED on the floor at steps of 10 cm along y-axis for LED_1 and along x-axis for LED_2 and LED_3); the two curves still well match for $LED_{2,3}$, while for LED_1 a larger discrepancy is observed.

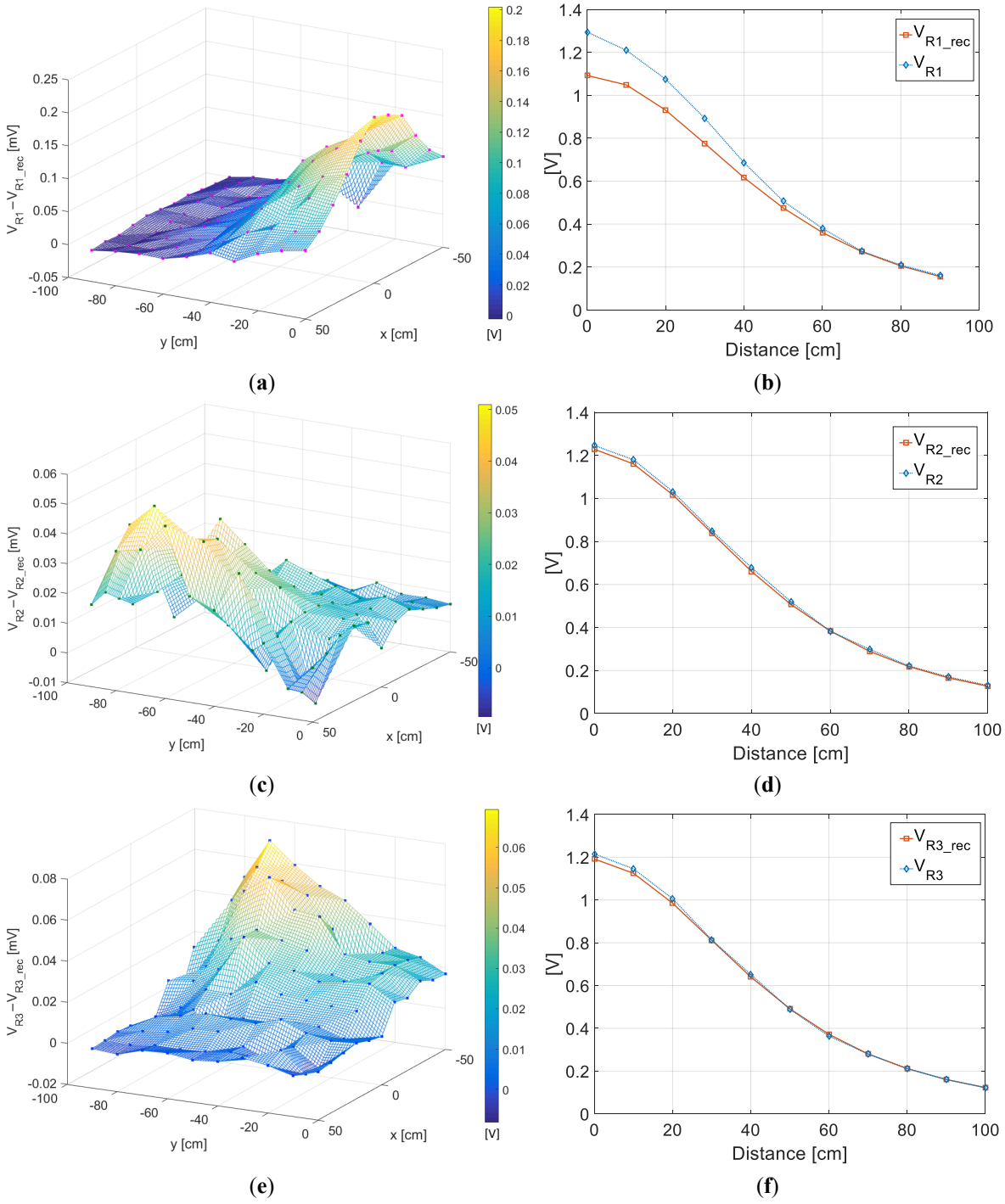

Figure 51. 3D distribution of the voltage error in mV computed as difference between V_{Ri} and V_{Ri_rec} respectively for LED_1 (**a**), LED_2 (**c**) and LED_3 (**e**); trend of the reconstructed voltage (in red) and of the extracted voltage (in blue) versus the distance respectively for LED_1 (**b**), LED_2 (**d**) and LED_3 (**f**).

To assess the capability of the proposed IPS to handle possible inaccuracies, two additional tests were performed. The first one concerned the effect of frequency inaccuracies related to the non-idealities of the clock on board of the node and of the oscillators used to drive the LEDs. This test consists in intentionally introducing a misalignment between clocks. The second test was aimed at confirming the robustness of the localization system toward the influence of background lights during the measurements. Concerning the first test, the optical receiver was moved along the entire measurement area in steps of 30 cm (i.e., 12 30 cm × 30 cm squares, 20 measurement points), and 20 measurements for each grid point were collected, 10 with Hann windowing before FFT, 10 without. An error of 1% in the frequency generation of LED_1 (i.e., f_1 = 1111 Hz instead of 1100 Hz) was injected to reproduce what is expected in realistic deployments where the lighting system are likely driven by low-cost and low-complexity relaxation oscillators instead of more precise and expensive signal generators, which would make the system not realizable in large scale. The RMSEs (root mean square errors) for the case with and without window are reported respectively in Figure 52a and Figure 52b; Figure 52c reports the same information on a grid representation: in red the points obtained without window, in green those obtained using the window, in blue the 'true positions' of the grid points. The usage of the window has the main effect of strongly reducing the variability of the results making the proposed system suitable even in case of large errors in the generation of the LED driving signals, as can be in case of real deployments. Indeed, an RMSE below the target value of 5 cm is ensured even in the presence of frequency deviations up to 1%. Note that the dispersion of the results without the window, due to spectral leakage, is related to the random phase among the signals.

Concerning the effect of external lights on the localization accuracy (i.e., modulated artificial lights used for indoor lighting, background artificial lights), a further test was performed by shielding the measurement area. The material used was not anti-reflective since the goal of the shielding was only to hinder the external light sources and not to avoid reflections. The optical receiver was moved with steps of 30 cm along the 14 points constituting the perimeter of the entire measurement area, since for the arranged measurement set-up these points were the most affected by the external light presence. The results are reported in Figure 52d: the proposed FFT-based approach is robust toward the additional modulated light sources, as the ones at 50 Hz employed for indoor lighting, and toward the presence of background light. Indeed, the background solar light can be discarded as a DC value in the FFT evaluation, whereas the interference of external modulated lights is mitigated

thanks to the accurate selection of the LED frequencies (i.e., greater than 50 Hz so that the higher harmonics of the other lights sources are significantly attenuated and do not interfere with the spectrum of the signals used for localization) and to the usage of the FFT, which selects only the RSSs at the specific LED frequencies. In this way, the alternated external light sources, together with the background light, contribute only increasing the mean average illuminance under the LEDs, which is a problematic issue only if it causes a significant reduction of the dynamic of the electronic front-end.

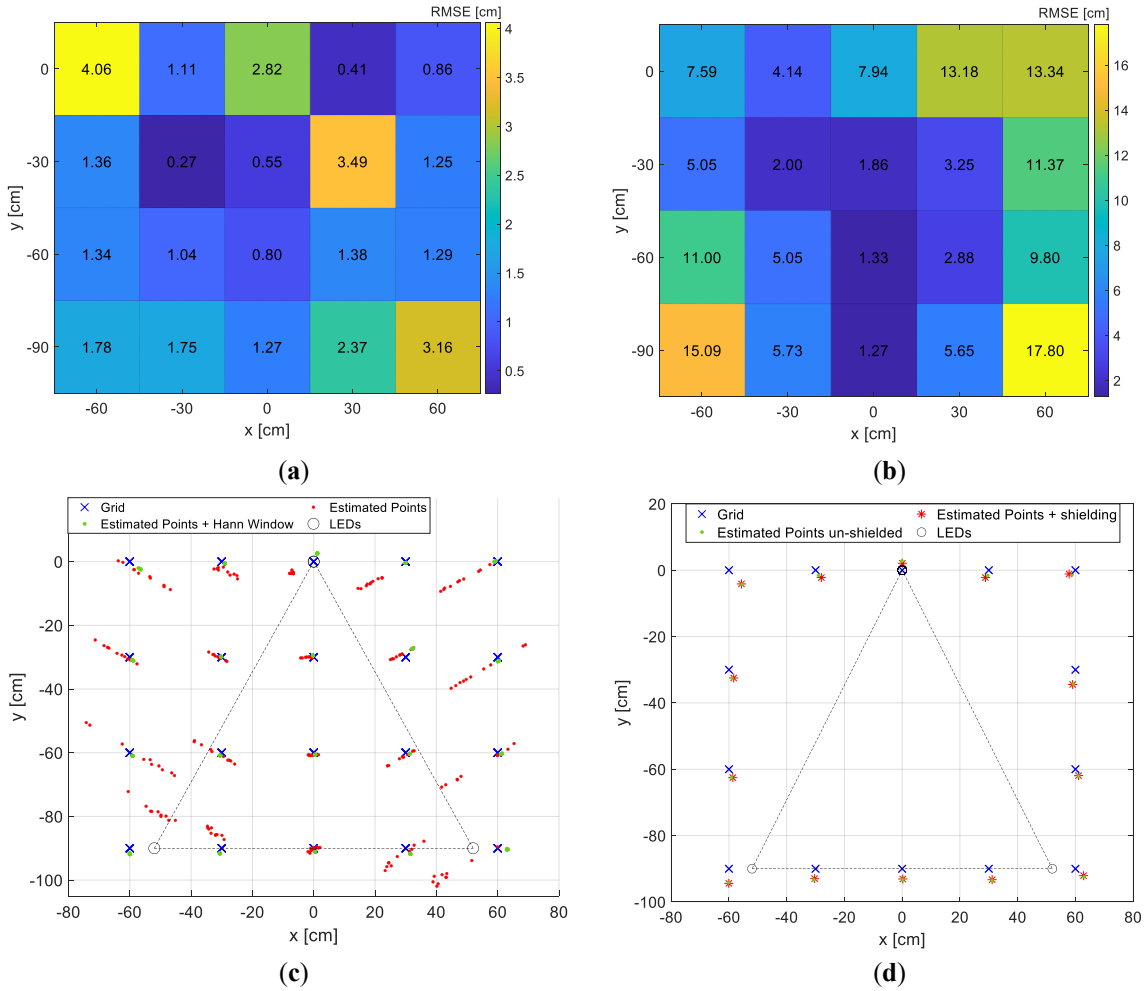

Figure 52. Results of the test performed introducing some inaccuracies: an error of 1% in the frequency generation of LED_1 (i.e., f_1 = 1111 Hz instead of 1100 Hz) and the presence of background lights. RMSEs in each grid position in case of frequency error respectively with (**a**) and without (**b**) windowing; the values in the heatmaps report the exact RMSEs in cm; (**c**) same results reported on a grid representation: in red the coordinates estimated without windowing, in blue the 'true positions' of the grid points, in green the coordinates estimated using the window. (**d**) Qualitative grid representation of the estimated coordinates for the test performed shielding the measurement area and considering the perimeter points: in blue the 'true positions' of the grid points, in red and green respectively the coordinates estimated shielding and non-shielding the area.

6.4.3. Node self-sufficiency tests

The tests to prove the energy autonomy of the proposed architecture using the solar cell both as energy harvester and optical receiver were carried out with the system located in the grid point (0, –60,0) where the minimum level of illuminance is experienced (i.e., 410 lx). The MCU was programmed to work in sleep mode, waking up periodically (i.e., every 15 min during the first test and every 10 min during the second test) to transmit via LoRa technology and LoRaWAN protocol the estimated position of the target. The voltage trend of the rechargeable Li-Ion battery, V_{Li-Ion}, was measured for the entire duration of the tests using the measurement set-up and technique described in Subsection 6.4.1. The battery voltage behavior, monitored for approximately 10 hours for each measurement campaign, is shown in Figure 53: the blue plot corresponds to the case of radio transmissions every 15 min while the red plot refers to transmissions every 10 min, the negative spikes are the voltage drops caused by the peak consumptions due to LoRa transmissions (i.e., 40 during the first test and 60 during the second test).

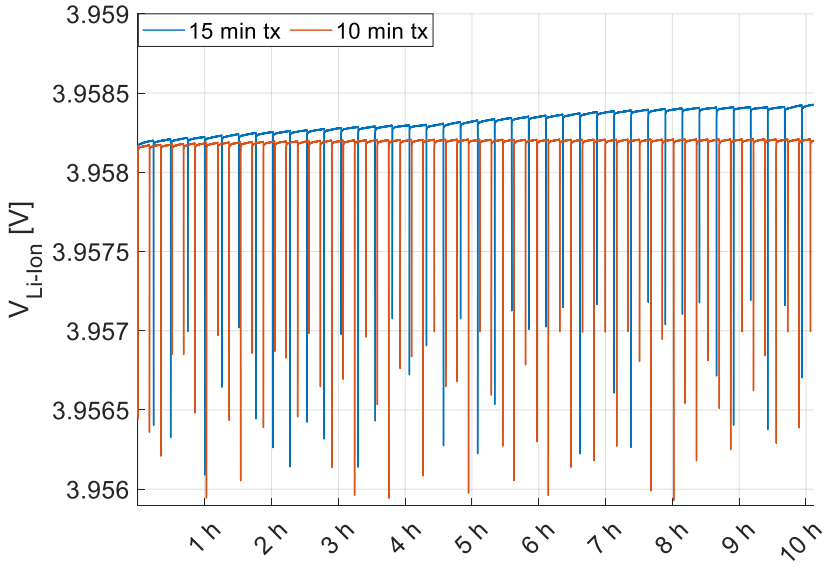

Figure 53. Li-Ion battery voltage behavior, V_{Li-Ion}, during two tests lasting 10 h each and performed in the grid point (0, –60,0) at the minimum level of illuminance (i.e., 410 lx). The blue plot corresponds to the case of radio transmissions every 15 min while the red plot refers to transmissions every 10 min.

The increase of the battery level, net of node consumption, is minimal since the average extracted power delivered by the cell at the operating point $0.8V_{OC}$ in the tested conditions of

minimum illuminance is $P_{OP} \simeq 305$ μW (with average voltage $V_{OP}=4.38$ V and average current $I_{OP}=70$ μA). However, the difference between the voltage level at the end and at the beginning of the tests is positive in both cases, meaning that the battery charge is surely increasing. In particular, while with transmissions every 15 min a battery charge, albeit small, is detectable, in the case of transmissions every 10 min a perfect balance between harvested and absorbed energy is achieved and an increasing trend can be detected only over a long period. Thus, these results validate the energy self-sufficiency of the system even in the case of minimum illuminance conditions and quite frequent transmissions. Indeed, one transmission every 10 min or at least 15 min can be considered a good transmission rate for those deployments where real-time localization is not required, as car tracking in a parking or goods inventory.

However, since the tests demonstrate that the power delivered by the PV module is sufficient for supplying the node operations, the proposed system may be further engineered to be fully battery-less, embedding at most a small supercapacitor to manage the peak current absorptions of the radio transmissions. In this case, the fact of foreseeing an energy provisioning procedure becomes a strength with respect to similar nodes relying on a rechargeable/disposable battery as onboard energy storage.

Chapter 7

Self-sufficient IoT node for indoor horticulture via harvesting from colored-spectrum artificial light

Most of the indoor deployments exploit artificial white lights, however in certain applications spectral compositions different from conventional white can be required. This is the case of indoor horticulture, where ad-hoc light treatments and spectra are investigated to improve the crop yield, boost specific morphological characteristics of plants, and reduce the environmental impact of the production cycles.

Nowadays, most fruit and vegetable production is carried out in greenhouses, as they allow for controlled environmental conditions. In this context, the advent of IoT architectures, distributed monitoring systems and LPWAN transmission technologies represents a viable solution to integrate traditional greenhouses with sensors, actuators, and wireless connectivity, additionally encouraged by the possibility of performing energy provisioning from the colored artificial light sources. Nonetheless, spectral response of PV modules is optimized for sun spectral distribution and sun intensity while indoor deployments involve spectral distributions and intensities very different from those of sun. In this respect, greenhouses represent a stimulating scenario, due to the great diversity of the adopted spectral compositions and to the multiplicity of environmental parameters to be monitored, some of them quite power-consuming, in conditions where grid connections may be difficult to be pervasively settled.

In this Chapter, the feasibility of an autonomous LoRaWAN-based sensor node aimed at monitoring physical (i.e., temperature, RH and pressure) and chemical quantities (i.e., CO_2 and O_2 concentrations) in a greenhouse is investigated; the self-sufficiency is attained using a polycrystalline silicon PV module to harvest energy from the artificial colored light source. The PV module is characterized, and the designed system is tested under two programmable LED lights, performing six different lighting treatments commonly employed in greenhouses combining spectral components in the blue, red, far-red and white 5700 K ranges [41, 43].

Great care is paid during the design phase to create low-power sensing circuits and strategies dealing with the low power extracted from the PV panel (i.e., in the mW range).

7.1. Greenhouse monitoring

Large efforts have been devoted to the definition of real-time monitoring and automation systems for outdoor crops [107], but several contributions are also focused on the definition of technological infrastructures for greenhouses [108], where the application requirements are different in terms of scale and complexity, but still pose significant challenges.

A wide range of architectures based on the use of IEEE 802.15.4 2.4 GHz radio modules, exploiting 6LowPAN and ZigBee protocols, has been presented in literature [109, 110, 111], differing for what concerns the parameters to be monitored, the overall nodes architecture or the data collection and storage system. With the explosion of IoT technologies, new solutions for greenhouse monitoring have emerged, exploiting data transmission techniques more efficient in terms of energy consumption and network coverage, including UHF RFID [112], Bluetooth Low Energy (BLE) [113] as well as LoRa [114]. The most notable parameters to be monitored in a greenhouse are environmental parameters such as soil moisture and temperature, air humidity, air quality index, temperature, light intensity, and gas concentrations (e.g., CO_2). Since these physical quantities vary quite slowly, real-time monitoring is generally not required, and the transmission of hourly data may be sufficient. However, some sensors, such as the CO_2 ones, can be critical from the point of view of the consumption if there are stringent limitations on the power available on board the nodes.

However, despite the great interest in setting up deploy-and-forget IoT infrastructures, little attention has been paid to the problem of power management, which may be in some cases an actual bottleneck because of the impossibility to set up a wired connection to the power grid. Indeed, notwithstanding the importance in identifying a solution for the autonomous operation of the nodes, no contribution proposing the adoption of energy harvesting techniques in this context has been found in literature, especially when considering energy scavenging from artificial and colored-spectrum light sources.

7.2. Artificial lighting in horticulture

The usage of artificial lighting in horticulture, both as exclusive light source and as a supplement to sunlight, is nowadays a trend topic since there is an increasing interest towards the thorough study of lighting protocols aimed at increasing the crop yield, improving the nutritional qualities of the products, speeding up the plants growth and performing an efficient use of water, nutrients, and chemical growth regulators. The plants photosynthetic reaction is developed in a limited portion of the sun spectrum, identified by the so-called Photosynthetically Active Radiation (PAR) region, which includes the wavelengths in the [400 nm, 700 nm] spectral range approximately correspondent to the visible light range [115]. Even in the PAR region, not all the frequencies are equally effective in generate a photosynthetic response since radiation is not well absorbed by the pigment of chlorophyll. Indeed, the relative quantum photosynthetic efficiency curve presents a drop of efficiency between 400 nm and 600 nm, corresponding to the green spectral components which are less capable to effectively produce photosynthetic reactions in plants, indeed they are reflected giving plants their green appearance (see Figure 54).

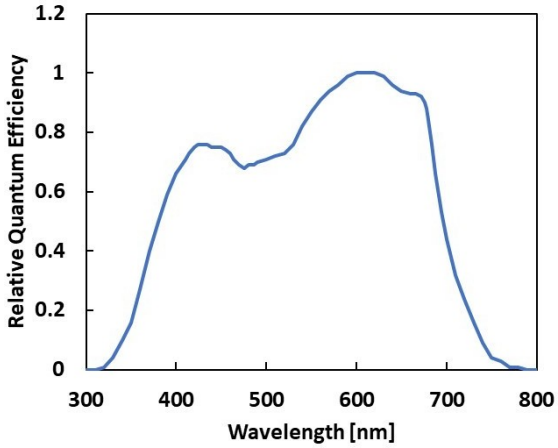

Figure 54. Normalized photosynthetic response action for photons (i.e., relative quantum efficiency) as a function of wavelength.

This spectral responsivity weighting function is analogous to the luminous efficiency function which represents the spectral sensitivity of human eye in the visible spectrum under photopic conditions. As the luminosity function can be used to translate absolute radiometric measurements into human perception-dependent photometric quantities, such as the illuminance and the luminous flux of a light source, similarly the relative quantum

photosynthetic efficiency can be used to define plants-dependent photometric quantities as Photosynthetic Photon Flux (PPF) and Photosynthetic Photon Flux Density (PPFD).

PPF quantifies in μmol/s the total number of photons within the PAR range emitted by a light source each second, it is analogous to the luminous flux of visible light. PPFD measures in μmol/(s·m^2) the total number of photons within the PAR range emitted by a light source each second over a 1 m^2 area, it is analogous to the illuminance for visible light. The PPFD can be theoretically computed by convoluting the spectral irradiance of the light source, $E_{R,\lambda}$, with the plant relative quantum efficiency at each wavelength, thus weighing the photons emitted by the lamp with the plant sensitivity curve. However, the relative quantum photosynthetic efficiency trend strongly varies with the considered crop, for this reason a different strategy is generally adopted for PPFD computation. In particular, the photosynthetic efficiency is not evaluated in terms of energy but in terms of number of photons, assuming constant relative quantum efficiency in the PAR range: the energy of a mole of photons, $Q_{mol-ph} = N_A \frac{hc}{\lambda}$ (with N_A =6,02214086×10^{23} 1/mol Avogadro constant), for each specific wavelength λ defined in the PAR is used, thus weighing in a different manner the photons of different wavelengths according to the following formula: $PPFD = \int E_{R,\lambda}(\lambda) Q_{mol-ph} d\lambda = \int E_{R,\lambda}(\lambda) N_A \frac{hc}{\lambda} d\lambda$, where the irradiance of the light source times the energy of a mole of photons is integrated in the PAR range. Indeed, the relative quantum efficiency is not constant in terms of energy since, for a given amount of energy, the number of emitted photons increases as the wavelength increases. Therefore, although the function used for PAR does not correspond to the effective function of any real plant, this approach is widely used since it gives quite refined results with a general validity, independent of the considered crop type.

Most of the morphogenesis plants reactions are triggered by radiation in the blue, in the red or in the far-red spectral regions, whilst green and yellow components have a minor effect on plant photomorphogenesis and a different participation on photosynthesis. Light is essential in plants growth because it provides energy for photosynthesis and because it influences the morphological characteristics and the physiological responses of plants [116, 117, 118]: different spectral components operate differently on stem elongation, foliar expansion, roots development, nutrients concentration and these interactions vary according to the plant species studied. This process is accomplished by means of proteins called photoreceptors, which are sensitive to different portions of the light spectrum ranging from

ultraviolet B to far-red. The primary five families are phytochromes (PHY), phototropins (PHOTO), cryptochrome (CRY), Zeitlupe (ZLT), and UVB-resistance locus 8 (UVR8).

The red light [625 nm, 720 nm] is indispensable for plant growth as its presence is sufficient to favor the normal photosynthesis even in the absence of the other spectral components. The far-red light [720 nm, 800 nm] as sole light source is unable to establish photosynthesis in the plant as it is outside the wavelength range defining the PAR. However, in conjunction with other spectral components such as red, blue and white ones, favors the development of some plant characteristics. In particular, different red:far-red ratios (R:FR) influence the growth and the functionality of the plants in various manners: low R:FR accelerates stem elongation, foliar expansion, and flowering to the detriment of branching, which appears dampened [119]. PHY are afamily of photoreceptors responsive to the red and far-red components. Also, the blue light [445 nm, 485 nm], used as a supplement to other spectral components, has positive effects on plant growth and nutrient concentration. The blue and UVA spectral components are mainly perceived by PHOTO, CRY and ZLT photoreceptors while the UVR8 receptors have a secondary effect on plants growth. Moreover, although the effect of green components is marginal in triggering photosynthetic reactions, even green light sensitive photoreceptors exist and influence some plant growth aspects. Furthermore, not only the light composition but also the photoperiod, namely the succession of light and dark periods, conditions some process as flowering and fruit production.

The remarkable technological developments undergone by LEDs in recent years and their availability also in small-sized and narrow spectral solutions, have favored the usage of this technology even in the horticulture field. With respect to traditional lamps, they have greater energy efficiency, longer lifetime (∼50000 h), low heat generation and they offer the possibility to select only specific wavelengths, without wasting energy for spectral components less significant for the photomorphogenesis and the photosynthesis of the plant. Moreover, the reduced radiant heat allows versatile lighting solutions as inter-lighting arrangements where the light source is placed within the plants canopy. Commercial LEDs for indoor horticultural applications are specifically designed to feature spectral power distribution in the PAR range and the power they deliver is generally measured in terms of PPFD. These light sources are usually composed of LEDs arranged in array or matrix geometries and they can have either the same or different peak emission wavelengths. Versatile lighting programs can be usually programmed with an ad-hoc software which allows

to choose the photoperiod, the intensity and the composition of the light spectrum. In general, the lighting treatments strongly depend on the cultivated plant species and there is no lighting program valid for each type of crop. However, the typical light intensities that can be found in literature are in the range from 100 μmol/m^2s to 300 μmol/m^2s, whilst typical photoperiods are 12 hd^{-1}, 16 hd^{-1} or 20 hd^{-1}. Concerning the light spectrum composition, blue, red and far-red components are often supplemented to white light in order to enhance the plant growth [117] or combined together in different ratios [116, 120, 121, 122, 123]. In [121, 122], the authors investigate the effect of different red and blue spectral fractions and different PPFDs on indoor cultivation of lettuce and basil, in order to find the lighting treatment giving the best compromise between crop yield, nutrients content and light use efficiency. The scientific contributions in [116, 117, 122] present results obtained by adding the far-red radiation to the lighting treatments, both mixed to red and blue components [116, 122], or as supplemental to white light [117]. In both cases, the papers demonstrate that the lighting protocols containing the far-red radiation promote the plant growth, determining higher yield in comparison with the other illumination programs.

7.3. System overview

A summary of the designed system is here presented, focusing on the employed light sources and the corresponding lighting treatments used to test the node self-sufficiency, and on the architecture of proposed sensor node, aimed at measuring with a satisfactory accuracy the physical and chemical quantity for the application of interest (i.e., temperature, RH, pressure, CO_2 and O_2 concentrations).

7.3.1. Light sources and lighting protocols

Two programmable light sources were used both for the characterization of the PV module and the self-sufficiency tests.

The first light source was a custom-designed solar simulator with spectral emission matching the requirement of IEC 60904-9. A total of 486 high power LEDs is uniformly distributed in a matrix of 9×9 cells covering a 300×300 mm^2 light emitting surface, each cell is arranged as a 3×2 LEDs structure with one LED for each spectral peak (i.e., 460 nm, 530 nm, 630 nm, 780 nm, 850 nm, and 940 nm). A total of 18 LED channels, monitored via

LabVIEW, control the 486 LEDs subdivided into 3 concentric zones, each managed independently to ensure the irradiance uniformity on the target surface.

The second light source was the FL384 by Flytech, a commercial solution specifically designed for the deployment of plant growth systems in indoors environments and in greenhouses. It is a flat panel composed of 10×5 cells arranged in a matrix form, each cell has 4 LEDs peaked in different wavelength ranges (i.e., [445 nm, 455 nm] (blue, B), [655 nm, 670 nm] (red, R), [720 nm,750 nm] (far-red, FR) and white 3000 K) for a total of 200 LEDs (50 for each channel) occupying an active area A = 22.3 cm × 50.0 cm. Each channel can be dimmed via software on a daily schedule by modifying the duty cycle of the signal driving the LEDs (250 Hz) and this requires filtering the cell output signal to stabilize it.

To design a self-sufficient node, six different realistic lighting conditions were considered, derived from the literature. Three of the selected lighting protocols were obtained as integration of the white light 5700 K (W) with the same amount of B, R or FR components, giving a total amount of 155 μmol/m^{2}s and considering a 20 hd^{-1} photoperiod [117]. Three additional treatments were obtained as combination in different percentages of B, R and FR components, with a 20 hd^{-1} photoperiod and always supplying a total amount of 155 μmol/m^{2}s [116, 122].

These lighting protocols are resumed in Table VI while the emitted spectral irradiances of the two different light sources, measured with an Ocean Insight USB4000 UV-VIS spectrometer equipped with a CC3 UV-S cosine corrector, are shown in Figure 55; the integral of each spectrum corresponds to the intensity measured by a Kipp & Zonen CMP3 pyranometer (nominal sensitivity 15.66 μV/(W/m^2), spectral range [300 nm, 2800 nm], 64-junction thermopile detector with a 4 mm glass dome).

Table VI. Spectral composition of the lighting protocols.

Lighting Protocol	White 5700 K (W) [μmol/m²s] (%)	Blue (B) [μmol/m²s] (%)	Red (R) [μmol/m²s] (%)	Far-red (FR) [μmol/m²s] (%)	TOT PPFD [μmol/m²s] (%)
WB	117 (75%)	38 (25%)	—	—	115
WR	117 (75%)	—	38 (25%)	—	115
WFR	117 (75%)	—	—	38 (25%)	115
BR1	—	25 (16%)	130 (84%)	—	115
BR2	—	38 (25%)	117 (75%)	—	115
BRFR	—	17 (11%)	112 (79%)	16 (10%)	115

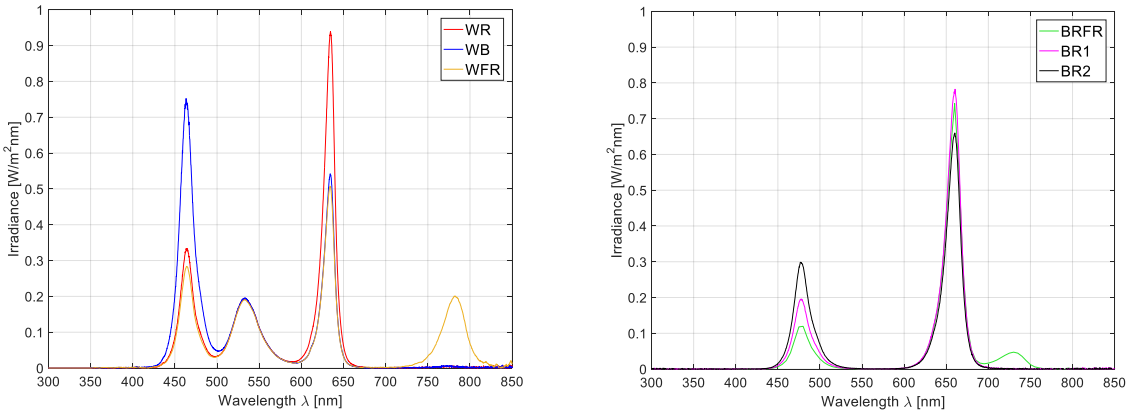

(**a**) (**b**)

Figure 55. Spectral irradiance measured by the spectrometer in case of custom-designed solar simulator (spectral compositions WB, WR and WFR) and commercial horticulture lamp (spectral compositions BRFR, BR1 and BR2); the integral of each spectrum corresponds to the intensity measured by the pyranometer.

7.3.2. System architecture

The architecture of the developed node is composed of two boards connected by means of some I/O pins of the used MCU, one housing the gas sensors and their electronic front-ends (i.e., the 'sensor board'), the other hosting the other environmental sensors, the radio module, the MCU, the harvesting and charging system and additional circuitry for reading the gas sensors (i.e., the 'main board'). The node architecture and prototype are depicted in Figure 56, where the two boards are highlighted. Great attention was paid to the selection of ultra-low power components, programming strategies and sensing solutions to guarantee the node self-sufficiency when performing energy scavenging from the previously presented lightning treatments. The preliminary analysis of the current absorptions reported in the following is an estimation from the datasheets of the components.

The polycrystalline silicon modules employed are the MSX-005F by BP Solar, they are composed of a series of 8 cells with active area A = 6.2 cm^2. They feature nominal power P=0.446 W, V_{OC}= 4.6 V and I_{SC}= 160 mA in STC. The choice of polysilicon instead of monocrystalline or amorphous silicon was justified by the fact that its spectral response is greater in the frequency range belonging to the R and FR spectrum [124], which are at the same time the spectral components that most favor the development of the morphological characteristics of plants.

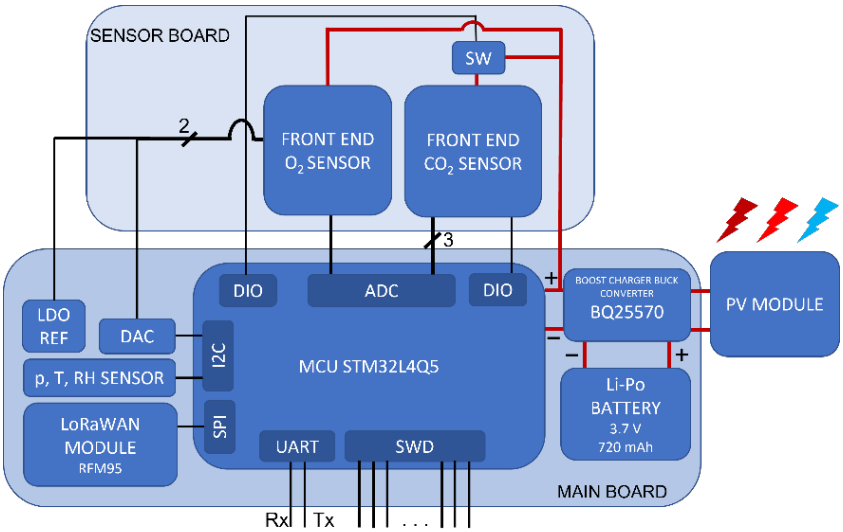

(**a**)

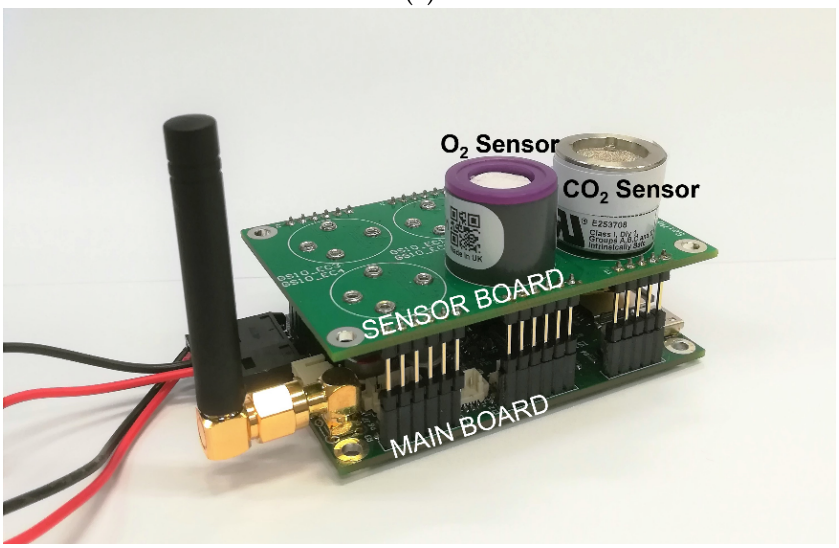

(**b**)

Figure 56. The architecture (**a**) and the prototype (**b**) of the designed node, distinguishing between the main board and the sensor board.

The sensor board

The sensor board embedded an amperometric electrochemical sensor O2-A3 (by Alpahsense) providing the measurement of the oxygen concentration with an accuracy lower than 1% and low drift for a period of 3 years by means of redox reduction of the target gas. This is a two-electrode active sensor not requiring an external excitation, thus the power consumption of the oxygen sensing was only related to the front-end circuit shown in Figure

56a, composed of a current-to-voltage converter and a biasing circuit based on ultra-low power OP-AMPs. The biasing circuit was designed to allow also for replacing the selected sensor with a three-electrodes electrochemical sensor, that requires a continuous power supply to avoid long transients related to the attainment of the chemical steady state. The electrodes in the Figure are indicated as "W" for the working electrode (exposed to the gas through a porous membrane, it's where the oxidation reaction occurs), "C" for the counter electrode (in contact with the W electrode through an electrolyte and where the complementary reduction reaction occurs) and "R" for the reference electrode (used to maintain a constant biasing potential with respect to the W electrode in case of a three-electrodes sensor). The current flowing between W and C ($I_{sens_{out}}$ in the figure) was converted through the transimpedance amplifier in a voltage theoretically proportional to the concentration of the target gas. When using the two-electrodes electrochemical sensor, the front-end exploited a regulated voltage V_{REF}=1.25 V obtained from an ultra-low power reference circuit (quiescent current <2 µA) to bias a voltage across the sensor between W and C. In the three-electrodes electrochemical sensor, the front-end exploited not only the regulated voltage reference V_{REF}, but also a voltage reference V_{BIAS} derived from an external DAC at 12 bits. The overall current absorption of the front-end supplied with 3.3 V was < 4 µA in the 2 electrodes case and <54 µA in the 3 electrodes configuration.

Electrochemical sensors provide a good trade-off between performance and cost; however, they suffer from short-term stability and low durability because of the degradation of the sensitive compounds. For the CO_2 monitoring, a sensor based on optical techniques was selected since it is the most robust measurement solution offering long-term stability, good sensitivity, high gas selectivity, and relatively short response time. Nevertheless, the main criticality encountered when embedding optical-based sensors is that they require very power-consuming optical sources, thus the integration of these solutions in low-power systems is quite challenging. The selected sensor was an IR21GM (SGX, Sensortech), a non-dispersive-infrared (NDIR) sensor operating with a pulsed power source at 4 Hz, 50% duty cycle, 3.3 V with a mean current absorption of 26 mA. It embeds a LM60 internal temperature sensor to perform temperature correction, absorbing about 100 µA. A power-on period longer than 40 s is needed for reliable CO_2 readings (i.e., 20 s of warm-up time + 20 s for response time). The schematic of its front-end electronics is shown in Figure 56b; the overall consumption comprising amplifiers, filters and output voltage adjustment was <200 µA.

A NDIR sensor exploits the principle of absorption in the IR spectrum of certain gas molecules, depending on the number and the masses of the atoms composing the molecules, and on the number and the typologies of the chemical bonds. Each gas has its own absorbing property to IR radiation, and thus a different absorption spectrum composed of a series of absorption lines at certain specific wavelengths or bands. A NDIR sensor is generally composed of an optical cavity with reflective surfaces and gas inlet and outlet, a broadband IR source, an IR active detector equipped with a fixed narrow bandpass optical filter tuned to the target gas, an IR reference detector with neutral filter tuned where no gas molecules absorb. The IR light interacts with the gas when passing through the optical cavity before impinging on the two detectors: if the target gas is present the intensity of light impinging on the active detector decreases, conversely the intensity of the light hitting the reference detector is not affected by the presence of the gas. Alternatively, a closed chamber containing a reference gas not excited by IR radiation (e.g., N_2) and mirroring the chamber where the target gas diffuses can be added to the sensor structure and used as reference channel. Both solutions allow to enhance the accuracy of the sensing and to compensate for the fluctuations of the light source since, by comparing the signal at the two detectors, the gas concentration in the target gas can be calculated. Indeed, as shown in Figure 40b, two mirrored front-end circuits are used to read both the active and the reference channels.

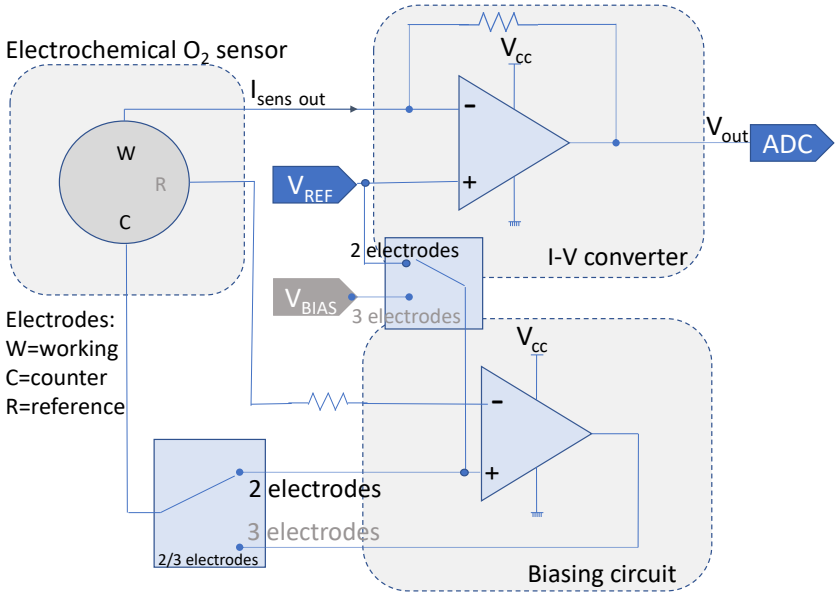

(**a**)

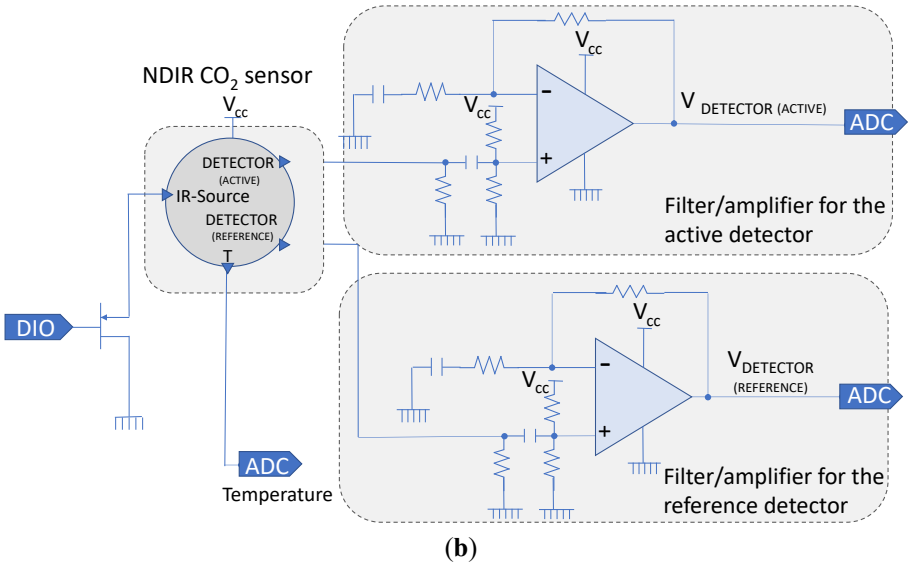

Figure 57. Front-end electronics of the (**a**) electrochemical O_2 sensor and the (**b**) NDIR CO_2 sensor.

The main board

The 'main board' housed the STM32L4Q5 MCU (ST microelectronics), the LoRa low-power transceiver module RFM95x equipped with a 2 dBi gain λ/8 antenna, the BMS, the environmental MEMS sensor BME280 (Bosch), the SWD ST Microelectronics proprietary programming interface and the UART TX-RX interface.

The environmental sensor provideed a digital output via I^2C or SPI for the measurement of temperature (1.2 °C accuracy), pressure (1.7 hPa accuracy) and RH (3% accuracy). The sensor was supplied at 3.3 V and provided 1 reading/s with a current absorption of 3.6 µA, in the presented application the average of 5 consecutive measurements was taken; 0.1 µA and 100 µA were the current absorptions respectively in sleep mode and for the I^2C communication bus.

The MCU with some active peripherals (i.e., I^2C, SPI, ADC, internal voltage reference, the needed GPIOs, two timers) sunk in run mode approximately 500 µA, whilst in sleep mode its current absorption dropped to 5 µA. It was programmed according to a sleep routine which periodically activated the MCU only for a limited time interval (120 s every hour) functional to the accomplishment of the firmware instructions, comprising the sampling of the three sensors, the processing of the data and the transmission via LoRaWAN of the hourly-collected samples every 8 h, hence with a rate of three transmissions per day. To avoid extra power consumption during the MCU sleep, one digital I/O port of the MCU was used to power the

CO_2 sensor front-end, switching it on just for the time needed to get a stable measurement (60 s).

The LoRa module was programmed according to the following radio settings: transmitting frequency 868 MHz, output power 14 dBm, CR 4/5, SF 7 and BW 125 kHz. The transceiver was powered at 3.3 V and in transmitting mode the current absorption reached 80 mA, after the transmission the device entered sleep mode with an absorption lower than <1 μA. Each LoRaWAN packet had a payload of 80 bytes, organized as 10 bytes per hour with 2 bytes of information for each one of the five measured physical quantities (i.e., temperature, RH, pressure, CO_2 and O_2 concentrations). The decision to use the lowest CR and SF was dictated by the need to favor the optimization of the power management to meet the low consumption requirement to the detriment of more reliable but also more consuming solutions. Indeed, SF 7 has the shortest ToA (~164 ms for 80 bytes payload size + 13 bytes overhead size) and the longest transmittable payload, with the drawback of the link margin reduction and the packet loss increase. However, these are relevant aspects especially in critical scenarios characterized by high noise and strong signal attenuation, which is not the case of a greenhouse deployment, where the radio coverage is supposed to be satisfactory.

Concerning the BMS, the nano-power DC-DC buck converter and boost charger module CJMCU-2557, based on the BQ25570 IC, was used. It dealt with the energy harvesting from the colored-spectrum lights and with the power supply of the entire system at 3.3 V. The internal MPPT functionality was set to $0.8\,V_{OC}$ which theoretically corresponds to the maximum power transfer condition for PV modules. More details about the BMS IC functioning are provided at the end of Section 3.3.

7.4. Tests and results

Several test campaigns were performed, when operating under the lighting treatments specified in Table VI, to prior characterize the used PV module under the selected light spectra and afterwards to evaluate the self-sufficiency of the node, whose architecture is described in Subsection 7.3.2. A proper test set-up was developed both for the characterization and the self-sufficiency testing.

7.4.1. Measurement set-up

During the measurement campaigns, the PV module was placed horizontally under the center of the lamps described in Subsection 7.3.1, at a fixed distance where the lighting was nominally uniform and setting the light source drivers so to have the desired (realistic) optical power impinging on the PV.

A Keithley 2401 source-electrometer was used to measure the I-V and P-V characteristics of the polycrystalline silicon PV module embedded in the node.

During the self-sufficiency tests on the complete node, the charge status of the onboard rechargeable Li-Po battery was monitored exploiting the same measurement set-up and technique used for the other self-sufficiency tests presented in this thesis (i.e., Subsections 4.3.1, 5.3.1 and 6.4.1). The battery voltage level was continuously acquired with sampling period of 1 s by using an Agilent 34410A multimeter (configured with 10 PLC and 6 ½ digit resolution) controlled via LabVIEW. Even in this case, the initial battery voltage level was set to approximately 3.9 V, i.e., in the range where the typical charge vs voltage characteristic for the battery is not flat, such that the voltage variation is a sufficient indication of the charge status of the battery. The uncertainty analysis presented in Subsection 4.3.1 remains valid for this test.

7.4.2. Solar cell characterization

The characteristic curves measured under the lighting treatments specified in Table VI are reported in Figure 58 while the main photovoltaic parameters extracted from the characterization are reported in Table VII.

The ratio between the peak power voltage, V_{MAX}, and the V_{OC} is also shown; in all the cases this value is around 70%, which is lower than the theoretical 80% generally corresponding to the point of maximum power transfer for solar cells and set by the MPPT algorithm of the BQ25570. This effect is related to the low FF% of the cells, in turn mainly due to the resistive contributions which cause the flattening of the I-V curves in low intensity conditions. The efficiency of the photovoltaic module is in the [5.4%, 6.4%] range, with highest values in case of BRFR; this is in line with the fact that the red and far-red light components belong to the range (peaked at 940 nm) where the spectral response of the polycrystalline silicon is higher. In the table, V_{MAX} and P_{MAX} are the voltages and the extracted powers at the peak point corresponding to $0.7V_{OC}$, while V_{OP} and P_{OP} are the voltages and the extracted powers at the operating point $0.8V_{OC}$; P_{inc} is the intensity measured by the Kipp & Zonen CMP3 pyranometer during the lighting protocol analysis reported in Subsection 7.3.1.

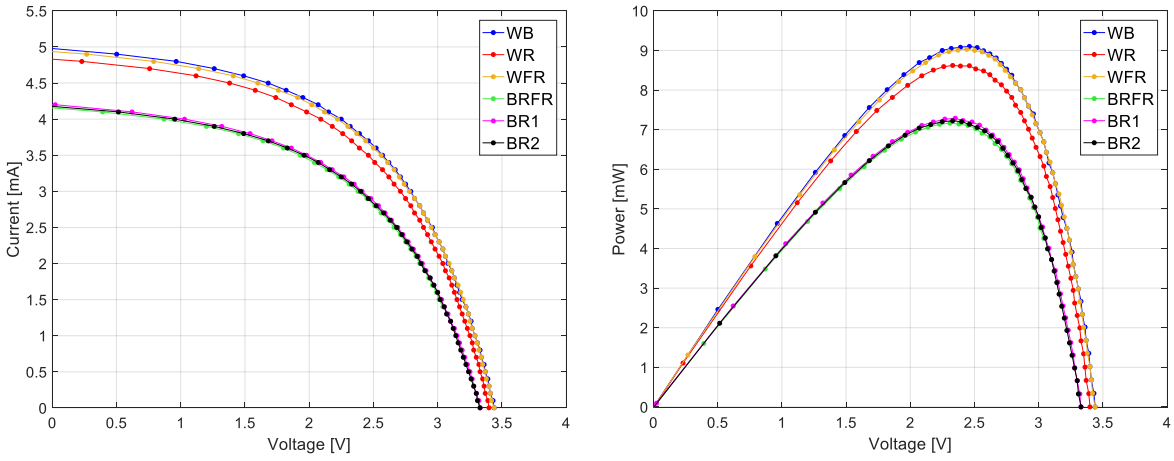

(a) **(b)**

Figure 58. (**a**) I-V and (**b**) P-V characteristics of the polycrystalline silicon PV module under the light spectra of Table VI.

Table VII. PV parameters extracted from the I-V and the P-V characteristics in the different lighting conditions, distinguishing between operating point ($0.8V_{OC}$) and peak point ($0.7V_{OC}$).

	WB	**WR**	**WFR**	**BRFR**	**BR1**	**BR2**
P_{inc} [W/m²]	36.00	33.00	32.00	23.00	24.00	24.00
I_{SC} [mA]	5.00	5.00	5.00	4.20	4.30	4.30
V_{OC} [V]	3.44	3.40	3.44	3.32	3.33	3.33
V_{MAX} [V]	2.46	2.33	2.44	2.31	2.35	2.33
V_{OP} [V]	2.75	2.72	2.75	2.66	2.66	2.66
V_{MAX}/V_{OC} %	72.00	68.00	71.00	70.00	71.00	70.00
P_{MAX} [mW]	9.09	8.62	9.02	7.16	7.27	7.22
P_{OP} [mW]	8.53	8.08	8.75	6.66	6.79	6.71
FF %	53.00	52.00	53.00	52.00	51.00	52.00
$Efficiency_{max}$ %	5.09	5.27	5.68	6.28	6.11	6.07
$Efficiency_{OP}$ %	4.78	4.94	5.51	5.84	5.70	5.64

7.4.3. Node self-sufficiency tests

One day-long tests were performed to prove the energy autonomy of the sensor node described in Subsection 7.3.2 under the six lighting protocols presented in Table VI considering 20 hd^{-1} of photoperiod.

The most energy-consuming activities are on one hand the LoRa radio transmissions, requiring working currents with peaks up to 80 mA but for a reduced time (~164 ms for each transmission, ~492 ms during the whole day considering 3 transmission per day), on the other hand the sampling of the CO_2 sensor, requiring working currents of ~26 mA for a total span of 1440 s (60 s for each sensor reading, repeated 24 times per day).

The first set of tests was performed using the solar simulator programmed to emit the three light spectra WB, WR and WFR, the second set of tests was performed using the commercial horticulture lamp programmed to give BR1, BR2 and BRFR spectra. The Li-Po battery voltage trends, V_{Li-Po}, during 24 h are shown in Figure 59a together with an inset reporting the same plots in the first 7200 s to highlight the charging slopes. The 20 h-long luminous periods and the 4 h-long dark periods can be distinguished: for each curve the twenty increasing segments correspond to the charging periods while the four decreasing parts are the hours of battery discharge in the absence of light; the equally spaced vertical lines are the absorption spikes caused by the CO_2 sensor readings which cause the lowering of the battery voltage for 60 s, the peaks corresponding to the LoRaWAN transmission cannot be appreciated because of their short duration and the low pass filtering action of the system.

In Figure 59b, the differences between the battery voltage level at the end and at the beginning of the six tests (ΔV_{Li-Po}) are reported: they are equal to 37 mV, 32 mV, 42 mV, 20 mV, 22 mV and 22 mV, respectively, for WB, WR, WFR, BRFR, BR1 and BR2 spectra. They show that a positive balance between battery charging and discharging is reached, and that the self-sufficiency of the system is achieved with all the tested spectra. In the tests containing the white component, a higher ΔV_{Li-Po} is attained: this can be justified considering that the incident powers P_{inc} are higher, although in general the efficiencies are lower than the ones achieved with the three spectra not exploiting the W component. Among the WB, WR and WFR spectra, the higher ΔV_{Li-Po} is the one obtained with the addition of FR light, thus validating the outcome derived from the polysilicon cell characterization. Indeed, although the three spectra are obtained by adding the same amount of B, R and FR μmol/m^{2}s and even though the blue light emissions carry more energy, the best result is obtained with the FR light, due to the maximum efficiency of the polycrystalline Si panel in this range. Concerning the other three spectra, the achieved ΔV_{Li-Po} is quite similar, in accordance with the P_{OP} and the operative efficiencies derived from the characterization.

Figure 59c shows the behavior of ΔV_{Li-Po} versus P_{OP}: the linear dependence is well-matched by the results of the six tests, especially by the WB, WR and WFR spectra which have higher P_{inc} and consequently higher P_{OP}. At lower P_{OP}, the results are still consistent with the fitting but slight variations from the linear trend can be noticed: these discrepancies can be modelled as a 3 mV error for the y-axis and 1% of P_{OP} error for the x-axis and can be justified with external factors affecting the battery charge, which are more detectable in presence of low operating powers and ΔV_{Li-Po} as in the case study.

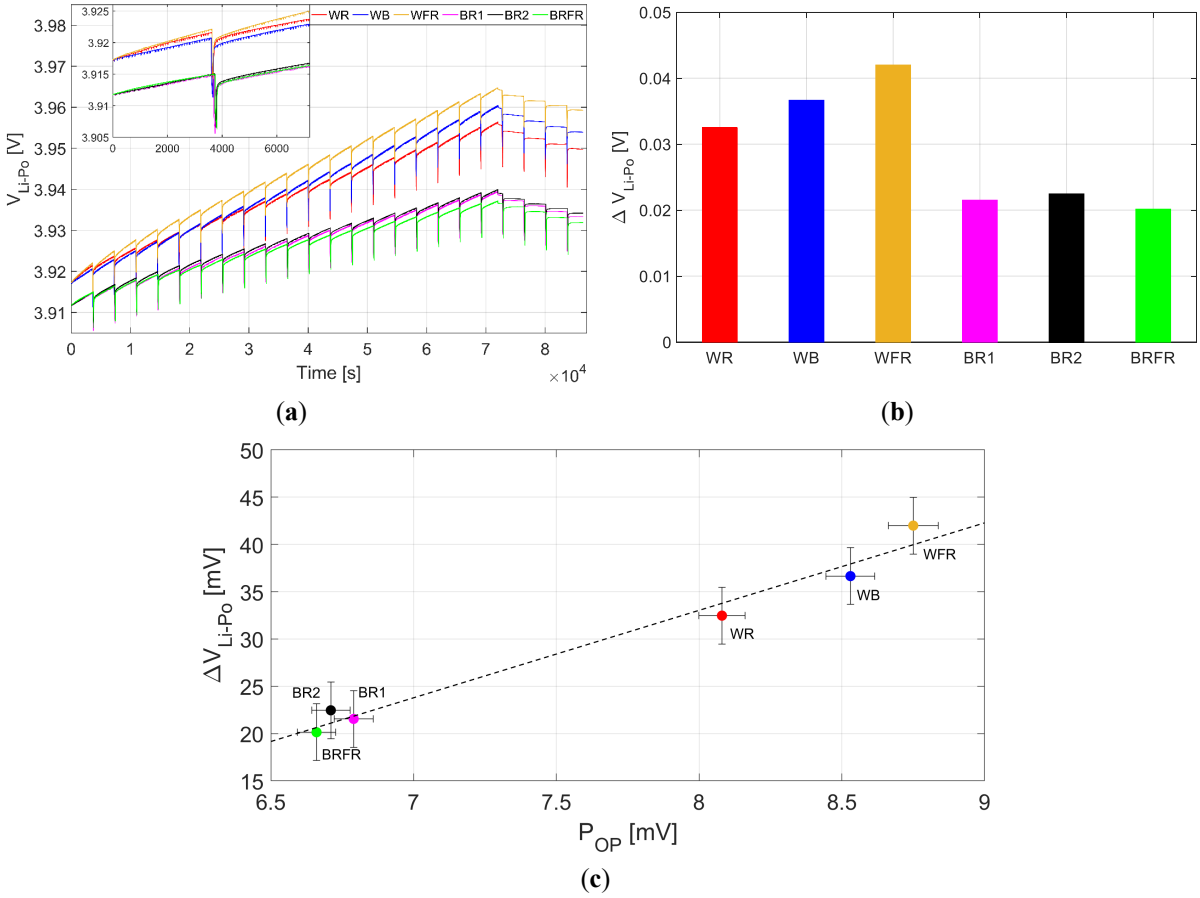

Figure 59. (**a**) Li-Po battery voltage, V_{Li-Po}, trends during 24 h tests with a photoperiod of 20 hd^{-1} employing the six light spectra of Table VI: WR (in red), WB (in blue), WFR (in yellow), BR1 (in magenta), BR2 (in black) and BRFR (in green). In the inset, the V_{Li-Po} trends during the first 7200 s are reported. (**b**) Difference between the battery voltage level at the end and at the beginning of the test, ΔV_{Li-Po}, under the six light spectra. (**c**) ΔV_{Li-Po} vs power output delivered by the PV module, P_{OP}, under the six light spectra: best fit shows a linear trend. The error on y-axis is fixed at 3 mV while the error on x-axis is 1% of P_{OP}.

The daily energy balance of the system between harvested and consumed energy is reported in Table VIII, identifying the contributions of the different parts composing the system. One reading of the sensors per hour and one data transmission every 8 h are assumed, while the current absorption of the BQ25570 is considered negligible with respect to the other contributions (in the order of hundreds of nA according to [125]). For the other electronic devices, the considered absorptions are those reported in Subsection 7.3.2. The maximum and minimum energies harvested by the PV panel during the 1 day-tests are also reported, respectively, under WFR and BRFR lighting protocols.

Table VIII. Daily energy balance of the system during the node operation, considering one reading of the sensors per hour and one data transmission every 8 h. The maximum and minimum harvested energies are computed, respectively, under WFR and BRFR lighting protocols.

	Component	**Energy per Day [J]**
Absorbed	O_2 (front-end)	1.1405
	CO_2 (front-end)	0.9504
	CO_2 (sensor)	124.0272
	BME280 (sensor)	0.0014
	I^2C bus	0.0396
	STM32L4Q5 (run mode)	4.7520
	STM32L4Q5 (stop mode)	1.3781
	RFM95x (run mode)	0.1299
	RFM95x (sleep mode)	0.2851
	TOT	132.7042
Harvested	PV module	Max 630.0000 Min 479.5200

As expected, the most energy-consuming activity of the node is the CO_2 sensor reading; therefore, the number of readings performed in a day is the critical factor affecting the energy self-sufficiency of the node. An energy surplus is obtained (i.e., 346.82 J in the minimum harvested energy case and 497.296 J in the maximum harvested energy case), which determines a net charge of the Li-Po battery. This implies that more frequent data collection and packet transmissions would be affordable with respect to those performed in the presented tests. Indeed, the maximum number of sensor readings and data transmissions per hour still guaranteeing the self-sufficiency of the node is three in the case of the minimum harvested energy and four in the case of the maximum harvested energy. However, in practice this estimation may be affected by additional losses, related to the non-ideality of the system,

which reduce the actual energy surplus. Assuming with a conservative approach that the surplus is halved, it follows that the maximum realistic number of sensor readings and transmissions per hour is two in both cases, hence it is approximately double compared with the protocol adopted during the tests. Given the fact that in this application timely data is not required, we assumed one measurement per hour to be an adequate sampling frequency for these preliminary tests. Moreover, the harvesting capability of the node can be further extended by resorting to higher PPFDs, as commonly employed in greenhouse deployments.

Conclusion

This thesis was focused on the development of self-sufficient low-power sensor nodes for monitoring tasks and exploiting different energy sources and harvesters. Two types of architectures were proposed, both provisioning energy from the surrounding environment, one operating just in the presence of the energy source and thus suitable for on-demand data collection, the other foreseeing a storage element on board which guarantees its functioning even in the absence of the energy source. An integrated approach was followed aimed at encompassing multiple aspects of the system as a whole, always accounting for the compliance with the low-power requirements. Firstly, the harvesting mechanism principles were investigated to guide the choice of the proper harvester depending on the available energy source; afterwards the careful selection of the hardware and software components was performed, also evaluating the actual performance of the employed radio technology in scenarios characterized by severe attenuation; finally, the energy autonomy of the system was analyzed in view of deploying install-and-forget pervasive monitoring sensor networks. The main challenging constraints were the low intensity of the exploited energy sources, the small amount of available harvested power (i.e., [μW, mW] range) and the coexistence of the ultra-low power requirement with some energy-consuming features as radio transmission and sensing.

The concrete realization of prototypes for different applications, even if starting from a common architecture, required the acquisition of heterogeneous knowledge belonging to different fields. In fact, depending on the developed prototype, the focus was placed on distinct aspects: the study of the energy source (as the preliminary lighting conditioning analysis reported in Chapters 5 and 7), the inspection of the transmission performance of the LoRa technology (as in Chapter 4 and in Appendix A [80, 81, 82]), the integration and the design of the sensors (as in Chapter 2 where the modeling and the characterization of the prototype soil moisture sensors were extensively treated [21, 22]) or the exploitation of the data acquired by the nodes during the in-field tests (as in Chapter 6 for the indoor localization task [126, 127]). Specifically, an RFID sensor tag for soil moisture measurements scavenging energy from the reader electromagnetic field [10, 11] and self-sufficient LoRaWAN-based sensor

nodes provisioning energy from thermoelectricity [30], diffused solar light [38], indoor white light [91] and artificial colored light [41, 43] were presented.

In some cases, the illustrated outcomes are the results of a preliminary analysis on the feasibility of quasi-real time data collection via LoRaWAN in conjunction with micro harvesting, as is the case of the activity of Chapter 4 dealing with the exploitation of thermoelectricity for supplying a general-purpose sensor node. In other cases, more advanced devices were designed tailored on specific applications such as the soil moisture monitoring, the indoor localization via artificial light and the measurement of environmental quantities in indoor greenhouses. In particular, regarding the sensor tag, the major efforts concerned the understanding of the chemical mechanisms of water vapor adsorption and conduction in the soil, functional to the electrical modeling of the sensors, and the design of front-ends compatible with the limitations imposed by the MCU and the small available power. The activity related to the indoor localization involved considerable challenges for the realization of a low-power receiver, capable of performing spectral analysis with a satisfactory level of accuracy, and for the conception of a localization strategy easily exportable into a MCU and based on a simplified calibration procedure. Concerning the prototype for indoor greenhouses, the major problems were encountered in the design of the multi-purpose node and especially in the integration of the CO_2 sensor, whose sampling was extremely onerous from the point of view of the power consumption.

Although self-sufficient IoT systems are widely present in the literature, in most cases the works address single aspects of the problem (e.g., the energy management, the programming strategies, the study of the harvester) and the different facets of the system are rarely studied as a whole. In this sense, the study of the transmission performance of LoRa technology via LoRaWAN protocol in extreme contexts like from underwater is one of the first presented in the literature. Moreover, some of the considered harvesting sources, such as the provisioning from artificial light with white and colored spectrum, are quite innovative, especially for applications in horticulture and indoor localization. Regarding this latter application, the development of a self-sufficient embedded node capable of self-locating by exploiting the same photovoltaic module both as harvester and as optical sensor represents a novelty in the scientific panorama. Similarly, the comparative study of the three different methodologies for the measure of soil moisture, especially the one that exploits the deposition of TiO_2 particles, is a novelty in the literature.

To conclude, the study presented in this thesis proved with promising results the feasibility of realizing complex wireless sensing solutions characterized by energy self-sufficiency feature, thus paving the way for the development of monitoring devices in all those contexts where the connection to the electricity grid and the human intervention are impractical. Possible future developments could consist in the realization of customized BMSs tailored on the specific applications and in the deployment of the designed prototypes in real operative scenarios, to evaluate their actual functioning and energy performance. Moreover, other harvesting sources can be studied in the future, following the same approach presented in this thesis.

Appendix A

LoRaWAN transmission analysis in critical environments

Although radio waves are known to be able to travel through water and ice, the aim of these studies is to demonstrate the feasibility of this transmission channel using low-cost off-the-shelf components and the employability of a LoRaWAN network for data acquisition in a plethora of applications where currently the real-time monitoring is not possible: these include superficial underwater sensor networks entailing the acquisition of biomedical parameters from water sports athletes as well from patients during water rehabilitation, the monitoring activities in rivers or lakes (e.g., fish-farming plants), the possibility of transmitting data from devices covered with ice. This preliminary investigation of the technology guided the choice of the most suitable radio configurations for the application scenarios proposed in this thesis and involving the design of autonomous sensor nodes, always seeking the compromise between performance and consumption optimization.

A.1. Electromagnetic transmission through lossy media and link budget model

An electromagnetic wave propagating in a generic lossy medium along z direction can be expressed as $\overrightarrow{E(z)} = E_0 e^{j\omega t - \gamma z} = E_0 e^{-\alpha z} e^{j(\omega t - \beta z)}$ [128, 129], where γ is the complex propagation constant accounting for the variations of the wave amplitude and phase during its propagation through the medium. The real component α is the attenuation coefficient, related to the wave amplitude decay; the imaginary component β is the phase constant, linked to the wave phase speed. The propagation constant has the following extended expression $\gamma = j\omega\sqrt{\tilde{\epsilon}\mu} = j\omega\sqrt{\mu(\epsilon' - j\epsilon'')} = j\omega\sqrt{\mu\epsilon\left(1 - j\frac{\sigma}{\omega\epsilon}\right)} = \alpha + j\beta$ where the magnetic permeability is defined as $\mu = \mu_0\mu_r = 4\pi \times 10^{-7}\text{H/m} \times \mu_r = 1.2566 \times 10^{-6}\text{ H/m} \times \mu_r$ with $\mu_r = 1$ in case

of non-magnetic medium (e.g., water and ice), the electrical permittivity of the lossy medium is defined as $\tilde{\epsilon} = \epsilon_0 \widetilde{\epsilon_r} = \epsilon_0(\epsilon_r' - j\epsilon_r'') = \epsilon - j\frac{\sigma}{\omega} = \epsilon' - j\epsilon''$and σ is the electrical conductivity of the medium in S/m. The real part $\epsilon' = \epsilon = \epsilon_0\epsilon_r'$ is related to the degree of polarization of the medium while the imaginary part $\epsilon'' = \epsilon_0\epsilon_r'' = \frac{\sigma}{\omega}$ concerns the losses inside the material. Moreover, the complex relative permittivity $\widetilde{\epsilon_r}$ has a dependence on conductivity and working frequency and therefore on factors such as salinity content and temperature. The components α and β employed in the model of the radio frequency channel can be computed as

$$\alpha = \frac{2\pi c}{\lambda_0}\sqrt{\frac{\mu\epsilon'}{2}\left(\sqrt{1+\left(\frac{\epsilon''}{\epsilon'}\right)^2}-1\right)} = \omega\sqrt{\frac{\mu\epsilon'}{2}\left(\sqrt{1+\left(\frac{\sigma}{\omega\epsilon'}\right)^2}-1\right)}\frac{1}{m} \quad (17)$$

$$\beta = \frac{2\pi c}{\lambda_0}\sqrt{\frac{\mu\epsilon'}{2}\left(\sqrt{1+\left(\frac{\epsilon''}{\epsilon'}\right)^2}+1\right)} = \omega\sqrt{\frac{\mu\epsilon'}{2}\left(\sqrt{1+\left(\frac{\sigma}{\omega\epsilon'}\right)^2}+1\right)}\frac{rad}{m} \quad (18)$$

In the situations analyzed in the following, the electromagnetic transmission is performed from inside a medium (i.e., fresh water and a block of ice) to the outside (i.e., air), therefore the reflective phenomena at the crossing of the medium-air surface must be accounted, since the two media have different refractive indexes (i.e. $n_{medium} = \sqrt{\epsilon_r'}$ and n_{air}=1.0003). In particular, in case of orthogonal incidence, the reflection and the transmission coefficients are defined as $\Gamma = \frac{\eta_{air}-\eta_{medium}}{\eta_{air}+\eta_{medium}}$ and $\tau = \frac{2\eta_{air}}{\eta_{air}+\eta_{medium}}$ where η_{air} and η_{medium} are the complex intrinsic impedances of the media computed as $\eta = \sqrt{\frac{j\omega\mu}{(j\omega\epsilon'+\sigma)}}\ \Omega$.

This theoretical analysis of the electromagnetic transmission across a lossy medium can be used to investigate the link budget model from the transmitter to the receiver considering both the propagation in medium and in air, with particular attention toward the path loss estimation, dependent on the crossed medium [130, 131, 132]. In particular, the total path loss (in dB) can be computed as $PL_{tot} = PL_{UM} + PL_{UM-AM} + PL_{AM} + PL_M$, where PL_{UM} concerns the losses experienced in the medium, PL_{UM-AM} accounts for the losses due to the reflections at the medium-air interface, PL_{AM} refers to the free space loss and PL_M is the term linked to the miscellaneous losses due to various sources (e.g., indoor noise, antenna mismatch). In more detail, $PL_{UM-AM} = 10\log_{10}(|\tau|^2 Re\{\frac{\eta_{medium}}{\eta_{air}}\})^{-1}$and depends on the

transmission coefficient at the interface τ and therefore on the intrinsic impedance mismatch between the two media; $PL_{AI} = 20\log_{10}\frac{4\pi\, d_{AM}}{\lambda_0} = 20\log_{10} d_{AM} + 20\log_{10} f - 147.5$ with f working frequency in Hz, d_{AM} distance in m travelled above the medium and λ_0 =0.3454 m wavelength in free air; finally $PL_{UI} = 10\log_{10} e^{2\alpha d_{UM}} + 20\log_{10}\frac{\lambda_0}{\lambda_{UM}} + 20\log_{10}\frac{4\pi\, d_{UM}}{\lambda_0} = 6 + 8.69\alpha d_{UM} + 20\log_{10} d_{UM} + 20\log_{10}\beta$ where d_{UM} is the distance in m travelled inside the medium before reaching the medium-air interface and λ_{UM} is the wavelength in the medium in m.

The attenuation and the phase coefficients α and β are obtained from Equations (17) and (18), once the two quantities ϵ_r' and ϵ_r'' are known. To this aim, the complex relative permittivity of the considered medium was computed following the model proposed by the International Telecommunication Union (ITU) in [133], which is valid for frequencies up to 10^3 GHz. Once the total path loss is estimated, the link budget can be computed as $P_R = P_T + G_R + G_T - PL_{tot}$ where P_r is the RSSI in dBm. Note that in the experimental verification of such model, the RSSI will be the power detected by the gateway downstream of the demodulation, whereas P_T is the transmitted power (i.e., 14 dBm), and G_R and G_T are the receiving and the transmitting antenna gains in dBi.

The complex relative permittivity for fresh water is derived as $\epsilon_r' = \frac{\epsilon_s - \epsilon_1}{1+\left(\frac{f_{GHz}}{f_1}\right)^2} + \frac{\epsilon_1 - \epsilon_\infty}{1+\left(\frac{f_{GHz}}{f_2}\right)^2} + \epsilon_\infty$ and $\epsilon_r'' = \frac{\left(\frac{f_{GHz}}{f_1}\right)(\epsilon_s - \epsilon_1)}{1+\left(\frac{f_{GHz}}{f_1}\right)^2} + \frac{\left(\frac{f_{GHz}}{f_2}\right)(\epsilon_1 - \epsilon_\infty)}{1+\left(\frac{f_{GHz}}{f_2}\right)^2}$ as a function of the working frequency in GHz, f_{GHz}, and of the operating temperature in Celsius, T. The terms ϵ_1, ϵ_s, ϵ_∞ are dimensionless numbers while f_1, f_2 are in GHz; they are computed as $\epsilon_s = 77.66 + 103.3$, $\epsilon_1 = 0.0671\epsilon_s$, $\epsilon_\infty = 3.52 - 7.52$, $f_1 = 20.20 - 146.4\Theta + 316\Theta^2$ GHz, $f_2 = 39.8 f_1$ GHz with $\Theta = \frac{300}{T+273.15} - 1$.

The complex relative permittivity for dry ice is derived as $\epsilon_r' = 3.1884 + 0.00091T$ and $\epsilon_r'' = \frac{A}{f_{GHz}} + B f_{GHz}$. The terms A and B are obtained as $A = (0.00504 + 0.0062 \cdot \Theta)e^{-22.1\Theta}$ and $B = \frac{0.0207}{T+273.15}\frac{e^{-t}}{(e^{-t}-1)^2} + 1.16\times 10^{-11} f_{GHz}^2 + e^{-9.963+0.0372T}$ with $t = \frac{335}{T+273.15}$ and Θ is computed as in water case. Even if the ITU model is thought for the modelling of the electric characteristic of dry ice (i.e., ice composed of frozen pure water), we can assume that the computed relative permittivity is a good approximation of the real one since the fresh water employed for the tests had a reduced content of impurities.

A.2. Under water to above water transmission

In this Section, the preliminary studies about the LoRa transmission, relied on the LoRaWAN protocol, in the radio channel from under fresh water to above water are presented. The experimental results, collected during a measurement campaign in a swimming pool, are compared with the outcomes of the theoretical model described in Section A.1, considering fresh water as transmission medium.

A.2.1 System architecture and measurement set-up

An experimental set-up based on a LoRaWAN sensor node positioned inside a waterproof IP68 ABS plastic box was developed. The sensor node was composed of a ATtiny84 microcontroller by Microchip connected to a RFM95x LoRa transceiver equipped with a 2 dBi gain λ/4 whip antenna. To ease the testing of the LoRaWAN node at several underwater depths, a plastic structure with aluminum ballasts was realized. The vertical elements were graded and allowed easy movement of the box containing the sensor node at the pre-set depth, reaching a maximum possible depth of 2 m. The distances between node and gateway were measured using a measurement tape with ± 0.1 cm of accuracy, however considering the difficult in taking measurements in water we can assume an accuracy of ± 2 cm up to the depth of 60 cm and an accuracy of ± 5 cm for depths greater than 60 cm.

The transmission tests were performed in a swimming pool with dimensions 14 m × 7 m: the gateway was in an elevated position at 100 ±2 cm and in line of sight with the sensor node, which was at 300 ±2 cm from the poolside, thus giving a $d_{AM} = d_{AW} = 316$ ±2 cm. We decided to keep the gateway as close as possible to the transmitter to lower the free space loss contribution, which is easily predictable, and to evaluate the maximum performance of the portion of the channel under the water surface. At the moment of the tests, the water level in the swimming pool was equal to 150 ±2 cm (fluctuations in this value have to be taken into account due to the intrinsic instability of the water surface). The absence of people inside the pool, the lack of wind and the shutdown of the water handling systems, made it possible to perform measurements with an almost flat-water surface and with diminished miscellaneous environmental noise.

A.2.1 Tests and results

Field tests were performed at different depths d_{UW} and with different radio settings obtained changing SF, CR and BW to evaluate their effect on the transmission performance and to find the maximum reachable underwater depth still guaranteeing the packets reception. For each radio configuration and each tested depth, 300 packets with constant packet length of 38 Bytes and power output of 14 dBm were sent, then the PLs were computed and the RSSIs and the SNRs were collected and evaluated in terms of mean and standard deviation. The eight tested radio configurations are resumed in Table IX; not all the SF and the CR were considered, in fact, testing these 3 SF and the lowest and the highest CR gives a thorough evaluation of the LoRaWAN transmission capability.

Table IX. Radio configurations adopted to test the node at variable d_{UW}.

Radio Configuration	SF	BW [kHz]	CR
1	7	125	4/5
2			4/8
3	7	250	4/5
4			4/8
5	10	125	4/5
6		125	4/8
7	12	125	4/5
8		125	4/8

The transmission node was lowered in steps of 20 ±2 cm starting from the water surface (i.e., 0 ±2 cm) until the maximum depth at which no transmission happened (i.e., 120 ±5 cm). Consequently, the tested depths were $d_{UW} = 0$ ±2 cm, 20 ±2 cm, 40 ±2 cm, 60 ±2 cm, 80 ±5 cm, 100 ±5 cm and 110 ±5 cm, that is the last depth at which some packets were still received by the gateway. The results are reported in Figure 60, Figure 61 and Figure 62 that show respectively mean values and standard deviations of RSSIs and SNRs and PL percentages for the eight radio settings at each underwater depth.

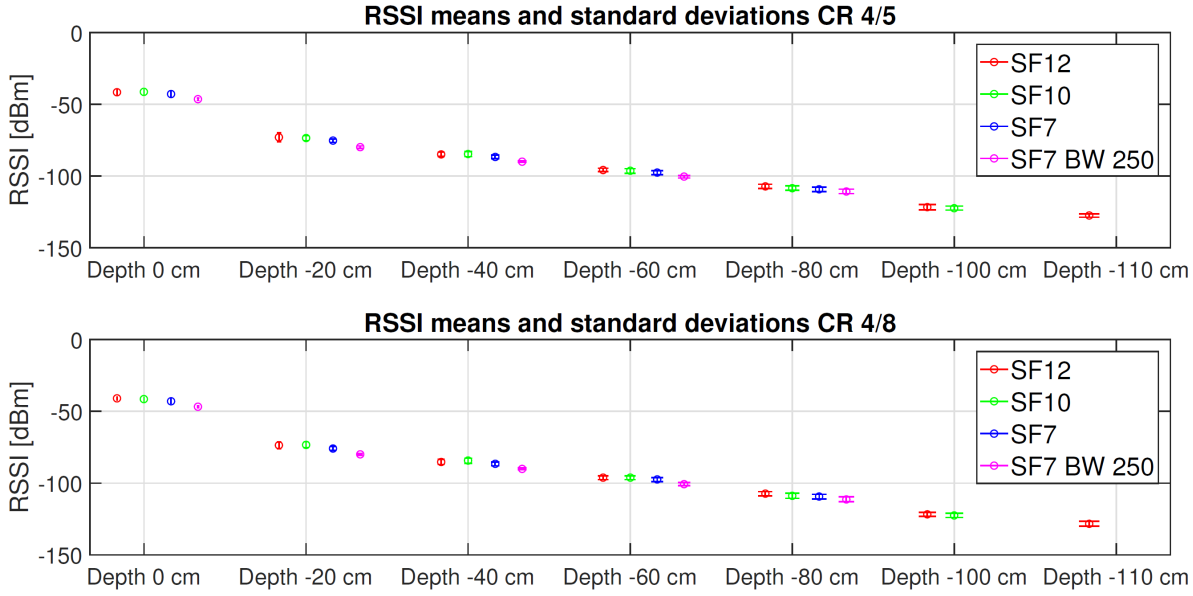

Figure 60. RSSI mean values and standard deviations for d_{UW} varying from 0 ±2 cm to 110 ±5 cm. Upper plot: configurations 1,3,5,7 of Table IX; lower plot: configurations 2,4,6,8 of Table IX.

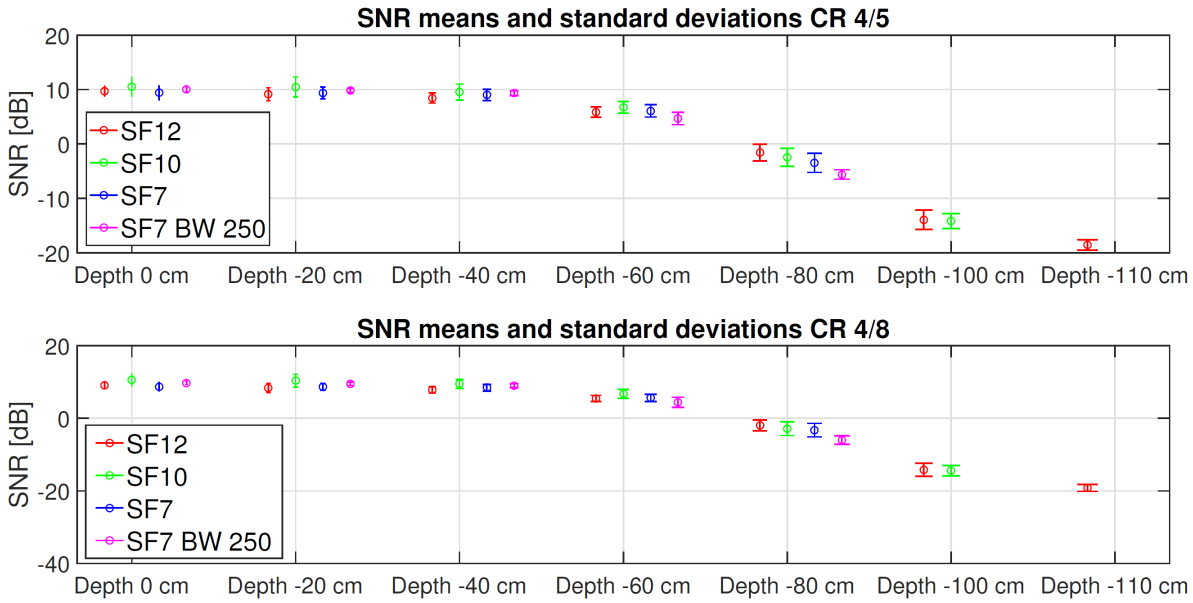

Figure 61. SNR mean values and standard deviations for d_{UW} varying from 0 ±2 cm to 110 ±5 cm. Upper plot: configurations 1,3,5,7 of Table IX; lower plot: configurations 2,4,6,8 of Table IX.

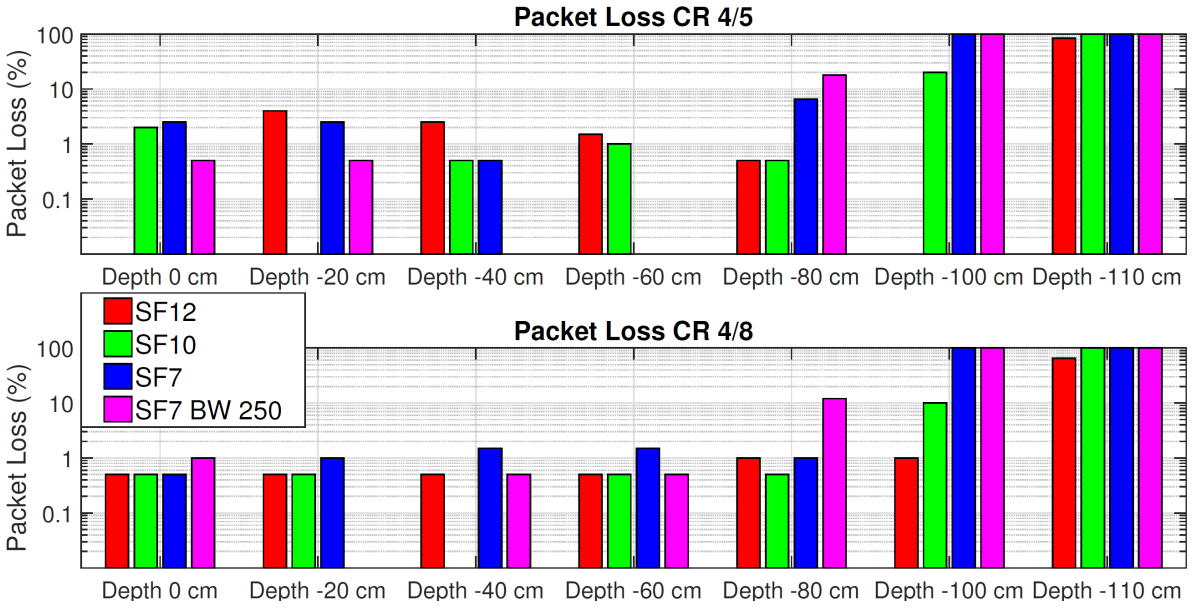

Figure 62. PL percentage for d_{UW} varying from 0 ±2 cm to 110 ±5 cm. Upper plot: configurations 1,3,5,7 of Table IX; lower plot: configurations 2,4,6,8 of Table IX.

These results confirm what was expected from the theory: the RSSI will not be significantly affected by the SF and the CR, and at critical depths below 80 ±5 cm the PL will be slightly lower in the CR=4/8 case since it guarantees a better error decoding at the receiver side. However, given that the performances of the two CRs are comparable, CR=4/5 is in general preferable since a lower CR causes also greater power consumption. Another aspect confirmed by practice is the one related to the 250 kHz bandwidth in the case SF=7 which, entailing the introduction of greater noise in the band, determines a higher PL and a lower SNR for depths higher than 80 ±5 cm. Moreover, moving from $d_{UW} = 60$ ±2 cm to $d_{UW} =$ 110 ±5 cm there is a significant worsening of the noise level in the radio channel, which compromises the success of the radio transmission at the following depth $d_{UW} = 120$ ±5 cm for all the three SFs tested, although there is still link margin available. For this reason, we decided to test the intermediate height of $d_{UW} = 110$ ±5 cm where the transmission was still feasible at SF=12 and 10, although in this last case we were very close to the maximum SNR limit, but it was no longer feasible at SF=7, probably because both the sensitivity and the SNR limits were violated.

Hence, for depths higher than $d_{UW} = 80$ ±5 cm, the performances of the LoRaWAN transmission are strongly degraded, especially for lower SF, with RSSI and SNR average

values very close to the theoretical constraints on the gateway sensitivity and noise floor level. However, the fact that the transmission is still reliable in such poor conditions, highlights the robustness of the LoRa modulation which has its strengths in the extremely high receiver sensitivity (–126 dBm for SF 7 and –137 for SF 12) and in its capability of correct demodulation even in presence of very noisy channels (noise limit –7.5 dB for SF 7 and –20 dB for SF 12). Furthermore, as expected, the PL increases as the SF decreases, but it remains compatible with systematic losses of the radio channel for all the SFs up to $d_{UW} = 60 \pm 2$ cm and still acceptable at $d_{UW} = 80 \pm 5$ cm. Once the depth $d_{UW} = 80 \pm 5$ cm is exceeded, the PL drastically increases for the SF 7, as it reaches the limit values of RSSI and SNR, while it remains below the 20% for the other two tested SFs.

At the considered operating conditions T = 20 °C, f = 868 MHz and fresh water as transmission medium, the formulas presented in Section A.1. become τ=1.8 for the transmission coefficient, $\eta_{medium} = \eta_{water} = 42.13\ \Omega$ and η_{air} =376.73 Ω for the intrinsic impedances of water and air, ϵ_r' =79.88 and ϵ_r'' =3.82 for the complex relative permittivity and consequently α=3.88 1/m and β=162.58 rad/m.

In Figure 63, the link budget trend obtained from the mathematical modelling (magenta plot) is reported with the RSSI actually measured during the tests and computed at each depth as the average of the three SFs in the case CR=4/5 (blue plot); the horizontal (in blue) and the vertical error bars (in red) are added to highlight the different uncertainty contributions. The horizontal ones account for the uncertainty experienced in the distance measurements (±2 cm up to $d_{UW} = 60$ cm and ±5 cm for d_{UW} greater than 80 cm).

It can be noticed a significant agreement between the two trends up to $d_{UW} = 60 \pm 2$ cm, then moving to lower depths the discrepancy between mathematical model and measured results increases up to ∼10 dBm of error for depths greater than 80 ±5 cm. This can be caused by factors that cannot be easily quantified such as the possible presence of miscellaneous losses, the reflections of the radio signal caused by the bottom of the pool and the greater imprecision in the demodulation phase due to the low reached SNR since for depths higher than $d_{UW} = 80 \pm 5$ cm, there is a significant degradation of the performance of the LoRaWAN transmission. Obviously, these results strongly depend on the considered test scenario because the presence of factors determining additional miscellaneous losses can lead to the degradation of the received signal strength, thus reducing the link margin and the maximum reachable depth.

The SF with the best performance is the 12 which, however, has higher power consumption. Therefore, depending on the type of application, it is advisable to select the lowest SF which allows a PL compatible with the required specifications and a good link margin on the RSSI. In the tests we performed, the SF=10 can be considered a good compromise, assuming satisfactory a PL lower than 20%.

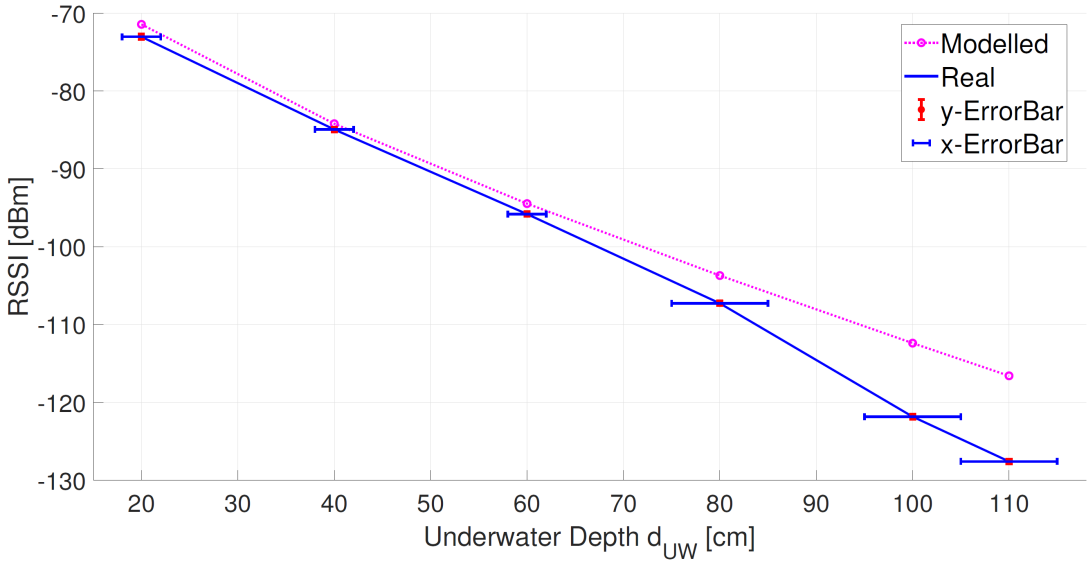

Figure 63. Comparison between the RSSI at the receiver side modelled according to the link budget equation (magenta line) and the RSSI measured during the tests (blue line) as a function of the underwater depth d_{UW}. Vertical (in red) and horizontal (in blue) error bars are added to the measured values.

A.3. Under ice to above ice transmission

In this Section, the capability of transmitting using LoRa technology and LoRaWAN protocol from a thick layer of ice was investigated. As in the underwater to above water channel, the experimental results are compared with the outcomes of the theoretical model described in Section A.1 assuming fresh ice as transmission medium.

A.3.1 System architecture and measurement set-up

The transmitter node was composed of an RFM95 LoRa transceiver equipped with a 2 dBi gain λ/8 dipole antenna and an ATtiny84 MCU. The tests were performed by

encapsulating it in a small IP68 enclosure, that was in turn submerged at the centre of a plastic bucket filled up with water. Afterwards, the water inside the bucket was frozen employing an ACS Angelantoni HYGROS 250 environmental chamber to reach a 10 cm-thick layer of ice around the transmitter box, thus $d_{UM} = d_{UI} = 0.1$ m. The receiver is a LG308 Dragino located at 1 m from the chamber window and at 1.1 m from the plastic bucket containing the receiver thus giving $d_{AM} = d_{AI} = 1.1$ m. We decided to keep the receiver and the transmitter at close distance to avoid the disturbances and the spurious interferences caused by the industrial environment used for the tests.

A.3.2 Tests and results

The transmission tests were performed by sending 500 LoRaWAN packets for each SF from 7 to 12 and with CR=4/5, then RSSIs, SNRs and PL have been collected and RSSIs and SNRs mean and standard deviation were computed to thoroughly investigate the system performance. The results are presented in Table X: the RSSI mean values settle around an average quantity of ∼66 dBm regardless of the variation in the SF. The packet loss is ∼0% for every SF and this aspect is also confirmed by the RSSIs well above the receiver sensitivity, and by the positive SNR mean values.

Table X. RSSIs and SNRs mean values and standard deviations and PLs for the under ice transmissions at d_{UI}= 0.1 m.

SF	RSSI		SNR [dB]		PL [%]
	μ_{RSSI} [dBm]	σ_{RSSI}[dB]	μ_{SNR}	σ_{SNR}	
7	–64.88	3.43	8.46	1.31	0
8	–65.18	3.36	9.90	1.28	0.8
9	–64.95	3.78	9.23	1.60	0
10	–65.48	4.39	7.97	1.39	0
11	–69.99	7.78	8.13	0.90	0
12	–66.36	7.91	6.90	1.28	0.2

At the operating conditions T = –10 °C, f = 868 MHz and fresh ice as transmission medium, the formulas presented in Subsection A.1 become τ=1.27 for the transmission coefficient, $\eta_{medium} = \eta_{ice} = 211.29\ \Omega$ and $\eta_{air} = 376.73\ \Omega$ for the intrinsic impedances of

ice and air, $\epsilon_r' = 3.18$ and $\epsilon_r'' = 3.73 \times 10^{-4}$ for the complex relative permittivity and consequently α=1.9 $\times 10^{-3}$ 1/m and β= 32.44 rad/m.

Applying the link budget model previously described under the assumption d_{AI} =1.1 m, the RSSI trend of Figure 64 can be obtained as a function of the under ice depth d_{UM} (steps of 5 cm). At the depth of interest, the RSSI is ~–30.65 dBm. The test result turns out to be worse than the estimate: this discrepancy was probably induced by the miscellaneous losses L_M not accounted in the path loss modelling and due to the additional dispersive phenomena caused by the industrial indoor environment which is characterized by several obstacles. One way to experimentally estimate these losses was to test the system under the same conditions but in the absence of ice, thus finding an attenuation value related to the test environment equal to L_M ≃32 dBm. Computing again the link budget equation accounting for the L_M, a new RSSI ~63 dBm is found, which deviates from the experimental result of less than 3 dBm, thus showing a good agreement with the prediction.

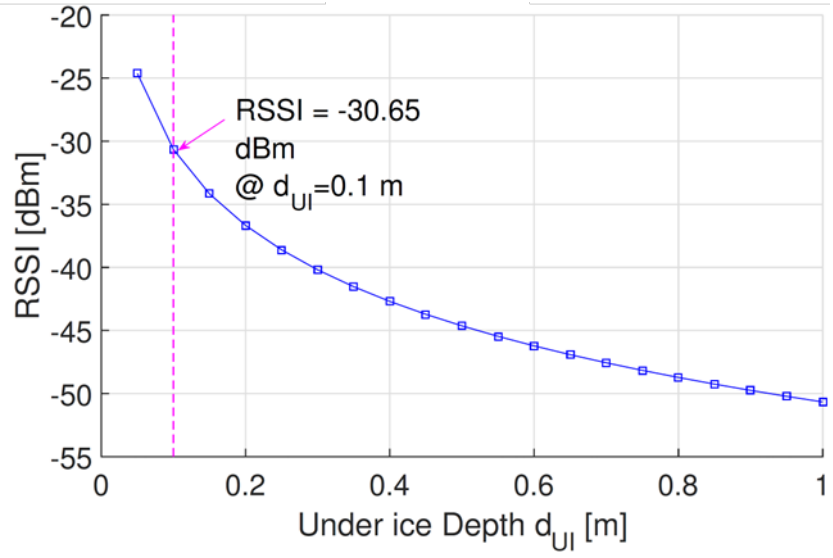

Figure 64. Link budget model of radio frequency transmission from under ice to above ice as a function of the under ice depth d_{UI}.

Bibliography

[1] "Global Digital Snapshot," [Online]. Available: https://datareportal.com/reports/digital-2021-global-overview-report. [Accessed October 2022].

[2] "IEA, Global Energy Review 2021, IEA, Paris," [Online]. Available: https://www.iea.org/reports/global-energy-review-2021. [Accessed October 2022].

[3] J. A. Ekchian, R. W. Hoffman, L. Ekchian and K. J. Gabriel, "Item identification tag for rapid inventory data acquisition system". U.S. Patent 4.862.160, 1989.

[4] J. L. Excoffer and L. E. Ehrlich, "Sample identification utilizing RFID tags". U.S. Patent 7.275.682, 2007.

[5] L. M. Ni, D. Zhang and M. R. Souryal, "RFID-based localization and tracking technologies," *IEEE Wireless Communications,* vol. 18, no. 2, pp. 45-51, 2011.

[6] A. Provotorov, D. Privezentsev and A. Astafiev, "A. Development of methods for determining the locations of large industrial goods during transportation on the basis of RFID," *Procedia engineering,* vol. 129, pp. 1005-1009, 2015.

[7] K. Finkenzeller, RFID handbook: fundamentals and applications in contactless smart cards, radio frequency identification and near-field communication, John Wiley & Sons, 2010.

[8] D. Paret, Design Constraints for NFC Devices, John Wiley & Sons, 2016.

[9] "ISO Organization," [Online]. Available: https://www.iso.org/home.html. [Accessed October 2022].

[10] I. Cappelli, A. Fort , M. Mugnaini, E. Panzardi, A. Pozzebon, M. Tani and V. Vignoli, "Battery-less HF RFID sensor tag for humidity measurements based on TiO2 nanoparticles," in *2020 IEEE International Instrumentation and Measurement Technology Conference (I2MTC)*, Virtual conference, May 2020.

[11] I. Cappelli, A. Fort, M. Mugnaini, E. Panzardi, A. Pozzebon, M. Tani and V. Vignoli, "Battery-less HF RFID sensor tag for soil moisture measurements," *IEEE Transactions on Instrumentation and Measurement,* vol. 70, pp. 1-13, 2020.

[12] S. Kim, T. Le, M. M. Tentzeris, A. Harrabi, A. Collado and A. Georgiadis, “An RFID-enabled inkjet-printed soil moisture sensor on paper for ‘smart’ agricultural applications,” in *IEEE Sensors*, Valencia, Spain, November 2014.

[13] N. S. S. M. Da Fonseca, R. C. S. Freire, A. Batista, G. Fontgalland and S. Tedjini, “A passive capacitive soil moisture and environment temperature UHF RFID based sensor for low cost agricultural applications,” in *2017 SBMO/IEEE MTT-S International Microwave and Optoelectronics Conference (IMOC)*, Águas de Lindóia, Brazil, August 2017.

[14] B. Stoddard, D. J. Selker and D. C. Udell, “Examining the effectiveness of commercial RFID tags as soil moisture sensors,” in *AGU Fall Meeting*, New Orleans, US, December 2017.

[15] J. F. Posada , J. J. Liou and R. N. Miller, “An automated data acquisition system for modeling the characteristics of a soil moisture sensor,” *IEEE transactions on instrumentation and measurement,* vol. 40, no. 5, pp. 836-841, 1991.

[16] W. Zhou, Z. Xu, D. Ross, J. Dignan, Y. Fan and Y. Hua, “Towards water-saving irrigation methodology: Field test of soil moisture profiling using flat thin mm-sized soil moisture sensors (MSMSs),” *Sensors and Actuators B: Chemical,* vol. 298, p. 12685, 2019.

[17] NXP, I2C-bus specification and user manual, 2014.

[18] T. Addabbo, A. Fort, M. Mugnaini, V. Vignoli and M. Bruzzi, “Quartz-crystal microbalance gas sensors based on TiO2 nanoparticles,” *IEEE Transactions on Instrumentation and Measurement,* vol. 67, no. 3, pp. 722-730, 2018.

[19] E. Barsotti, S. Tan, S. Saraji, M. Piri and J. H. Chen, “A review on capillary condensation in nanoporous media: Implications for hydrocarbon recovery from tight reservoirs,” *Fuel,* vol. 184, p. 344–361, 2016.

[20] P. Faia, A. Ferreira and C. Furtado, “Establishing and interpreting an electrical circuit representing a TiO2–WO3 series of humidity thick film sensors.,” *Sensors and Actuators B: Chemical,* vol. 140, no. 1, p. 128–133, 2009.

[21] I. Cappelli, A. Fort, A. Lo Grasso, E. Panzardi, M. Mugnaini and V. Vignoli, “RH sensing by means of TiO2 nanoparticles: A comparison among different sensing techniques based on modeling and chemical/physical interpretation,” *Chemosensors,* vol. 8, no. 4, 2020.

[22] T. Addabbo, I. Cappelli, A. Fort, M. Mugnaini, E. Panzardi, V. Vignoli and C. Viti, "The Effect of Au Nanoparticle Addition on Humidity Sensing with Ultra-Small TiO2 Nanoparticles," *Chemosensors,* vol. 9, no. 7, p. 170, 2021.

[23] B. Torún, C. Kunze, C. Zhang, T. Kuhne and G. Grundmeier, "Study of water adsorption and capillary bridge formation for SiO2 nanoparticle layers by means of a combined in situ FT-IR reflection spectroscopy and QCM-D set-up.," *Physical Chemistry Chemical Physics,* vol. 16, p. 7377–7384, 2014.

[24] R. Porretta and F. Bianchi , "Profiles of relative permittivity and electrical conductivity from unsaturated soil water content models," *Annals of Geophysics,* vol. 59, no. 3, 2016.

[25] J. Gakkestad and L. Hanssen, "Powering wireless sensor networks nodes in Northern Europe using Solar cell panel for energy harvesting," in *Proceedings of 4th IFIP International Conference on New Technologies, Mobility and Security*, Paris, France, February 2011.

[26] H. Sharma, A. Haque and Z. A. Jaffery, "Solar energy harvesting wireless sensor network nodes: A survey," *Journal of Renewable and Sustainable Energy,* vol. 10, no. 2, p. 023704, 2018.

[27] A. Jushi, A. Pegatoquet and T. N. Le, "Wind energy harvesting for autonomous wireless sensor networks," in *2016 Euromicro Conference on Digital System Design (DSD)*, Limassol, Cyprus, August 2016.

[28] A. Chandrasekhar, V. Vivekananthan and S. Kim, "A fully packed spheroidal hybrid generator for water wave energy harvesting and self-powered position tracking," *Nano Energy,* vol. 69, p. 104439, 2020.

[29] A. Casi, M. Araiz, L. Catalan and D. Astrain, "Thermoelectric heat recovery in a real industry: From laboratory optimization to reality," *Applied Thermal Engineering,* vol. 184, p. 116275, 2021.

[30] I. Cappelli, S. Parrino, A. Pozzebon and A. Salta, "Providing Energy Self-Sufficiency to LoRaWAN Nodes by Means of Thermoelectric Generators (TEGs)-Based Energy Harvesting," *Energies,* vol. 14, no. 21, p. 7322, 2021.

[31] S. Chamanian, H. Uluşan, Ö. Zorlu, S. Baghaee, E. Uysal-Biyikoglu and H. Külah, "Wearable battery-less wireless sensor network with electromagnetic energy harvesting system," *Sensors and Actuators A: Physical,* vol. 249, pp. 77-84, 2016.

[32] S. Farhangdoust, C. Mederos, B. Farkiani, A. Mehrabi, H. Taheri and D. Younesian, "A creative vibration energy harvesting system to support a self-powered internet of thing (IoT) network in smart bridge monitoring," in *Proceedings of ASME International Mechanical 588 Engineering Congress and Exposition*, Virtual conference, November 2020.

[33] O. Rubes, J. Chalupa, F. Ksica and Z. Hadas, "Development and experimental validation of self-powered wireless vibration sensor node using vibration energy harvester," *Mechanical Systems and Signal Processing,* vol. 160, p. 107890, 2021.

[34] U. Muncuk, K. Alemdar, J. D. Sarode and K. R. Chowdhury, "Multiband ambient RF energy harvesting circuit design for enabling 590 batteryless sensors and IoT," *IEEE Internet of Things Journal,* vol. 5, no. 4, pp. 2700-2714, 2018.

[35] A. Mecocci, G. Peruzzi, A. Pozzebon and P. Vaccarella, "Architecture of a hydroelectrically powered wireless sensor node for underground environmental monitoring," *IET Wireless Sensor Systems,* vol. 7, no. 5, pp. 123-129, 2017.

[36] E. Osorio de la Rosa, J. Vázquez Castillo, M. Carmona Campos, G. R. Barbosa Pool, G. Becerra Nuñez, A. Castillo Atoche and J. Ortegón Aguilar, "Plant microbial fuel cells–based energy harvester system for self-powered IoT applications," *Sensors,* 2019.

[37] M. A. Saeed, H. C. Kang, K. A. F. K. Yoo, J. J. Lee and J. W. Shim, "Cosensitization of metal-based dyes for high-performance dye-sensitized photovoltaics under ambient lighting conditions," *Dyes and Pigments,* vol. 194, p. 109624, 2021.

[38] M. Bruzzi, I. Cappelli, A. Fort, A. Pozzebon and V. Vignoli, "Development of a Self-Sufficient LoRaWAN Sensor Node with Flexible and Glass Dye-Sensitized Solar Cell Modules Harvesting Energy from Diffuse Low-Intensity Solar Radiation," *Energies,* vol. 15, no. 5, p. 1635, 2022.

[39] A. Hande, T. Polk, W. Walker and D. Bhatia, "Indoor Solar energy harvesting for sensor network router nodes," *Microprocessors and 602 Microsystems,* vol. 31, no. 6, pp. 420-432, 2007.

[40] C. Yang, R. Xue, X. Li, X. Zhang and Z. Wu, "Power performance of Solar energy harvesting system under typical indoor light sources," *Renewable Energy,* vol. 161, pp. 836-845, 2020.

[41] M. Bruzzi, I. Cappelli, A. Fort, A. Pozzebon, M. Tani and V. Vignoli, "Polycrystalline silicon photovoltaic harvesting for indoor IoT systems under red-far red artificial light," in *Proceedings of 2021 IEEE Sensors Applications Symposium (SAS)*, Virtual conference, August 2021.

[42] V. Pecunia, L. G. Occhipinti and R. L. Hoye, "Emerging Indoor Photovoltaic Technologies for Sustainable Internet of Things," *Advanced Energy Materials,* p. 2100698, 2021.

[43] I. Cappelli, A. Fort, A. Pozzebon, M. Tani, N. Trivellin, V. Vignoli and M. Bruzzi, "Autonomous IoT Monitoring Matching Spectral Artificial Light Manipulation for Horticulture," *Sensors,* vol. 22, no. 11, p. 4046, 2022.

[44] D. Enescu, "Thermoelectric energy harvesting: basic principles and applications, Chapter 1," in *Green energy advances*, IntechOpen, 2019.

[45] G. J. Snyder, "Thermoelectric Energy Harvesting. Chapter 11," in *Energy Harvesting Technologies*, Springer, 2009.

[46] S. Twaha, J. Zhu, Y. Yan and B. Li, "A comprehensive review of thermoelectric technology: Materials, applications, modelling and performance improvement," *Renewable and sustainable energy reviews,* vol. 65, pp. 698-726, 2016.

[47] G. J. Snyder and E. S. Toberer, "Complex thermoelectric materials," *Materials for sustainable energy ,* pp. 101-110, 2011.

[48] M. Bass, Handbook of Optics: Volume II – Devices, Measurements and Properties, McGraw-Hill, 1995.

[49] A. H. S. Luque, Handbook of photovoltaic science and engineering, John Wiley & Sons, 2011.

[50] V. U. G. A. Hoffman, Photovoltaic Solar Energy Generation. Optical Sciences, Springer, 2005.

[51] M. A. Green, "Self-consistent optical parameters of intrinsic silicon at 300 K including temperature coefficients.," *Solar Energy Materials and Solar Cells,* vol. 92, no. 11, pp. 1305-1310, 2008.

[52] Z. C. D. Holman, B. L. A., F. Z. Fernandez, J. P. Seif, S. De Wolf and C. Ballif, "Current Losses at the Front of Silicon Heterojunction Solar Cells," *IEEE Journal of Photovoltaics,* vol. 2, no. 1, pp. 7-15, 2012.

[53] NREL, "Best Research-Cell Efficiency Chart," [Online]. Available: https://www.nrel.gov/pv/cell-efficiency.html.. [Accessed October 2022].

[54] J. Zhao, A. Wang, M. A. Green and F. Ferrazza, "19.8% efficient "honeycomb" textured multicrystalline and 24.4% monocrystalline silicon solar cells," *Applied physics letters,* vol. 73, no. 14, pp. 1991-1993, 1998.

[55] O. Schultz, S. W. Glunz and G. P. Willeke, "Multicrystalline silicon solar cells exceeding 20% efficiency," *Progress in photovoltaics: Research and Applications,* vol. 12, no. 7, pp. 553-558, 2004.

[56] R. B. Bergmann, C. Berge, T. J. Rinke, J. Schmidt and J. H. Werner, "Advances in monocrystalline Si thin film solar cells by layer transfer," *Solar energy materials and solar cells,* vol. 74, no. 1-4, pp. 213-218, 2002.

[57] "Gcell," [Online]. Available: https://gcell.com/gcell-products/indoor-solar-cells. [Accessed January 2022].

[58] A. Sacco, "Electrochemical impedance spectroscopy: Fundamentals and application in dye-sensitized solar cells," *Renewable and Sustainable Energy Reviews,* vol. 79, pp. 814-829, 2017.

[59] Y. Tachibana, J. E. Moser, M. Grätzel, D. R. Klug and J. R. Durrant, "Subpicosecond interfacial charge separation in dye-sensitized nanocrystalline titanium dioxide films," *The Journal of Physical Chemistry,* vol. 100, no. 51, pp. 20056-20062, 1996.

[60] S. A. Haque, Y. Tachibana, D. R. Klug and J. R. Durrant, "Charge recombination kinetics in dye-sensitized nanocrystalline titanium dioxide films under externally applied bias," *The Journal of Physical Chemistry B,* vol. 102, no. 10, pp. 1745-1749, 1998.

[61] Q. Wang, S. Ito, M. Grätzel, F. Fabregat-Santiago, I. Mora-Sero, J. Bisquert, T. Bessho and H. Imai, "Characteristics of high efficiency dye-sensitized solar cells," *The Journal of Physical Chemistry B,* vol. 110, no. 50, pp. 25210-25221, 2006.

[62] A. Touihri, A. E. and G. R. T., "Transient current effect on the dye sensitized solar cells I–V characterization," *IET Science, Measurement & Technology,* vol. 15, no. 1, pp. 70-76, 2021.

[63] H. Tian, J. Zhang, X. Wang, T. Yu and Z. Zou, "Influence of capacitance characteristic on I–V measurement of dye-sensitized solar cells," *Measurement,* vol. 44, no. 9, pp. 1551-1555, 2011.

[64] K. Takagi, S. Magaino, H. Saito, T. Aoki and D. Aoki, "Measurements and evaluation of dye-sensitized solar cell performance," *Journal of Photochemistry and Photobiology C: Photochemistry Reviews,* vol. 14, pp. 1-12, 2013.

[65] K. D. Jäger, O. Isabella, A. H. Smets, R. A. van Swaaij and M. Zeman, Solar energy: fundamentals, technology and systems, UIT Cambridge, 2016.

[66] G. Callebaut, G. Leenders, J. Van Mulders, G. Ottoy, L. De Strycker and L. Van der Perre, "The Art of Designing Remote IoT Devices–Technologies and Strategies for a Long Battery Life," *Sensors,* vol. 21, p. 913, 2021.

[67] Y. Kadohiro, S. Cheng and J. Cross, "All-Day Energy Harvesting Power System Utilizing a Thermoelectric Generator with Water-Based Heat Storage," *Sustainability,* vol. 12, p. 3659, 2020.

[68] M. Ibrahim, H. Rezk, M. Al-Dahifallah and P. Sergeant, "Hybrid photovoltaic-thermoelectric generator powered synchronous reluctance motor for pumping applications.," *IEEE Access,* vol. 7, p. 146979–146988, 2019.

[69] A. Proto, J. Vondrak, M. Schmidt, J. Kubicek, O. Gorjani, J. Havlik and M. Penhaker, "A Flexible Thermoelectric Generator Worn on the Leg to Harvest Body Heat Energy and to Recognize Motor Activities: A Preliminary Study," *IEEE Access,* vol. 9, p. 20878–20892, 2021.

[70] J. Stevens, "Performance factors for ground-air thermoelectric power generators," *Energy conversion and management,* vol. 68, p. 114–123, 2013.

[71] L. Sigrist, N. Stricker, D. Bernath, J. Beutel and L. Thiele, "Thermoelectric energy harvesting from gradients in the Earth surface," *IEEE Transactions on Industrial Electronics,* vol. 67, p. 9460–9470, 2019.

[72] M. Meli and L. Hegetschweiler, “Harvesting energy from trees in order to power LPWAN IoT nodes.,” in *Proceedings of the Wireless Congress 2018*, Munich, Germany, March 2018.

[73] L. Catalan, A. Garacochea, A. Casi, M. Araiz, P. Aranguren and D. Astrain, “Experimental Evidence of the Viability of Thermoelectric Generators to Power Volcanic Monitoring Stations.,” *Sensors,* vol. 20, p. 4839, 2020.

[74] L. Hou, S. Tan, L. Yang, Z. Zhang and N. Bergmann, “Autonomous Wireless Sensor Node with Thermal Energy Harvesting for Temperature Monitoring of Industrial Devices,” *International Journal of Online Engineering,* vol. 13, pp. 75-82, 2017.

[75] U. Raza, O. Kulkarni and M. Sooriyabandara, “Low power wide area networks: An overview,” *IEEE Communications Surveys & Tutorials,* vol. 19, no. 2, pp. 855-873, 2017.

[76] S. Devalal and A. Karthikeyan, “LoRa Technology - An Overview,” in *2018 Second International Conference on Electronics, Communication and Aerospace Technology (ICECA)*, Coimbatore, India, March 2018.

[77] J. De Carvalho Silva, J. J. Rodrigues, A. M. Alberti, P. Solic and A. L. Aquino, “LoRaWAN low power WAN protocol for Internet of Things: A review andopportunities,” in *2017 2nd International Multidisciplinary Conference on Computer and Energy Science (SpliTech)*, Split, Croatia, July 2017.

[78] LoRa Alliance, LoRaWAN Specification, 2017.

[79] “LoRa Developers,” [Online]. Available: https://lora-developers.semtech.com/documentation/tech-papers-and-guides/lora-and-lorawan/. [Accessed October 2022].

[80] I. Cappelli, A. Fort, M. Mugnaini, S. Parrino, A. Pozzebon and V. Vignoli, “Underwater to above water LoRa transmission: technical issues and preliminary tests,” in *Proceedings of IMEKO TC-4 International Symposium*, September 2020.

[81] I. Cappelli, A. Fort, M. Mugnaini, S. Parrino and A. Pozzebon, “Underwater to above water LoRaWAN networking: Theoretical analysis and field tests,” *Measurement,* vol. 196, p. 111140, 2022.

[82] I. Cappelli, G. Di Renzone, A. Fort, M. Mugnaini, A. Pozzebon and V. Vignoli, “Long Range (LoRa) Transmission Through Ice: Preliminary Results,” in *2021 IEEE*

International Instrumentation and Measurement Technology Conference (I2MTC), Virtual conference, May 2021.

[83] D. Devadiga, M. Selvakumar, P. Shetty and M. S. Santosh, "Dye-Sensitized Solar Cell for Indoor Applications: A Mini-Review," *Journal of Electronic Materials,* pp. 1-20, 2021.

[84] P. Poulose and P. Sreejaya, "Indoor Light Harvesting Using Dye Sensitized Solar Cell," in *Proceedings of 2018 International CET Conference on Control, Communication, and Computing (IC4)*, Thiruvananthapuram, India, July 2018.

[85] M. Rasheduzzaman, P. B. Pillai, Mendoza, A. N. C. and M. M. De Souza, "A study of the performance of Solar cells for indoor autonomous wireless sensors," in *Proceedings of 2016 10th International Symposium on Communication Systems, Networks and Digital Signal Processing (CSNDSP)*, Prague, Czech Republic, July 2016.

[86] A. Aslam, U. Mehmood, M. H. Arshad, A. Ishfaq, J. Zaheer, A. U. H. Khan and M. Sufyan, "Dye-sensitized Solar cells (DSSCs) as a potential photovoltaic technology for the self-powered internet of things (IoTs) applications," *Solar Energy,* vol. 207, pp. 874-892, 2020.

[87] K. Yamamoto, K. Okada, M. Nakayama, T. Taguchi, K. Kaneeda, H. Hayashi and H. Kito, "Wireless environmental sensor node using energy harvesting technology," Fujikura Technical Review, 2015.

[88] C. C. Wu, W. Y. Chuang, C. D. Wu, Y. C. Su, Y. Y. Huang, Y. J. Huang, S. Y. Peng, S. A. Yu, C. T. Lin and S. S. Lu, "A self-sustained wireless multi-sensor platform integrated with printable organic sensors for indoor environmental monitoring," *Sensors,* vol. 17, no. 4, p. 715, 2017.

[89] A. C. Gueymard, "The SMARTS spectral irradiance model after 25 years: New developments and validation of reference spectra," *Solar Energy ,* vol. 187, pp. 233-253, 2019.

[90] "Wunderground," [Online]. Available: https://www.wunderground.com/weather/it/siena/ISIENA36. [Accessed January 2022].

[91] I. Cappelli, F. Carli, A. Fort, F. Micheletti, V. Vignoli and M. Bruzzi, "Self-Sufficient Sensor Node Embedding 2D Visible Light Positioning through a Solar Cell Module," *Sensors,* vol. 22, no. 15, p. 5869, 2022.

[92] Y. Zhuang, L. Hua, L. Qi, J. Yang, P. Cao, Y. Cao, W. Yongpeng, J. Thompson and H. Haas, "A survey of positioning systems using visible LED lights," *IEEE Communications Surveys & Tutorials,* vol. 20, no. 3, pp. 1963-1988, 2018.

[93] S. Sadowski and P. Spachos, "Rssi-based indoor localization with the internet of things.," *IEEE Access,* vol. 6, pp. 30149-30161, 2018.

[94] A. B. M. Rahman, T. Li and Y. Wang, "Recent advances in indoor localization via visible lights: A survey," *Sensors,* vol. 20, no. 5, p. 1382, 2020.

[95] H. Obeidat, W. Shuaieb, O. Obeidat and R. Abd-Alhameed, "A review of indoor localization techniques and wireless technologies," *Wireless Personal Communications,* vol. 119, pp. 289-327, 2021.

[96] B. Wei, W. Xu, C. Luo, G. Zoppi, D. Ma and S. Wang, "SolarSLAM: Battery-free loop closure for indoor localisation," in *2020 IEEE/RSJ International Conference on Intelligent Robots and Systems (IROS)*, Las Vegas, US, October 2020.

[97] W. Mao, H. Xie, Z. Tan, Z. Liu and M. Liu, "High precision indoor positioning method based on visible light communication using improved Camshift tracking algorithm," *Optics Communications,* vol. 468, p. 125599, 2020.

[98] Y. Liu, H. Y. Chen, K. Liang, C. W. Hsu, C. W. Chow and C. H. Yeh, "Visible light communication using receivers of camera image sensor and solar cell," *IEEE photonics journal,* vol. 8, no. 1, pp. 1-7, 2015.

[99] X. Fan and W. D. Leon-Salas, "A circuit for simultaneous optical data reception and energy harvesting," in *2017 IEEE 60th Inter-national Midwest Symposium on Circuits and Systems (MWSCAS)*, Boston, US, August 2017.

[100] C. W. Hsu, J. T. Wu, H. Y. Wang, C. W. Chow, C. H. Lee, M. T. Chu and C. H. Yeh, "Visible light positioning and lighting based on identity positioning and RF carrier allocation technique using a solar cell receiver," *IEEE Photonics Journal,* vol. 8, no. 4, pp. 1-7, 2016.

[101] X. Chen, C. Min and J. Guo, "Visible light communication system using silicon photocell for energy gathering and data receiving," *International Journal of Optics,* 2017.

[102] A. Chaabna, A. Babouri and X. Zhang, "An indoor positioning system based on visible light communication using a solar cell as receiver," in *International Conference in Artificial Intelligence in Renewable Energetic Systems*, Tipaza, Algeria, October 2017.

[103] Y. Umetsu, Y. Nakamura, Y. Arakawa, M. Fujimoto and H. Suwa, "Ehaas: Energy harvesters as a sensor for place recognition on wearables," in *2019 IEEE International Conference on Pervasive Computing and Communications (PerCom)*, Kyoto, Japan, March 2019.

[104] H. Chen, W. Guan, S. Li and Y. Wu, "Indoor high precision three-dimensional positioning system based on visible light com-munication using modified genetic algorithm," *Optics Communications,* vol. 413, pp. 103-120, 2018.

[105] H. Zhang, J. Cui, L. Feng, A. Yang, H. Lv, B. Lin and H. Huang, "High-precision indoor visible light positioning using modi-fied momentum back propagation neural network with sparse training point," *Sensors,* vol. 19, no. 10, p. 2324, 2019.

[106] F. Gu, X. Hu, M. Ramezani, D. Acharya, K. Khoshelham, S. Valaee and J. Shang, "indoor localization improved by spatial context-A survey," *ACM Computing Surveys (CSUR),* vol. 52, no. 3, pp. 1-35, 2019.

[107] M. S. Farooq, S. Riaz, A. Abid, K. Abid and M. A. Naeem, "A Survey on the Role of IoT in Agriculture for the Implementation of Smart Farming," *IEEE Access,* vol. 7, p. 156237–156271, 2019.

[108] R. Shamshiri, F. Kalantari, K. Ting, K. R. Thorp, I. Hameed, C. Weltzien, D. Ahmad and Z. Shad, "Advances in greenhouse automation and controlled environment agriculture: A transition to plant factories and urban agriculture," *International Journal of Agricultural and Biological Engineering,* vol. 11, p. 1–22, 2018.

[109] S. Laura and R. Sumalan, "Plant growth and development monitoring through integrated sensor systems," *Journal of Horticulture, Forestry and Biotechnology,* vol. 17, p. 307–311, 2013.

[110] L. Ting, Z. Man, J. Yuhan, S. Sha, J. Yiqiong and L. Minzan, "Management of CO2 in a tomato greenhouse using WSN and BPNN techniques," *International Journal of Agricultural and Biological Engineering,* vol. 8, p. 43–51, 2015.

[111] K. Ferentinos, N. Katsoulas, A. Tzounis, T. Bartzanas and C. Kittas, "Wireless sensor networks for greenhouse climate and plant condition assessment," *Biosystems engineering,* vol. 153, p. 70–81, 2017.

[112] A. Rennane, F. Benmahmoud, A. Cherif, R. Touhami and S. Tedjini, "Design of Autonomous Multi-Sensing Passive UHF RFID tag for Greenhouse Monitoring," *Sensors and Actuators A: Physical,* vol. 331, p. 112922, 2021.

[113] S. Khan and M. Hussain, "IoT enabled plant sensing systems for small and large scale automated horticultural monitoring," in *Proceedings of the 2019 IEEE 5th World Forum on Internet of Things (WF-IoT)*, Limerick, Ireland, April 2019.

[114] J. Wu, X. Tang and J. Lei, "Design of wireless monitoring system for greenhouse based on LoRa," *Journal of Physics: Conference Series,* vol. 1650, p. 022075, 2020.

[115] K. Mccree, "The action spectrum, absorbance and quantum yield of photosynthesisin cropplants," *Agricultural Meteorology,* vol. 9, p. 191–216, 1972.

[116] M. Rahman, M. Vasiliev and K. Alameh, "LED Illumination spectrum manipulation for increasing the yield of sweet basil (Ocimum basilicum L.)," *Plants,* vol. 10, p. 344, 2021.

[117] M. Lee, J. Xu, W. Wang and C. Rajashekar, "The Effect of Supplemental Blue, Red and Far-Red Light on the Growth and the Nutritional Quality of Red and Green Leaf Lettuc," *American Journal of Plant Sciences,* vol. 10, p. 2219–2235, 2019.

[118] V. Galvao and C. Fankhauser, "Sensing the light environment in plants: Photoreceptors and early signaling steps," *Current opinion in neurobiology,* vol. 34, p. 46–53, 2015.

[119] S. Demotes-Mainarda, T. Peron, A. Corot, J. Bertheloot, J. Le Gourrierec, S. Pelleschi-Travier, L. Crespel, P. Morel, L. Huche-Thelier, R. Boumaz, A. Vian, V. Guerin, N. Leduc and S. Sakr, "Plant responses to red and far-red lights, applications in horticulture," *Environmental and Experimental Botany,* vol. 121, pp. 4-21, 2016.

[120] I. Paucek, G. Pennisi, A. Pistillo, E. Appolloni, A. Crepaldi, B. Calegari, B. Calegari, F. Spinelli, A. Cellini, X. Gabarrell, F. Orsini and G. Gianquinto, "Supplementary LED interlighting improves yield and precocity of greenhouse tomatoes in the Mediterranean," *Agronomy,* vol. 10, p. 1002, 2020.

[121] G. Pennisi, F. Orsini, S. Blasioli, A. Cellini, A. Crepaldi, I. Braschi, F. Spinelli, S. Nicola, J. Fernandez, C. Stanghellini, G. Gianquinto and L. F. M. Marcelis, "Resource

use efficiency of indoor lettuce (Lactuca sativa L.) cultivation as affected by red: Blue ratio provided by LED lighting," *Scientific reports,* vol. 9, p. 14127, 2019.

[122] G. Pennisi, A. Pistillo, F. Orsini, A. Cellini, F. Spinelli, S. Nicola, J. Fernandez, A. Crepaldi, G. Gianquinto and L. Marcelis, "Optimal light intensity for sustainable water and energy use in indoor cultivation of lettuce and basil under red and blue LEDs," *Scientia Horticulturae,* vol. 272, p. 109508, 2020.

[123] M. Johkan, K. Shoji, F. Goto, S. Hashida and T. Yoshihara, "Blue light-emitting diode light irradiation of seedlings improves seedling quality and growth after transplanting in red leaf lettuce," *HortScience,* vol. 45, p. 1809–1814, 2010.

[124] Y. Jestin, "Down-Shifting of the Incident Light for Photovoltaic Applications," in *Comprehensive Renewable Energy*, Elsevier, 2012, pp. 563-585.

[125] TexasInstruments, "bq25570 Nano Power Boost Charger and Buck Converter for Energy Harvester Powered Applications Datasheet," [Online]. Available: https://www.ti.com/lit/ds/symlink/bq25570.pdf.

[126] I. Cappelli, F. Carli, I. Intravaia, F. Micheletti and G. Peruzzi, "A Machine Learning Model for Microcontrollers Enabling Low Power Indoor Positioning Systems via Visible Light Communication," in *In 2022 IEEE Measurement and Networking (M&N)*, July 2022.

[127] I. Cappelli, F. Carli, A. Fort, M. Intravaia, F. Micheletti, G. Peruzzi and V. Vignoli, "Enhanced Visible Light Localization Based on Machine Learning and Optimized Fingerprinting in Wireless Sensor Networks," *IEEE Transactions on Instrumentation and Measurement,* vol. 72, pp. 1-10, 2023.

[128] M. N. Sadiku, Elements of electromagnetics, Oxford university press, 2014.

[129] J. S. Seybold, Introduction to RF propagation, John Wiley & Sons, 2005.

[130] K. P. Hunt, J. J. Niemeier and A. Kruger, "RF communications in underwater wireless sensor networks," in *2010 IEEE International Conference on Electro/Information Technology*, Normal, US, May 2010.

[131] Z. H. I. Sun, I. F. Akyildiz and G. P. Hancke, "Dynamic connectivity in wireless underground sensor networks," *IEEE Transactions on Wireless Communications,* vol. 10, no. 12, pp. 4334-4344, 2011.

[132] G. Hattab, M. El-Tarhuni, M. Al-Ali, T. Joudeh and N. Qaddoumi, “An underwater wireless sensor network with realistic radio frequency path loss model,” *International journal of distributed sensor networks,* vol. 9, no. 3, p. 508708, 2013.

[133] International Telecommunication Union (ITU), Electrical characteristics of the surface of the Earth, 2019.

Publications from the author

[1] Cappelli, I., Fort, A., Mugnaini, M., Panzardi, E., Pozzebon, A., Tani, M., Vignoli, V. Battery-less HF RFID sensor tag for humidity measurements based on TiO2 nanoparticles. In 2020 IEEE International Instrumentation and Measurement Technology Conference (I2MTC), pp. 1-6, May 2020.

[2] Cappelli, I., Fort, A., Mugnaini, M., Parrino, S., Pozzebon, A., Vignoli, V. Underwater to above water LoRa transmission: technical issues and preliminary tests. In Proceedings of IMEKO TC-4 International Symposium, September 2020.

[3] Cappelli, I., Fort, A., Lo Grasso, A., Mugnaini, M., Panzardi, E., Vignoli, V. RH sensing by means of TiO2 nanoparticle, a comparison among different sensing techniques based on modeling and chemical/physical interpretation. *Chemosensors*, **2020**.

[4] Cappelli, I., Fort, A., Mugnaini, M., Panzardi, E., Pozzebon, A., Tani, M., Vignoli, V. Battery-less HF RFID sensor tag for soil moisture measurements. *IEEE Transactions on Instrumentation and Measurement*, **2020**, 70, pp. 1-13.

[5] Cappelli, I., Di Renzone, G., Fort, A., Mugnaini, M., Pozzebon, A., Vignoli, V. Long Range (LoRa) Transmission Through Ice: Preliminary Results. In 2021 IEEE International Instrumentation and Measurement Technology Conference (I2MTC), pp. 1-6, May 2021.

[6] Addabbo, T., Cappelli, I., Fort, A., Mugnaini, M., Panzardi, E., Vignoli, V., Viti, C. The Effect of Au Nanoparticle Addition on Humidity Sensing with Ultra-Small TiO2 Nanoparticles. *Chemosensors*, **2021**, 9(7), 170.

[7] Bruzzi, M., Cappelli, I., Fort, A., Pozzebon, A., Tani, M., Vignoli, V. Polycrystalline silicon photovoltaic harvesting for indoor IoT systems under red-far red artificial light. In 2021 IEEE Sensors Applications Symposium (SAS), pp. 1-6, August 2021.

[8] Cappelli, I., Parrino, S., Pozzebon, A., Salta, A. Providing Energy Self-Sufficiency to LoRaWAN Nodes by Means of Thermoelectric Generators (TEGs)-Based Energy Harvesting. *Energies*, **2021**, 14(21), 7322.

[9] Cappelli, I., Fort, A., Pozzebon, A., Tani, M., Trivellin, N., Vignoli, V., Bruzzi, M. Autonomous IoT Monitoring Matching Spectral Artificial Light Manipulation for Horticulture. *Sensors*, **2022**, 22(11), 4046.

[10] Bruzzi, M., Cappelli, I., Fort, A., Pozzebon, A., Vignoli, V. Development of a Self-Sufficient LoRaWAN Sensor Node with Flexible and Glass Dye-Sensitized Solar Cell Modules Harvesting Energy from Diffuse Low-Intensity Solar Radiation. *Energies*, **2022**, 15(5), 1635.

[11] Cappelli, I., Fort, A., Mugnaini, M., Parrino, S., Pozzebon, A. Underwater to above water LoRaWAN networking: Theoretical analysis and field tests. *Measurement*, **2022**, 196, 111140.

[12] Cappelli, I., Carli, F., Fort, A., Micheletti, F., Vignoli, V., Bruzzi, M. Self-Sufficient Sensor Node Embedding 2D Visible Light Positioning through a Solar Cell Module. *Sensors*, **2022**, 22(15), 5869.

[13] Cappelli, I., Carli, F., Intravaia, I., Micheletti, F., Peruzzi, G. A Machine Learning Model for Microcontrollers Enabling Low Power Indoor Positioning Systems via Visible Light Communication. In 2022 IEEE Measurement and Networking (M&N), July 2022.

[14] Cappelli, I., Carli, F., Fort, A., Intravaia, M., Micheletti, F., Peruzzi, G., Vignoli, V. Enhanced Visible Light Localization Based on Machine Learning and Optimized Fingerprinting in Wireless Sensor Networks. *IEEE Transactions on Instrumentation and Measurement*, **2023**, 72, 1-10.

[15] Pozzebon, A., Cappelli, I., Campagnaro, F., Francescon, R., Zorzi, M. LoRaWAN Transmissions in Salt Water for Superficial Marine Sensor Networking: Laboratory and Field Tests. *Sensors*, **2023**, 23(10), 4726.